Cosmic-Ray All-Electron Spectrum with MAGIC

Yating Chai

MAX-PLANCK-INSTITUT
FÜR PHYSIK

München 2023

Cosmic-Ray All-Electron Spectrum with MAGIC

Yating Chai

Dissertation
an der Fakultät für Physik
der Ludwig–Maximilians–Universität
München

vorgelegt von
Yating Chai
aus Hebei, China

München, den 19. September 2023

Dissertation

an der Fakulät für Physik
der Ludwig-Maximilians-Universität München
vorgelegt von Yating Chai
am 19. September 2023.

Erstgutachter: Prof. Dr. Christian Kiesling
Zweitgutachter: Prof. Dr. Masahiro Teshima
Vorsitzender: Prof. Dr. Gerhard Buchalla
Weiteres Mitglied: Prof. Dr. Katia Parodi

Tag der mündlichen Prüfung: 10. November 2023

Contents

List of Figures

List of Tables

Abstract

Studying high-energy cosmic-ray electrons and positrons is crucial in understanding nearby cosmic-ray sources. These particles experience significant energy loss during their propagation through the Interstellar Medium (ISM) via synchrotron radiation and inverse-Compton scattering, leading to a short and energy dependent path-length in our Galaxy. Electrons and positrons with energies in the TeV ranges are expected to originate from sources within a distance of approximately one kiloparsec. In addition to the astrophysical origin, the possibility of a Dark Matter scenario makes the study of these particles even more intriguing.

Numerous experiments, including balloon-borne and satellite missions, as well as ground-based Imaging Atmospheric Cherenkov Telescopes (IACTs), have extensively studied the energy spectrum of cosmic-ray electrons and positrons. Although IACTs are designed to detect γ-rays, electrons and positrons can also be detected due to the similar air shower development process. Due to their large collection areas, IACTs can provide large statistics electrons and positrons at TeV energies. However, extracting the electron and positron events against the dominating hadronic background remains a significant challenge for IACTs. Additionally, the ability to reconstruct the spectrum of cosmic-ray electrons and positrons demonstrates the capabilities of IACTs to study diffuse sources.

In this thesis, two methods are introduced for estimating the background cosmic-ray hadron events in order to further extract the electron and positron events based on Random Forest (RF) algorithm: the RF-Fit method, which is a template fit method, and the Two-Step RF method, which is a hard cut method based on two steps of RF training. The RF-Fit method is a commonly used technique for analyzing the cosmic-ray electron and positron spectrum with IACTs, which has been validated by instruments like H.E.S.S. and VERITAS. To adapt this method for use with MAGIC, I designed a Monte-Carlo (MC) tracking simulation method to ensure that the simulated background template precisely matches the Field of View (FoV) of the observation data. The Two-Step RF method is a novel approach that uses RF to accurately train between signal events and signal-like background events. By applying a tight cut of a few percent for the electron survival rate, the background events can be reduced to approximately 20%. After thorough evaluations of the systematics, both methods yield consistent reconstructed cosmic-ray electron and positron spectra in the energy range between 300 GeV and 6 TeV. The spectra can be

described by a broken power-law and confirm the presence of an energy break around 900 GeV from MAGIC data for the first time, which is consistent with previous measurements.

Afterwards, the contribution to the cosmic-ray electron and positron spectrum from Supernova Remnant (SNR) and pulsar models are compared with MAGIC data. The model preferred by MAGIC suggests that a Monogem pulsar is a source of the broken power law spectrum, where the pulsar appears above the background but experiences suppression at high energies.

Zusammenfassung

Die Untersuchung von Elektronen und Positronen der hochenergetischer kosmischer Strahlung ist für das Verständnis naher kosmischer Strahlungsquellen von entscheidender Bedeutung, da diese Teilchen während ihrer Ausbreitung durch das interstellare Medium (ISM) durch Synchrotronstrahlung und inverser Compton-Streuung einen erheblichen Energieverlust erfahren, was zu einer kurzen und energieabhängigen Weglänge in unserer Galaxie führt. Es wird erwartet, dass Elektronen und Positronen mit Energien im TeV-Bereich von Quellen in einer Entfernung von etwa einem Kiloparsec stammen. Neben dem astrophysikalischen Ursprung machen auch mögliche Dunkle-Materie-Szenarien die Untersuchung dieser Teilchen noch interessanter.

Zahlreiche Experimente, darunter Ballon- und Satellitenmissionen sowie abbildende atmosphärische Cherenkov-Teleskope (IACTs) auf der Erde, haben das Energiespektrum von Elektronen und Positronen der kosmischer Strahlung eingehend untersucht. Obwohl IACTs für den Nachweis von γ-Strahlen ausgelegt sind, können aufgrund des ähnlichen Entstehungsprozesses der Luftschauer auch Elektronen und Positronen nachgewiesen werden. Aufgrund ihrer großen Sammelflächen können IACTs Elektronen und Positronen bei TeV-Energien in großen Mengen messen. Die Extraktion der Elektronen- und Positronensignale im Vergleich zu dem dominierenden hadronischen Hintergrund bleibt jedoch eine große Herausforderung für IACTs. Die Fähigkeit, das Spektrum von Elektronen und Positronen der kosmischen Strahlung zu rekonstruieren, zeigt allerdings auch die Fähigkeit von IACTs, diffuse Quellen zu untersuchen.

In dieser Arbeit werden zwei Methoden zur Evaluierung der Hintergrundereignisse der kosmischen Hadronenstrahlung vorgestellt, um die Elektronen- und Positronensignale auf der Grundlage des Random-Forest-Algorithmuses (RF) zu extrahieren: die RF-Fit-Methode, eine Template-Fit-Methode, und die Two-Step-RF-Methode, eine Hard-Cut-Methode, die auf zwei Schritten des RF-Trainings basiert. Die RF-Fit-Methode ist eine weit verbreitete Technik zur Analyse des Elektronen- und Positronenspektrums kosmischer Strahlung mit IACTs, die von Instrumenten wie H.E.S.S. und VERITAS validiert wurde. Um diese Methode für die Verwendung mit MAGIC anzupassen, habe ich eine Monte-Carlo (MC) Tracking-Simulationsmethode entwickelt, um sicherzustellen, dass die simulierte Hintergrundvorlage genau dem Sichtfeld (FoV) der Beobachtungsdaten entspricht. Die zweistufige RF-Methode ist ein neuartiger Ansatz, der RF verwendet, um exakter zwischen Sig-

nalereignissen und signalähnlichen Hintergrundereignissen zu unterscheiden. Durch die Anwendung eines harten Kriteriums von einigen Prozent für die Elektronenüberlebensrate können die Hintergrundereignisse auf etwa 20 Prozent reduziert werden. Nach gründlicher Auswertung der Systematik, liefern beide Methoden konsistente rekonstruierte Elektronen- und Positronenspektren der kosmischen Strahlung im Energiebereich zwischen 300 GeV und 6 TeV. Die Spektren können durch ein gebrochenes Potenzgesetz beschrieben werden und bestätigen zum ersten Mal das Vorhandensein eines Energiebruchs um 900 GeV aus MAGIC-Daten, was mit früheren Messungen übereinstimmt.

Anschließend wird der Beitrag zum Elektronen- und Positronenspektrum der kosmischen Strahlung von Supernovaüberresten (SNR) und Pulsarmodellen mit MAGIC-Daten verglichen. Das von MAGIC bevorzugte Modell legt nahe, dass ein Monogem-Pulsar die Quelle des gebrochenen Potenzspektrums ist, wobei der Pulsar über dem Hintergrund erscheint, aber bei hohen Energien unterdrückt wird.

Chapter 1

Cosmic-Ray Electrons and Positrons

In this chapter, I will provide an introduction to the spectrum of cosmic-ray electrons and positrons, building upon the energy spectrum of all particle components, which is referred to as the all-particle cosmic-ray spectrum discussed in Section 1.1. Cosmic-ray electron and positron spectrum as part of the all-particle cosmic-ray spectrum and the object of this thesis is introduced in Section 1.2. In Section 1.3, the transport and energy loss of cosmic-ray electrons and positrons are introduced. As energy loss is vitally important for the cosmic-ray electrons and positrons, this point is explained in detail. The possible sources contributing to the observed cosmic-ray electrons and positrons are introduced in Section 1.4.

1.1 Cosmic Rays

Cosmic Rays (CRs) were discovered by the Austrian physicist Victor HESS in 1912 (Hess, 1912). Although discovered more than 100 years ago, there are still many unanswered questions about them, such as their spectrum, origin, and composition. In this section, I will briefly introduce CRs from three aspects: the all-particle cosmic-ray energy spectrum, the composition of the local CRs, and their origin.

1.1.1 Spectrum

Figure 1.1 shows the all-particle cosmic-ray energy spectrum alongside the spectra of protons (p), antiprotons ($\bar{p}$), electron and positron ($e^+ + e^-$), positron only (e^+), Diffuse Galactic Emission (DGE) (γ) generated from Galactic CRs interactions with the ISM, the Isotropic Gamma-Ray Background (IGRB), representing residual all-sky gamma-ray emissions, and the upper limits on neutrinos ($\nu + \bar{\nu}$). In our analysis, it is not possible to discern between all-electrons and γ-rays. However, the contribution from γ-rays is less than 1% thanks to the careful data selection.

Additionally, the estimated rates of all-particle flux at energies of 100 GeV, 3 PeV, and 5

EeV are indicated on the plot. The differential energy spectrum is described by power-law distributions, with the index α of $dN/dE \propto E^{-\alpha}$ varying. Below the *knee*, at the energy between 10^{15} eV and 10^{16} eV (around 3 PeV), the spectrum has $\alpha \sim 2.7$. Above the *knee*, the spectrum steepens at the *second knee* at 10^{17} eV (100 PeV), with $\alpha \sim 3.1$. Above $10^{18.5}$ eV (3 EeV) so called the *ankle*, the spectrum flattens to $\alpha \sim 2.6$ and reaching a cutoff at around 5×10^{19} eV (Workman and Others, 2022; Gaisser et al., 2016). The cosmic-ray spectra span an extensive range of 12 decades from 10^9 eV to 10^{21} eV. CRs such as protons, helium, and heavier particles with energies below a few hundred TeV per nucleus can be directly detected by satellites outside the Earth's atmosphere or by high-altitude balloon experiments. To explore the higher energy range, detectors with larger collection areas are needed, and indirect air shower detectors on the ground play a crucial role in this regard.

1.1.2 Composition and Origin

In general, protons account for 90%, and helium accounts for 9% of the CRs. The remaining 1% are heavier nuclei, electrons, positrons, and antiprotons, etc. (Workman and Others, 2022). However, the composition of CRs is different depending on the energy range. The composition spectra can be described in four different ways:

- Particles per energy-per-rigidity, which assumes that the behavior of protons, helium, and other nuclei at a given rigidity is the same. The rigidity is defined as $R = \frac{pc}{Ze} = r_L B$, where r_L is the gyroradius and B is the magnetic field;
- Particles per energy-per-nucleon, which determines the fragmentation of nuclei;
- Nucleons per energy-per-nucleon, which is related to the intensity of nucleons per energy-per-nucleon produced as secondary CRs in the atmosphere;
- Particles per energy-per-nucleus, which is related to air shower experiments that measure the energy of individual particles per energy-per-nucleus.

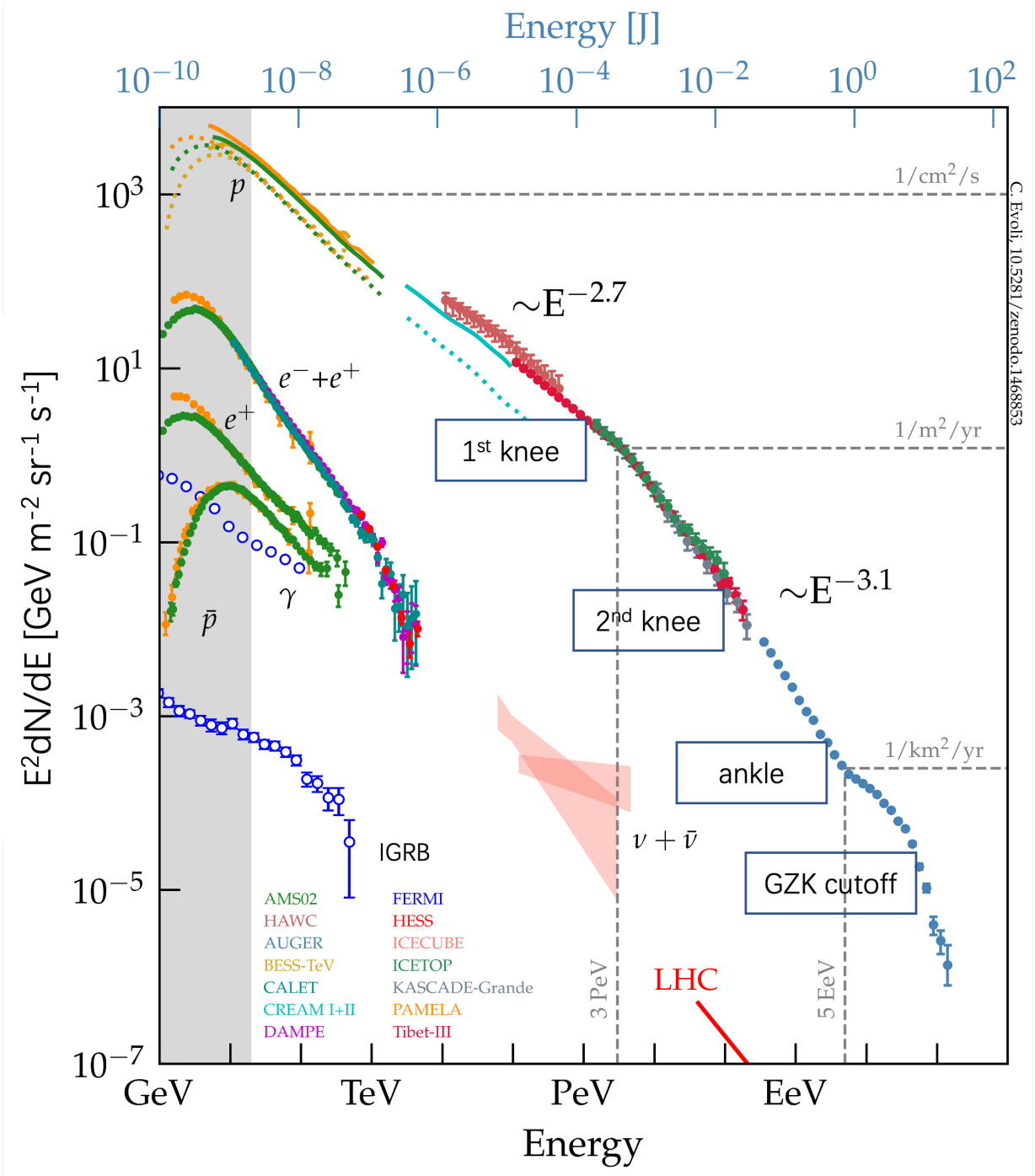

Figure 1.1: Whole range all-particle cosmic ray energy spectra with data form different measurements. Adapted from Evoli (2018).

The relative abundance of each element in CRs varies across different energy ranges and types of spectra. As shown in Figure 1.2, fluxes of primary protons and helium in number of particles per energy-per-nucleus are comparable to each other, however, the H/He ratio

of particles per energy-per-rigidity is around 3/1 for particle with rigidity of 1000 GeV. In this thesis, my work is the study of CRs using the data of the air shower experiment MAGIC, so my focus is on the composition of CRs in terms of the number of particles per energy-per-nucleus. This is important when considering the background contamination in my study. For very high-energy CRs, the individual elements are very difficult to measure separately, and models proposed by Globus et al. (2015), Aab and et al. (2016), Unger et al. (2015) have been developed to predict the compositions.

The origin of the CRs is still not completely understood, but it is quite established that high-energy CRs are from outside the solar system with only a few particles from solar activity influencing the spectrum at several GeV levels. Particles below the *knee* are believed to be accelerated by the Galactic sources, however, the specific source remains unknown. Sources that can accelerate the particles up to PeV are the so-called "PeVatrons". The *knee* indicates the maximum energy of protons that can be accelerated by most energetic accelerators in our Galactic. The *second knee* is believed to have the same origin as the *knee* but is caused by the steepening of the heavy Galactic nuclei (such as iron), which become dominant slightly below 10^{17} eV (Globus et al., 2015). The composition above the first *knee* cannot be directly discerned through detection alone. The detector can only provide the spectrum encompassing all elements. However, various models exist to predict the composition in this energy range, including models considering both light nuclei and heavy nuclei (Workman and Others, 2022). Finally, the possible origin of the *ankle* is the extragalactic flux starting to govern the spectrum (Bird et al., 1994). As ultra-high-energy CRs travel through extragalactic distances, they are expected to undergo inelastic interactions with the cosmic microwave background, which leads to a rapid change in the spectrum (known as the GZK feature) at around 5×10^{19} eV.

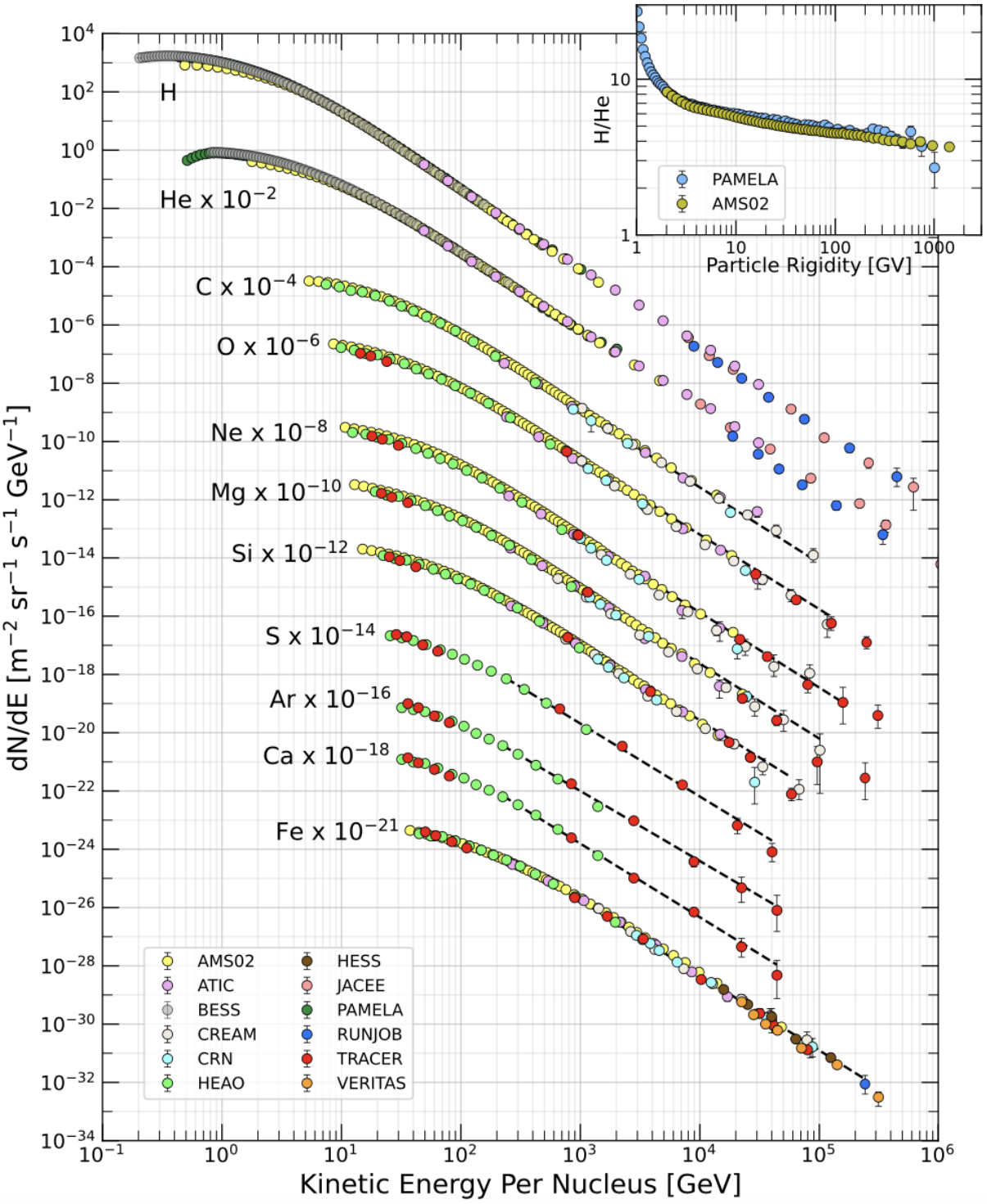

Figure 1.2: Fluxes of primary particles per energy-per-nucleus. The plot in the inset shows the ratio of H/He as a function of rigidity (Workman and Others, 2022)

1.2 Cosmic-Ray Electrons and Positrons

Cosmic-ray electrons and positrons the so-called all-electrons ($e^+ + e^-$) account for a relatively small fraction of the all-particle CRs, comprising less than 1% of the total cosmic-ray population. Despite their small contribution, they are crucial in investigating nearby sources because of their significant energy loss at the TeV scale. Among the all-electron components, positrons also constitute a minor fraction of approximately 10% (Aguilar and et al., 2013). The positron fraction spectrum is particularly important for exploring possible sources. This section introduces the observation and energy spectrum of the all-electron spectrum and the positron fraction spectrum.

1.2.1 All-Electron Spectrum

Direct observation of the all-electron spectrum ($e^+ + e^-$) has been performed by space-based measurements like PAMELA (Adriani and et al., 2011) (note: the data in this PAMELA paper includes electrons only), AMS-02 (Aguilar and et al., 2019), CALET (Adriani et al., 2017), DAMPE (Ambrosi et al., 2017) and *Fermi*-LAT (Abdollahi et al., 2017), as well as the balloon-borne experiment CAPRICE (Boezio et al., 2000). Among them, the very low energy range ($E \lesssim 10$GeV) is covered by PAMELA, AMS-02 and CAPRICE as shown in Figure 1.3 (the data are plotted in square markers). Solar modulation can account for the differences of the flux from these three experiments for $E \lesssim 20$GeV, since the data were taken during different time intervals. The spectrum steepening at 5 GeV is an obvious feature in the all-electron spectrum. Data from AMS-02, PAMELA, DAMPE, CALET and *Fermi*-LAT have a very good consistency with each other from 10 GeV to around 300 GeV.

For energy above 300 GeV, indirect measurements can be performed with ground-based IACTs. Thanks to their large collection areas (of the order of $1km^2$), IACTs can provide large event statistics for CR studies. The data from direct measurements DAMPE, CALET and *Fermi*-LAT and indirect measurements H.E.S.S. (Aharonian et al., 2008; Aharonian, F. and et al., 2009) and VERITAS (Staszak, 2015) are in general consistent with each other within the statistical error. There is a break around 1 TeV, which was first detected by H.E.S.S. and confirmed by VERITAS, DAMPE and CALET. The MAGIC collaboration reported a single power-law all-electron spectrum in two previous studies, one in 2011 (D. Borla Tridon, 2011) and the other in 2017 (Mallot, 2017). These studies had limitations stemming from, among several causes, the usage of data taken with only one telescope for the former study, and the usage of a less performant energy estimation method for the latter. Compared to those studies, many novelties have been introduced in the MAGIC analysis chain, together with a better understanding of the instrument, leading to an improved performance of the MAGIC telescopes. Therefore, we took advantage of such improvements to study the all-electron spectrum with MAGIC once again.

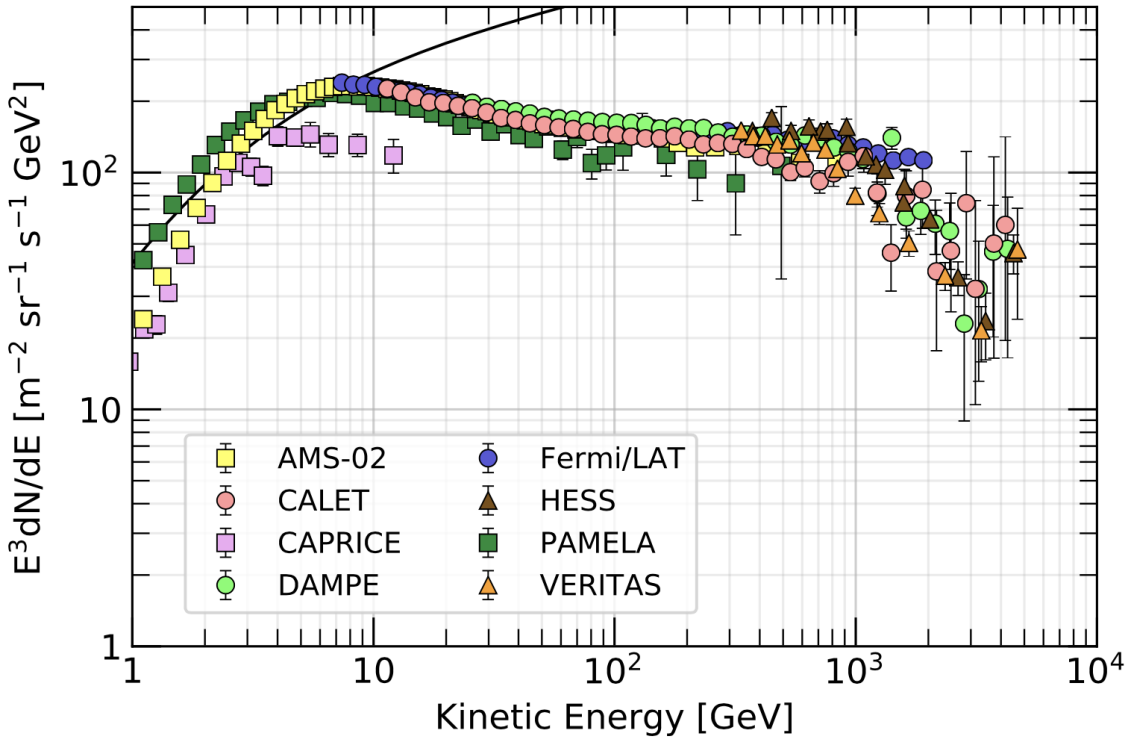

Figure 1.3: The cosmic-ray all-electron spectrum multiplied by E^3. The black line represents the proton spectrum divided by 100, as summarized by the Particle Data Group (PDG) (Workman and Others, 2022).

1.2.2 Positron Fraction

For IACTs, electrons and positrons are indistinguishable, and thus, only the sum of these two components can be measured by MAGIC. Antiparticles normally contribute only a small fraction to the CRs. The positron fraction f_{e^+}, defined in Equation 1.1:

$$f_{e^+}(E) = \frac{\Phi_{e^+}(E)}{\Phi_{e^+}(E) + \Phi_{e^-}(E)} \tag{1.1}$$

with $\Phi_{e^+}(E)$ and $\Phi_{e^-}(E)$ the flux of positrons and electrons at energy E respectively. Figure 1.4 shows the positron fraction spectra measured by several experiments, including AMS-02 (Aguilar and et al., 2013; Accardo and et al., 2014), PAMELA (Adriani, 2009; Adriani et al., 2009), and the balloon-borne HEAT-pbar instrument (Beatty et al., 2004; Barwick et al., 1997). These detectors, which include magnets, can determine the sign of a charged particle based on the bending direction. The Figure 1.4 demonstrates a significant deviation from the "standard model" represented by the thick black line (refer to Section 5.1) for energies above 10 GeV, which has gained considerable attention. The latest measurement from AMS-02, also presented in Figure 1.4, suggests a possible cutoff

at a few hundred GeV for the first time, which could help distinguish the origin of the positron excess.

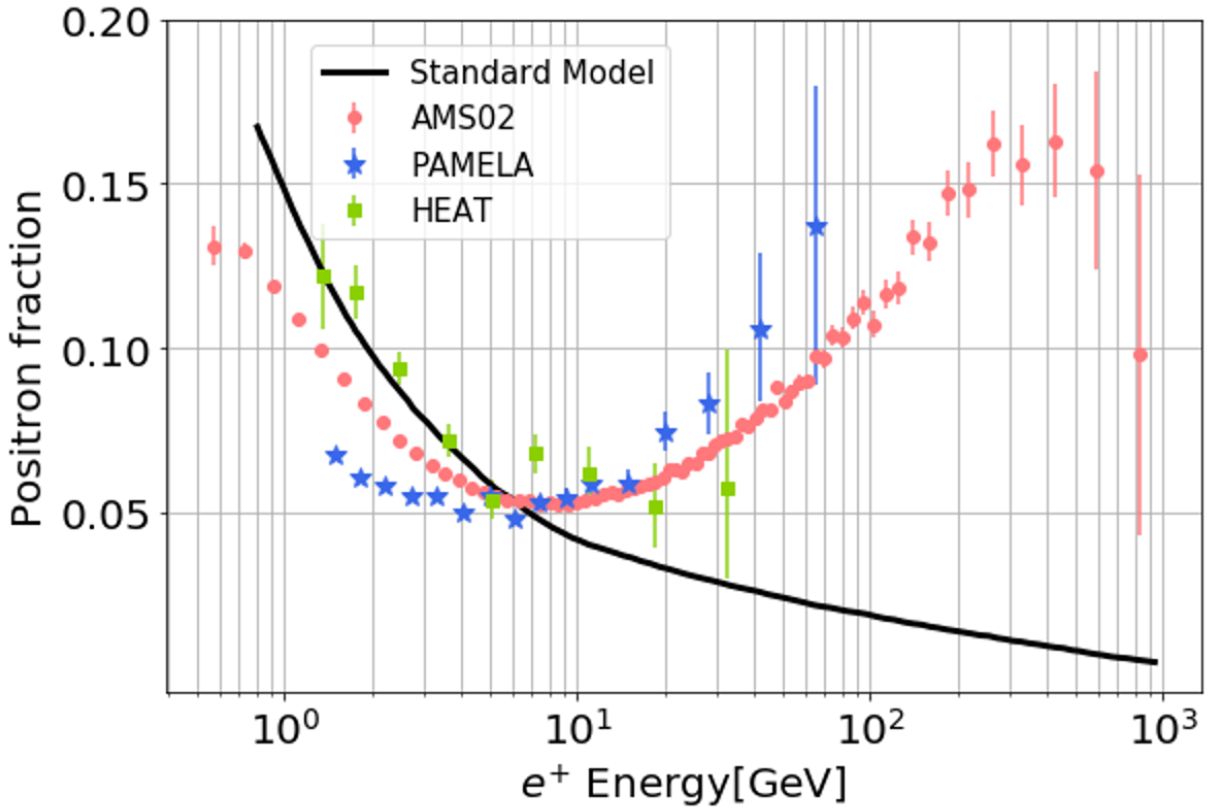

Figure 1.4: The positron fraction (ratio of the flux of positron to the flux of all-electron). The heavy black line represents a model of pure secondary production (Blasi, 2009).

1.3 Propagation and Energy Loss for Cosmic-Ray Electrons and Positrons

This Section discusses the processes affecting electrons and positrons during their propagation before they are detected at Earth. Once they are produced, these particles diffuse from their sources and experience continuous energy loss. The transport equation of electrons can be written as in Longair (2011):

$$\frac{\partial N(E,t)}{\partial t} = \nabla \cdot [D(E)\nabla N(E,t)] + \frac{\partial}{\partial E}[b(E)N(E,t)] + Q(E,t) \tag{1.2}$$

Where $N(E)$ is the number of electrons and positrons with energy E, $D(E)$ is the diffusion coefficient, $Q(E)$ is the continuous injection of the particles from the source, and $b(E)$ describes the energy loss. Here, the effects of convection and re-acceleration on electrons

are neglected, as they are not important when their energy exceeds a few GeV (Delahaye, T. et al., 2009).

1.3.1 Diffusion

The amount of matter that GeV energy CRs can traverse is approximately 5-10 g/cm^2 on average (Gaisser et al., 2016). Compared with the thickness of the Galactic disk (around 10^{-3} g/cm^2), CRs travel through an amount of matter thousands of times greater than the thickness of the Galactic disk due to the diffusion process (Gaisser et al., 2016). As charged particles travel through the ISM, they interact with the Galactic magnetic field, which has a strength of approximately 3 μG (Gaisser et al., 2016). This magnetic field can be approximated by a homogeneous field with turbulence. The turbulent electric and magnetic fields are caused by a magnetohydrodynamic fluid, which consists of interstellar plasma and magnetic field. Irregularities in the magnetic field lead to the random walk of cosmic-ray particles (Shalchi, 2009; Moraal, 2013). Figure 1.5 provides some examples of distorted magnetic fields and illustrates how charged particles diffuse around them.

The term $\nabla \cdot [D(E)\nabla N(E,t)]$ in Equation 1.2 represents the diffusion process, which has a significant impact on the spectral index of observed CRs. For instance, the spectrum of protons in acceleration sites is expected to have an index of approximately -2. However, due to the diffusion process, the observed spectrum appears softer, with an index of around -2.7. More details regarding this phenomenon will be discussed in the propagation models presented in Section 1.3.3.

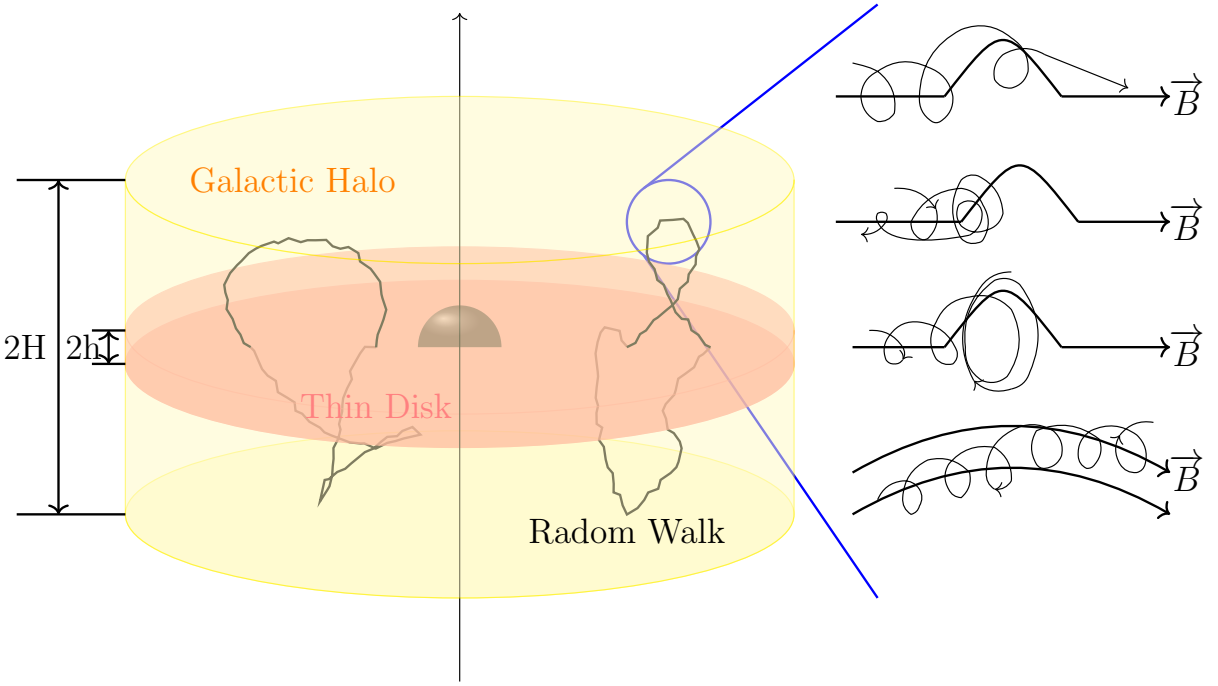

Figure 1.5: Cosmic-ray propagation region in the Galaxy. The pink region illustrates the thin disk with a height of $h \approx 150$ pc and radius $R \approx 20$ kpc, where cosmic-ray sources and molecular clouds predominantly reside. The magnetic halo, represented by the light yellow region, has a height of $H \approx 4$ kpc, which is much larger than the thin disk but much smaller than R ($h \ll H \ll R$). The black lines depict the random walk of cosmic-ray particles in the Galaxy, scattered by the irregular magnetic fields. On the right-hand side, several examples of charged particle trajectories in different magnetic fields are shown: particles are scattered forward, backward, or confined in the first three cases, and drift to a neighboring magnetic field line in the last example.

1.3.2 Energy Losses

Ionisation Losses

When high-energy charged particles pass through a material, the electrons of the atoms and molecules of the material are removed by the electrostatic force acting on the electrons by the high-energy charged particles. The ionisation loss rate is:

$$\left(\frac{dE}{dt}\right)_{ion} = -7.64 \times 10^{-15} n(3\ln\gamma + 1.98)\ eVs^{-1} \propto \ln\gamma \tag{1.3}$$

where n is the number density of hydrogen atoms in the unit particles m^{-3} with $n = 10^6$ in the ISM, and γ is the Lorentz factor of the particle.

Bremsstrahlung

When a moving charged particle is deflected by another charged particle, it decelerates, and the electromagnetic radiation is produced, called bremsstrahlung radiation. The reduction in the kinetic energy of the moving particle is converted into the production of a photon. The energy loss rate in case of ultra-relativistic electrons via bremsstrahlung is proportional to E, considering $\gamma = E/(mc^2)$, therefore is proportional to γ:

$$\left(\frac{dE}{dt}\right)_{brems} = -4nZ^2 r_e^2 \alpha c \bar{g} E \propto E \propto \gamma, \tag{1.4}$$

where α is the fine structure constant, Z is the atomic number of the atom of the medium and Z^2 can be replaced by $Z\,(Z+1.3)$ in case the interactions with the bound electrons are taken into account. The classical electron radius r_e is equal to $e^2/\left(m_e c^2\right) = 2.818 \times 10^{-13}$ cm; $\bar{g}$ is a Gaunt factor and defined as:

$$\bar{g} = \begin{cases} \ln\gamma + 0.36, & \text{if nuclei are unscreened} \\ \ln\left(183Z^{-1/3}\right) - \frac{1}{18}, & \text{if nuclei are total screened} \end{cases} \tag{1.5}$$

Synchrotron Radiation

When relativistic electrons are traveling in the magnetic field, they gyrate along the magnetic field lines and emit synchrotron radiation. The total rate of energy loss due to synchrotron radiation can be calculated using the expression given by Longair (2011):

$$\left(\frac{dE}{dt}\right)_{sync} = -\frac{4}{3}\sigma_T c u_B \beta^2 \gamma^2 \propto \gamma^2 \tag{1.6}$$

where σ_T is the Thomson cross section:

$$\sigma_T = 8\pi r_e^2/3 \tag{1.7}$$

where u_B is the energy density in the magnetic field, defined as $u_B = \frac{B^2}{8\pi}$; and $\beta = v/c$ is the velocity of the electrons relative to the speed of light c.

Inverse Compton Scattering

In the inverse Compton Scattering process, low energy photons are scattered to higher energy by ultra-relativistic electrons. During the process, the electron loses kinetic energy while the photon gains energy. Two regimes can be defined according to the energy of photon in the electron rest frame:

- Thomson regime: When the energy of the photon in the electron rest frame is much lower than the rest mass of electron, i.e., $\gamma\hbar\omega \ll m_e c^2 \approx 511$keV. The Thomson cross section (as given in Equation 1.7) can be used for the interaction between the radiation field and the electron.

- Klein-Nishina regime: When the energy of photon in the electron rest frame is larger than the rest mass of electron $\gamma\hbar\omega \gg m_e c^2$. The cross section of the process is defined as in Equation 1.8. The scattering is less efficient compared to the Thomson scattering, so the energy-loss is suppressed in the high-energy range.

$$\sigma_{KN} = \sigma_T \frac{3}{4} \left\{ \frac{1+x}{x^3} \left[\frac{2x\,(1+x)}{1+2x} - \ln\left(1+2x\right) \right] + \frac{1}{2x} \ln\left(1+2x\right) - \frac{1+3x}{\left(1+2x\right)^2} \right\} \quad (1.8)$$

  where $x = 2\pi\omega/m_e c^2$.

The energy loss rate via inverse Compton scattering in the Thomson regime is (Longair, 2011):

$$\left(\frac{dE}{dt}\right)_{IC} = -\frac{4}{3}\sigma_T c u_{ph} \beta^2 \gamma^2 \propto \gamma^2. \quad (1.9)$$

Here, $u_{\rm ph}$ represents the energy density of target photons, which corresponds to the Interstellar Radiation Fields (ISRFs) involved in inverse Compton scattering. The ISRFs include the cosmic microwave background radiation at 0.26 eV cm^{-3}, optical and ultraviolet radiation from stars at 0.45 eV cm^{-3}, and infrared radiation from dust at 0.20 eV cm^{-3} (Mathis et al., 1983). After considering the Klein-Nishina effect, the energy loss is given as (Fang et al., 2021):

$$\left(\frac{dE}{dt}\right)_{IC(KN)} = -\frac{20 c \sigma_T u_{ph} \gamma^2}{\pi^4 m_e c^2} Y(\gamma, T). \quad (1.10)$$

In this expression, $Y(\gamma, T)$ represents a segmented function, which can be expressed as $Y(\alpha)$ in terms of $\alpha = 4\gamma kT/(m_e c^2)$. There is a transition phase from the Thomson regime to the extreme Klein-Nishina regime. For the low-energy range, Equation 1.10 is well approximated by Equation 1.9. In the intermediate regime, a sixth-order polynomial function is employed.

The expression in Equation 1.9 is quite similar to the total energy loss rate of a relativistic electron due to synchrotron radiation, as shown in Equation 1.6. This similarity arises because the electron does not care about the origin of the electric field; it only depends on the electric field accelerating the electron in its instantaneous rest-frame. In the case of inverse Compton scattering, the electric field experienced by the electron originates from the incident electromagnetic wave. For synchrotron radiation, the electric field is generated by the motion of the electron in the magnetic field ($\boldsymbol{v} \times \mathbf{B}$).

Energy Loss Time

Once the energy loss is known, the energy loss time can be defined as:

$$t^i_{loss}\left(E\right) = \left(-\frac{1}{E} \left(\frac{dE}{dt}\right)_i \right)^{-1}, \quad (1.11)$$

where the index i indicates different energy loss processes. The energy loss term in Equation 1.2 is given by Equation 1.12.

$$b(E) = -\sum_i \left(\frac{dE}{dt}\right)_i = A_1 \left(ln\frac{E}{m_e c^2} + 19.8\right) + A_2 E + A_3 E^2. \tag{1.12}$$

The cooling timescale of an electron due to different energy-loss mechanisms are shown in the Figure 1.6. The energy loss rate of an high-energy electron is dominated by inverse Compton and synchrotron radiation, which is proportional to E^2 and therefore increases rapidly with the electron energy. The energy loss due to ionization and bremsstrahlung can be neglected on average. Ultimately, the total energy loss term is expressed as in Equation 1.13.

$$\frac{dE}{dt} = -A_3 E^2 \tag{1.13}$$

The term A_3 can be expressed as in Equation 1.14. By only considering the energy loss from Equation 1.6 and Equation 1.9, and taking into account $\beta = 1$ in the ultrarelativistic case.

$$A_3 = \frac{4}{3}\sigma_T c \left(\frac{1}{m_e c^2}\right)^2 \left(\omega_{ph} + \frac{B^2}{8\pi}\right) \tag{1.14}$$

Finally, the cooling time in total is expressed as:

$$t_{loss}^{total}(E) = \left(\sum_i \frac{1}{t_{loss}^i(E)}\right)^{-1} \simeq \frac{1}{A_3 E} \tag{1.15}$$

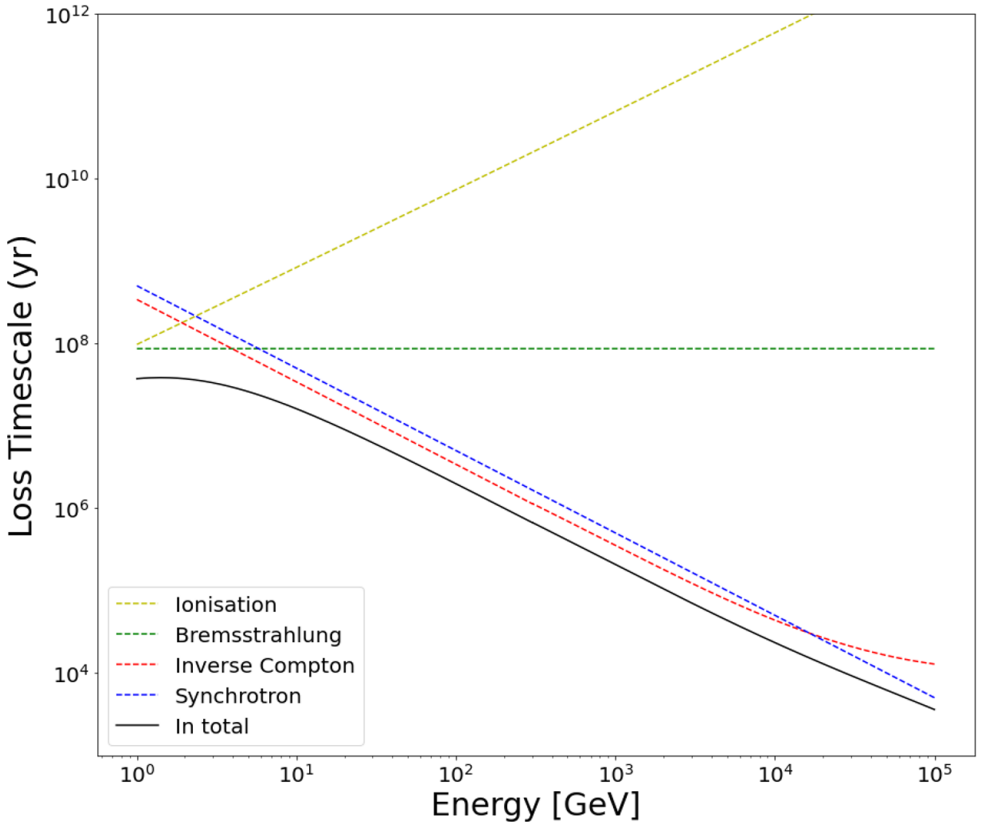

Figure 1.6: The electrons' energy loss timescale, estimated in years within the ISRFs. The cooling timescale of an electron due to ionization, bremsstrahlung, synchrotron, and inverse Compton processes is shown with yellow, green, blue, and red lines, respectively. The Klein-Nishina effect is taken into consideration in the inverse Compton scattering process. The timescale for an electron to loose all its energy through these four mechanisms is depicted by the black solid line.

1.3.3 Propagation Models

The Leaky Box Model

The *Leaky box* model is a very simple model to describe the cosmic-ray confinement volume. In the *leaky box* model, the high-energy CRs are reflected at the boundaries, and at each encounter of the boundaries they have a constant probability of escaping per unit time, given by τ_{esc}^{-1} (a Poisson process) from the volume. Inside the confinement volume, the density of CRs is uniform, and CRs propagate freely. After time t, a particle remains inside the confinement volume with probability $\exp[-t/\tau_{esc}]$. On average, the time of a particle stays within the confinement volume is τ_{esc} and the amount of matter traversed is $\lambda_{esc} = \rho\beta c\tau_{esc}$, where ρ is the average background density and $\beta = v/c$ is the velocity of the CRs relative to the speed of light c.

As mentioned in Section 1.3.1, cosmic-ray particles can travel the amount of matter thousands of times larger than the thickness of the Galaxy's disk ($c\tau_{esc} \gg h$), so the diffusion term in Equation 1.2 can be substituted by the term N/τ_{esc}. If we ignore the energy loss term and $N(E)$ is constant in time, the relation between observed spectrum $N(E)$ and source spectrum $Q(E)$ can be described as:

$$N(E) = Q(E)\tau_{esc}(E) \tag{1.16}$$

The observed all-electron spectrum is determined by the source spectrum and how τ_{esc} changes with energies $\tau_{esc} \propto E^{-\delta}$. δ can be estimated by primary-to-secondary ratios, for example the Boron to Carbon ratio, which is around 0.333 (Aguilar and et al., 2016b).

Diffusion Model

The *Leaky Box* model is a very rough approximation in which the distribution of CRs is treated uniformly. A more realistic model, called the Diffusion model, takes density gradients into account (Ginzburg and Syrovatskii, 1964; Ptuskin, 2012). A sketch of the diffusion model is shown in Figure 1.5. In this model, the Galaxy is assumed to be cylindrical. The cylinder's radius, $R \approx 20$kpc, is much larger than its height, $H \approx 4$kpc. Cosmic-ray sources are distributed within the Galactic disk, which has a height of $h \approx 150$pc. CRs produced in the disk reach the surfaces at height H and then permanently escape from the system. The characteristic time of escape can be expressed as:

$$T_H \approx \frac{H^2}{2D}. \tag{1.17}$$

Assuming the halo of the Galaxy has a height $H \gg h$ and a gas density much lower than that in the disk. The gas density in the disk is denoted as $\rho_g\,(\sim 1\ proton/cm^3)$. If we assume that the gas in the disk is distributed uniformly over the entire volume of both the halo and the disk, the mean gas density of the entire volume can be expressed as follows:

$$\rho_H = \rho_g \frac{h}{H} \tag{1.18}$$

The escape length in the diffusion model is:

$$\lambda_{esc} = \rho_H \beta c t_H = \rho_g \beta c \frac{hH}{D}, \tag{1.19}$$

where, $\lambda_{\rm esc}$ is a function of energy, with $\lambda_{\rm esc} \propto E^{-\delta}$, which implies that $H/D \propto E^{-\delta}$. Once again, the index δ can be estimated from the ratio of boron to carbon.

Considering the diffusion coefficient as $D = (2-5) \times 10^{29}\,(E/\mathrm{TeV})^{0.3}\,(\mathrm{cm^2 s^{-1}})$ for the energy range from 50 GeV to 1 TeV (Kobayashi et al., 2004), and the energy loss timescale as $T = 1/bE = 2.5 \times 10^5 \mathrm{yr}/\,(E/\mathrm{TeV})$, after accounting for the Klein-Nishina effect, the diffusion distance $X = \sqrt{2DT}$ is 0.6-0.9 kpc for energy at 1 TeV. This suggests that TeV cosmic-ray electron sources must be local.

1.4 Production of Cosmic-Ray Electrons and Positrons

In the previous section, I described the propagation effects for cosmic-ray electrons and positrons. To understand the all-electron spectrum measured at Earth, it is necessary to investigate two more important aspects. The first aspect is the acceleration mechanism, and the second is the sources responsible for the acceleration.

1.4.1 Acceleration Mechanism

The Second-Order Fermi Acceleration

Enrico Fermi proposed an idea for cosmic-ray acceleration in 1949 (Fermi, 1949) . Particles are accelerated by the reflection of moving Galactic clouds, which carry magnetic fields, as illustrated in Figure 1.7. When a particle with energy E_1 encounters a cloud moving with velocity V in the Galactic rest frame, and the incidence angle is θ_1, the particle in the cloud will be caused by the irregular magnetic field of the cloud, and the outgoing angle $\theta_2^{'}$ is randomized. Due to the change of the reference frame, before scattering, the energy of the particle in the cloud's rest frame is $E_1^{'}$. After scattering, the energy is $E_2^{'}$ in the cloud's reference frame and E_2 in the Galactic reference frame. The relation between E_1 and $\mathrm{E}_1^{'}$, E_2 and $\mathrm{E}_2^{'}$ is calculated in Equation 1.20:

$$\begin{cases} E_1^{'} = \gamma E_1 \left(1 - \beta \cos\theta_1\right) \\ E_2 = \gamma E_2^{'} \left(1 + \beta \cos\theta_2^{'}\right) \end{cases} \tag{1.20}$$

where γ is the Lorentz factor and $\beta = \frac{V}{c}$ is the velocity of the cloud in the Galactic frame, respectively.

Inside the cloud, it is generally assumed (with a reasonable level of approximation) that only the particle's direction is changed, and the energy of the particle in the cloud frame has the relation: $E_2^{'} = E_1^{'}$. Suppose the particles are sufficiently relativistic, i.e., $E \simeq pc$. Together with Equation 1.20, we can obtain the expression of E_2 in terms of E_1 and the energy change for a particular encounter (incident angle θ_1 and flying-out angle $\theta_2^{'}$):

$$E_2 = \gamma^2 E_1 \left(1 - \beta \cos\theta_1\right) \left(1 + \beta \cos\theta_2^{'}\right) \tag{1.21}$$

$$\frac{\Delta E}{E} = \frac{E_2 - E_1}{E_1} = \frac{\beta^2 - \beta\cos\theta_1 + \beta\cos\theta_2^{'} - \beta^2\cos\theta_1\cos\theta_2^{'}}{1 - \beta^2} \tag{1.22}$$

The particles experience an isotropic diffusion in the clouds, hence $\left\langle \cos\theta_2^{'} \right\rangle = 0$. The probability of a collision with an incidence angle θ_1 is proportional to the relative velocity between the particle and the cloud, i.e., $P\left(\theta_1\right) \propto c - V\cos\theta_1$, so that $\left\langle \cos\theta_1 \right\rangle = -\beta/3$.

Substituting the averaged values of θ_1 and θ_2' into Equation 1.21, the average energy change is:

$$\left\langle \frac{\Delta E}{E} \right\rangle \approx \frac{4\beta^2}{3} \tag{1.23}$$

On average, particles gain energy, but each individual particle may either gain or lose energy depending on the specific configuration of the encounter. The average energy gain ratio is proportional to β^2, which characterizes the acceleration mechanism known as second-order Fermi acceleration. With a typical value of a cloud's velocity β around 10^{-4}, the acceleration rate is $\beta^2 \sim 10^{-8}$. Consequently, it takes approximately a billion years for a particle to double its energy, making this acceleration process highly inefficient for particle acceleration.

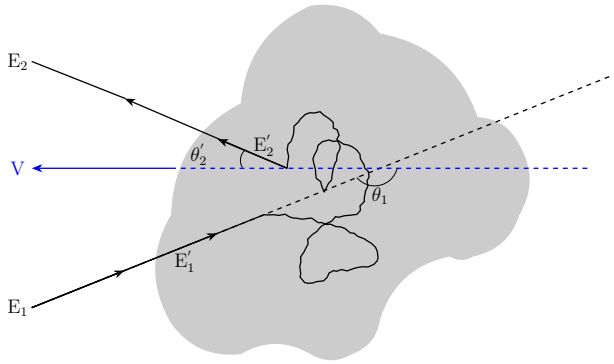

Figure 1.7: Acceleration by a moving plasma cloud: Primed quantities represent the cloud frame, while unprimed quantities refer to the Galactic frame. The cloud moves with a velocity of V in the Galactic frame.

The First-Order Fermi acceleration

Even though the original Fermi acceleration mechanism cannot explain the cosmic-ray acceleration, inspired by Fermi's idea, many scientists Axford (1969) Krymskii (1977) Bell (1978) and Blandford and Ostriker (1978) discovered the first-order Fermi acceleration, also known as the Diffusive Shock Acceleration (DSA) process in the late 1970s. In the original Fermi acceleration process, one particle can gain or lose energy at each encounter, so the rate of net energy gain is too slow to be accounted for as the main acceleration mechanism of cosmic-ray particles. If a particle can always gain energy at each collision, the averaged energy gain will be much more efficient, which can be achieved when the conditions: $\cos\theta_1 < 0$ and $\cos\theta_2' > 0$ (head-on collision) are always satisfied, according to the Equation 1.22. The presence of a shock wave can provide such an acceleration mechanism.

A shock is formed when a perturbation travels at a velocity greater than the speed of sound and *Alfvèn* speeds of the ISM. The shock front outlines a surface of an abrupt change in physical quantities. In the shock rest frame, the medium approaching the shock front with

velocity u_1 is referred to as the upstream. Meanwhile, the downstream medium moves away from the shock front with a velocity u_2. A set of conservation laws must be satisfied when gas passes from *upstream* to *downstream*. They can be used to determine the relationship between the medium density ρ_1 and ρ_2, pressure P_1 and P_2, and temperature T_1 and T_2 (the subscript "1" and "2" indicate the physical quantities in the upstream and downstream regions, respectively):

Mass conservation: $\rho_2 u_2 = \rho_1 u_1$
Momentum flux conservation: $P_2 + \rho_2 u_2 = P_1 + \rho_1 u_1$
Energy conservation: $\rho_2 u_2 \left(u_2^2 + \frac{p_2}{\rho_2} + e_2\right) = \rho_1 u_1 \left(u_1^2 + \frac{p_1}{\rho_1} + e_1\right)$
Where e_i is the energy density $e_i = \frac{1}{\gamma_a - 1}\frac{P_i}{\rho_i}$ and γ_a is the adiabatic index of the gas.
The solutions for the conservation equations are:

$$\frac{u_2}{u_1} = \frac{\rho_1}{\rho_2} = \frac{\gamma_a - 1 + 2M_1^{-2}}{\gamma_a + 1} \tag{1.24}$$

$$\frac{P_2}{P_1} = \frac{2\gamma_a M_1^2 - (\gamma_a - 1)}{\gamma_a + 1} \tag{1.25}$$

$$\frac{T_2}{T_1} = \frac{\left[2\gamma_a M_1^2 - (\gamma_a - 1)\right]\left[\gamma_a - 1 + 2M_1^{-2}\right]}{(\gamma_a + 1)^2} \tag{1.26}$$

Where $M_1 = \frac{u_1}{u_{1,sound}}$ is the Mach number, representing the ratio of shock velocity past the upstream to the local speed of sound. For a strong shock, where $M_1 \gg 1$, $u_2 = \frac{u_1}{r}$ with $r \simeq \frac{\gamma_a + 1}{\gamma_a - 1}$, and r is defined as the compression ratio. For monoatomic gas with an adiabatic index $\gamma_a = 5/3$, the compression ratio is $r = 4$. According to the laws of conservation, after the upstream crosses the shock front, the flowing medium is compressed ($\rho_2 > \rho_1$, $P_2 > P_1$), heated ($T_2 > T_1$), and slows down ($u_2 < u_1$).

To understand the principle of DSA, here we only focus on the change of the velocities. In the rest frame of upstream, the shock front is coming with a velocity u_1, and the downstream is also coming with a velocity $\Delta v = u_2 - u_1$. In the rest frame of downstream, the shock front is leaving with a velocity u_2, but the upstream is again coming with with velocity $\Delta v = u_2 - u_1$.

As illustrated in the Figure 1.8, imagine a particle coming from the upstream with energy E_1 in the upstream rest frame, it will see the downstream like a "magnetised cloud" coming towards it ($\cos\theta_1 < 0$). After coming across the shock frame and just before collision, the energy of the particle is $E_1^{'}$ in the reference of the downstream's rest frame. After it collides with the irregular magnetic field in the "cloud", it will be diffused back to the upstream again with angle $\theta_2^{'}$ and ($\cos\theta_2^{'} > 0$), and the energy after the collision are $E_2^{'}$ in the reference of the downstream's rest frame and E_2 in the reference of upstream's rest frame. On a cycle of changing the reference frame: *upstream* $\rightarrow$ *downstream* $\rightarrow$ *upstream*, the particle is always gaining energy. The relation between E_1 and $E_1^{'}$, E_2 and $E_2^{'}$ have the same expression

as in Equation 1.20. The parameter γ and β, instead of corresponding to the velocity of the cloud in the *second − order Fermi acceleration*, correspond to the relative velocity between the upstream and downstream, where $\beta = \Delta v/c$ and $\gamma = \frac{1}{\sqrt{1-\Delta v^2/c^2}}$. Because of the elastic collision $E_2^{'} = E_1^{'}$. The expression of E_2 in terms of E_1 in Equation 1.21, and the expression of the energy gain in Equation 1.22 are still valid.

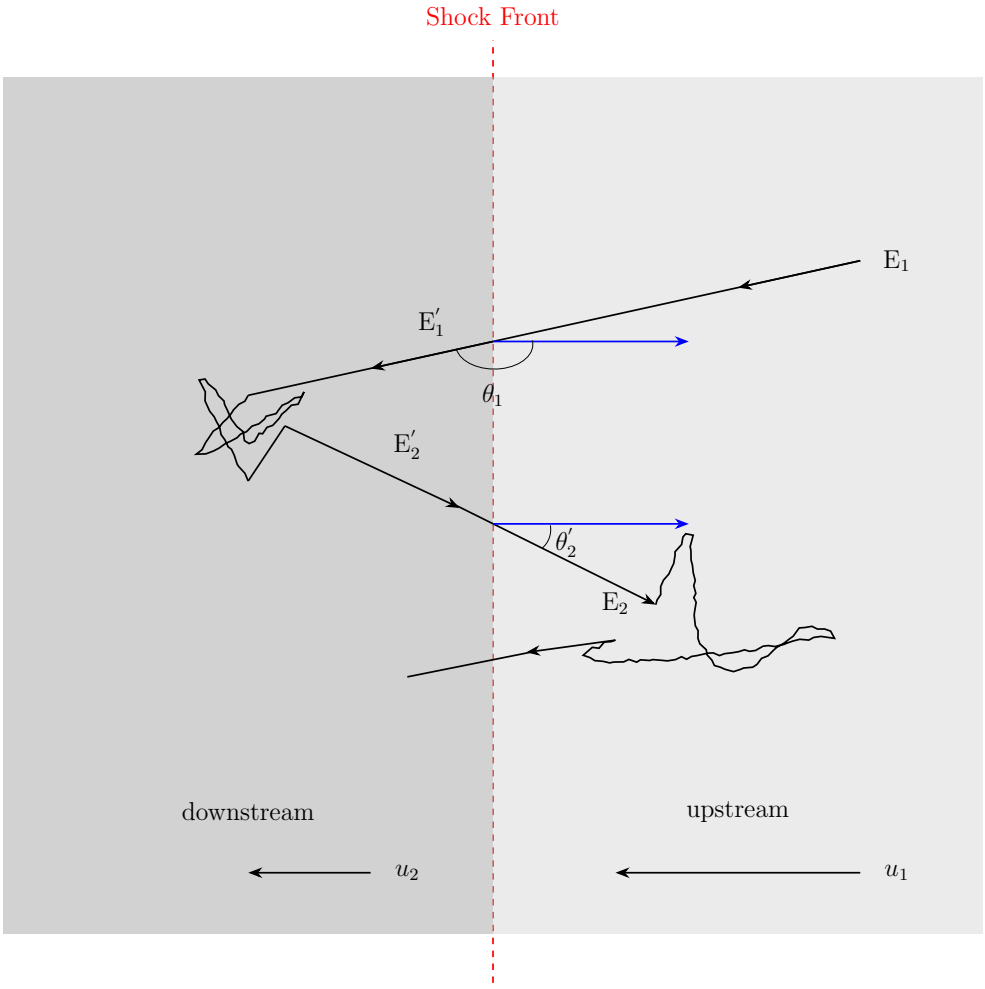

Figure 1.8: Acceleration at a plane shock front. Primed quantities refer to the downstream frame and the unprimed quantities refer to the upstream frame. At the rest frame of the shock front, upstream is moving towards the shock front with a velocity of u_1. The downstream is the medium already shocked with the front, and leave the shock front with a slower velocity of u_2. The medium density ρ_i, pressure P_i and temperature T_i also change abruptly through the shock front.

The average fractional energy gain in DSA can be calculated by averaging the values of $\cos\theta_1$ and $\cos\theta_2^{'}$. The probability of a particle crossing the shock within an angle θ to $\theta + d\theta$ is proportional to $\sin\theta d\theta$, and the rate of the particle approaching the shock front

is proportional to $\cos\theta$. Therefore, the probability of crossing the shock is proportional to $\cos\theta\sin\theta d\theta$. After normalization, we obtain $P(\theta) = 2\sin\theta d\theta$. According to the discussion above, the conditions for θ_1 and $\theta_2^{'}$ are $\frac{\pi}{2} \leq \theta_1 \leq \pi$ and $0 \leq \theta_2^{'} \leq \frac{\pi}{2}$, respectively. Hence, $\langle\cos\theta_1\rangle = -2/3$ and $\langle\cos\theta_2'\rangle = 2/3$. Substituting these values into Equation 1.22, the average fractional energy gain after one encounter cycle is:

$$\left\langle \frac{\Delta E}{E} \right\rangle = \frac{4}{3}\beta = \frac{4}{3}\beta_{sh}\left(\frac{r-1}{r}\right) \tag{1.27}$$

Where $\beta_{sh} = u_{sh}/c$, u_{sh} represents the velocity of the shock in the upstream rest frame, with $u_{sh} = u_1$.

In the DSA mechanism, the fractional energy gain is proportional to the first order of β, and therefore, it is referred to as *first − order Fermi acceleration*. This mechanism is much more efficient compared to the *second − order Fermi acceleration*.

Spectrum of Accelerated Particles

To estimate the spectrum from first order fermi acceleration, we need to know the number of cycles one particle can achieve before it escapes from the acceleration region. The fractional energy gain on average from one cycle: *upstream* → *downstream* → *upstream* is shown in Equation. 1.27. We can define E_1 the energy after one cycle as:

$$E_1 = (1+k)E_0 \tag{1.28}$$

where $k = \frac{4}{3}\beta$, and E_0 the initial energy.

The escape probability P_{esc} after one cycle can be defined as the ratio of the number of particles carried away by the downstream to a distant region ϕ_{esc} to the number of particles crossing the shock from upstream to downstream ϕ_{ud}.

$$P_{esc} = \frac{\phi_{esc}}{\phi_{ud}} \simeq \frac{4u_{sh}}{rc} \tag{1.29}$$

Where r is the the compression ratio. After n cycles, the energy E_n is:

$$E_n = (1+k)^n E_0 \tag{1.30}$$

The number of particles for energy above E_n is:

$$N_n = N(E_n) = N_0(1-P_{esc})^n = N_0(1-P_{esc})^{\frac{\ln(E/E_0)}{\ln(1+k)}} \tag{1.31}$$

where N_0 is the initial injected number of particles.

And hence:

$$N(\geq E) = N_0\left(\frac{E}{E_0}\right)^{\frac{\ln(1-P_{esc})}{\ln(1+k)}} = N_0\left(\frac{E}{E_0}\right)^{-\frac{P_{esc}}{k}} \tag{1.32}$$

when $P_{esc} \ll 1$ and $k \ll 1$.

Therefore, the number of particles $N(E)\,dE$ between E and $E + dE$ is

$$N(E) = (x-1)\,\frac{N_0}{E_0}\left(\frac{E}{E_0}\right)^{-x} \tag{1.33}$$

Substituting $r = 4$ for a monoatomic gas, we get $x = \frac{r+2}{r-1} = 2$. Thus, the spectral index x has a universal value of 2, and the accelerated particles follow a power-law distribution.

Acceleration Time & Maximum Energy

The time t_{cycle} for one cycle of *upstream* $\rightarrow$ *downstream* $\rightarrow$ *upstream* is given in the Equation 1.34 (Lagage and Cesarsky, 1983):

$$\langle t_{cycle}(E)\rangle = 4\left(\frac{D_1(E)}{u_1 c} + \frac{D_2(E)}{u_2 c}\right) \tag{1.34}$$

Where D_1 and D_2 are the diffusion coefficient in upstream and downstream respectively. The diffusion coefficient can be estimated according to the Bohm approximation: $D_{Bohm}(R) = \frac{1}{3} l_{scat}(R)\, v$, where l_{scat} is the mean free path of the particle. Assuming the mean free path l_{scat} is equivalent to the Larmor radius $r_L = \frac{Pc}{ZeB}$ and the particle is traveling ultra-relativistic, the diffusion coefficient is:

$$D_{Bohm}(R) = \frac{1}{3} r_L(R)\, c \sim \frac{1}{3}\frac{Ec}{ZeB} \tag{1.35}$$

Assuming $D_1 = D_2 = D_{Bohm}$, and from the Equation 1.27, the time to accelerate a particle to achieve energy E is:

$$\langle t_{acc}(E)\rangle = \frac{\langle t_{cycle}(E)\rangle}{\Delta E/E} \simeq 20\frac{D_{Bohm}}{u_{sh}^2} \tag{1.36}$$

From the Equation 1.35 and the Equation 1.36 The maximum energy E_{max} corresponds to the acceleration time is:

$$E_{max}(t_{acc}) = \frac{3}{20} u_{sh}^2 ZeBt_{acc} \tag{1.37}$$

For a SNR (see the detail in the Section 1.4.2) with $u_{sh} = 3000 kms^{-1}$, $B = 100\mu G$ and free expansion lasts 1000 yr, the maximum energy of a proton is around 1 PeV. Because of the nonlinear effects of the magnetic field in the source, it is believed that the maximum energy is estimated to be 30 to 100 times lower than the estimation given by Lagage and Cesarsky (1983).

1.4.2 Accelerators of Electrons and Positrons

The sources accelerating CRs in the observed energy range should satisfy the "Hillas criterion". The basic idea is that the maximum energy a source can accelerate a particle to is limited by the size of the or acceleartion region. More specifically, the Larmor radius of the particle cannot be larger than the size of the source, as otherwise, it would escape from the source. Hillas (1984) proposed a diagram to find the sources able to accelerate the particles to energies of 10^{20} eV. An example of Hillas Plot is shown in the Figure 1.9. The sources with different sizes and magnetic fields are compared with the lines calculated from the Equation 1.38 for different energies.

$$r_L(E) = 1.1 \times \left(\frac{E}{Z \times 10^{15} V}\right) \left(\frac{B}{\mu G}\right)^{-1} pc, \tag{1.38}$$

where r_L is the size of acceleration site, B is the magnetic field and E is the energy of the accelerated particle. The escape capability only depends on the rigidity of the particles, so the proton and electron with the same rigidity should behave in the same manner. Moreover, due to the same atomic number Z, the maximum energy to escape the acceleration site should be the same for protons and electrons. However, "Hillas criterion" is an over-optimistic prediction, since particle confinement is the only condition that is taken into account.

Age and energy loss processes should also play important roles in the estimation of the maximum energy. From Equation 1.6, the energy loss rate via synchrotron radiation strongly depends on the mass of the particle, which is proportional to M^{-4}, where M is the mass of the particle. Electrons have mass much smaller than protons ($M_{electron} \sim \frac{1}{2000} M_{proton}$), so for electrons, the maximum energy is more likely to be restricted by the energy loss via synchrotron radiation compared to protons.

The energy loss process of an electron is discussed in the Section 1.13 for the transportation process of the particle in the ISM. In case of ISM, the magnetic field is assumed to be around $B = 3\ \mu G$, under this condition the energy loss via synchrotron radiation and inverse Compton scattering are comparable as shown in the Figure 1.6. Inside the acceleration site, the magnetic field can be much stronger than in the ISM. This is due to the amplification of the magnetic field, a factor directly related to the compression ratio. The compression ratio is, in turn, determined by the speed of the shock (Donnert et al., 2018). Therefore synchrotron radiation becomes the most import energy loss process. Taking into account the synchrotron radiation to estimate the maximum energy that an electron can achieve in the source, it can be estimated when the energy loss time $t_{loss}^{syn}(E)$ in the Equation. 1.11 equals to the acceleration time $t_{acc}(E)$ in the Equation. 1.36. The maximum energy is given by Equation. 1.39:

$$E_{max} = 7.6 \times 10^{10} eV \left(\frac{u_{sh}}{kms^{-1}}\right) \left(\frac{\mu G}{B}\right)^{\frac{1}{2}} \tag{1.39}$$

If we use the parameters $u_{sh} = 3000\ kms^{-1}$, $B = 100\ \mu G$ again for a typical SNR, the maximum energy for electron is around 23 TeV, while the maximum energy for proton is 1 PeV according to the Equation. 1.37.

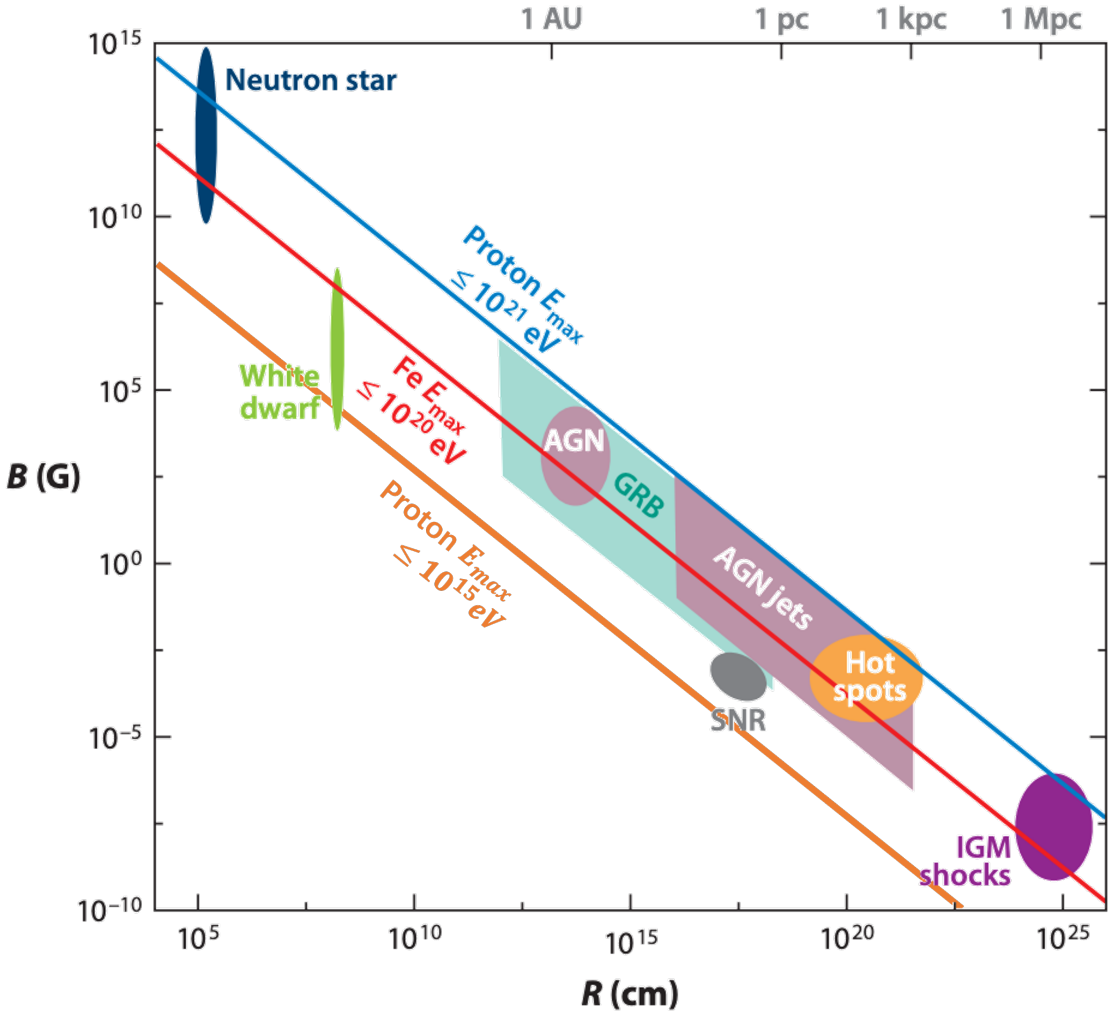

Figure 1.9: Hillas Plot showing sources with different characteristics in terms of size and magnetic B. Sources above the orange and blue line can accelerate the proton to the energy above 10^{15}eV and 10^{21} eV respectively. The sources above the red line can accelerate the Fe to the energy above 10^{21} eV. Adaptted from Kotera and Olinto (2011).

Secondary positrons and electrons

Secondary CRs are created through the collision between cosmic-ray nuclei, primarily protons, helium, and atoms in the ISM. This process, as described by Equation 1.40, can

generate positrons and electrons.

$$\begin{array}{lll} p + ISM \rightarrow \pi^+, & \pi^+ \rightarrow \mu^+ + \nu_\mu, & \mu^+ \rightarrow e^+ + \bar{\nu}_\mu + \nu_e \\ p + ISM \rightarrow \pi^-, & \pi^- \rightarrow \mu^- + \bar{\nu}_\mu, & \mu^- \rightarrow e^- + \nu_\mu + \bar{\nu}_e \end{array} \tag{1.40}$$

The contribution of secondary CRs to the all-electron spectrum is negligible for energies above 10 GeV (Orusa et al., 2021), which is much lower than the lowest energy of 300 GeV which is relevant to this thesis. However, secondary CRs are very important in the discussion of the positron fraction spectrum. Due to the charge asymmetry of CRs and interstellar material, the production of secondary positrons and electrons are not equal (Moskalenko and Strong, 1998), a small deficit of secondary electron compared to secondary positron is expected. In the secondary spectrum originating from a proton spectrum, the deficit of secondary electrons decreases with energy (Kamae et al., 2006). Therefore, it is possible to dismiss the idea that the energy dependence of the deficit could explain the increase observed in the positron fraction spectrum.

Supernova Remnants

SNRs are believed to be the most likely cosmic-ray accelerators in the Galaxy. These remnants are formed when massive stars reach the end of their lives and explode. Hoyle and Fowler (1960) classify supernovae into two types based on their progenitor stars: Type Ia supernovae occur in binary systems when a thermonuclear explosion is triggered by accretion of matter onto a white dwarf from a massive red-giant companion. In contrast, Type II, Ib, and Ic supernovae are caused by the core collapse of massive main sequence stars, typically with a massive red giant companion. The larger classification is based on the the presence or absence of specific spectral lines: Type 1 - No Hydrogen spectral lines, and Type 2 - Hydrogen spectral lines.

The ejection of supersonic plasma from the explosion of the supermassive star creates a shock on the background ISM, which is an ideal acceleration site for cosmic-ray particles by DSA mechanism (Ellison et al., 2007; Tatischeff, 2009; Cristofari et al., 2013; Blasi, 2013). The evolution of the SNR can be described by four phases (Woltjer, 1972):

- **Free expasion phase**

  When a progenitor star explodes, ejecta with a mechanical energy of approximately $\sim 10^{51}$ erg are released. During this phase, the dynamics of the SNR are not significantly affected by radiative losses. As the ejected material propagates supersonically, a shock wave called the $blast - wave$ shock forms ahead of the ejecta, compressing and heating the interstellar material.

  During this stage, the mass of the compressed gas is much less than the mass of the ejecta, and the shell of the shock is expected to propagate freely with a constant velocity around $v_{sh} \sim [5000, 10000]\, km\ s^{-1}$, and shock radius $R_{sh} \propto t$ (Gaisser et al., 2016). This stage can last tens to a few hundred years in general depending on the

characteristics of the surrounding gas and the ejecta from the explosion. During the expansion of the shock, upstream particles are overtaken by the expanding shock and accelerated by the DSA mechanism.

Towards the end of the free expansion phase, as the mass of the swept-up ISM accumulates with the outwards-moving shock, the ISM begins to exert increasing pressure on the ejecta. This leads to the formation of a contact discontinuity between the shocked ejecta and the shocked ISM. Behind the contact discontinuity, a reverse shock is produced where ejecta is decelerated (Gaensler and Slane, 2006). The unshocked ejecta continues to maintain its free expansion motion until it encounters the reverse shock. A spherically symmetric SNR is illustrated in Figure 1.10.

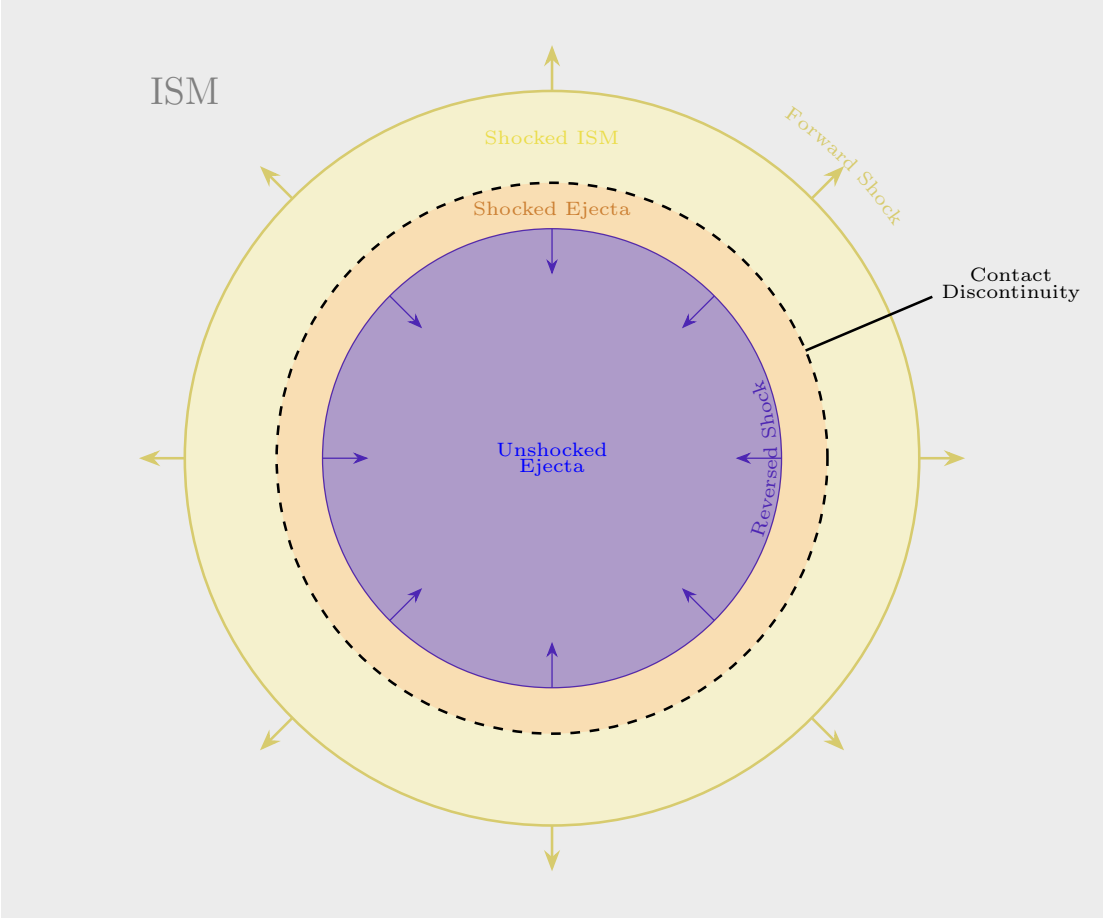

Figure 1.10: Sketch of a SNR's structure.

- **Sedov – Taylor phase**

  When the shock has swept up the mass of the ambient medium equivalent to the ejected material, almost all of the mechanical energy of the ejecta is transferred to the swept-up material, so the shock slows down. During this phase, the temperature

of the gas behind the shock (the downstream medium) is so high that the radiative cooling is unimportant, thus the energy is conserved and also called the adiabatic expansion phase (Velazquez et al., 1998). This phase can last around 10^4 years with shock velocity evolving with time as $v_{sh} \propto t^{-3/5}$, the shock radius $R_{sh} \propto t^{2/5}$. It is also important to note since the shock speed is now slowing down, that the magnetic field also decreases and then CRs are generally released in this stage. In this phase, the reverse shock is able to change the direction by the deceleration of the ejecta, and arrive at the center of the remnant within finite time (Truelove and McKee, 1999).

- **Pressure – driven snowplow**

  As the expansion continues, radiative losses become significant, causing the temperature of the shell of the shocked ISM drops below 10^6K. Cooling through optical line emissions from the recombination of ionized ions becomes important. A thin and dense shell is formed around the hot inner region. The shell is pushed away by the pressure of the hot interior, just like a snowplow. In this stage, the shock radius changes with time as $R_{sh} \propto t^{2/7}$.

- **Momentum – conserving snowplow**

  When the hot interior also losses energy and cools down, the shell continues driven by its own momentum. In this stage, the momentum is conserved, and the shock radius changes with time as $R_{sh} \propto t^{1/4}$.

  In the end, the shock becomes subsonic and the material merges with the surrounding ISM.

Pulsars

Pulsars are rapidly rotating neutron stars. The compact and magnetized neutron stars are formed when the core of the massive stars ($m \geq 8M_{\odot}$) is compressed during a core-collapsed supernova. Neutron stars have very strong magnetic field ranging from 10^8 G to 10^{15} G (Bransgrove et al., 2017). In the simplest assumption, a pulsar can be regarded as a fast rotating, perfectly conducting sphere with a strong magnetic field, behaving like a unipolar generator. An induced electron field at distance $\boldsymbol{r}$ is expected to be $\boldsymbol{E_i} = \boldsymbol{v} \times \boldsymbol{B} = (\boldsymbol{\Omega} \times \boldsymbol{r}) \times \boldsymbol{B}$, where $\boldsymbol{B}$ is the dipolar magnetic field with a magnetic moment $\boldsymbol{u}$ and $\boldsymbol{\Omega}$ the angular frequency of the neutron star rotating aligned with $\boldsymbol{u}$. The rearranged charges produce an internal electric field $\boldsymbol{E}$ to balance this induced electric field (Cerutti and Beloborodov, 2016):

$$\boldsymbol{E} + (\boldsymbol{\Omega} \times \boldsymbol{r}) \times \boldsymbol{B} = \boldsymbol{0} \tag{1.41}$$

The polarized sphere produces electric potential, if the rotator is in the vacuum, the external electrostatic potential ϕ is (Pétri et al., 2002):

$$\phi = -\frac{B_0 \Omega R^5}{6r^3} \left(3\cos^2\theta - 1\right) \tag{1.42}$$

Where B_0 is the magnetic strength at the pole, R the radius of the star, and θ is the angle respective to the pole of the star. The electric field just above the pole of the pulsar ($\theta = 0$) is obtained as $E = \Omega R B_0$ by differentiating the Equation 1.42 in the radial direction. For a young pulsar like Crab with $B_0 = 10^{12}\ G$, $\Omega = 200\ rad\ s^{-1}$ and $R = 10\ km$, the electric field amounts to $E \simeq 3{\times}10^{13}\ Vm^{-1}$ at the pole. With such strong electric field, the Lorentz force on an electron is much larger than that of the gravitational force, therefore electrons are extracted from the surface of the star and accelerated in the strong electric field, forming a plasma-filled magnetosphere. The electrons radiate γ rays via curvature radiation, and the γ rays will be absorbed almost instantaneously by the strong magnetic field and produce a pair of electron and positron. The process continues to create electromagnetic cascade (Sturrock, 1971; Daugherty and Harding, 1982), and the vacuum is broken by the initiated cascade (Goldreich and Julian, 1969; Ceribella, 2021).

The pulsar is surrounded by the fully conducting plasma formed by the cascade, which changes the magnetic and electric fields' distribution in the magnetosphere. The external induced electric field is neutralised by the electric field of the surrounding plasma $\boldsymbol{E} + (\boldsymbol{v} \times \boldsymbol{B}) = \boldsymbol{0}$, where $\boldsymbol{v}$ is the velocity of the surrounding plasma. According to the *Alfvén* theorem, for an infinite electric conductivity, the flow of electrons and positrons would be trapped in the magnetic field lines. Under the "force free" condition where $\boldsymbol{E} \cdot \boldsymbol{B} = 0$, the charges slide along the magnetic field lines, which coincide with the electrostatic equipotential lines. For the region close to the star, the particles co-rotate with the star with in the poloidal magnetic field.

At the distance $r_c = c/\Omega$ respective to the rotation axis, the co-rotation speed reaches the speed of light. For the region less than r_c, the particles can co-rotate with the star, and the surface of the region is called *light cylinder*. The magnetic field lines that cross the *light cylinder* will not come back to the star and form toroidal open field lines, that reach far away from the star and merge with the interstellar magnetic field.

The charge distribution in the inner magnetosphere can be approximated by the Goldreich-Julian density in the Equation 1.43. I refer the readers to Sob'yanin (2016) for the detailed calculations.

$$\rho_{GJ} = -\frac{\boldsymbol{\Omega} \cdot \boldsymbol{B}}{2\pi c} \frac{1}{1 - (\Omega r/c)^2 \sin^2\theta} \tag{1.43}$$

From Equation 1.43, we can find: when $\boldsymbol{\Omega} \cdot \boldsymbol{B} = \boldsymbol{0}$, there is a surface with charge density 0, named *null charge surface*. This surface also separates the co-rotating regions with net positive charges and negative charges. The Equation 1.43 diverges when $r_c = c/\Omega$, where the transition from poloidal magnetic field lines to toroidal magnetic field lines takes place.

The pulsar magnetosphere is separated into *near zone* and *wind zone* as illustrated in the Figure 1.11. In the near zone, the magnetic field lines can close themselves and return to the surface of the star, and they are predominantly poloidal. The particles bond in these field lines co-rotate with the star and trapped in the near zone forever. In the wind zone,

the magnetic field lines cross the light cylinder, that acquire a toroidal component, and cannot come back to the surface of the star. Particles move along the open field lines will leave the star and form the pulsar wind.

The simple and ideal Goldreich-Juilan model indicates a force-free condition $\boldsymbol{E} \cdot \boldsymbol{B} = 0$, where the electric field $\boldsymbol{E}_{||}$ component parallel to the magnetic field is completely screened. Under such condition, the particle acceleration is impossible, therefore no high-energy γ-ray emission would be expected as a consequence of accelerated particles, which is contradictory to the observations. This means there should be some regions where $\boldsymbol{E}_{||}$ is not completely screened by the particles, and a charge-depleted region should be responsible for it. Several models are proposed to explain the particle acceleration regions: the Polar Cap model (Ruderman and Sutherland, 1975; Daugherty and Harding, 1996), the Slot Gap (Harding, 2007) and the Outer Gap (Cheng et al., 1986). The corresponding regions are shown in the Figure 1.11. The electron and positron pair production may occur efficiently in these regions. The electron and positron pairs escape from polar cap and outer gap (Chi et al., 1996) or outer gap only (Zhang and Cheng, 2001) are accelerated by the low-frequency electromagnetic wave, and contribute to the electron and positron spectrum. Novel numerical technique, such as Particle-In-Cell simulation Venter (2017) Brambilla et al. (2018) proposed a scenario in which charged particles are accelerated and flowing in and out along a current sheet. On the equatorial of the pulsar and outside the light cylinder, the current sheet, the last closed field line and the light cylinder meet at a point named as *Y point*.

Pulsar Wind Nebulae

According to the observations, the spin period of an isolated pulsar increases with time indicating a spin-down evolution. The extraction of energy by the electromagnetic wind causes the rotational energy loss of the star (Ostriker and Gunn, 1969; Bogovalov, 1999; Tong, 2015). The pulsar wind is confined by the slow-moving ejecta of the SNR and inflating a hot bubble, called Pulsar Wind Nebula (PWN), which is consists of relativistic particles and magnetic field.

A strong termination shock is formed to balance the wind ram pressure and pressure of the PWN (Rees and Gunn, 1974). The termination shock separates the upstream pulsar wind and the downstream wind nebula bubble, and propagates back towards the pulsar. This is a possible particle acceleration site via DSA process as discussed in the Section 1.4.1. The accelerated particles enter the nebula and are trapped by the magnetic field of the nebulae until they are released to the ISM, 10 kyr and 100 kyr after the pulsar formation. It is believed that electron and positron pairs are injected in a very short time, and can be treated as a burst-like source of electrons and positrons (Grasso and et al., 2009).

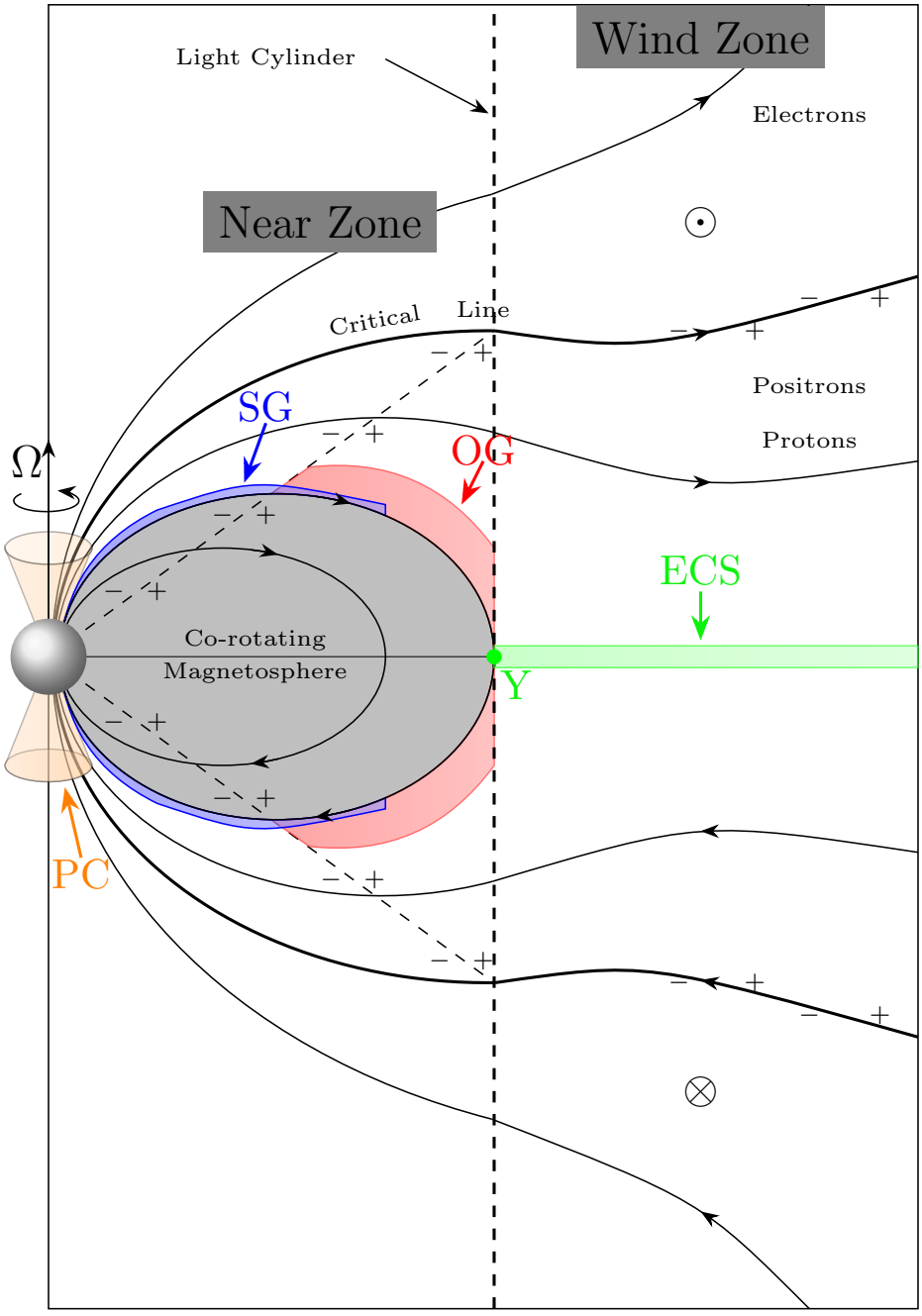

Figure 1.11: The illustration of pulsar magnetosphere. The rotation axis is parallel to the magnetic moment $\boldsymbol{u}$. Magnetic field lines are shown as solid lines. The shaded region is the co-rotating magnetosphere, where particles cannot escape from the magnetosphere. The vertical dashed line shows the light cylinder. The magnetic field lines that cross the light cylinder are the open field lines, where particles can stream out along these lines. The signs show the particle charges when $\boldsymbol{\Omega} \cdot \boldsymbol{u}$, divided by the *null charge surface* in the near zone and *critical field line* in wind zone. The charge-depleted regions responsible for the charge acceleration are illustrated in the different colors: PC (Polar Cap) in orange, SG (Slot Gap) in blue, and OG (Outer Gap) in red. CS (Current Sheet) is shown in green. Green dot is the Y Point.

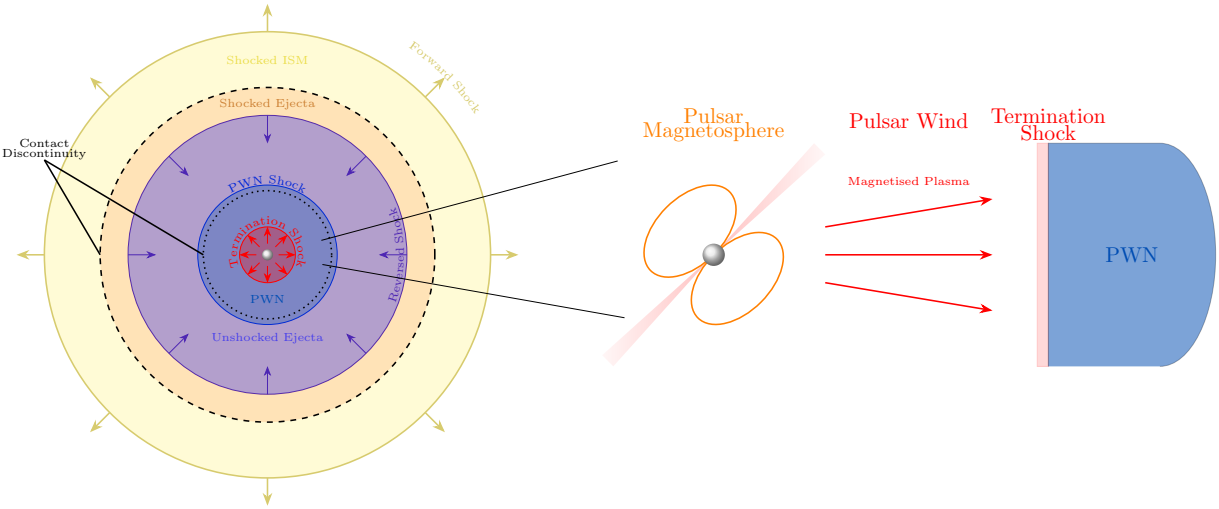

Figure 1.12: The sketch shows a SNR powered by a pulsar at the center. The symmetric structure suggests a relatively young system before evolving. A relativistic pulsar wind terminates at a strong termination shock, separating the upstream pulsar wind and the downstream wind nebula bubble. A bubble of shocked material forms a nebula starting from the termination shock and is bounded by a strong PWN shock. The reverse shock is propagating inward, separating the unshocked and shocked ejecta. The zoomed-in view on the right side shows the structure of the pulsar wind and PWN.

Dark Matter

The unexpected excess of positron fraction has attracted significant attention towards the dark matter scenario. dark matter was proposed based on observational evidence that the visible mass of a cluster of galaxies cannot explain the gravitational balance (Zwicky, 1937). The idea of dark matter was confirmed by (Rubin and Ford, 1970) by observing the rotational speed of stars on the outer edge of galaxies. dark matter is expected to account for 85% of the total mass and 27% of the energy budget of the universe (Planck Collaboration et al., 2014).

dark matter is suggested to be composed of new elementary particles, with one of the main candidates being the so-called Weakly Interacting Massive Particles (WIMPs) (Jungman et al., 1996) (see Bertone et al. (2005), Silk et al. (2010) and Feng (2010) for reviews). The compelling evidence for WIMP dark matter is partially due to the coincidence between the thermal relic density of WIMPs and the observed dark matter density, referred to as the “WIMP miracle”. So far, the only clue to the existence of dark matter is through its gravitational imprint. WIMPs are massive particles with a mass ranging from a few GeV (Boehm et al., 2004) to hundreds of TeV (Griest and Kamionkowski, 1990). They only interact weakly, primarily through the gravitational force and, perhaps, the weak nuclear force.

There are several potential channels through which dark matter could contribute to the production of electrons and positrons:

- dark matter particles are expected to directly annihilate or decay into e^+e^-, or they can first annihilate or decay into quarks, bosons, and other leptons, and then further decay into e^+e^-;
- dark matter particles can annihilate into pairs of light scalar or vector particles and then decay into leptons.
- The combination of the above channels.

1.5 Crab Nebula

The Crab Nebula, the remnants of a supernova that occurred in 1054 CE, is one of the most extensively studied celestial sources. Its emission has been observed across the entire electromagnetic spectrum, including very high energy gamma rays. The optical image is shown in the left panel of Figure 1.13. It was first detected at energies greater than 25 GeV in 2008 by the MAGIC (Aliu and et al., 2008). Subsequently, the detection at 100 TeV was announced in 2020 (Acciari and et al., 2020b). The Crab Nebula is often considered a standard candle in high-energy astrophysics, serving as a calibration source for high-energy instruments due to its consistent emission. The spectral energy distribution of the Crab Nebula, obtained using the upgraded MAGIC telescopes to demonstrate the performance of MAGIC is shown the right panel of Figure 1.13. The analysis methods used in this thesis is highly non-standard. In Chapter 3, the Crab spectrum will be utilized as a benchmark to validate these analysis methods.

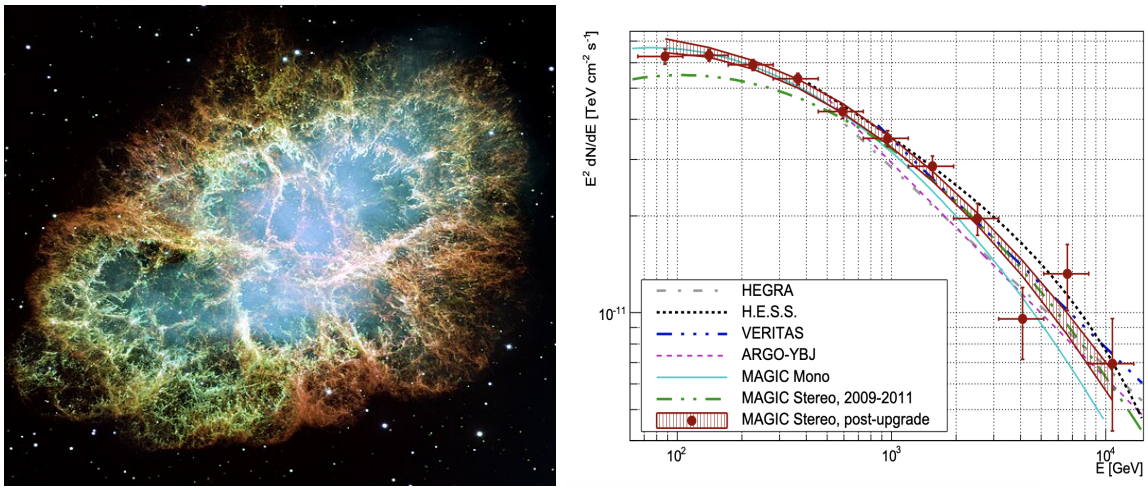

Figure 1.13: Left: Optical image of the Crab nebula. Image credits: Hubble Space Telescope. Right: The spectral energy distribution of the Crab Nebula, obtained using the upgraded MAGIC telescopes, is shown as red points and shading in comparison to results from other experiments (Aleksić and et al., 2016)

Chapter 2

MAGIC Telescopes and the Standard Analysis Method

The full name of MAGIC is Major Atmospheric Gamma-ray Imaging Cherenkov. As the name suggests, the MAGIC telescopes are primarily designed to detect γ-ray sources. However, during observation, various types of CRs are also detected as background due to the observation technique used, known as Imaging Atmospheric Cherenkov Technique (IACT), which will be introduced in Sections 2.1 and 2.7. In Section 2.4, I will explain the standard analysis chain for γ-ray sources before introducing the analysis method for cosmic-ray electrons and positrons in Chapter 3 and highlighting the differences in the analysis between γ-rays and CRs.

2.1 Extensive Air Shower

When very-high-energy CRs enter the Earth's atmosphere, the primary cosmic-ray particles interact with the nuclei in the atmosphere and create secondary particles. Numerous particles are created through successive interactions, and the cascade of particles is called an Extensive Air Shower (EAS). There are two types of EAS: electromagnetic showers, which are produced from very high energy γ-rays and cosmic-ray electrons and positrons, and hadronic showers, which are produced from cosmic-ray hadronic particles with higher nuclei, mainly protons and helium.

2.1.1 Electromagnetic Shower

Electromagnetic showers are initiated through two main interaction processes: bremsstrahlung and pair-production. The rate of energy loss is proportional to the energy:

$$\frac{dE(X)}{dX} = -\frac{1}{X_0}E(X) \tag{2.1}$$

where X_0 is the radiation length, the distance over which the energy of an electron decreases by a factor of $1/e$ due to bremsstrahlung radiation (for electrons in the air, $X_0 = 37 g/cm^2$).

Pair production is the process in which a pair of particles, an electron and a positron, are formed when a photon interacts with the Coulomb field of a nucleus. This process only occurs when the energy of the photon is greater than the mass of two electrons, which is 1.02 MeV. The mean free path for pair production is $\frac{9}{7}$ times the radiation length X_0.

The development of an electromagnetic shower can be described by the Heitler model (Matthews, 2001, 2005). When a high energy photon enters the atmosphere and encounters the Coulomb field of air nuclei, a pair of electrons and positrons is created via the pair production process. The electron-positron pair then radiate secondary photons through bremsstrahlung. The growth of the particles continues as a cascade until the energy of each particle falls below the critical energy $E_c \simeq 85$ MeV, at which point the energy losses by radiative processes are equal to the energy loss by ionization and excitation. As shown in the sketch in Figure 2.1, when either bremsstrahlung or pair production occurs, the energy splits into two. The distance between two interaction depths is $\lambda = \ln 2 X_0$ for bremsstrahlung and $\lambda = \ln 2 \left(\frac{9}{7} X_0\right)$ for pair production (Workman and Others, 2022).

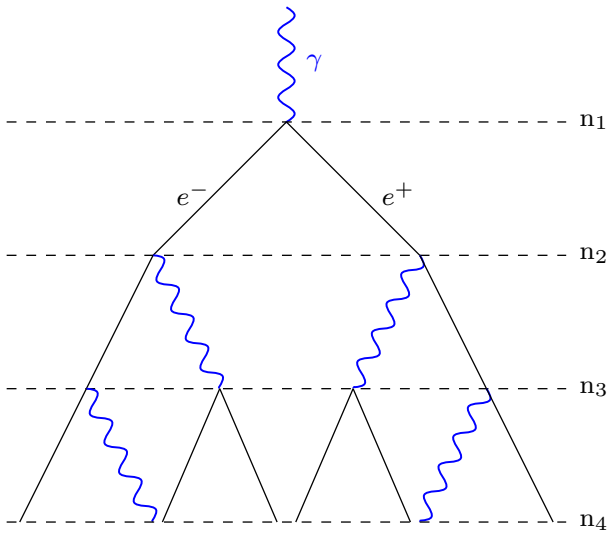

Figure 2.1: Heitler model for electromagnetic shower.

The number of particles at depth X is:

$$N(X) = 2^{X/\lambda} \tag{2.2}$$

where X is the interaction depth the particle travels from the first interaction point. The number of particles reaches the maximum at E_c:

$$N(X_{max}) = E_0/E_c \tag{2.3}$$

where X_{max} is the depth where the maximal particles of the shower are created, and E_0 is the initial energy of primary particle. From Equation 2.2 and 2.3, X_{max} can be expressed

as:

$$X_{max} = \lambda \frac{ln(E_0/E_c)}{\ln 2} \tag{2.4}$$

According to Equation 2.3 and 2.4, Heitler model predicts that both N_{max} and X_{max} are proportional to E_0.

After taking into account particle losses, the development of an electromagnetic shower can be described by more complicated models such as the one proposed in the paper by Rossi and Greisen (1941). The number of electrons and positrons in the shower can be calculated as follows:

$$N_e(t) \sim \frac{0.31}{\sqrt{\ln(E_0/E_c)}} \exp\left[t(1 - \frac{3}{2}\ln s)\right] \tag{2.5}$$

where the parameter s is defined as the shower age $s = \frac{3}{1+2X_{max}/X}$, which is a dimensionless quantity that measures the longitudinal development of the shower. At $s = 1$, the shower development reaches its maximum. The parameter t represents the interaction depth in terms of the unit of X_0. The longitudinal development of showers with different initial energies is shown in Figure 2.2.

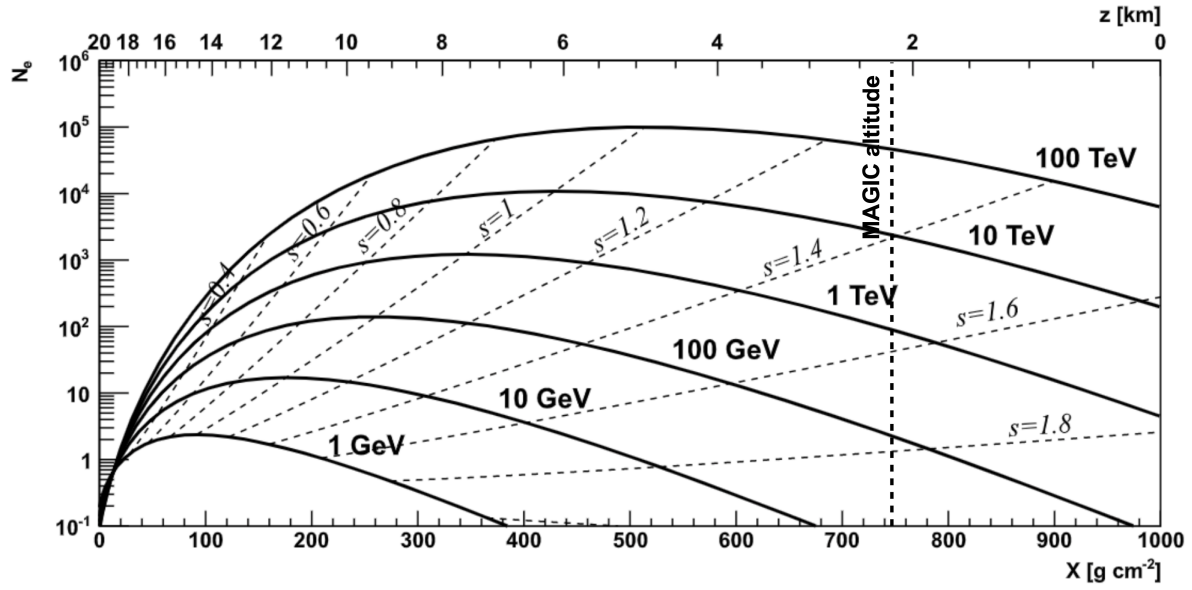

Figure 2.2: Electromagnetic shower development as function of interaction depth for γ-ray with different energies. $s = 1$ indicates the position of shower maximum. Adapted from de Naurois and Mazin (2015).

2.1.2 Hadronic Shower

The development of a hadronic shower consists of different primary fragments that further collide or decay into various particles. Hadronic cascades are much more complicated compared to electromagnetic showers, but it is essential to understand their properties, especially for studying background estimation. When high-energy hadronic cosmic-ray particles enter the atmosphere, secondary particles are created through interactions with atmospheric nuclei governed by the strong force. The secondary particles include baryons such as protons and neutrons, as well as a large amount of mesons like pions and kaons. Neutral pions decay into photons within a very short time, as described in Equation 2.6.

$$\pi^0 \rightarrow 2\gamma \tag{2.6}$$

These photons can then initiate electromagnetic sub-showers. This indicates that the electromagnetic component is part of the hadronic shower, accounting for, on average, less than one third of the energy of the primary particles, assuming a simple production rate of $\pi^+ : \pi^- : \pi^0 = 1 : 1 : 1$. The initiated electromagnetic sub-shower follows the same development as described in Section 2.1.1. However, the similarity between the electromagnetic component of the hadronic shower and γ-ray showers can be very misleading, especially when extracting excess events.

The charged pion can interact further and produce a charged or neutral pion, as long as the energy is above the critical energy $E_c^\pi = 20$ GeV. The interaction length of a proton is $\lambda_{proton} = 70$ g/cm^2, which means that a proton has a lower first interaction point compared to a γ-ray. According to the model proposed by Matthews (2005), the interaction length of a hadronic shower is $\lambda = \ln 2\lambda_\pi$, and the interaction length for pions is $\lambda_\pi = 120$ g/cm^2 (Gaisser, 1990). Once the charged pions reach the critical energy, they decay following the decay channel given by Equation 2.7.

$$\begin{aligned} \pi^+ &\rightarrow \mu^+ + \nu_\mu \\ \pi^- &\rightarrow \mu^- + \nu_{\bar{\mu}} \end{aligned} \tag{2.7}$$

The muons produced in the decay, which have a long lifetime, can reach the ground in substantial numbers. A sketch of the hadronic interaction process is shown in Figure 2.3. Heavier primary particles with mass A can be regarded as the superposition of A independent nucleons (Gaisser et al., 2016).

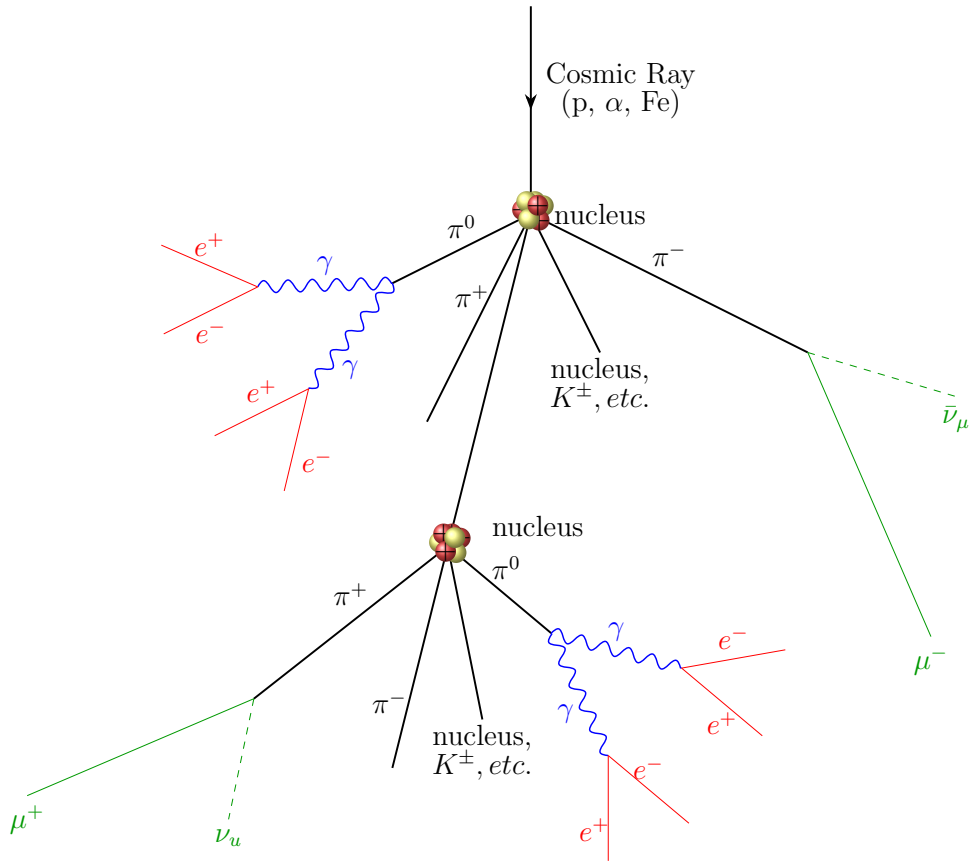

Figure 2.3: Hadronic shower development initiated by a cosmic particle. The cosmic ray particle interacts with the nucleus in the atmosphere and produce pions and kaons. The neutral pions decay into γ-rays immediately, and the charged pions decay into muons and muonic neutrinos.

2.1.3 Cherenkov Radiation from the Extensive Air Shower

Cherenkov radiation, discovered in 1934, occurs when a charged particle travels faster than the phase velocity of light in a dielectric medium. When a charged particle with velocity $v = \beta c$ passes through a medium with an index of refraction n, it polarizes the atoms or molecules of the medium and forms dipoles. The dipole radiation is constructive if the particle travels faster than the speed of light in the medium, which is c/n. Therefore, the condition for Cherenkov radiation to occur is $\beta > 1/n$. The radiation can be visualized as illustrated in Figure 2.4. The light emits in a sphere as the particle propagates. The sphere grows with a speed of c/n, while the particle travels at a faster speed v and moves ahead of the sphere. The spheres created at different locations superimposed, and a wavefront is formed. The Cherenkov light is emitted in a conical shape at an angle θ_c to the particle direction. The opening angle θ_c is given by:

$$\cos\theta_c = \frac{1}{n\beta} \tag{2.8}$$

Where θ_c ranges from $\theta_{min} = 0$ which corresponds to the minimum speed to have Cherenkov radiation to $\theta_{max} = arccos\left(\frac{1}{n}\right)$ corresponding to the limit of the particle speed $\beta \to 1$.

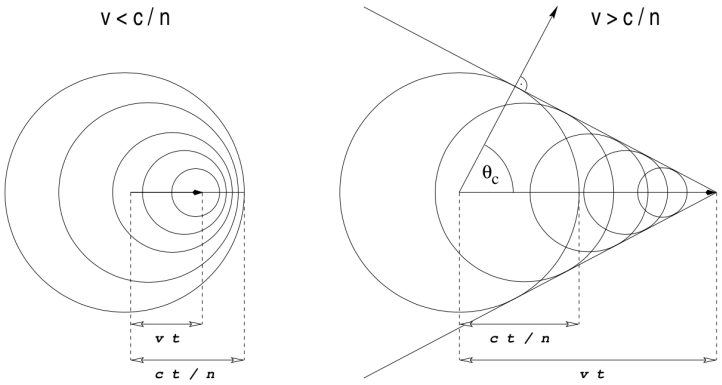

Figure 2.4: The interference of the dipole radiation is destructive when $v < c/n$ (left), and becomes constructive (right) when $v > c/n$. The Cherenkov wave front is determined by the velocity of the particle and the speed of light in the medium c/n. Image taken from Hengstebeck (2007).

As depicted in the bottom plots of Figure 2.5, Cherenkov photons accumulate in a disk-shaped area known as the "light pool" upon reaching the ground. The "light pool" exhibits three critical features: (1) its radius is approximately 150 m; (2) in the case of an electromagnetic shower, photon density within the "light pool" increases with distance from the shower axis until it peaks at the disk's edge (known as the "hump") before dropping to zero; and (3) for a hadronic shower, in addition to the electromagnetic subshower component, the hadronic elements generate muon rings on the ground. These rings have a dense core at their center due to their extended lifetime.

The limited size of the Cherenkov "light pool" can be attributed to the small Cherenkov angle, which is approximately 0.2° at an altitude of 30 km and increases to approximately 1.5° at sea level due to the varying refractive index with altitude, as illustrated in the left panel of Figure 2.6 (Stone, 1996). Owing to the variation in the Cherenkov angle, photons accumulate at distances around 150 m from different altitudes. The top right panel of Figure 2.6 displays the lateral profile of the Cherenkov photon density for different energies at sea level.

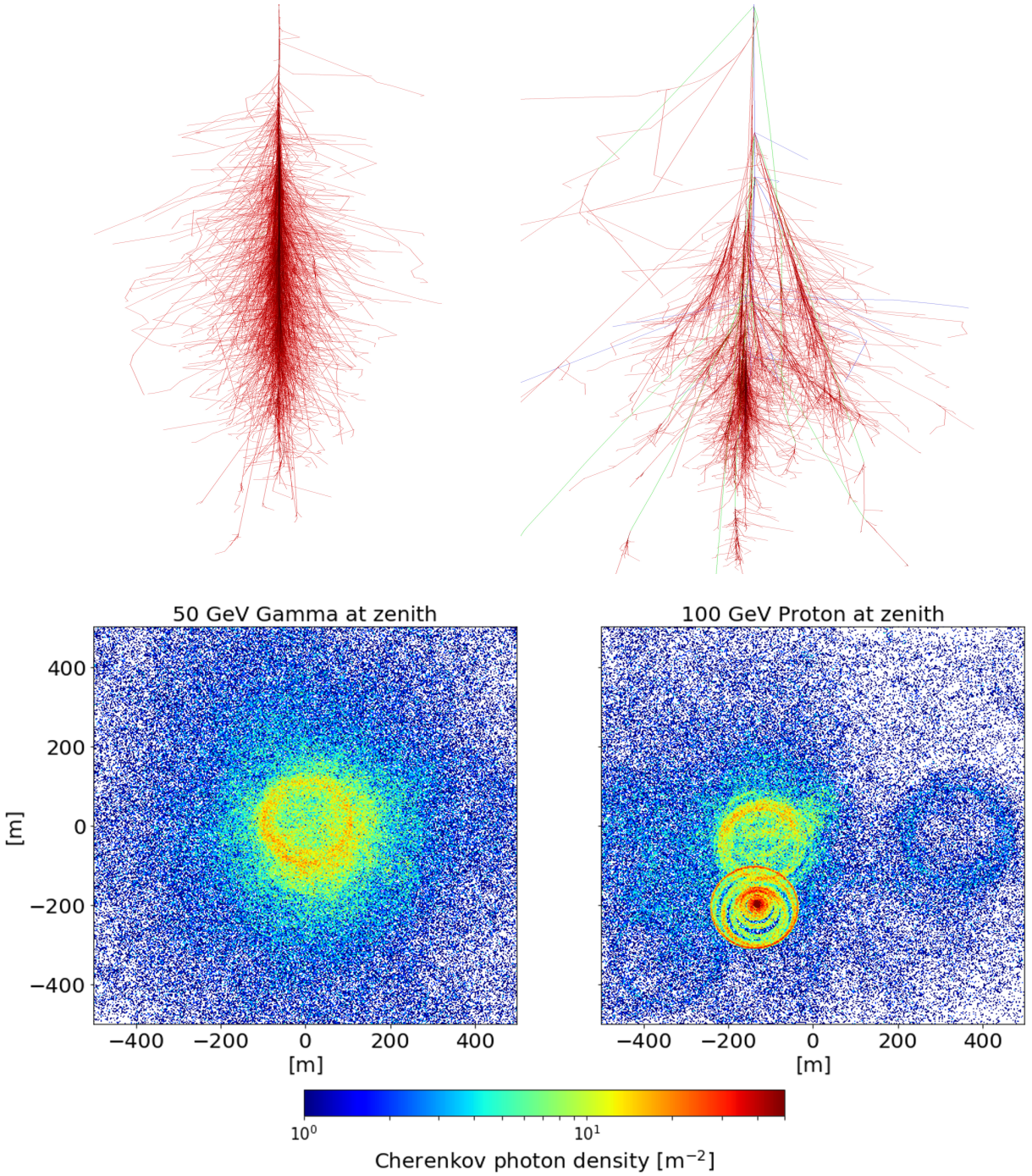

Figure 2.5: Simulated air showers of 50 GeV γ-ray shower (upper left) and 100 GeV hadronic shower (upper right) (F. Schmidt, 2005). The Cherenkov photons in the wavelength range of 290-700 nm generated from the showers projecting on the ground are shown bellow the shower images.

The Cherenkov photon also exhibits an important feature, namely the spread of the arrival time, with a typical arrival time spread on the ground of a few nanoseconds. Two effects determine this time spread. The first effect is related to the fact that the charged particle travels faster than the speed of light, resulting in lower altitude photons arriving earlier in the direction of the shower axis, where both photon and particle travel the same distance. The second effect is due to the geometrical trajectory, with photons emitted at lower altitudes taking a longer path to reach observation points located at larger distances from the shower axis, thereby arriving later than photons emitted from higher altitudes. These two effects compete and reach a balance at around 120 m, where the time spread of the shower is minimum.

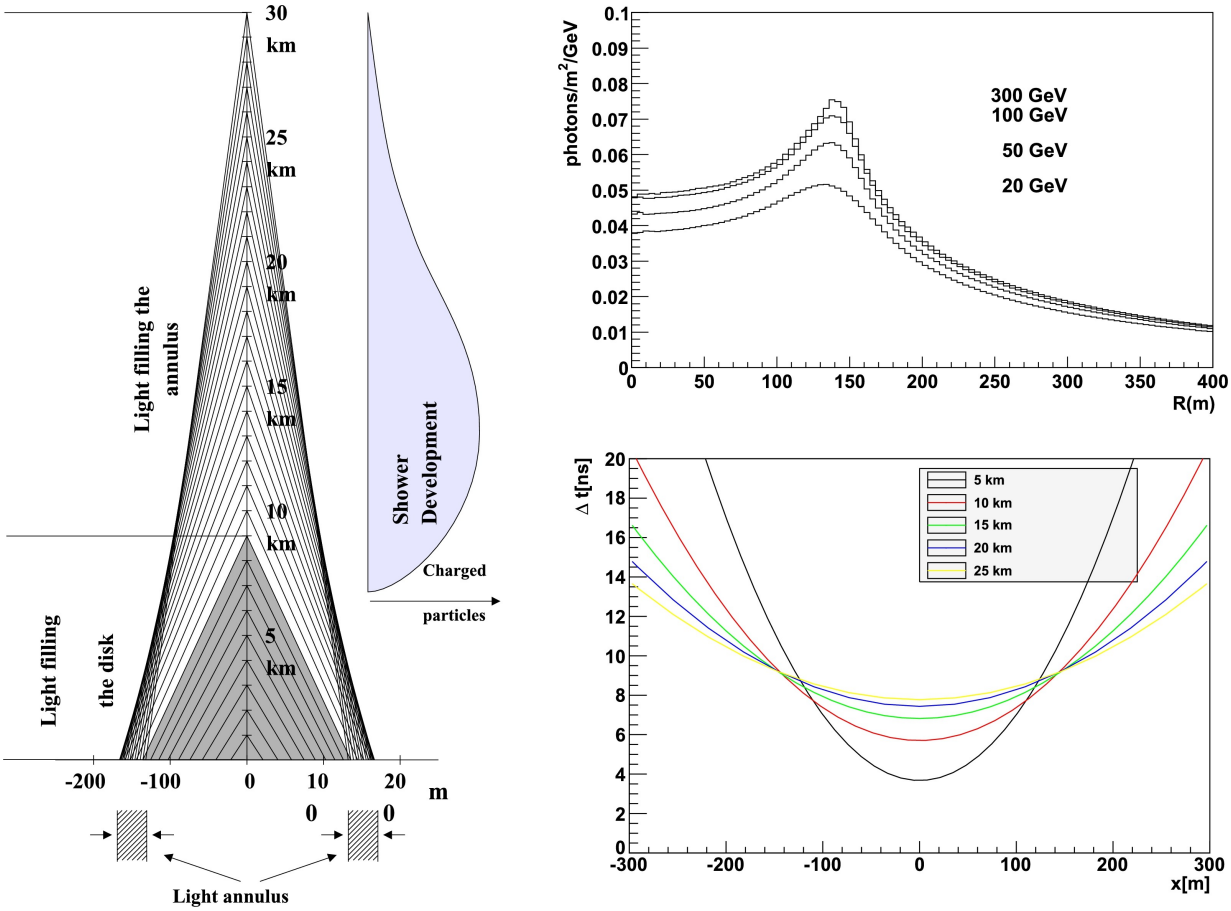

Figure 2.6: Shower development (left panel): The lines indicate the Cherenkov radiation from an EAS. The lateral profile of the Cherenkov photon density of different energies at sea level (top right). Time spread of the shower as a function of lateral distance for different altitudes (bottom right) (de Naurois and Mazin, 2015).

2.2 The Imaging Atmospheric Cherenkov Technique

The Cherenkov radiation from EAS provides an opportunity for it to be detected by the IACT , and the initial information of the corresponding EAS can be reconstructed. The first detection of Cherenkov light of CR as short pulses was done by Galbraith and Jelley (1953) in 1953. The technique finally became mature after 30-year efforts, and led to the detection of Crab Nebula by the Whipple telescope (Weekes et al., 1989).

The current design of IACTs typically involves large optical telescopes that detect the Cherenkov radiation emitted from EAS. These telescopes usually have large parabolic mirrors that collect as many photons as possible. The camera is equipped with quick-response pixels, and a fast readout system is necessary to capture the signal within the nanosecond scale (López Coto, 2017). The mirrors project light at the same incoming angle onto a single point, resulting in a uniform distance from the camera center in the camera plane. However, photons emitted from different parts of the EAS have different Cherenkov angles and are reflected at different distances with respect to the camera center, resulting in a shower image captured, as illustrated in the right panel of Figure 2.7. The properties of the shower can be reconstructed from the shower image, with essential parameters such as impact and incoming direction estimated roughly by a single telescope. However, the reconstruction is more reliable with stereoscopic observations, which is the same EAS is observed from two telescopes located in the different locations (Kohnle and et al., 1996). Further details on telescope design and reconstruction methods will be introduced in Section 2.3.1 and Section 2.4.

2.3 MAGIC Telescopes

The MAGIC telescopes consist of a system of IACTs, each with a 17 m diameter reflector, located at the Observatorio de Roque de los Muchachos on the Canary Island of La Palma (28°45′42″N; 17°53′25″W) at an altitude of 2200 m above sea level. A picture of the MAGIC telescopes is displayed in Figure 2.8. The first telescope (MAGIC-I) began operation in 2004 in standalone mode until the second telescope (MAGIC-II) was completed in 2009. The two telescopes are located 85 m apart (Aleksić and et al., 2012). In 2011 and 2012, a significant upgrade was performed on the trigger, readout systems, and camera of MAGIC-I to enhance its performance (Aleksić and et al., 2016). MAGIC can detect γ rays with energies ranging from tens of GeV (Acciari and et al., 2020a) to hundreds of TeV (Acciari and et al., 2020b). The standard trigger has an energy threshold of approximately 50 GeV for observations at zenith angles less than 25°, while the new electronic sum-trigger can lower the threshold to around 25 GeV (García et al., 2014; Aliu and et al., 2008).

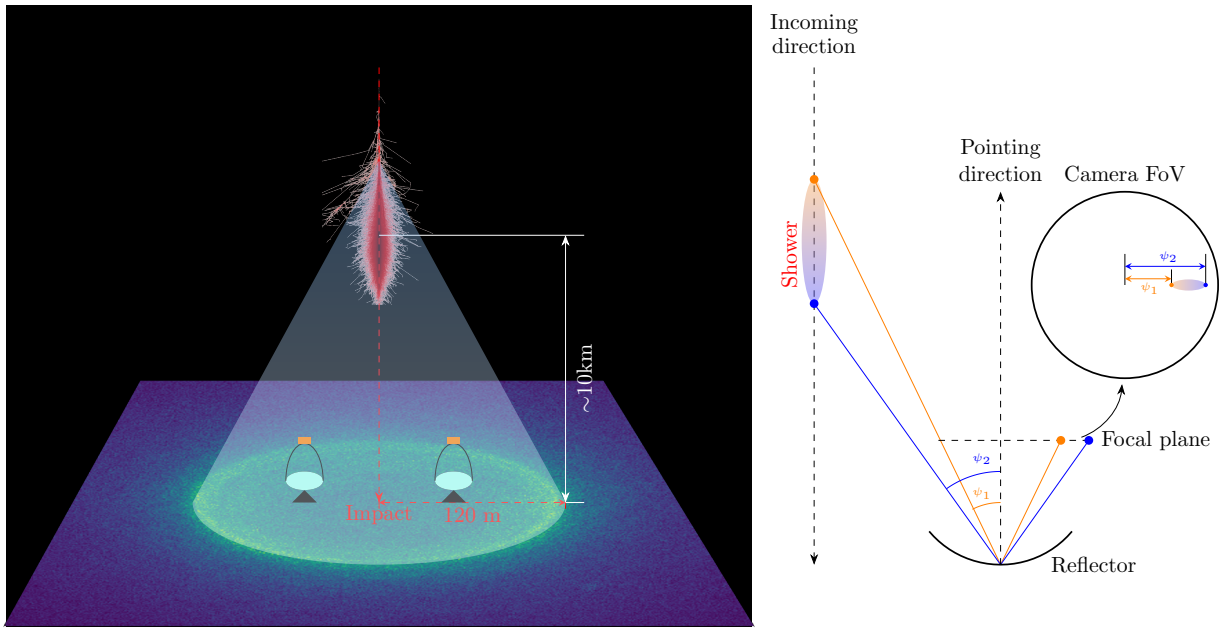

Figure 2.7: A sketch of IACT . Left panel illustrating the Cherenkov light emitted from a γ-ray shower that illuminates a light pool on the ground, with telescopes situated inside the light pool. Typically, γ-ray showers originate from 10 km above the telescopes, with the light pool having a radius of approximately 120 m. In the right panel of the sketch, photons with different incoming angles are converted to different distances from the camera center in the camera plane.

Figure 2.8: Magic telescopes on the island of la Palma. Image credits: Daniel L*ó*pez/IAC

2.3.1 Structure, Drive System and Reflector

The design and performance of the telescope structure, drive system, and reflector of MAGIC are briefly introduced in the following sections. They are important for efficient and accurate data collection.

Structure and Drive System

The telescope structure and drive system of MAGIC are designed for fast repositioning, with the structure designed to be as light as possible to achieve this goal. To achieve this, the telescopes use a steel and carbon fiber structure, which is both lightweight and robust, allowing each telescope to have a total weight of around 70 tons. The drive system of MAGIC can move in both the azimuthal and zenith axes (Bretz et al., 2009), with each telescope powered by two 11 kW electric motors (Lorenz, 2004). During repositioning, the telescopes move at a speed of 4°/s, which can increase to 7°/s in the fast movement mode.

Reflector

Each MAGIC telescope has a reflector system consisting of approximately 250 segmented mirrors, with a total area of 236 m^2 and a diameter of 17 m, and a parabolic reflector with a focal length to diameter ratio of f/D=1. The individual mirrors, each with a spherical surface area of 1 m^2, are controlled by the Active Mirror Control (AMC) system (Doro et al., 2008; Biland et al., 2007) to focus the light onto the camera. To evaluate the focused performance of the reflector, bright stars at different zenith distances are pointed towards the telescope, and the focused starlight is displayed on a removable plate in front of the camera. A CCD camera at the center of the reflector captures an image of the focused starlight, enabling the evaluation of the optical Point Spread Function (PSF). Typically, a PSF below 10 nm is expected for low zenith angles. The parabolic structure also allows the synchronous light's time spread to be negligible compared to the time spread of the Cherenkov pulse, making it possible to use the arrival time information during analysis.

2.3.2 Camera, Trigger and Readout

In the following discusion, the camera, trigger, and readout systems of the MAGIC telescopes are introduced. They play essential roles in the detection, discrimination, and digitization of incoming signals for further analysis.

Camera

Each MAGIC telescope is equipped with a camera consisting of 1039 Photo Multiplier Tubes (PMTs) arranged in a hexagonal lattice, with each pixel having a FoV of 0.1°. To fill the gaps between the detectors and enhance light collection, hexagonal Winston cones are placed in front of the PMTs. For efficient maintenance, the PMTs are grouped into several clusters, each with seven pixels. The camera covers a FoV of 3.5° (Aleksić and

et al., 2012; Cortina et al., 2009). When photons arrive at the photo cathode of a PMT, they stimulate electrons via the photoelectric effect, which are then immediately amplified by the dinodes (Nakajima et al., 2013). Vertical cavity surface emitting lasers (VCSELs) convert the amplified signal into optical signals, which are then transmitted via optical fibers to the counting house for digitization and readout.

Trigger

To discriminate air shower events from false events arising from the Night Sky Background (NSB), the MAGIC telescopes are equipped with a trigger system comprising three stages:

- **Level 0 (L0) trigger**: The first stage of the MAGIC trigger system is a pixel-wise trigger produced at the receiver boards, which checks whether the analog signal is above a given discrimination threshold (DT). DT is calibrated to ensure that the sensitivity for each pixel is flat in terms of photon density, and DTs are constantly adjusted during observations according to the observation conditions. The L0 (level zero) trigger is then transferred to the Level 1 trigger.

- **Level 1 (L1) trigger**: The second stage of the MAGIC trigger system is a single-telescope trigger that searches for the number of neighboring pixels that pass the L0 trigger, known as the next-neighbor (NN) pixels. The NN pattern ranges from 2NN (two neighboring pixels) to 5NN (five neighboring pixels), with MAGIC using 3NN. For the Level 1 (L1) trigger, only the central region of the camera (547 inner pixels covering a FoV of 2.4°), colored in cyan in Figure 2.9 is used. The L1 triggers from both telescopes are then sent to the third level of the trigger system.

- **Level 3 (L3) trigger**: The third and final stage of the MAGIC trigger system is a stereo trigger. Each Level 1 (L1) trigger is stretched to a width of 100 ns to ensure a stereo trigger efficiency and is delayed according to the zenith and azimuthal angle of observation to compensate for time differences originating from the different telescope positions (Aleksić and et al., 2016). Only if the signals from both telescopes overlap within a time window of approximately 180 ns, the Level 3 (L3) trigger transfers a signal to the readout system of both telescopes.

Readout

The optical signals transmitted through the fibers are converted back to electric signals by dedicated receiver boards (Tescaro, 2012). The analog signals are then digitized by the digitization system, which is based on the Domino Ring Sampler 4 (DRS4) chip (Bitossi et al., 2016). The DRS4 chip is a switched capacitor array with 1024 cells serving as a physical buffer, and it can be operated at sampling frequencies between 700 MHz and 5 GHz. The sampling frequency used in MAGIC is 1.64 GHz (Aleksić and et al., 2016; Sitarek et al., 2013). Whenever a trigger occurs, 50 samples in the time region of interest are read out by analog-to-digital converters (ADCs). The readout process leads to a dead time of approximately 27 μs, which is negligible considering the L3 trigger rate of 250 Hz.

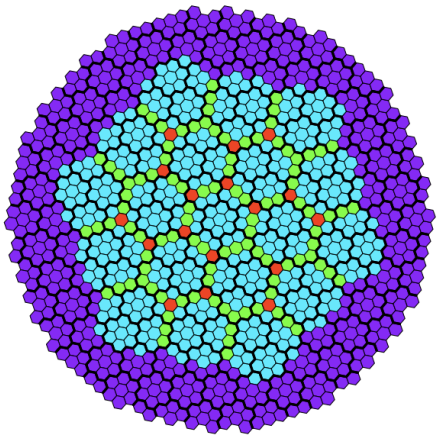

Figure 2.9: Geometry of the MAGIC cameras. The thick black lines outline the cluster of pixels. The 19 L1 trigger macrocells are shown in the cyan hexagons (each hexagon has 36 pixels). Pixels that are covered by two macrocells are illustrated in green and red pixel is overlapped by three macrocells. Taken from Aleksić and et al. (2016)

2.3.3 Observation

For the observation of IATCs, it is essential to monitor atmospheric conditions and measure background levels accurately. Several instruments and techniques have been developed to address these challenges. In this section, we will discuss two atmospheric monitoring systems, Light Detection and Ranging (LIDAR) and Pyrometer, as well as the wobble observation technique, which offers a practical approach to estimating background levels during IACT observations.

Wobble Mode

A simple way to estimate the background level in IACTs observations is to take background data under the same conditions as the source observations: pointing at a sky region where no γ-ray sources are expected, using the same camera region and atmospheric conditions, and following the same trajectory as the source. However, this approach requires allocating half of the observation time to background observation and introduces systematic errors because it is impossible to clone the exact same observation conditions. To address these issues, the wobble observation mode (Fomin et al., 1994) is commonly used in IACTs. In this mode, the telescope pointing direction is offset from the source position by a certain angle, typically around 0.4°. This allows for simultaneous observations of both the source (on-source region, or ON region) and the background (off-source region, or OFF region). The OFF region is defined as the area at the same distance from the camera center where the camera acceptance is symmetric. To reduce systematic errors caused by inhomogeneities in the individual PMTs distributed over the camera, four wobble positions are typically used. In MAGIC, the telescopes switch to the next wobble position every 20

minutes.

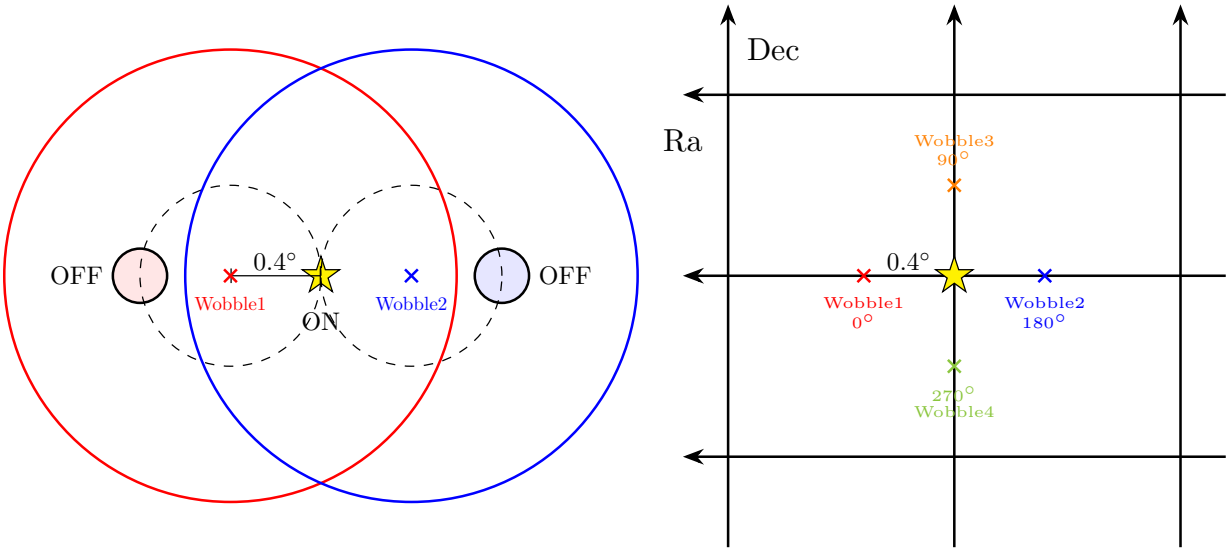

Figure 2.10: Sketch illustrating the wobble observation mode. The yellow star presents the source position in the camera plane. One pair of wobble positions (Wobble1 in red and Wobble2 in blue) are shown in the left panel. In each wobble position, the camera center is 0.4° offset from the source position. The OFF region is in the opposite sides of source position with respect to the camera center. The right panel shows the 2 pairs of wobble positions (Wobble1 and Wobble2; Wobble3 and Wobble4) given in right ascension (R.A.) and declination (Dec). The number and the wobble position can be adjusted for the specific observation purpose or to reduce the influence from bright stars.

LIDAR

To assess atmospheric conditions during observations, the observatory employs a LIDAR instrument (Fruck and et al., 2022). Situated atop the counting house's dome. This instrument comprises a 60 cm optical telescope with a 1.5 m focal length, a Nd:YAG laser operating at a 532 nm wavelength, and a Hybrid Photo Detector (HPD). Atmospheric transmission can be influenced by factors such as cloud cover or airborne dust. The LIDAR evaluates transmission at a different hights for MAGIC, corresponding to the typical height of the shower maximum (Fruck et al., 2014; Fruck, 2015). To prevent accidental triggers from laser flashes, the LIDAR's pointing direction is slightly offset from that of the telescopes.

IR Pyrometer

Another system for monitoring atmospheric conditions is a Heitronics KT19.82 pyrometer affixed to MAGIC-I. This pyrometer assesses the presence of clouds within the observation range. Clouds, reflecting the Earth's thermal radiation, increase the temperature relative

to clear skies. Taking into account the zenith distance, air temperature, and humidity, a parameter called "cloudiness" is calculated, ranging from 0 to 100. This serves as an additional tool for evaluating data quality, particularly when LIDAR information is unavailable (Will, 2017).

2.4 Standard Data Analysis

In this section I will present the standard analysis chain of MAGIC for the γ-ray point sources. The analysis is done based on the package named MAGIC Analysis and Reconstruction Software (MARS) (Moralejo et al., 2009; Zanin, 2013) developed by the MAGIC collaboration, which uses C++ routines combined with ROOT (Brun and Rademakers, 1997).

2.4.1 Signal Extraction

The signals recorded by the readout system are stored in the raw data as a waveform consisting of 50 samples (30 ns). In order to extract the charge in photoelectrons and the arrival time, the baseline of the waveform is estimated using the pedestal runs taken before and during observations. A sliding window of 5 consecutive samples is used to search for the maximum signal above the baseline. The maximal signal region is then integrated as ADC counts and converted to photoelectron (phe) units, with the conversion factor determined by the F-factor method through a calibration process. Calibration events are taken before and during observations for all pixels. The relation between the input Poisson-distributed number of phes with mean N and standard deviation $\sqrt{N}$ and the output FADC signal from the PMT with mean $\langle Q \rangle$ and standard deviation σ_Q is determined based on this calibration.

$$F\frac{\sqrt{N}}{N} = \frac{\sigma_Q}{\langle Q \rangle} \tag{2.9}$$

Where F is an intrinsic factor for individual PMT and is measured in the laboratory. The conversion factor C is computed as:

$$C = \frac{N}{Q} = F^2 \frac{\langle Q \rangle}{\sigma_Q^2} \tag{2.10}$$

The arrival time is determined by averaging the 5 time slices weighted by counts.

2.4.2 Image Cleaning

Image cleaning aims at identifying the pixels from the EAS emission and removing the rest of the information from the NSB or electronic noise. The cleaned image will be used to compute the shower image parameters. The cleaning procedure consists of two steps based on the charge and time information (Aleksić and et al., 2011; Ahnen and et al., 2017):

- Identifying the core pixels (the bright pixels): the summation of the charge in groups of neighboring pixels (2NN, 3NN, 4NN) is above a given threshold and the arrival time difference is within a certain time window (Aleksić and et al., 2016). The signal of each pixel is clipped at a certain level to prevent a single bright pixel from dominating the core. The threshold is defined as 2× 1.8× Q_1 and 1.1 ns for 2NN, 3× 1.3 × Q_1 and 0.7 ns for 3NN and 4× 1.0 × Q_1 and 0.5 ns for 4NN. For for dark nights (no moon condition), $Q_1 = 6$ [phe].

- Determination the boundary pixels: the pixels around the core pixels exceeds a given threshold Q_2=3.5 [phe] for dark nights and the arrival time offset from the adjacent core pixels is limited to be 1.5 ns.

An example of the shower image before and after image cleaning is depicted in Figure 2.11.

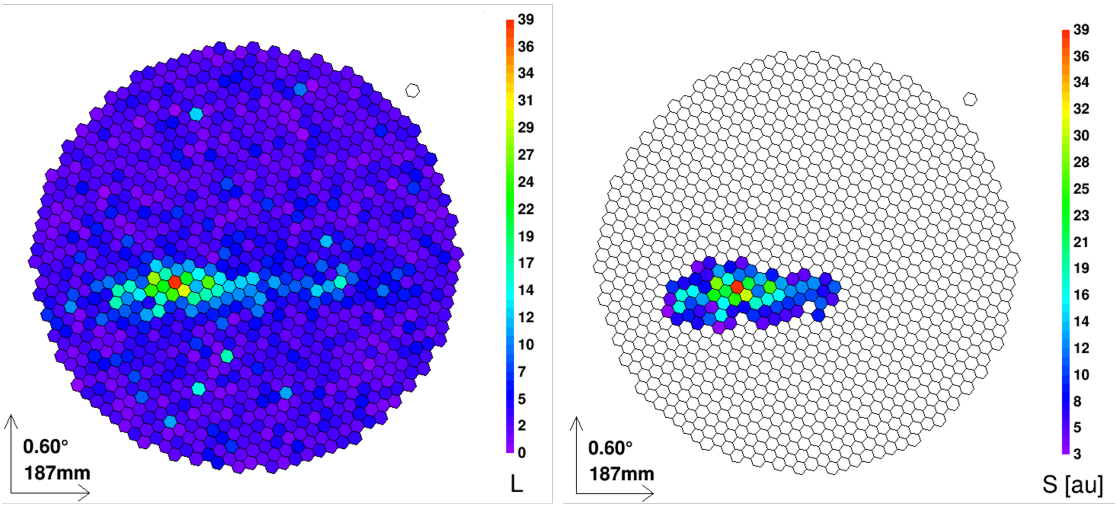

Image before cleaning Image after cleaning

Figure 2.11: The example of a simulated shower image shown in the camera before and after cleaning.

2.4.3 Monte-Carlo Simulation of Extensive Air Shower

The analysis procedure cannot proceed without MC simulation, which simulates the whole process of EAS from the particle interactions and light penetrating the atmosphere to the characteristic response of the telescopes.

Purpose of MC simulation

In the standard MAGIC analysis pipeline, extensive γ-rays are simulated. According to the properties of the target sources, γ-rays are simulated in two ways:

- **Ring wobble** MC: The incoming directions in the camera coordinate is distributed in a ring shape with radius equal to the wobble offset. Ring wobble MCs are used to the point-source analysis.
- **Diffuse** MC: The incoming directions in the camera coordinate is distributed in a disk with radius of 1.5° or 2.5°. Diffuse MC are used for the analysis of extended sources.

The simulated samples are divided into two groups during the analysis. One group is called "train" sample, which is used for the event reconstruction of observation data. The simulated event with known physical properties works as a reference to discern potential γ-ray event as well as estimated its incoming direction and energy. The detail of event reconstruction will be introduced in the Section 2.4.5. The other group is called "test" sample, which is used to evaluate the characteristic response of detector. The MC data processed with the same pipeline of real observations tell the ratio of survived γ-ray and the number of events originally simulated, which will be used to calculate the spectrum.

In diffuse analysis, such as the one conducted in this thesis, MC simulations play a crucial role beyond serving as a means of "train" and "test". They are also used to investigate the background event rate and estimate the contamination rate, as explained in detail in Chapter 3.

Programs of Simulation

Cosmic Ray Simulations for KASCADE (CORSIKA)(Heck et al., 1998) is a program for the simulation of development of EAS in the atmosphere initiated by different kinds of particles. The simulation is based on detailed theoretical models of the interaction between primary particles and atmosphere. Several hadronic interaction models are implemented in CORSIKA. The most commonly used ones for high energies (greater than 70GeV) are QGSJET-II-04 (Ostapchenko, 2011), SibyII (Fletcher et al., 1994; Ahn et al., 2009) and EPOS LHC (Pierog et al., 2015). It was developed for the analysis of KASCADE experimental data, and then was refined to be used also by many other groups including IACT .

In MAGIC, a modified version of CORSIKA, Mmcs is used to get the Cherenkov photons from EAS (Majumdar et al., 2005). CURVED atmosphere option is used which takes into account the Earth's curvature. This enables the possibility of Very Large Zenith Angle (VLZA) study in MAGIC. A specific atmosphere model for MAGIC winter with atmospheric refraction for Cherenkov photons is supplied. The softwares simulate the mirrors of telescopes to "focus" the Cherenkov photons, the PMT camera to "detect" the photons, as well as readout system and triggers of the telescopes (Moralejo, 2003). The MC "raw" events are processed with the same analysis chain as observation data.

Analysis Period

Specific MCs are produced for different analysis periods. This is because MAGIC has undergone several major hardware interventions throughout its history, such as changing the readout system from DRS2 to DRS4, upgrading the MAGIC-I camera, and minor changes of hardware. Additionally, due to the unstable weather conditions, the performance of the telescopes is different. Every change marks a beginning of a period. The MC data should be updated in each period in order to simulate the reality accurately. The basic information of the MC data sets used in this thesis are listed in the table 2.1.

Tag	Time Period	Description
ST0306	2014.11.24 - 2016.04.28	Data after PSF improvement in spring 2016
ST0307	2016.04.29 - 2017.08.02	Data after change of sampling to 1.64 GHz
ST0311	2018.11.01 - 2019.09.15	Data with recovered reflectivity

Table 2.1: The basic information of the MC data sets used in this thesis are listed in the table.

2.4.4 Event Parameterization

To better understand the characteristics of the cleaned image, a parameterization process is needed. The first proposed parameterization was by Hillas (1985) and is called Hillas parameterization. For some parameters, the charge and arrival time distribution over pixels contained in the cleaned images is the only ingredients required for the parameterization. These parameters are listed as follows:

- **Center of Gravity(CoG)** : a pair of values (X, Y) shows the position of the weighted mean signal in the camera reference frame.
- **Length and Width** : describe the ellipse shape of the cleaned image in the camera. Length and Width are defined as the half distance along the major and minor axis of the ellipse.
- **Size** : summation of the charges of all the survived pixels after the image cleaning in the unit of phe.
- **Leakage** : the fraction of phe distributed in the outmost ring of camera pixel (leakage1) or the second ring from the outer edge (leakage2).
- **Time Gradient** : describes the arrival time development. The arrival times of the image pixels are projected to along the major axis, and fitted by a first order polynomial function. The slope of the function is the time gradient (Aliu and et al., 2009).
- **Number of Islands** : number of groups of pixels belong to the cleaned images. Typically, γ-ray and electrons produce only one island.

- **Time RMS** : Root Mean Square (RMS) of the arrival time distribution of the survived pixels.

There are some other parameters taking advantage of the geometrical information of the two telescopes. By combining the shower image parameters from both telescopes, three dimensional parameter can be reconstructed:

- **Shower Axis**: there are two methods of defining the direction of shower axis. The classical method is using the intersection of the major axes of the two images superimposed on one camera. This method can have very large uncertainty if the relative positions of the two shower images in the camera plane is parallel to each other. The other method is called *Disp* method which will be introduced in the Section 2.4.5.

- **Impact Parameter**: the shower axis projected on the ground is named as impact point. The distance between the impact point and each telescope is called impact parameter as illustrated in the Figure 2.12.

- **Shower Maxheight**: the height of the shower maximum above the ground. Shower maxheight is determined by the crossing point of three direction vectors – the shower axis and the projection of Center of Gravity (CoG) of the shower images of two cameras into the sky. However, three lines are difficult to have a perfect intersection in the three dimension, in reality, the shower maxheight is defined as the altitude where the perimeter of the triangle determined by the three lines is the smallest as the blue triangle shown in the Figure 2.12.

- **Cherenkov Radius and Density**: the radius and the density of Cherenkov light distribution on the ground, which is produced by a 85 MeV (the critical energy) electron at the altitude of the shower height of maximum shower development..

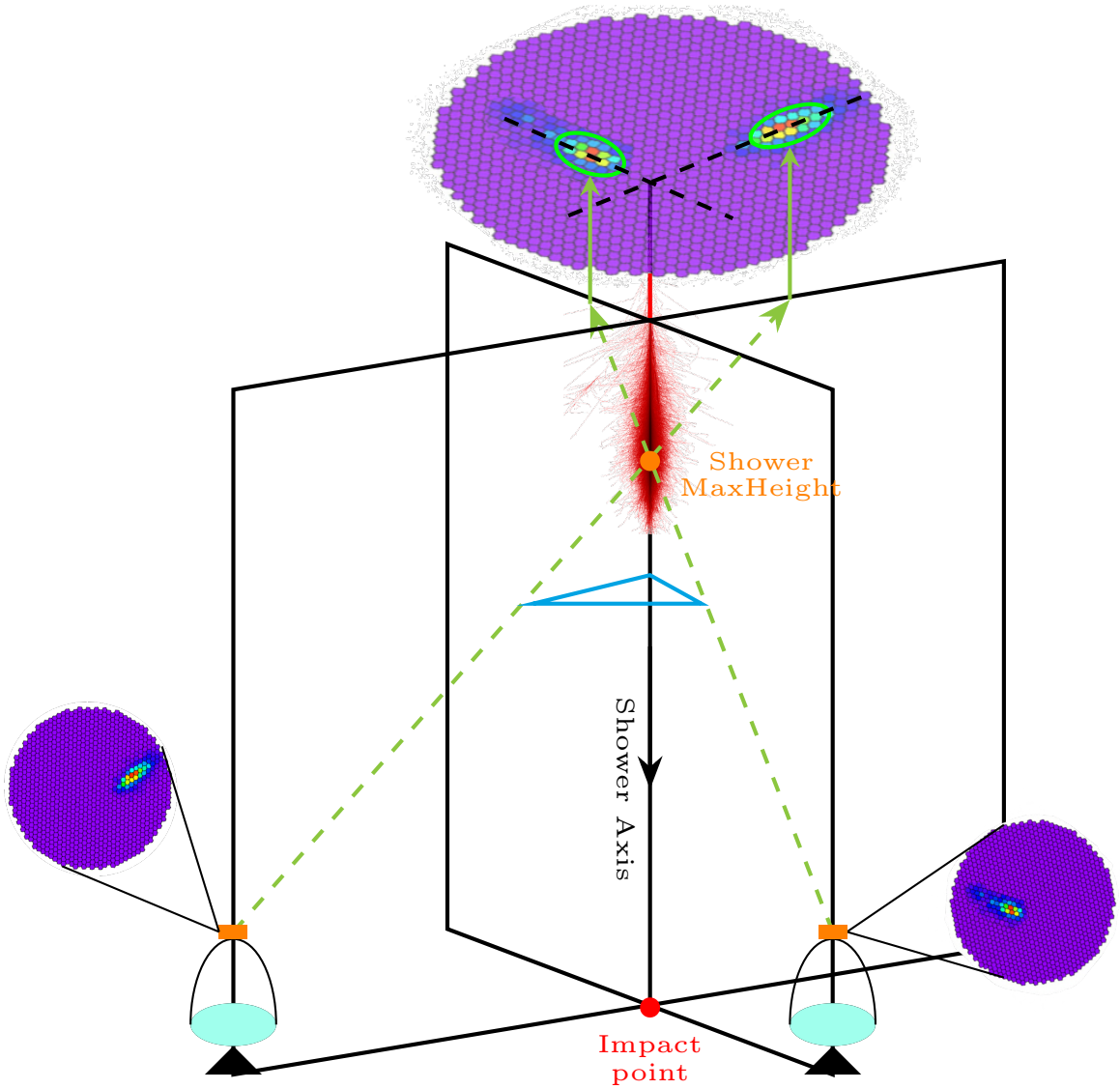

Figure 2.12: Stereo reconstruction of the shower parameters.

2.4.5 Event Reconstruction

The parameters computed from the previous section can be used to estimate the properties of the observed events. In order to investigate the nature of a γ-ray source, three essential pieces of information are needed: the particle type (whether it is a γ-ray or not), the energy, and the incoming direction.

Gamma/Hadron Separation

To identify the particle species, a new parameter called hadronness is calculated. The goal of computing hadronness is to estimate the probability of a particle being a γ-ray or a hadron. By applying a hadronness cut, the number of background events can be reduced. As introduced in Section 2.4.4, many parameters are already computed, and there are significant differences between the distributions of γ rays and hadrons among some of these parameters. For example, the Width distribution of MAGIC-I and the shower MaxHeight are illustrated in Figure 2.13. These parameters can be used to reject hadrons by applying proper cuts. However, finding the cut values for each parameter would be very complicated. To discriminate hadronic events more efficiently, RF is used to obtain the hadronness (Albert and et al., 2008).

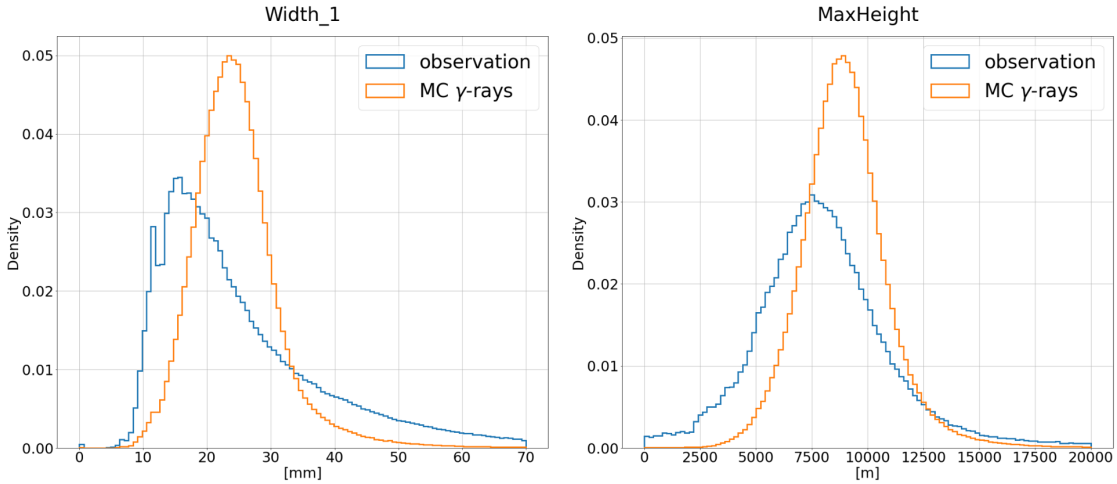

Figure 2.13: Width and MaxHeight distribution of MC γ-ray and real data.

RF is a machine learning technique that was first proposed by Breiman (2001). It consists of a collection of decision trees that search for the best cut conditions based on different parameters. After the input training samples are given, the decision tree grows by searching for the best parameters and cut conditions in each node at each depth, as shown in the example in Figure 2.14. The selection of parameters and optimized cuts in each node splitting is guided by the Gini index Q_{Gini}, which evaluates the inequality between two statistical populations. The Gini index is mathematically defined as:

$$Q_{Gini}(K) = 4 \cdot \frac{N_r N_h}{(N_r + N_h)^2}, \tag{2.11}$$

where K represents the node at which the index is being calculated, N_r and N_h denote the number of gamma and hadron events in the node, respectively. For each parameter, the selected cut is the one that leads to the greatest reduction in the Gini index.

The standard analysis uses simulated γ-ray events as the signal sample and actual data

without any γ-ray signal as the background sample for the hadronic events to train the algorithm. Once the training is complete, the hadronness at each node is calculated using Equation 2.12, assuming the contribution from γ-ray events is 0 and the contribution from hadron events is 1. The hadronness output of the RF algorithm can then be used to efficiently discriminate between hadronic and γ-ray events by applying a cut at a specific threshold value.

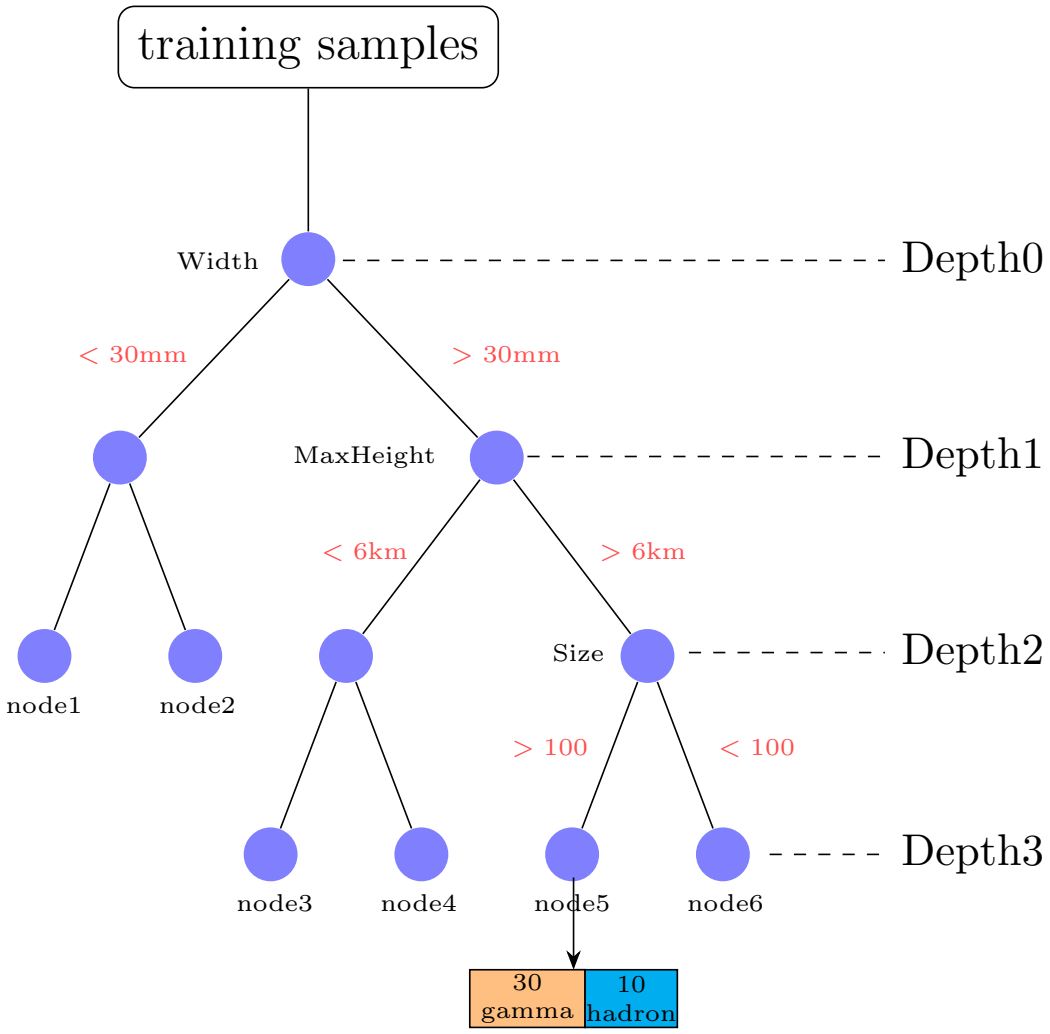

Figure 2.14: Decision tree grows by randomly choosing the best parameters and cut values in each node.

$$\text{hadronness}(nodex) = \frac{N_{electron}(nodex) \cdot 0 + N_{hadron}(nodex) \cdot 1}{N_{electron}(nodex) + N_{hadron}(nodex)} \tag{2.12}$$

For example, if the training finishes at the Depth=3, there are 30 γ-rays and 10 hadrons

at node1, the hadronness at this node is calculated by

$$\text{hadronness}(node5) = \frac{30 \cdot 0 + 10 \cdot 1}{30 + 10} = 0.25 \tag{2.13}$$

To prevent the decision trees from being sensitive to a particular data sample, multiple trees are generated by randomly selecting different groups of samples, which leads to the creation of a forest as shown in Figure 2.15. The final hadronness of an event is then determined by taking the average of the hadronness values calculated by all the trees in the forest.

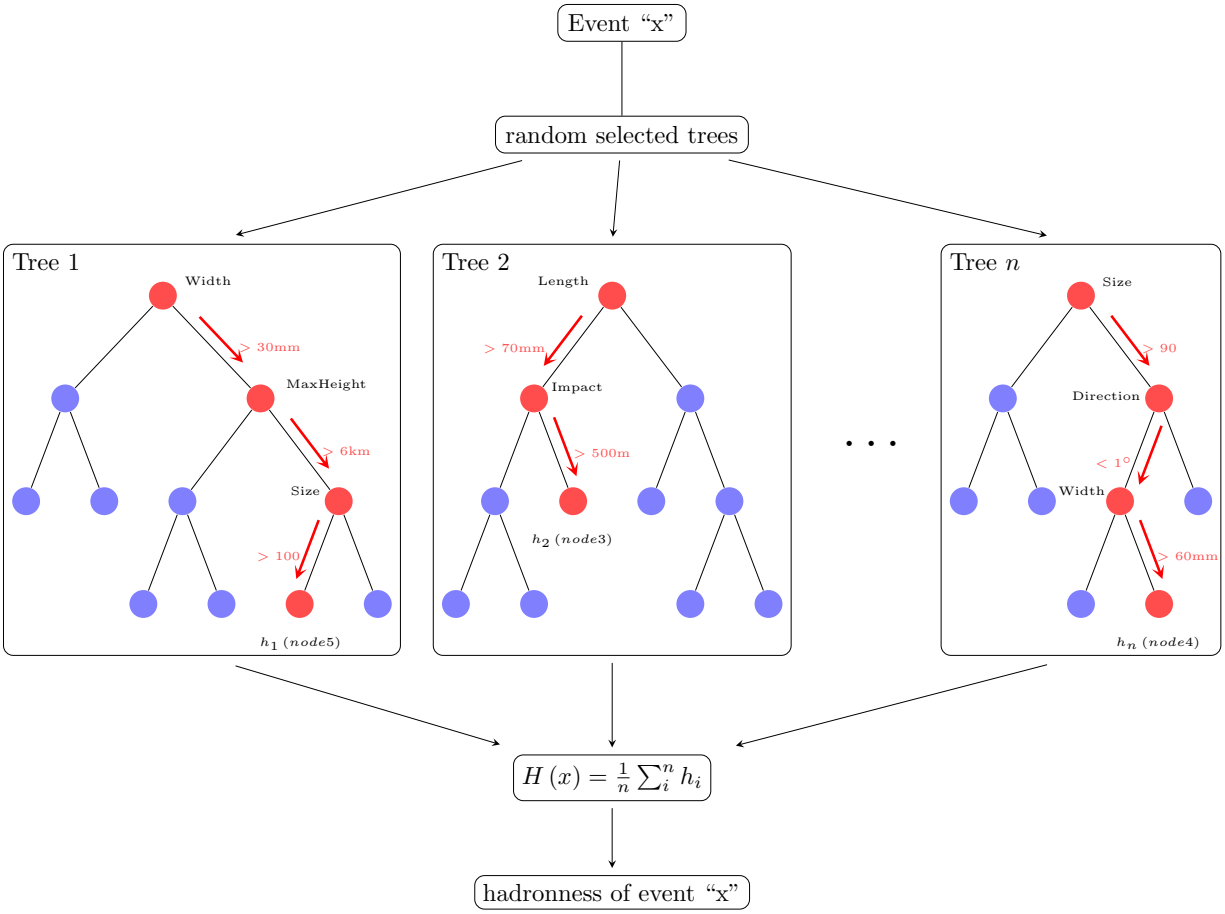

Figure 2.15: An example of how the hadronness of Event "x" is calculated. When an Event "x" is inputted, it traces down the nodes that represent binary decisions in each tree. At the terminal of each tree, a hadronness value is assigned. The ultimate hadronness value of an event is the mean of the hadronness values assigned by all trees in the forest.

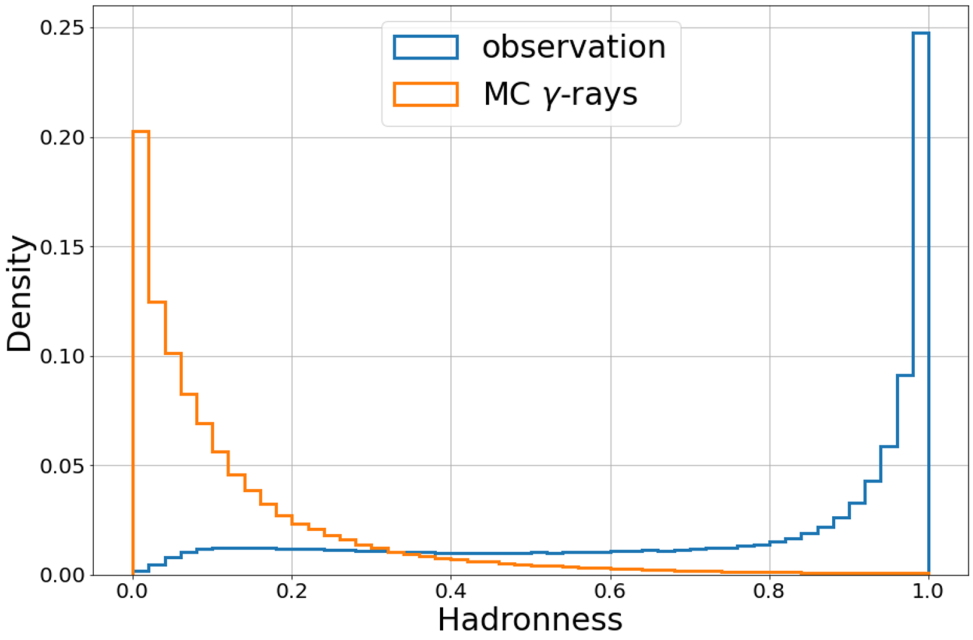

Figure 2.16: Hadronness distribution of MC γ-rays and observation data.

Energy Reconstruction

In MAGIC, there are two methods to estimate the energy of particle. The first one is called Look-Up Table (LUT) method. LUTs are constructed using MC γ-rays, where the known energies are binned according to some parameters. Size is approximately proportional to the number of electrons in the shower, hence to the primary energy of the particle. In addition to size, the telescope distance to the shower also plays a role in the energy estimation, therefore impact is used for the correction of estimated energy. The observed event will belong to one of these bins and the corresponding energy is assigned. For each event, the energy is obtained by averaging the energies estimated by two LUTs for individual telescopes. The second method is based on an RF designed to solve the regression problem. It learns how the energy of MC γ-rays is correlated with other parameters and develops decision trees. The energy is constructed after applying the estimator generated by numerous decision trees. RF energy estimation is a novel method and has been proven to be able to improve the energy bias and resolution (Ishio, 2020). In the analysis of this thesis, the RF energy estimation method is used.

Incoming Direction

The event-wise direction reconstruction is also based on RF. The so-called *Disp* method was originally developed for single-telescope analysis Lessard et al. (2001). Disp is the angular distance between the CoG and the incoming direction. The simulated γ-ray events with the known disp values provide the training information for RF. The training process is similar to the one used for energy estimation. The image parameters correlated with

disp are combined to estimate the disp for each telescope (Ishio, 2020). There are two possible incoming directions for the image from each telescope, as shown in Figure 2.17. The most possible incoming direction should be close to each other based on the estimation of two telescopes. To find the closest incoming direction estimated by the two telescopes, 4 pairs of distances are calculated after the superposition of two images. The two points connecting the smallest distance are chosen (1a and 2a as shown in Figure 2.17). The final reconstructed incoming direction is obtained by weighting the number of pixels in each image. Direction reconstruction is a very powerful tool to discard background events. If all of the 4 pairs of distances fail to have a small enough value, this event is discarded. This is because the disp is estimated based on the information of γ-ray shower, the hadronic event is difficult to construct a reasonable incoming direction. The distance between the reconstructed direction and the source is called θ (Aleksić and et al., 2016).

2.4.6 Signal Significance

Before extracting the number of excess events, event cuts are applied. One of the most import cuts is the Size cut, which can reject background fluctuation. The size cut is adjusted based on the NSB level (Ahnen and et al., 2017). Background events can be rejected significantly after applying a proper hadronness cut. Until this step, the number of excess N_{exc} are computed by comparing the number of events in the ON region and the OFF regions. The γ-ray events come from the source should have the reconstructed direction spread around the source region within certain radius, therefore the events binned in θ^2 to the ON direction is plotted. To estimate the number of background events, θ^2 target to the OFF direction is also plotted as shown in 2.18.

$$N_{exc} = N_{on} - \alpha N_{off} \tag{2.14}$$

Where α takes into account the difference between the observation time on ON an OFF regions. According to a null hypothesis, the expected signal is assumed to be from the background. The significance of the signal S is computed by the Li&Ma expression (Li and Ma, 1983)

$$S = \sqrt{2}\left\{N_{on}\ln\left[\frac{1+\alpha}{\alpha}\left(\frac{N_{on}}{N_{on}+N_{off}}\right)\right] + N_{off}\ln\left[(1+\alpha)\left(\frac{N_{off}}{N_{on}+N_{off}}\right)\right]\right\}^{1/2} \tag{2.15}$$

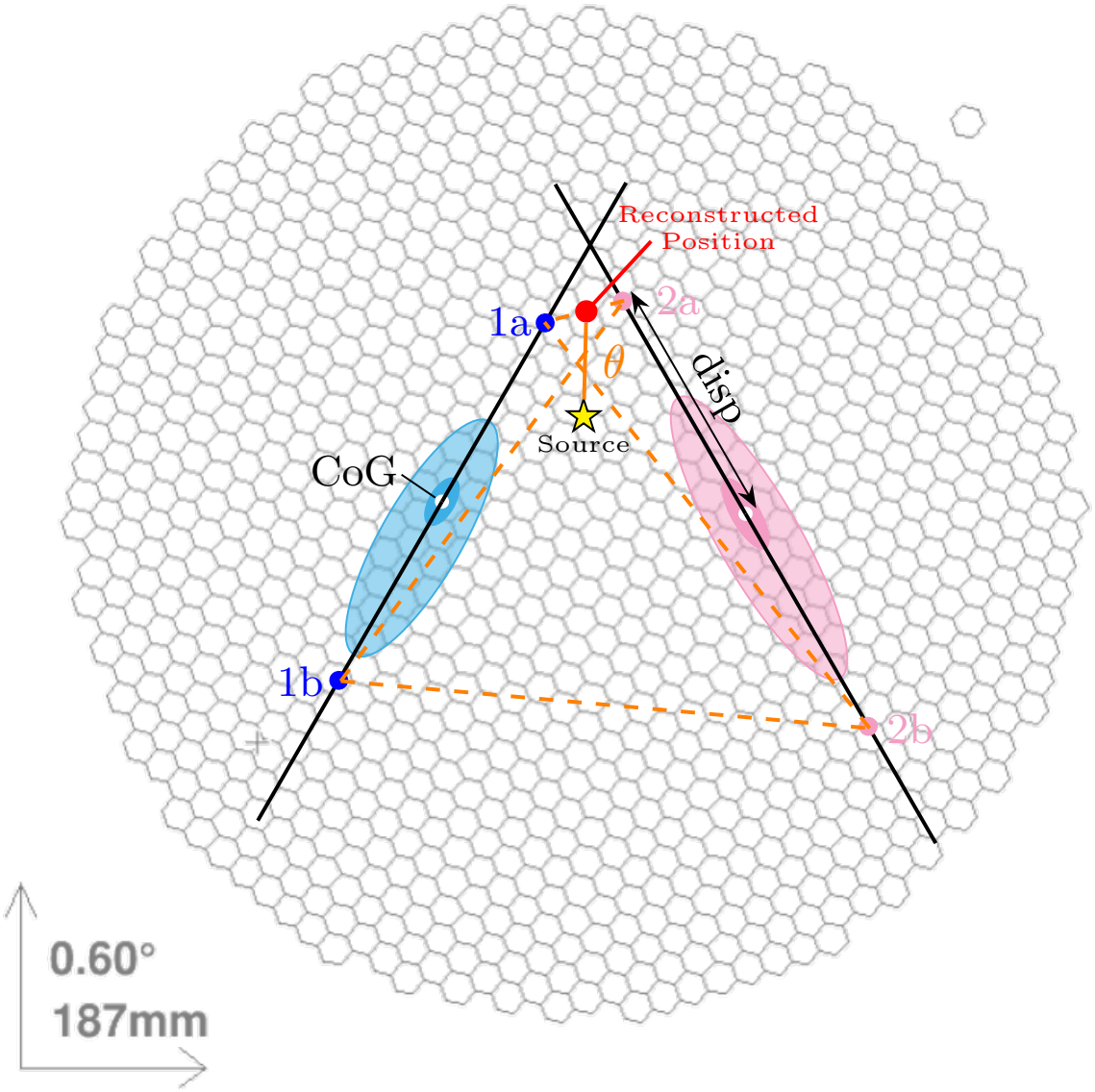

Figure 2.17: Sketch of the illustrating the Stereo *Disp* method. The major axes of the shower images are shown in the black lines. Along each major axis, two filled circles are plotted representing the disp distance. 4 pairs of distances (the orange dashed lines) are computed. The two points (1a and 2a) connecting the smallest distance are selected. The reconstructed incoming positron is defined as the weighted average position of the two selected points (the red filled circle). The assumed source direction is shown as the yellow star. The distance between the reconstructed direction and the source is called θ.

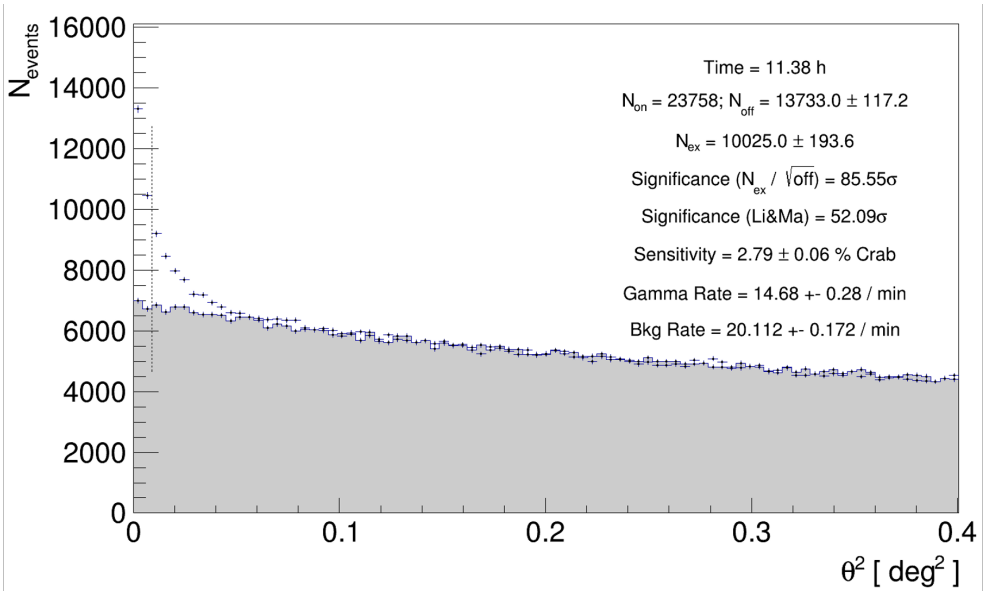

Figure 2.18: An example θ^2 distribution using Crab data.

Chapter 3

Cosmic-Ray All-Electron Spectrum Analysis

As discussed in the Section 2.4.6, the number of background events for γ-ray point source analysis is determined by evaluating the number of events in the"Off" region. However, due to the diffuse nature of cosmic-ray electrons and positrons, this method cannot be applied. In the following, I will introduce two methods optimized for calculating the number of cosmic-ray all-electrons that I developed as part of my doctoral course. Ensuring an accurate estimation and appropriate treatment of the background is critical for the all-electron spectrum analysis using IACTs. The detection and potential contamination due to hadrons will be discussed in Section 3.1, while the principle of data selection and quality cuts will be introduced in Section 3.2. Detailed explanations of the two methods for evaluating background events and obtaining the number of cosmic-ray electron and positron events will be provided in Section 3.3 and Section 3.4, respectively. The flux determination and performance tests regarding energy and directional reconstruction of both methods will be discussed in Section 3.5. Finally, the pros and cons of both methods will be summarized in the last section, Section 3.6.

3.1 Detection Method and Expected Background

3.1.1 Detection of Electron and Positron

Electrons and positrons are detectable by IACTs. The process of air shower starting from electron and positron is the same as that of γ-rays after the first interaction, and the first interaction point is indistinguishable because of the similar slant depth. It is obvious that telescopes designed for detecting γ-ray signal can also detect electrons and positrons, however such fact also leads to the problem that γ-rays become an indiscernible contamination.

3.1.2 Contamination from γ-rays

Diffuse Galactic Emission

In our analysis chain, γ-ray, electrons and positrons are indistinguishable, therefore it is unavoidable to have a contamination from γ-rays, despite that we can reduce the amount of contamination as much as possible at the data selection step. The majority of γ-rays come from the known point sources and diffuse emission in the Galactic Plane, thus we select the pointings away from the Galactic Plane with Galactic latitude cut $|b| > 20°$. According to the H.E.S.S. (Abramowski et al., 2014), the DGE at TeV energy range is hardly to extend to $|b| > 2°$. However, *Fermi*-LAT (Neronov and Semikoz, 2020) has reported a much stronger DGE originating from the inner Galactic region, with the DGE spectrum extending up to higher Galactic latitudes. Even if we consider the stronger DGE emission estimated from *Fermi*-LAT, the contamination is still less than 0.5% at 300 GeV (Neronov and Semikoz, 2020) at middle Galactic latitudes $10° < |b| < 30°$ and high Galactic latitudes $|b| > 50°$. Although DGE shows a harder spectrum at energy from 300 GeV to 3 TeV with slope $\Gamma = 2.40 \pm 0.05$, the contamination at 1 TeV is still less than 1% based on the calculation from Figure 3.1.

Isotropic γ-ray Diffuse Background

The flux of IGRB for Galactic latitudes $|b| > 20°$ was also calculated by *Fermi*-LAT (Ackermann et al., 2015), covering the energy range from 100 MeV to 820 GeV. The spectrum can be described by a power law with exponential cutoff:

$$\frac{\mathrm{d}N}{\mathrm{d}E} = I_{100} \left(\frac{E}{100MeV} \right)^{-\gamma} exp \left(\frac{-E}{E_{cut}} \right) \tag{3.1}$$

Where the power law index is $\gamma \approx 2.3$, cutoff energy $E_{cut} \approx 250GeV$ and intensity $I_{100} \approx 10^{-7}$ after considering different diffuse Galactic emission models. According to this formula, the flux of IGRB at 300 GeV would be around 0.05% of the expected all-electron fluxes. The comparison between DGE and IGRB is illustrated in Figure 3.1.

Known Point γ-ray Sources

In this work, we use the MAGIC pointings associated to non-detected MAGIC sources in order to avoid the known γ-ray flux contributions to the all-electron spectrum.

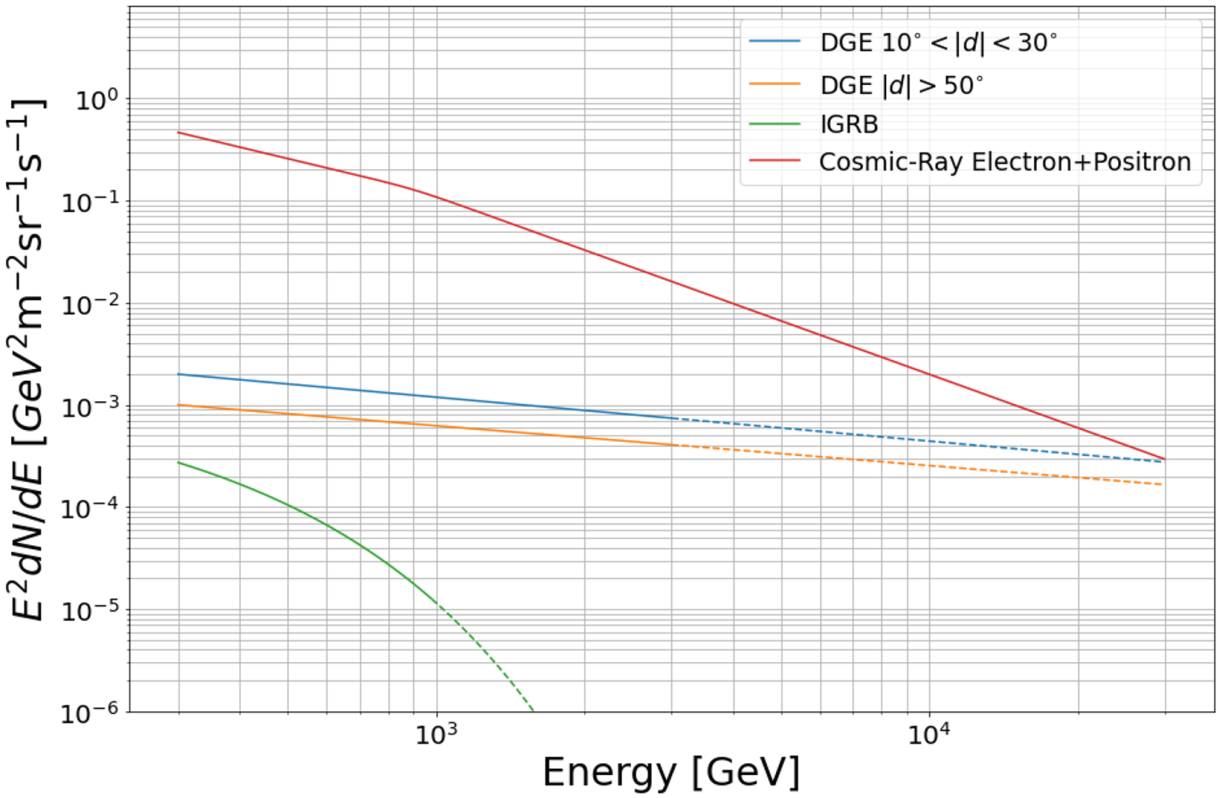

Figure 3.1: Comparison of DGE, IGRB and cosmic-ray all-electron spectrum at middle $10° < |b| < 30°$ and high $|b| > 50°$ Galactic latitudes. The solid lines show how the spectra of DGE estimated by Fermi/LAT (Neronov and Semikoz, 2020) from 300 GeV to 3 TeV, while the dashed lines show the spectra extrapolate beyond 3 TeV. The spectrum of IGRB before 980 GeV is taken from Ackermann et al. (2015), and extrapolated until higher energy range as shown in the dashed line. The all-electron spectrum is from Kraus (2018).

3.1.3 Contamination from Cosmic-Ray Hadrons

The main contamination in this work is from γ-ray-like hadronic showers, decaying from neutral pions produced by the interaction between cosmic-ray hadrons and the atmosphere. From the all-particle cosmic-ray spectrum shown in Figure 1.1, the flux level of the main cosmic-ray components, protons and helium is at around 3 orders of magnitude higher than cosmic-ray electrons and positrons, with a harder power law index of -2.6 for energy above 100 GeV/nucleon (Green, 2016). This kind of background cannot be eliminated as in the standard IACT analysis by "On−Off" method, because there is no "Off" region for the background estimation. In order to estimate the background, two methods: **RF-Fit** (Section 3.3) and **Two-step RF** (Section 3.4) are used.

3.2 Data Selection

3.2.1 Source Selection

The selection of the observation FoVs is critical and need to be meticulous, as can be seen from the preceding discussion. MAGIC has been conducting dark matter searches for many years, and some of the data obtained perfectly meet our requirements. The information of the selected sources are listed in Table. 3.1.

Source name	Period	Teff [h]	zd [deg]	az [deg]	b [deg]
M15	ST0306	86.2	16∼30	175∼250	-27.3
M15	ST0307	54.2	16∼30	175∼250	-27.3
Draco	ST0307	35.5	29∼35	-25∼25	34.7
Coma Berenices	ST0311	48.3	4∼35	80∼270	83.6

Table 3.1: Basic information of the selected data: source name, observation period, corresponding effective time after the correction of the triggered dead time, zenith distance range, azimuth range and the distance to the Galactic Plane.

The basic rules of data selection are summarized as followings:

- Located at Galactic latitude $|b| > 20^\circ$
- No known point γ-ray emission from the FoVs
- No bright stars in the FoVs

Galactic Latitude

Based on the discussion in the Section 3.1.2, the position of the sources relative to the Galactic Plane is crucial in order to minimize contamination from diffuse γ-rays as much as possible. In this work, the sources at Galactic latitude $|b| > 20^\circ$ are selected. The sky coordinates of the selected sources are marked in the Figure 3.2 and listed in the Table 3.1.

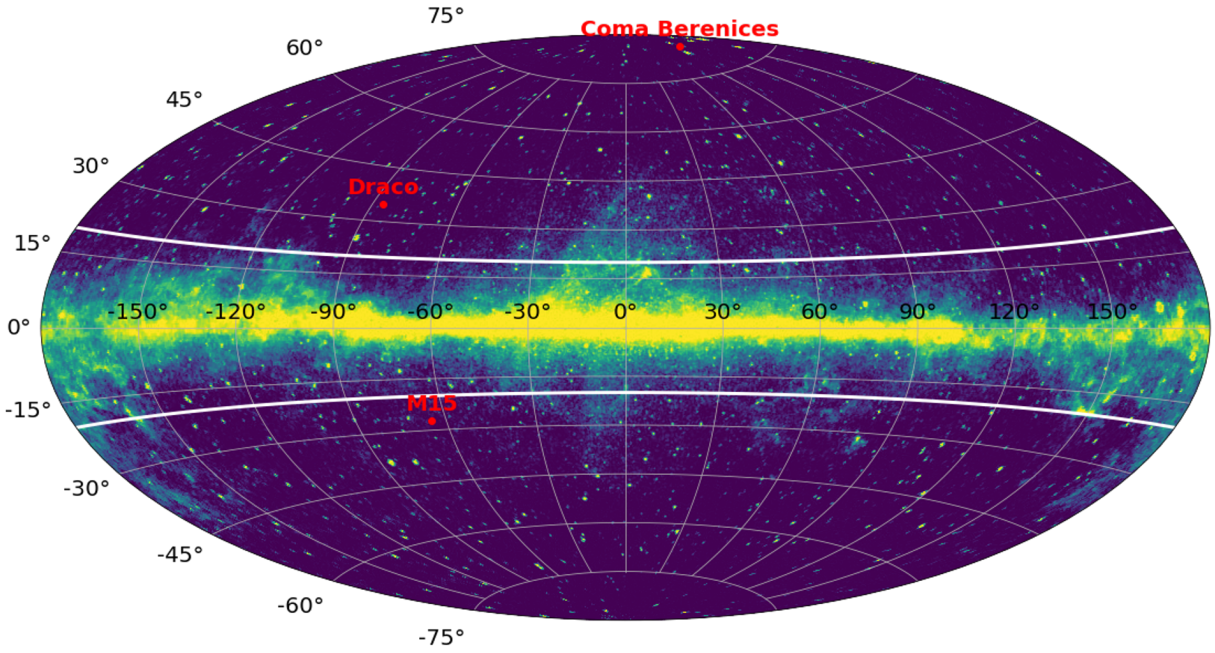

Figure 3.2: The sky coordinates of the selected sources. The two white lines indicate the Galactic latitude $b = \pm 20°$. Composition of the *Fermi*-LAT's Five-year View of the γ-ray Sky [1]

No Detected Source in the FoVs

It is possible to use known point-like γ-ray sources to calculate the all-electron spectrum by applying a θ^2 (introduced in Section 2.4.6) cut to remove the known γ-ray flux, but this method can introduce systematics in the calculation of the collection area. In this study, I prefer to use the FoVs associated with no γ-ray signal that allow for a larger FoV and less systematics. The Test Statistic (TS) value maps of these sources are shown in (Figure 3.3). The TS values [2] are lower than 4 sigma in areas within a 1° radius FoV of the MAGIC telescopes relative to the pointing directions. This suggests that there is no point γ-ray emission from those particular regions.

[1] URL: `https://svs.gsfc.nasa.gov/11342`

[2] Our test statistic is Li and Ma (1983) eq. 17, applied on a smoothed and modelled background estimation. Its null hypothesis distribution mostly resembles a Gaussian function, but in general can have a somewhat different shape or width.

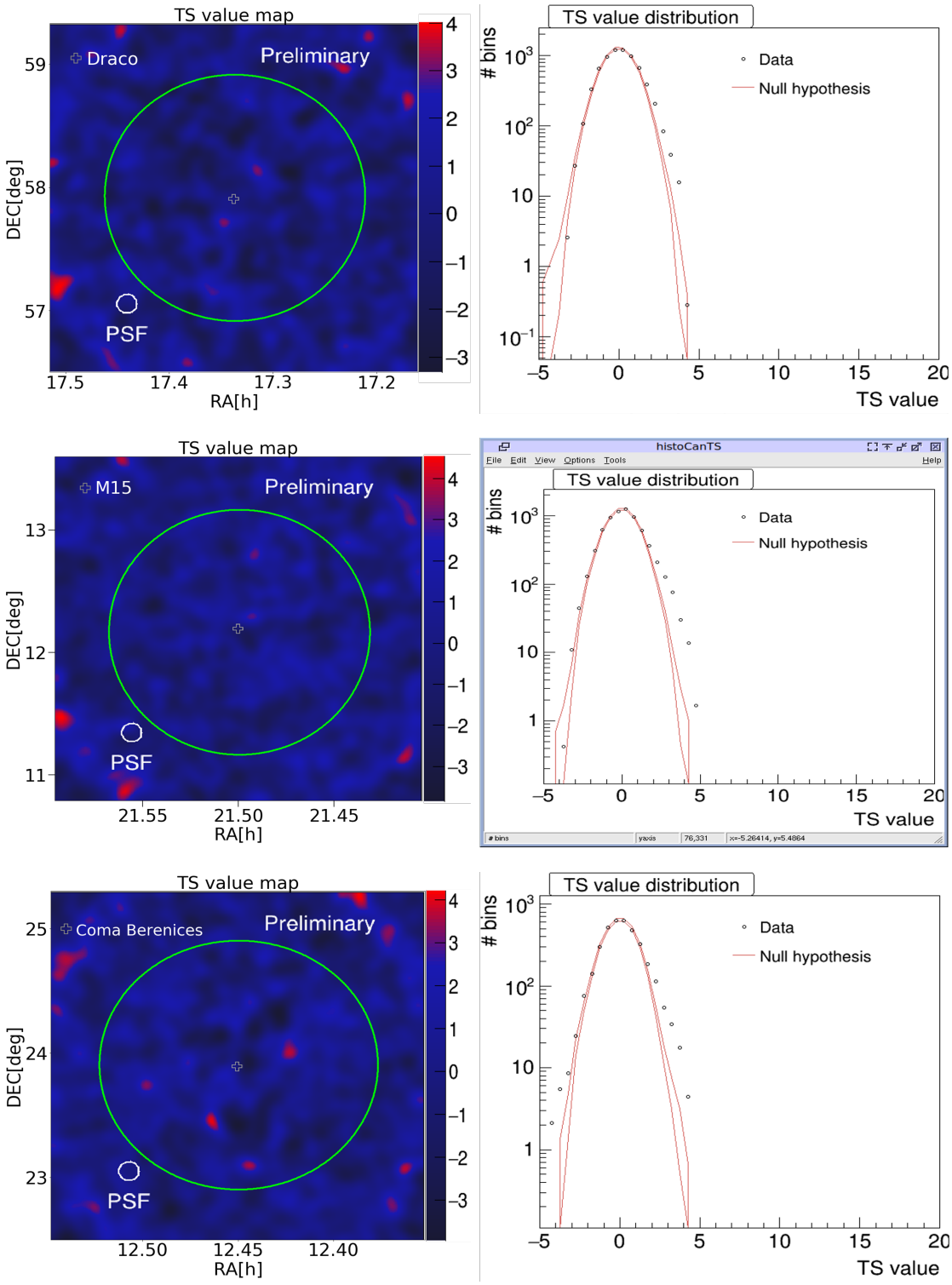

Figure 3.3: The left panel shows the TS value maps for the FoV of the selected sources analyzed using the MAGIC standard analysis chain. The green circles indicate the 1 deg distance to the camera center. The left panel shows the TS distribution of corresponding FoV.

Bright Stars

It is also important to avoid the pointings that contain bright stars within the FoV, as their light can cause noise for IACTs. Additionally, extremely bright starlight can potentially endanger PMTs. To protect the PMTs, the High Voltage of the pixels affected by the bright stars will be automatically ramped down by the camera control software. At the data analysis stage, starlight can affect the Hillas parameterization and cause problems for event classification.

3.2.2 Event Selection

The next step is to select the data with good quality. As an important part of the detector system, atmospheric conditions play a crucial role in the quality of the data. If it is available, LIDAR measurements are used to evaluate the transmission of the light. If not, the cloudiness conditions are used. MC Simulation and observation data show a discrepancy for very large zenith distance, and this discrepancy becomes more and more significant with as zenith distance increases. In this work, only the pointings with zenith distance less than 35° are selected.

The quality cuts are listed below:

- Transmission of laser from an altitude of 9 km above the ground must larger than 0.8
- Cloudiness is less than 45
- Zenith distance less than 35°

The effective time of each source survived the event cuts is also listed in the Table 3.1.

3.3 RF-Fit method

As discussed in Section 2.4, to extract the point-like γ-ray signal from the large amount of background events, there are two crucial steps. Firstly, by applying certain parameter cuts, especially the hadronness cut, the majority of background events that look very much like hadrons can be rejected. Secondly, the number of background events that survive the hadronness cut can be estimated by counting the surviving events in the "Off" region. However, the biggest challenge is that there is no "Off" region for cosmic-ray electrons and positrons, as they arrive from all directions within the camera FoV. To estimate the expected number of background events that survived from the hadronness cut, simulated protons are used. Several steps in this method are highly non-standard and are generally not part of the standard MAGIC analysis pipeline:

- **Samples for RF**: diffuse electrons and protons are used as training samples to process RF. (Section 3.3.1)

- **Tracking MC stimulation**: a method of MC simulation to ensure the simulation data have the exact same pointing trajectory as the observational data.(Section 3.3.2)
- **Additional event cuts**: Before fitting the hadronness, more stringent cuts are applied compared to standard analysis to ensure that the hadronness distribution can be fitted as accurately as possible. (Section 3.3.3)
- **Fit hadronness distribution**: An extended likelihood fitting method is used to fit the hadronness distribution of protons and electrons, in order to extract the excess of electrons and positrons from the total distribution. (Section 3.3.4).

3.3.1 Training Samples of Random Forest

As mentioned in Section 2.4.5, the RF for gamma/hadron separation in the standard analysis is trained using simulated γ-ray events as the signal sample and real data without γ-ray signal as the background sample. The real data, serving as a background sample, contains a small fraction of electrons and positrons. Since the contamination from electrons and positrons is significantly low, the background sample should work in principle, as the RF algorithm is concerned with the overall distribution of the training samples. For example, VERITAS uses real data as background training sample for their all-electron spectrum study (Archer et al., 2018). However, this may lead to systematics caused by the imperfect nature of simulated data.

If the real data events represent hadrons and the MC events represent signals as the training samples, due to the imperfect nature of simulated data, the RF algorithm may make biased decisions based on the differences between the real and simulated data rather than the differences between the hadrons and signals during the training process. Consequently, when using MC data to estimate the background, the resulting hadronness distribution of background may more closely resemble signals, while the hadronness distribution of the observed data may resemble hadrons. This effect can be cancel out for the standard analysis, since the background is estimated using the real data from the"Off" region. To minimize the systematics caused by the aforementioned bias, simulated data are used to represent both background and signal for the RF training process. Additionally, dedicated RFs are produced for each FoV in each period to minimize the systematics caused by zenith distance, azimuth and analysis period.

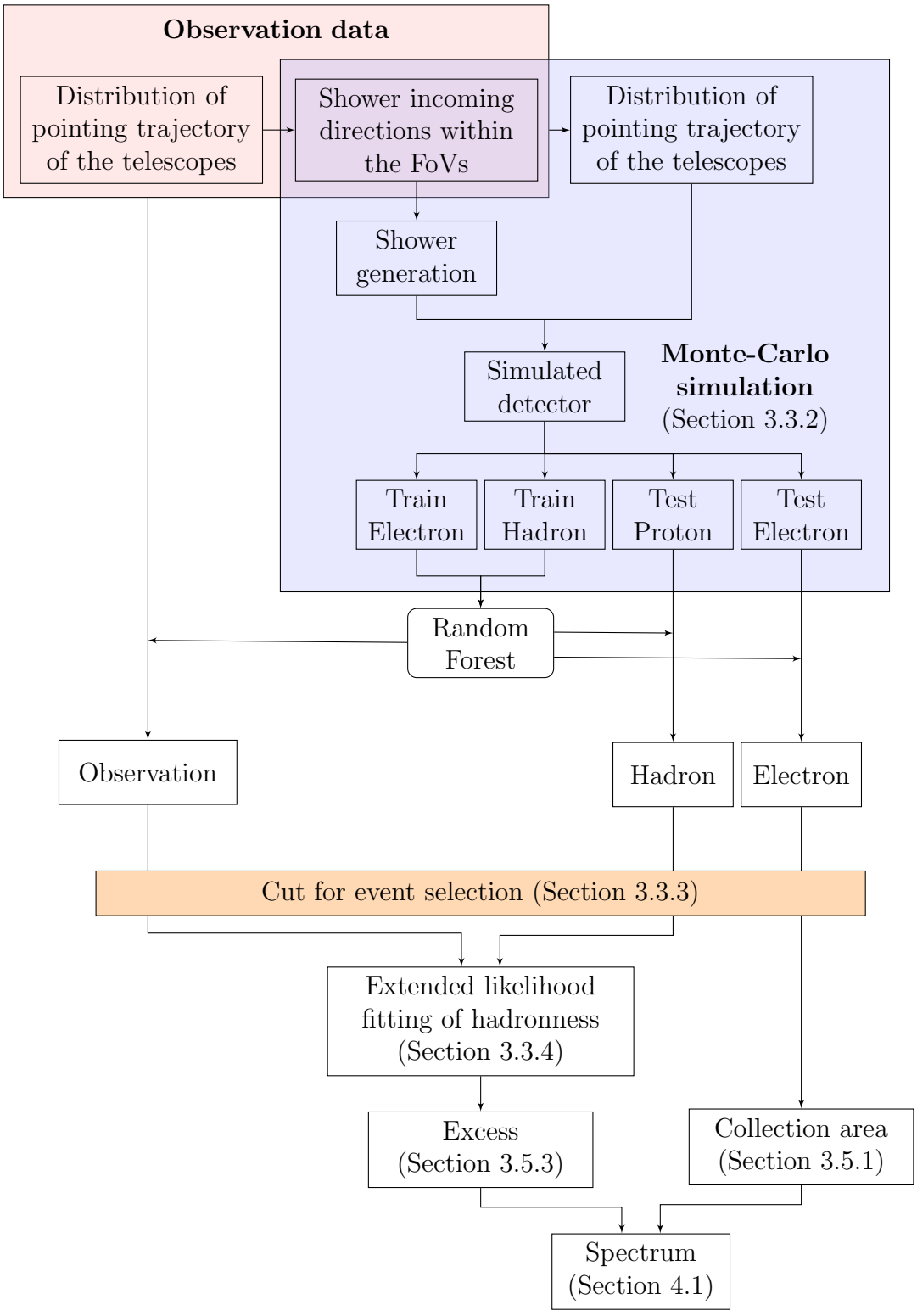

Figure 3.4: The flow chart of **RF-Fit** method analysis process. The region depicting the distribution of incoming direction for each event in the observation data overlaps with the simulation data, indicating that these two types of data share the same FoV. The simulated pointing directions for the telescopes are chosen based on the trajectory of the real observations.

3.3.2 Tracking MC Simulation

The **RF-Fit** method uses simulated hadrons to estimate the background that cannot be rejected by the hadronness cut. To achieve a precise evaluation of the background, it is important that the simulation closely replicates the real observation trajectory. A novel MC simulation method—tracking MC simulation is developed for this purpose. Figure 3.5 demonstrates that the hadronness distribution varies over the trajectory and observation period. If the simulation does not reproduce the same observation conditions, the hadronness distribution will not match that of the observation. For this reason, the background can be overestimated or underestimated, leading to significant systematic uncertainties.

In the standard MC simulation, the distribution of zenith distance and azimuth is averaged within a certain range. This is because the γ-ray MC is only used as a training sample for the RF and to calculate the collection area. Using the averaged-pointing γ-ray MC as a training sample for the RF is not problematic, as long as that the MC covers the same zenith distribution as the observed data to ensure that the RF learn all the necessary information about γ-rays for analyzing the observed data. For calculating the collection area, a program called "flute" weights the MC γ-ray events based on the effective on-time spent in each zenith angle bin in the analyzed data sample, since the collection area heavily relies on the zenith angle. A similar procedure can also be applied to weight the MC based on the azimuth distribution for more precise analysis, and coarse binning may be required to preserve sufficient statistics.

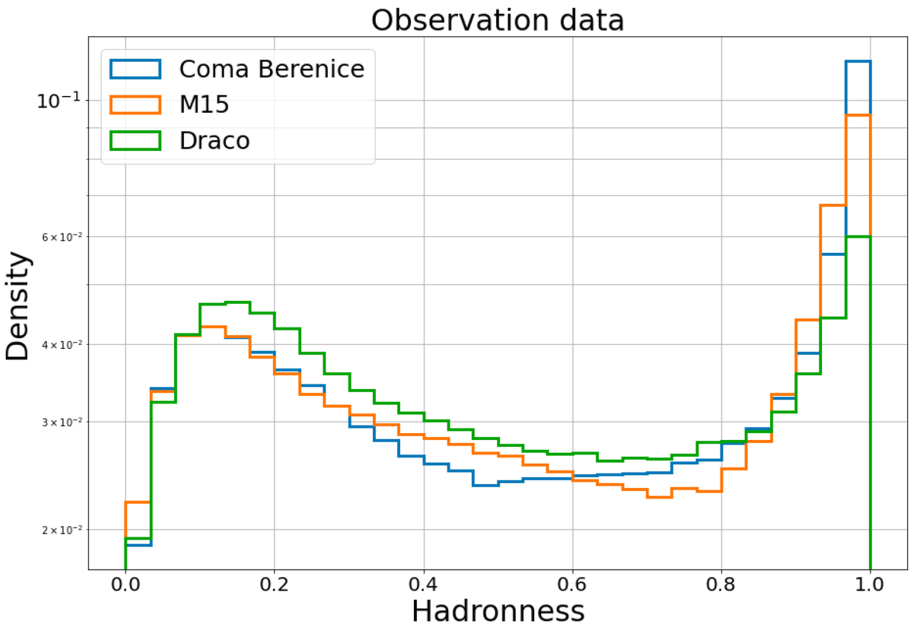

Figure 3.5: Hadronness distribution of observation data of different sources at different zenith distance, different azimuth and different observation period. The hadronness region (0 to 0.4) is used to fit between observation and simulation.

However, for the RF-Fit method tracking MC simulation is needed. In addition to serving as RF training samples and for calculating the collection area, simulated data are also used for estimating the background level. MAGIC is unique with respect to the other IACTs due to its unique two-telescope configuration (described in Section 2.3), which leads to a greater asymmetry in background calculations compared to other IACTs like H.E.S.S. and VERITAS that utilize data from four telescopes. This asymmetry introduces an azimuthal dependence that is crucial to consider in the study.

To minimize the systematics caused by the zenith distance and azimuth distribution, the simulated pointing directions must match the observation data, which can be achieved by weighting each zenith distance and azimuth bin as "flute" dose for the collection area calculation. However, the statistics in the desired bins are expected to be significantly lower. Therefore, I developed a tracking MC simulation method that simulates the path of FoVs as viewed from La Palma. This approach is just like the standard wobble-mode observation, in which the "On" and "Off" regions are observed simultaneously to reduce the systematic effects caused by different pointing directions between the two regions.

In the traditional simulation, the telescopes' pointing azimuth and zenith distance range are specified in the CORSIKA input card as the incoming directions of the showers. For the diffuse simulation, the pointing directions are randomly generated within a view cone around the incoming directions. The distribution of pointing directions in the standard simulation is shown in the right plot of Figure 3.6. In the tracking MC method, the FoV corresponding to each pointing direction is calculated beforehand, as illustrated in Figure 3.7, and then used as the shower's azimuth and zenith distance coordinates in the CORSIKA input card. The pointing directions of the telescopes are randomly selected with respect to the shower incoming directions from the actual observation sample. The distribution of the pointing directions in the tracking MC is shown in the middle plot of Figure 3.6, which is identical to the actual observation distribution shown in the left plot of Figure 3.6.

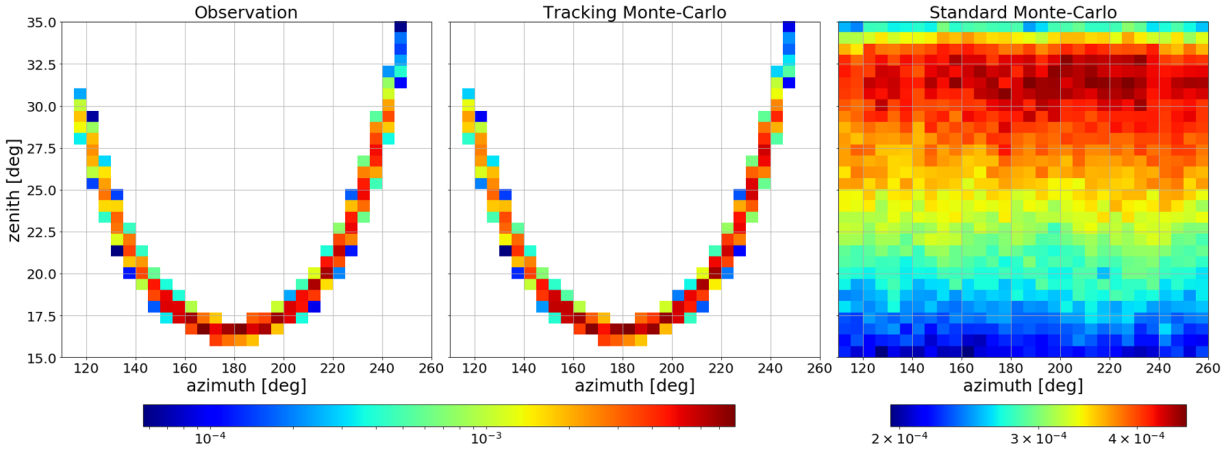

Figure 3.6: The comparison of pointing directions of observation data with Monte-Carlo tracking method and standard method.

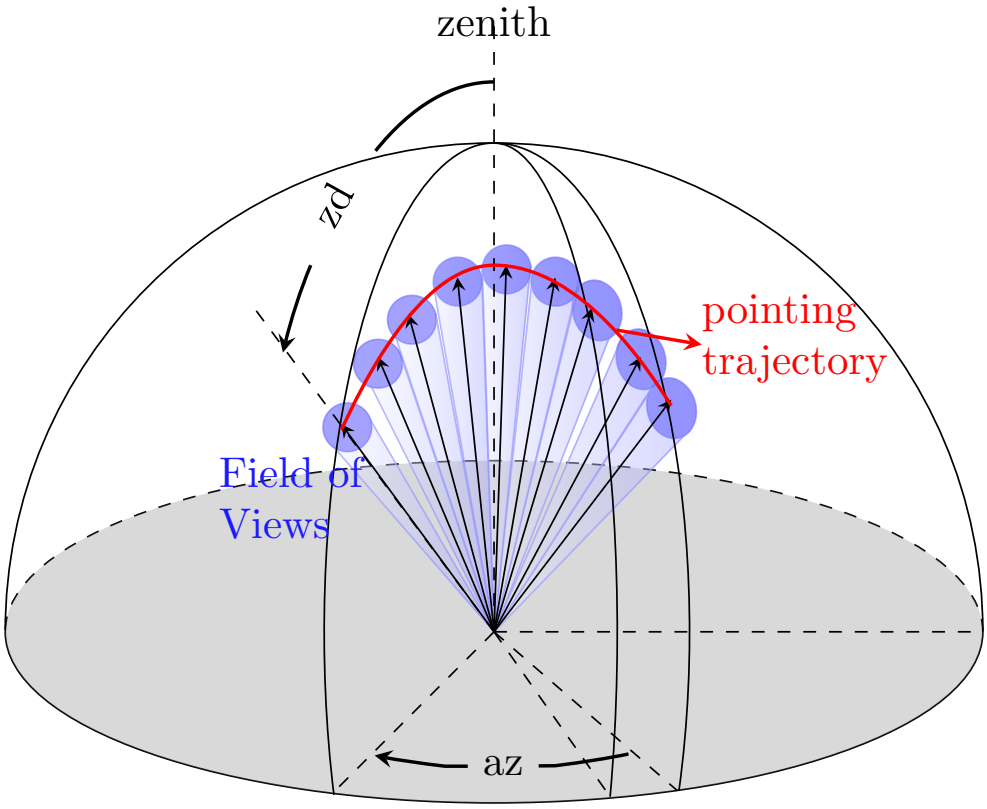

Figure 3.7: The demonstration of the tracking MC Simulation. The red curved line represents the pointing trajectory of the telescopes on the sky. Following the trajectory the FoVs can be calculated.

Important Parameters for the Simulation

As mentioned in Section 2.4.3, various hadronic models are available for EAS simulations, after some investigation and comparison, I found QGSJET-II-04 is commonly used in high-energy astronomy, therefore in this work, the hadrons are simulated by the QGSJET-II-04 model. The simulation involves a large number of protons and helium on $\mathcal{O}(10)$ for accurate background estimation, and the key parameters are listed in Table 3.2. The simulation of EAS is computationally expensive, and increasing statistics is essential, especially for diffuse MC simulation. One way to achieve this is by reusing an event of EAS. The first approach to reuse the EAS event is to alter the location of the telescopes relative to the EAS. This allows for the storage of Cherenkov photon distributions for different telescope locations on the ground, which can be considered as another EAS arriving at a different impact point. In CORSIKA, one event is used ICERML times, and the area the shower core can reach is defined by the MinImpact and MaxImpact, which can be done within the CORSIKA configuration by specifying the keyword CSCAT:

CSCAT ICERML MinImpact MaxImpact

The second approach is to change the pointing orientation of the telescopes, which enables one EAS to be used for different incoming directions with respect to the telescopes' pointing directions. This can be achieved by changing the pointing direction of the telescopes in the program for simulating the performance of the reflector. An event is reused $NPointing$ times. In order to minimize computation time and disk space usage, Cherenkov photons with the number of Cherenkov photons less than the number "Bunch Size" are considered to have the same wavelength and sent along a straight line in a compact bunch at each tracking step. "Bunch Size" is selected by the keyword CERSIZ in the CORSIKA input card.

To accumulate a sufficient number of high-energy events, the proton and helium spectrum indexes used in this work is -1.5 instead of the standard value of -2.6. During the fitting process, a weighted value of $E^{-1.1}$ is applied for each event. The low-energy limit for the hadronic model QGSJET-II-04 is 80 GeV, and the target highest energy for this work was 30 TeV. The energy transferred to the sub-shower from a pion (π^+, π^- or π^0) component is typically on average one-third of the primary particle energy. Usually, only one sub-shower from a hadronic shower can trigger the telescope due to the large opening angle. In order to distinguish between electromagnetic events and hadronic events, RF should be trained using events with protons that have at least three times the energy of the electrons. Therefore, in order to train the RF to differentiate between electrons and protons, simulated hadrons need to have a highest energy that is 3 times higher than that of electrons. The values used in the simulation are optimized based on the cut conditions.

	For train			For test			
Paticle Name	Electron	Positron	Proton	Electron	Positron	Proton	Helium
Particle ID	2	3	14	2	3	14	402
MaxImpact [m]	900	900	900	600	600	600	600
View Cone [deg]	5	5	5	4	4	3&4	3
NPointing	10	10	10	10	10	5&10	5
Spectrum Index	-1.6	-1.6	-1.5	-1.6	-1.6	-1.5	-1.5
Energy Range [GeV]	1e1-6e4	1e1-6e4	8e1-1e5	1e1-3e4	1e1-3e4	8e1-1e4 8e1-1e5	1e1-1e4
ICERML	20	20	20	20	20	20	20
Bunch Size	5	5	5	5	5	5	5
Simulated Events	9.00e8		4.50e8	1.95e9		9.7e9	7.4e9

Table 3.2: Important parameters for the Monte-Carlo simulation.

3.3.3 Event Cut

In addition to the zenith distance cut, several other cuts are applied to remove incorrectly reconstructed events:

- Size $>$ 100 PhE

  The MAGIC standard analysis typically applies a size cut of 50 PhE. Because events with a size smaller than 50 PhE are often very dim and difficult to accurately simulate to match observations. In this study, a more aggressive size cut of 100 PhE is used to ensure a better match between the simulation and observations. Additionally, smaller-sized events are more prone to be muon-induced, which are generated when muon axes are far from the reflector, resulting in only a partial ring or an arc being visible.

- Number of Islands ≤ 1

  Usually, electromagnetic showers result in a single island, while hadron-initiated showers tend to contain two or more islands. Multi-island shower images typically induced by hadrons or local muons.

- Incoming direction to the camera center $<$ 1 deg

  Shower particles that arrive at the inner region of the camera tend to have better preservation of the completed shower images. As a result, the Hillas parameters can be more accurately determined in the inner region of the camera, leading to better electron and hadron separation power.

Based on the discussion above, it is evident that the contributions from local muons play a significant role in the event selection criteria, i.e., these cut conditions are determined to remove the local muon events as much as possible. This is because the muon component is a significant challenge when attempting to fit the hadronness distributions. Firstly, the actual amount of muon production is subject to large uncertainty, as simulations do not produce the same number of muons as observed, because of uncertainty in the head-on collision cross section and other factors. Secondly, muon-induced hadron-like images make it theoretically impossible to accurately trace back the original energy of the shower. Consequently, this can disturb the hadronness distribution as a function of energy, making it difficult to fit the background hadronness distribution to the observed data.

3.3.4 Extended likelihood Fitting Method

Up to this point, the hadronness distribution of the signal (simulated electron and positron) as well as the background (simulated proton and helium) have been plotted against the observed data. A template fit is then employed to determine the normalization factors of both the signal and background distributions, ensuring that their combined distribution aligns with that of the observed data.

Hadronness Distribution of Different Elements

The primary cosmic rays consist mainly of protons and helium contributing to almost 90% of the total. Figure 3.8 displays the ratio of H/He versus energy per nucleus. The yellow shaded region in the plot corresponds to the energy range of interest for this study, which spans from 300 GeV to 6 TeV. Within this range, the ratio of protons to helium is approximately 1.3 to 1.

To understand how they contribute to the background, it is necessary to investigate their respective hadronness distributions. Figure 3.9 shows one example of the hadronness distribution of protons and helium for the estimated energy range from 598.6 GeV and 753.6 GeV, with the simulated number of events for each element being the same and with the same energy index of -1.5. The hadronness distributions are re-weighted event-wise with the factor $E_{true}^{-1.1}$ for both proton and helium. The hadronness distribution of protons and helium are distinct from each other: helium has more hadronic-like events and contributes much fewer events in the low hadronness region. Due to the lower surviving rate of helium and its more distinguishable hadronic features, the low hadronness region is dominated by protons. But the the contribution from helium is not negligible. A rough estimate suggests that the number of excess events of electrons and positrons is underestimated by approximately 5% at TeV energies and up to 10% at lower energy ranges in the order of a few hundred GeV. The hadronness distribution of protons and helium in the different energy ranges are shown in Figure B.1.

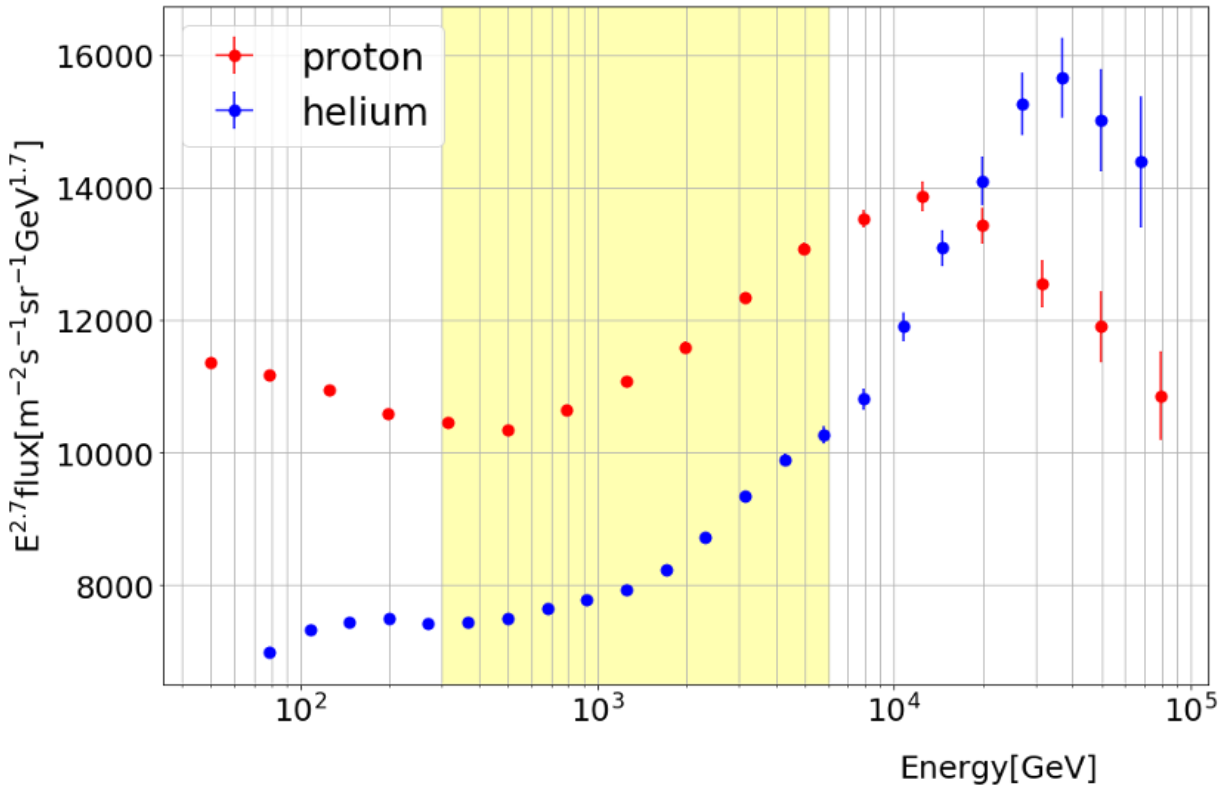

Figure 3.8: The ratio of H/He as a function of energy per nucleus. The fluxes of proton (An et al., 2019) and helium (Alemanno and et al., 2021) are from DAMPE collaboration The energy range of interest for this study, ranging from 300 GeV to 6 TeV, is highlighted in yellow shading.

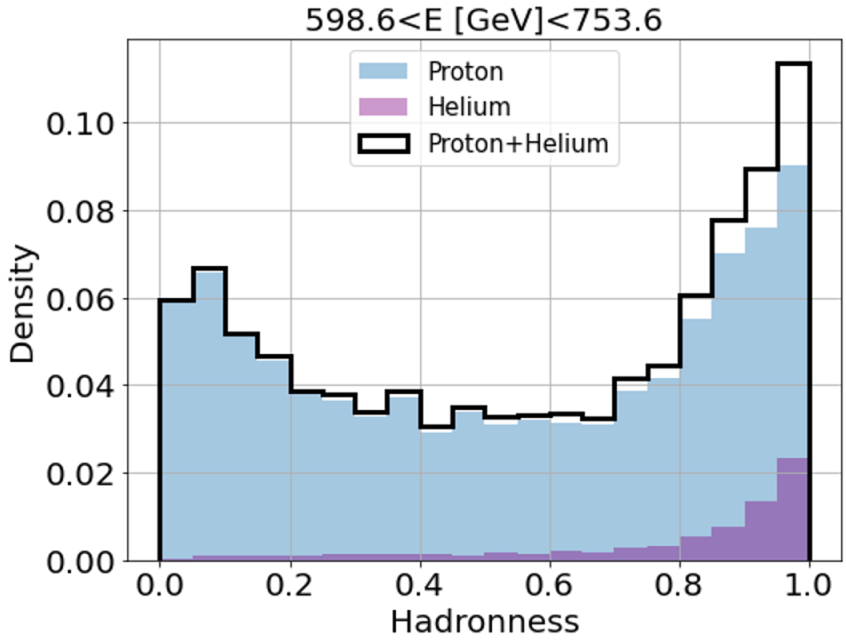

Figure 3.9: The hadronness distribution of protons, helium, and their sum in the estimated energy between 598.6 GeV to 753.6 GeV, after applying all event cuts and considering the same number of events for both components.

Extended Maximum likelihood fitting of hadronness

The extended maximum likelihood (EML) method is frequently used in high energy physics to find the normalization parameters of the physics process. During a specific time period, the number of observation data events in each hadronness bin can fluctuate around the hadronness distribution of the simulation, following a Poisson distribution. To account for this effect, a Poisson term can be included in the likelihood function as a multiplicative factor, leading to the extended likelihood (Olaf Behnke, 2013; Barlow, 1990):

$$L(x;\nu,\theta) = e^{-\nu}\frac{\nu^N}{N!}\prod_{i=1}^{N} f(x_i;\theta) \tag{3.2}$$

where ν is the number of events of observation data, x the number of events of the simulation, θ the scaling factor, and N the number of hadronness bins. For this study, the scaling factors for simulated electrons and protons in the low hadronness range of 0 to 0.4 were calculated. The log-likelihood function can be expressed as:

$$\ln L\left(x;\nu,\theta\right) = \sum_{i=1}^{N} \ln f\left(x_i;\theta\right) + N\ln\nu - \nu + constant \tag{3.3}$$

As previously mentioned, the hadronness distributions for both proton and helium are re-weighted on an event-by-event basis using the factor $E_{true}^{-1.1}$, leading to a background

distribution with an energy spectrum index of -2.6. Similarly, the hadronness distributions for electron and positron are re-weighted on an event-by-event basis using the factor $E_{true}^{-1.6}$, resulting in a signal distribution with an energy spectrum index of -3.2, which is known a *priori*. The hadron template consists of MC proton and MC helium in all energy ranges, with a ratio of 1.3:1. The hadron and signal templates, which are simulated specifically for the corresponding FoVs, are also weighted according to the observation time of those pointings. One example of the template fit in the energy range between 598.6 GeV and 753.6 GeV is shown in Figure 3.10 with reduced $\chi^2 = 24/18$. The template fits for each energy range are shown in Figure C.1. The reduced χ^2 is defined as:

$$\chi^2 = \sum_i \frac{(O_i - S_i)^2}{\sigma_i^2} \tag{3.4}$$

where σ_i^2 is the variance of all parameters, and O_i is the number of observation data, and S_i the number of events of the templates in the ith hadronness bin. The degree of freedom is N-m=18, with N=20 the number of fitted bins and m=2 the number of scaling factors. The reduced χ^2 of the template fits are listed in the table 3.3. It can be observed that the MC hadron templates provide a good description of the data across most energy ranges.

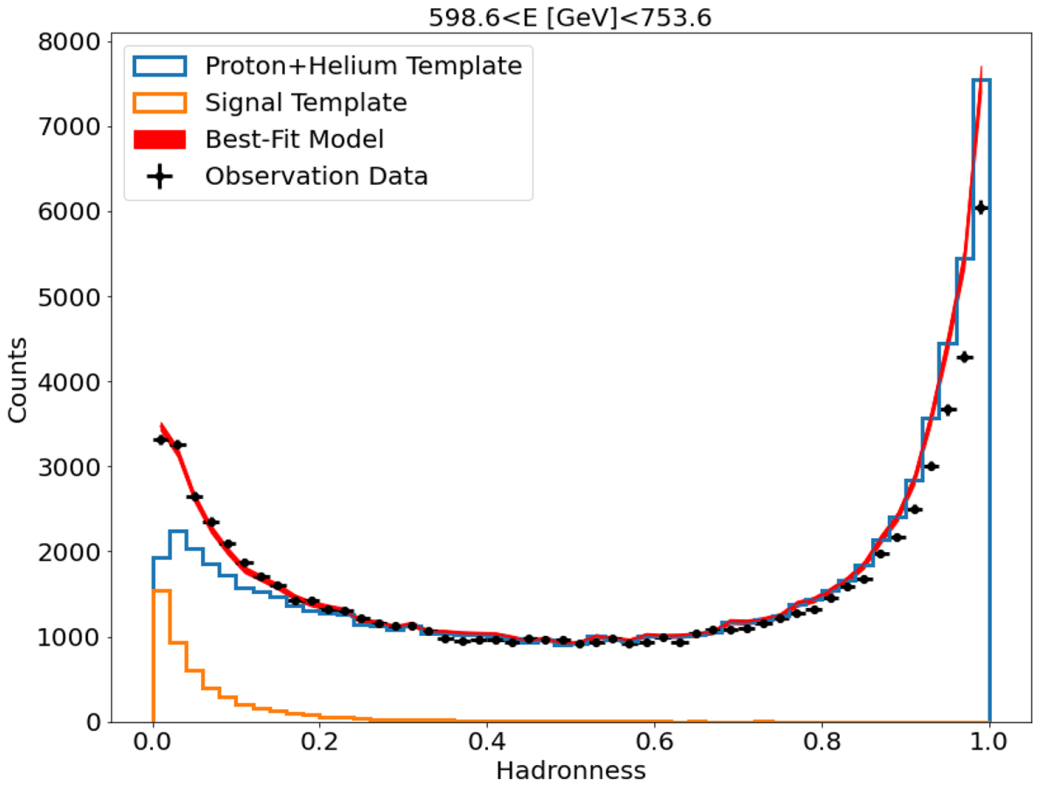

Figure 3.10: An example of a template fit for the estimated energy range between 598.6 GeV and 753.6 GeV. The hadronness distributions of proton+helium and signal are depicted by blue and orange histograms, respectively. The best fit model is indicated by the red band.

To enhance the signal-to-noise ratio, the positions of the hadronness cuts were determined based on the $N_s/\sigma(N_s)$ value. Since hadronness varies with energy, the positions of the cuts also vary with energy. Figure 3.11 displays the significance for different hadronness cuts across different energy ranges. The hadronness values that correspond to the highest significance were then used to set the cut values. The resulting cut values are presented in Table 3.3.

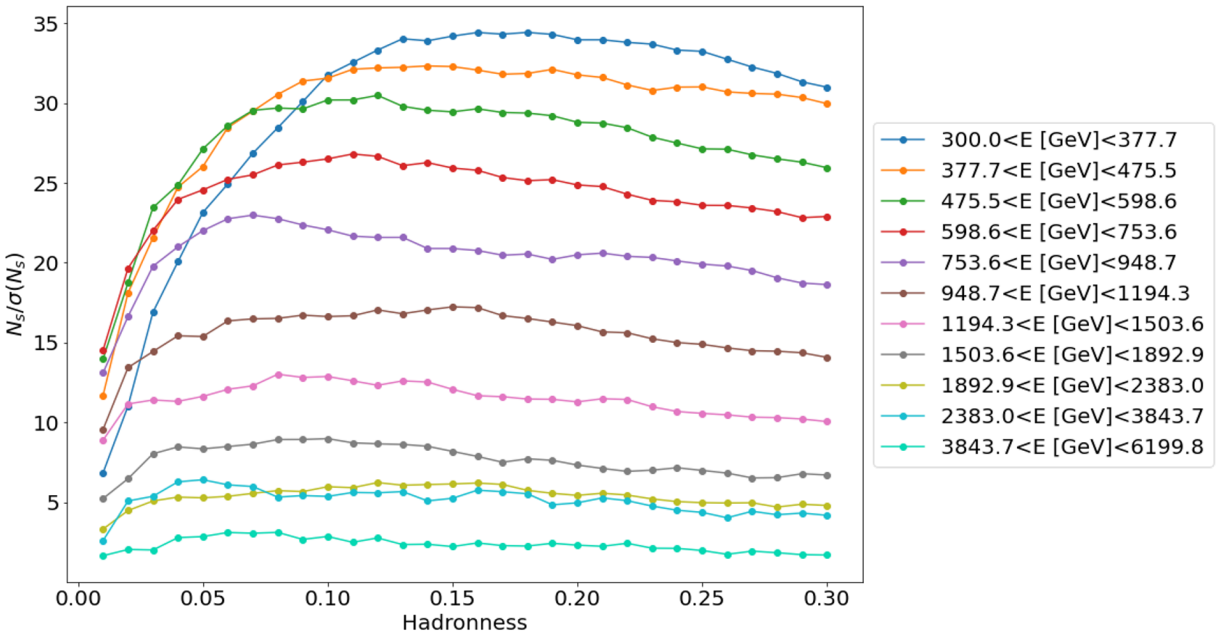

Figure 3.11: The significance for different hadronness cuts at each estimated energy bin.

3.3.5 Crab Test

In order to validate this method, the Crab spectrum was obtained using the same approach. Instead of estimating the background using an "Off" region as in the standard analysis, simulated protons located at the same distance from the camera center as the Crab were used as shown in the Figure 3.12. The resulting best-fit hadronness distribution is displayed in Figure C.2. In this test, a total of 34 hours of Crab data, comprising 20 hours from Period ST0307 and 14 hours from Period ST0306 are used. Both the "On" region and the selected proton regions have a radius of 0.2 deg. The Crab spectrum is shown in the Figure 3.13. The data points of "On-Off" is obtained using the standard MAGIC analysis chain on the same dataset as "On-Proton". The fluxes calculated from "On-Proton" is slightly higher than "On-Off" region. This is because the number of excess calculated from "On-Proton" includes electrons and positrons from the On region defined in the Figure 3.12. The Crab spectrum is reconstructed using proton MC simulations as the off-data, and it agrees well with the standard Crab spectrum previously measured by MAGIC, with the reconstructed values falling within the expected uncertainties.

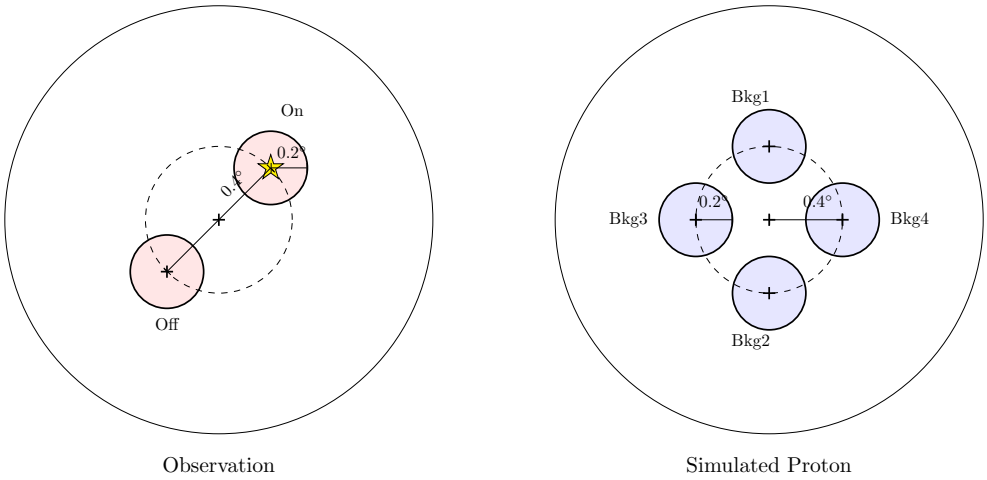

Figure 3.12: The sketch in the left-hand side shows the wobble observation for Crab. "On" is the direction of the source and "Off" is the simultaneous off direction in the camera. In the Crab test, to increase the statistics, four background regions are chosen at the same distance from the camera center. Each background region is a disk with radius 0.2° the same as the "On" region. This "On" region with radius 0.2° includes the signal from Crab and cosmic-ray electrons from the background.

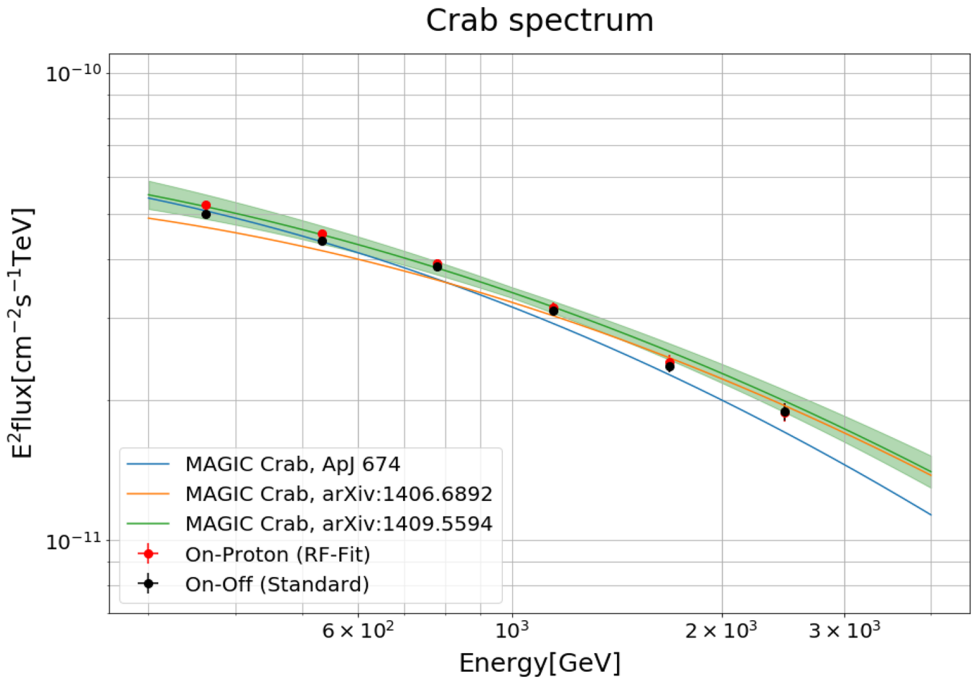

Figure 3.13: The crab spectrum with **RF-Fit** method. The red points are calculated from the number of excess events from the Crab on region minus simulated proton. The excess events of black points are from Crab On region minus Off region. Only statistical errors are included for the data points.

3.4 Two-Step RF Method

The **Two-Step RF** method is a novel method that uses the RF twice for the particle identification. The initial idea behind this method is to apply an extremely stringent hadronness cut and assume that only a minimal number of background events can pass through this cut. The contamination from the hadrons can be estimated. The analysis chain of **Two-Step RF** is illustrated in the flow chart in Figure 3.14.

3.4.1 Limitation of First Step RF

The **Two-Step RF** method is also based on RF. The initial idea behind this method is to apply a very strict hadronness cut and assume that the events that survive this cut are primarily composed of electrons and positrons with only a small number of protons present. The template fit of the hadronness distributions of signals and background after the first RF has already been shown in Figure 3.10. It is obvious that even for the first bin (width 0.02) around hadronness zero, the contribution from protons exceeds 50%.

This suggests that relying only on the estimator from the first RF has its limitations for

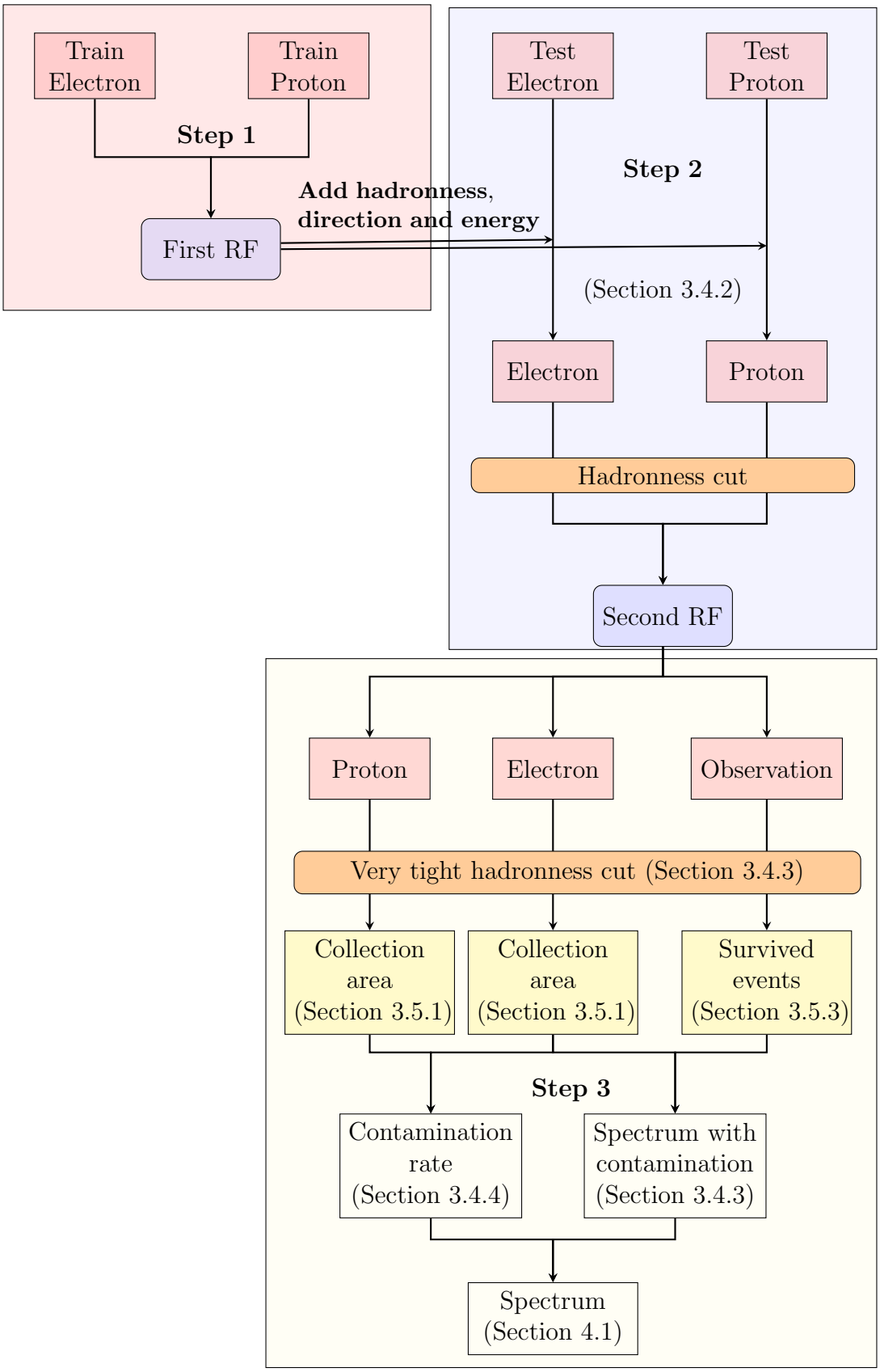

Figure 3.14: The flow chart of **Two-Step RF** method analysis process.

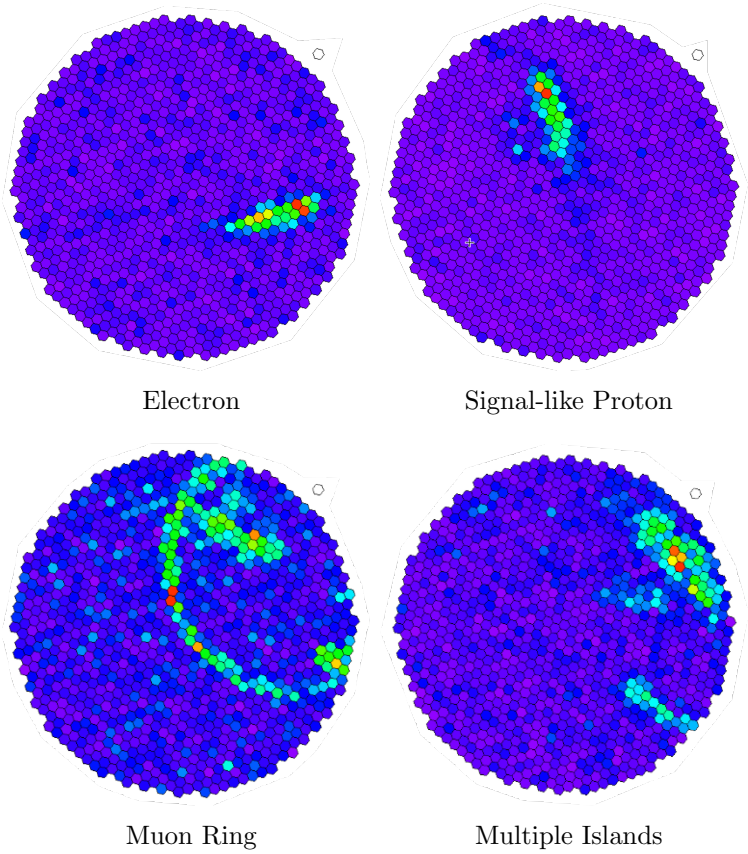

Figure 3.15: Some examples of electron and proton shower images on the camera. Local muons can be identified by their ring shape. Similarly, protons with more than one island are easily distinguishable from electrons. However, for protons with Hillas parameters similar to those of typical electrons, the first RF method cannot differentiate between the two particle types.

the tight cut method. The process of generating the estimator of the first RF is explained in section 2.4.5. The hadronness of an event depends on the hadronness of the nodes that the event ends up in. In MAGIC, the number of training events for gamma and hadron are automatically equalized in the zenith distance and size dimensions. The large fraction of hadron samples has very different characteristics compared to electromagnetic shower samples, as shown in the Figure 2.13, protons with a Width less than 20 mm and $MaxHeight$ less than 500 m can be separated from electron events easily because they have very unique characteristics like the examples of shower image with Muon Ring or multiple islands as seen in in Figure 3.15. For a small proportion of protons with a $Width$ around 30 mm and $MaxHeight$ around 800 m, they can still mix with electrons until the nodes of last Depth, like the one with shower image named "Signal-like Proton" in Figure 3.15. As the Decision Tree grows deeper, the proportion of proton events significantly reduces, which leads to a lack of training samples from the hadron side for the RF.

3.4.2 Second Step RF

The second RF uses training samples consisting only of particles with hadronness values less than 0.3, which excludes some of the electrons and a large fraction of protons and almost all helium. More specifically, after applying the hadronness cut from the estimation of the first step RF, the same amount of signal-like hadron events and signal events are used as training samples in the second RF. The second RF can thoroughly and delicately learn the subtle differences between these two groups from the beginning until the last Depth throughout the decision tree. This level of precision cannot be achieved simply by increasing the number of decision tree depths, as the proportion of signal-like hadron events is too small to compare their characteristics with those of the electrons.

The comparison of the variables' importance in classifying electrons and protons between the first and second RF is shown in Figure 3.16. This validates the necessity for using the Two-Step RF approach. In the initial RF, the two variables with the highest importance index measured by Gini decrease (see the detail in Section 2.4.5) are Width of M1 and M2, which are almost double that of Maxheight in third place, and 3 to 5 times higher than the other variables. In the second RF, there are no dominant parameters for the classification but rather several parameters that contribute equally.

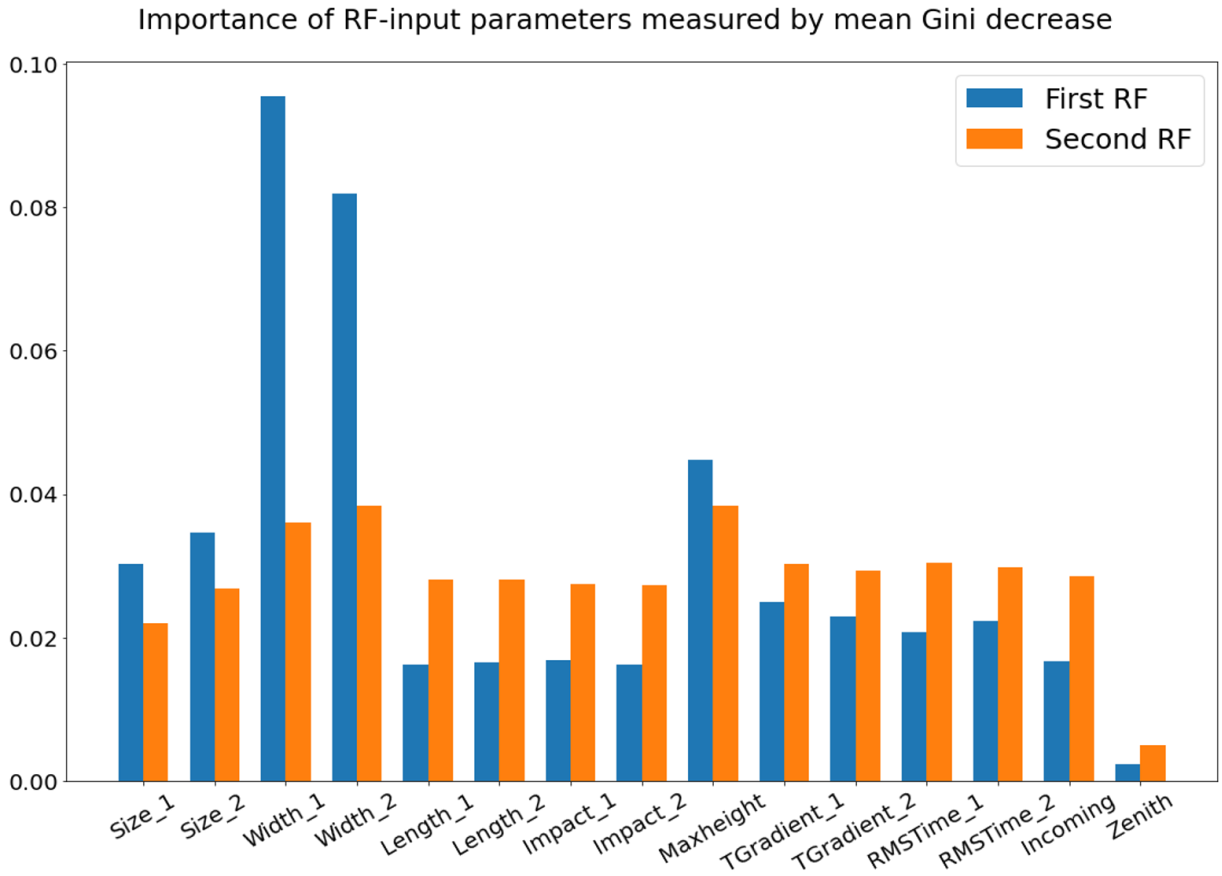

Figure 3.16: The importance of RF-input parameters can be compared by the mean Gini decrease between the First RF and Second RF. The suffix "_1" corresponds to M1 and the suffix "_2" corresponds to M2. The official names of the parameters are listed in Appendix A.1. The distribution of the parameters are shown in Figure A.2. In the first RF, Width_1 and Width_2 are the most important parameters for classifying electrons and protons. However, to differentiate between electrons and protons that survived the first RF, the importance of Width_1 and Width_2 is significantly reduced, and all the other parameters contribute almost equally to the second RF.

The hadronness distribution of protons, calculated by the First Step RF and the Second Step RF, from 0 to 0.5 is shown in Figure 3.17. For hadronness estimated by the First RF, the number of proton events gradually increases from 0 to 0.1 and remains flat from 0.1 to 0.5. In contrast, for hadronness estimated by the Second RF, the number of proton events is significantly reduced in the low hadronness region. The number of events then gradually increases in the very low hadronness region and rapidly rises from 0.4 to 0.5, reaching a point where the number of events becomes comparable at a hadronness value of approximately 0.47.

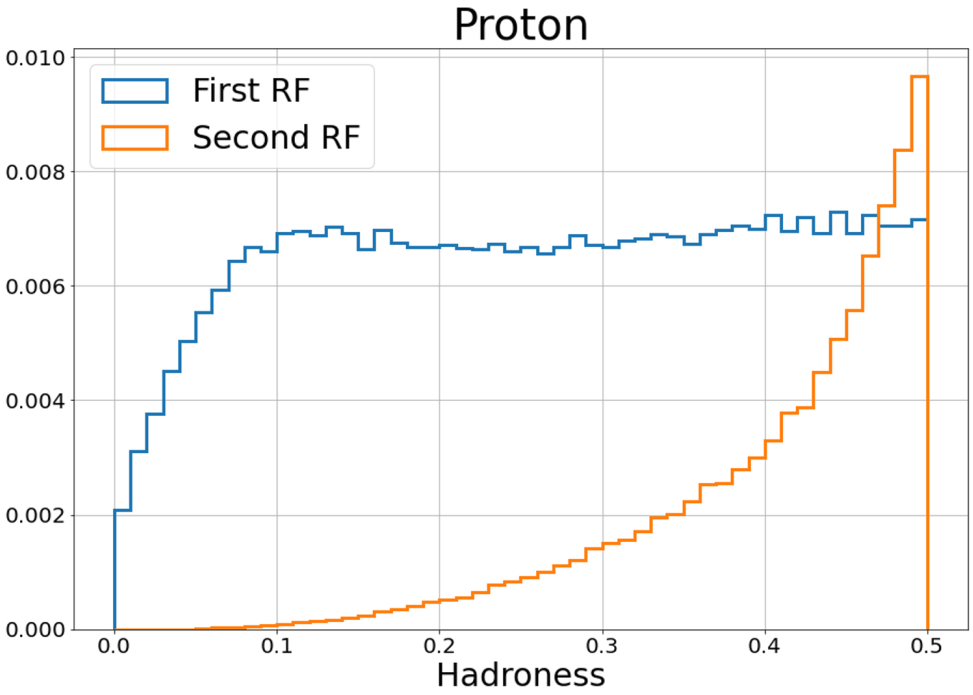

Figure 3.17: Comparison of the hadronness distribution of protons calculated by the First Step RF and the Second Step RF. The number of proton events in the low hadronness region is significantly reduced, which makes it possible to get the signal events as pure as possible by applying a very tight hadronness cut.

3.4.3 Hadronness Efficiency Cuts

To obtain as pure all-electron events as possible, very strict hadronness efficiency cuts are applied. However, since the hadronness distribution varies with the energy range, the positions of the hadronness efficiency cuts depend on the energy. The cuts are determined based on the flux in terms of electron survival efficiencies, as illustrated in Figure 3.18. Theoretically, as the hadronness efficiency increases, the flux also gradually rises because of the increase in contamination. Some fluctuations are observed at very low hadronness efficiency levels, but it eventually reaches a stable stage. The fluctuations in the first several bins can be caused by either the lack of statistics or the discrepancy between the MC and observation data due to the too low efficiency cut, and/or both factors could be contributing to the observed fluctuations. The best-cut position, represented by the red dot, is determined by selecting the point with the lowest contamination after considering the observed fluctuations. The blue dots in Figure D.1 illustrate the variation of the flux $\times E^3$ with different efficiencies and best-cut positions in various energy ranges. The values of best efficiency cuts for each energy range are listed in Table 3.3.

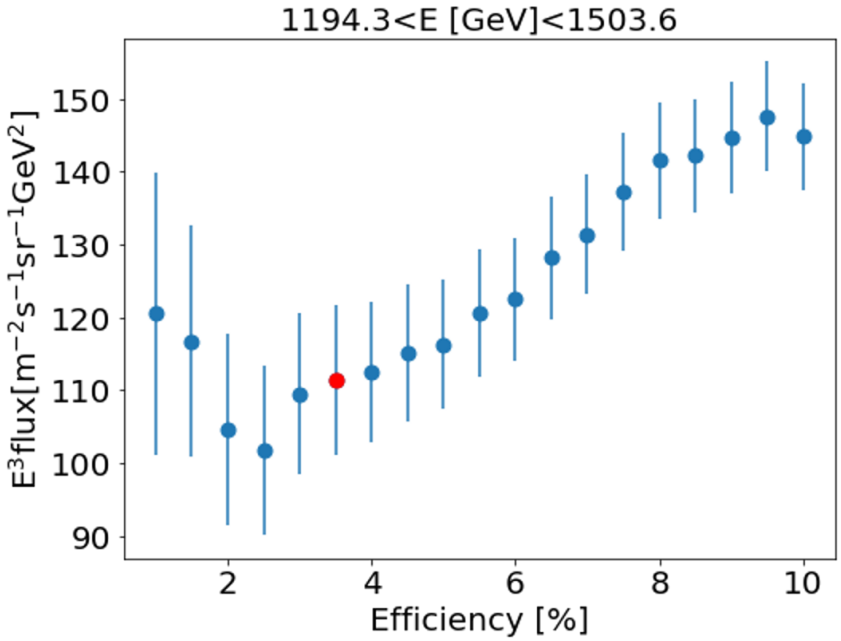

Figure 3.18: The flux distribution varies with changes in the electron efficiency for energy rangy from 1194.3 GeV to 1503.6 GeV. The best-cut efficiency is indicated in red.

3.4.4 Expected Contamination Rate

In the **Two-Step RF** method, it is crucial to determine the expected contamination rate with simulated protons and helium. The contamination from helium based on the best efficiency cuts at the target energy range is negligible, therefore only the contamination rate from protons is calculated in this section.

First the ratio of the collection area of electrons and protons is calculated based on the estimated energy using the energy estimator of electrons, as shown in Figure 3.19. A detailed explanation of the effective collection area is given in the Section 3.5.1. It is important to note that the collection area ratio considers events in all hadronness ranges, and the ratio is significantly increased after applying a proper hadronness cut. At energies of a few hundred GeV, the effective area for electrons is around one hundred times larger than that for protons. However, this ratio gradually decreases as the energy increases and becomes only a few tens of times larger at around 10 TeV. The spectral index of proton is assumed to be -2.6 as shown in Equation 3.5. The spectral index of all-electron electron spectrum is assumed to be -3.1 for energy less than 1 TeV and -3.6 for electron higher than 1 TeV as described in the Equation 3.6. The flux ratio of protons and electrons is around 530 at energy 400 GeV, where the fluxes of proton and electron at 400 GeV are from AMS collaboration taken from Zhao et al. (2021) and Aguilar and et al. (2014), respectively.

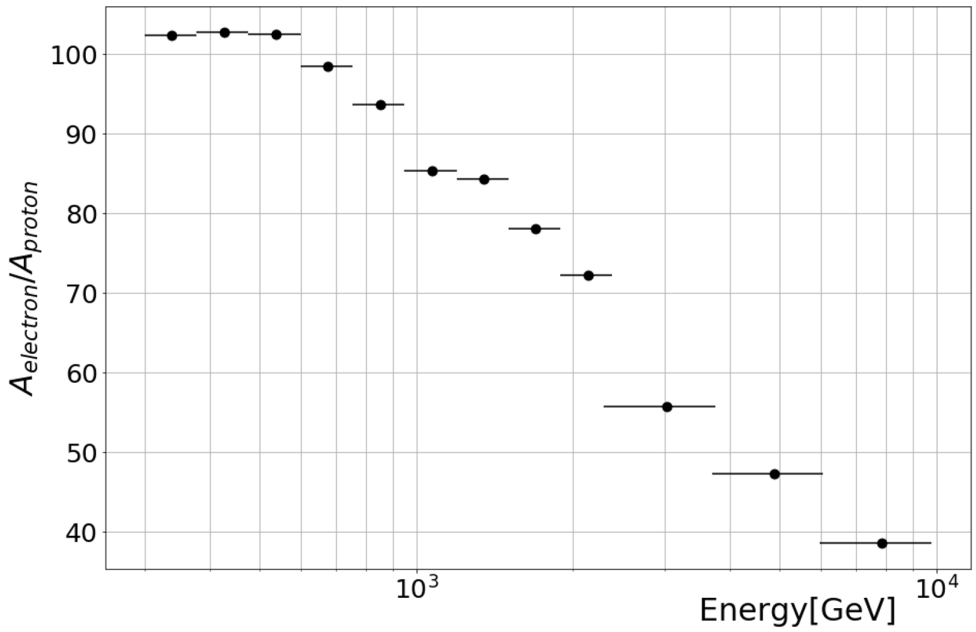

Figure 3.19: The electron-to-proton ratio of effective areas before applying any hadronness cut.

$$F_{proton}(E) = AE^{-2.6} \tag{3.5}$$

$$F_{electron} = \begin{cases} BE^{-3.1} : E < 1TeV \\ BE^{-3.6} : E > 1TeV \end{cases} \tag{3.6}$$

According to Equation 3.6 and Equation 3.5, and considering
$F_{proton}(400GeV)/F_{electron}(400GeV) = 530$, the energy dependent flux weighting factor is:

$$\frac{F_{proton}(E)}{F_{electron}(E)} = \begin{cases} 26.4E^{0.5} : E < 1TeV \\ 0.67E : E > 1TeV \end{cases} \tag{3.7}$$

The estimation of the contamination rate is calculated by:

$$contamination\ rate = \frac{F_{proton}(E)/F_{electron}(E)}{A_{electron}(E)/A_{proton}(E)} \cdot \frac{P_{proton}(E)}{P_{electron}(E) + P_{proton}(E)} \tag{3.8}$$

Where P_{proton} and $P_{electron}$ are the fraction of protons and electrons survived the efficiency cuts. The expected contamination rates for the best cut positions in each energy rage are listed in Table 3.3. The left panel of Figure 3.20 shows an example of the contamination rates at different electron efficiency cuts for energy from 1194.3 GeV to 1503.6 GeV. After subtracting the expected proton contamination from the surviving number of events, the fluxes at different efficiencies remain relatively stable as represented by the orange dots in the right panel of Figure 3.20. The fluxes without contamination vs. efficiencies in

different energy ranges are depicted by the orange dots in Figure D.1. The However, there is still a systematic difference between the best-cut position and the efficiency cut of 10%. This difference is considered when assessing the overall systematic uncertainty of the final spectrum, which is shown in detail in Section 4.2.2. The contamination rates in each energy range for different efficiency cuts are shown in the Figure E.1.

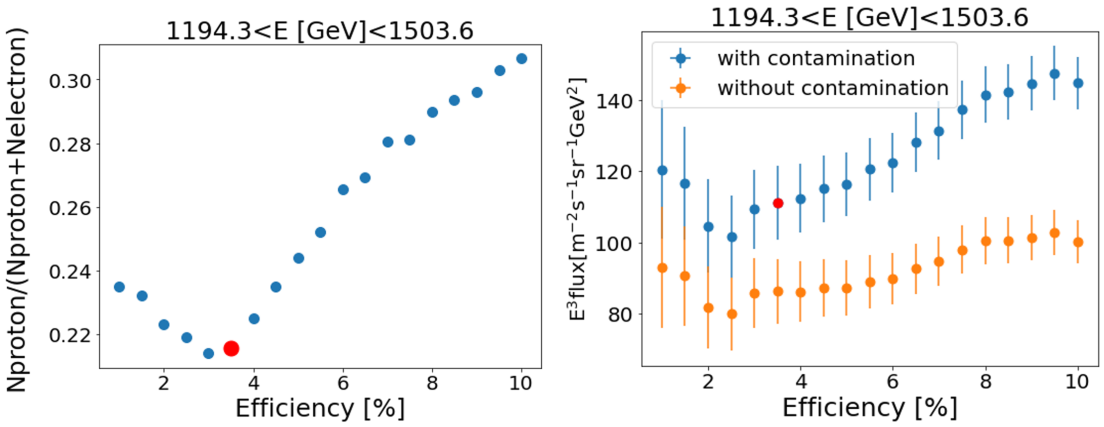

Figure 3.20: The left panel shows the contamination rates vary with changes in the electron hadronness efficiency for energy range from 1194.3 GeV to 1503.6 GeV. The right panel shows the flux$\times E^3$ after the subtraction of contamination.

3.4.5 Crab Test

The validation using the Crab spectrum is essential for the **Two-Step RF** method. When applying very strong cuts, the MC/data discrepancy may become apparent, leading to inconsistency in the reconstructed Crab spectrum. The Crab test for the **Two-Step RF** method was conducted using the same data as the **RF-Fit** method, from periods ST0306 and ST0307, at zenith distance angles ranging from 5 to 35 degrees, with an effective observation time of 34 hours. After applying very tight cuts, the number of surviving events in the "Off" region is negligible, as shown in Figure 3.21, and the surviving events in the "Off" region are likely to be electrons from "Onregion. The Crab spectrum, shown in Figure 3.22, was successfully reconstructed even with low statistics and efficiency. This suggests that the MC and real data remain consistent even with very low efficiency cuts.

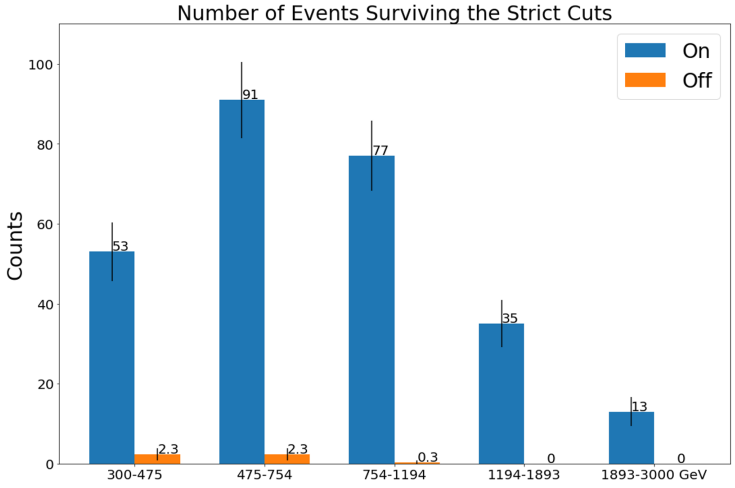

Figure 3.21: Surviving number of events after the tight cut conditions for "On" and "Off" regions for the estimated energy ranges.

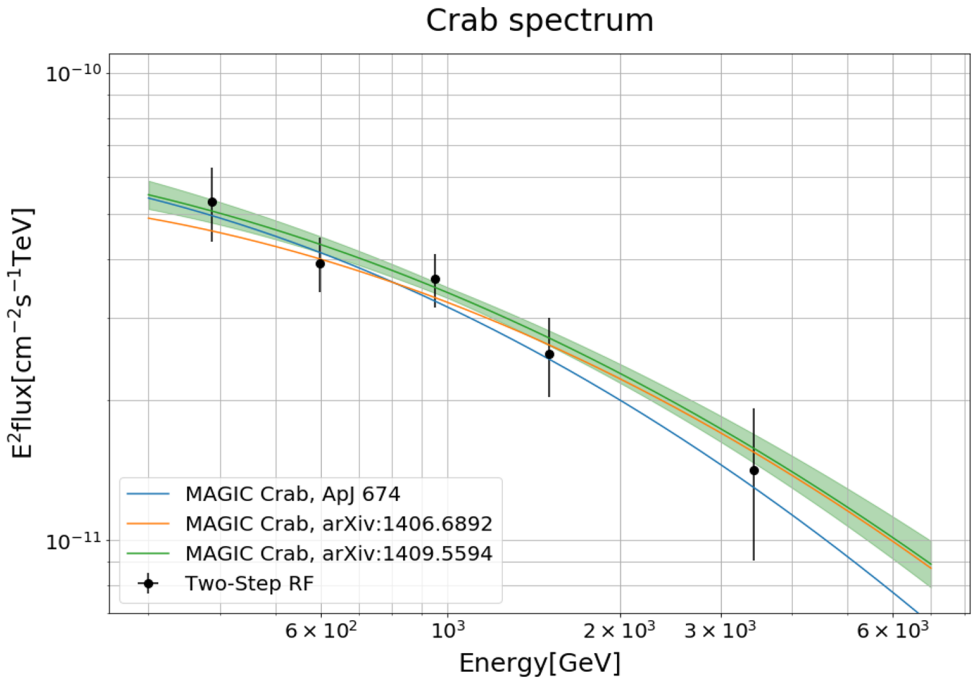

Figure 3.22: Crab test for **Two-Step RF** method. The black dots are reconstructed using the surviving number of events from "On" region obtained by the **Two-Step RF**. The lines are the previous published MAGIC Crab spectra, which are obtained by the standard MAGIC analysis.

3.5 Flux Determination

The differential energy spectrum of cosmic-ray electrons and positions is defined as the number of electrons and positrons per energy bin, per unit area, per unit time, per solid angle, which can be calculated as:

$$\Phi[E] = \frac{dF}{dE} = \frac{dN(E)}{dE \cdot dt_{eff} \cdot d\tau(E)} \tag{3.9}$$

where $N(E)$ is the number excess events, $d\tau(E) = dA \cdot d\Omega$ the acceptance of the telescopes with the collection area dA and solid angle $d\Omega$, and t_{eff} is the effective time.

3.5.1 Acceptance of the Telescopes

The acceptance of the MAGIC telescopes is determined by the total collection area of cosmic-ray showers, the FoV of the telescopes, and the surviving efficiency through the trigger and analysis. The size of the reflector is not the effective collection area of the telescopes, because this is indeed determined by the size of the Cherenkov light pool and the distance between where the shower reaches the ground and the location of the telescopes. Additionally, for diffuse analysis, the shower's incoming direction to the camera center is also a factor as the camera acceptance decreases from the center to the outer layer. The acceptance is given in Equation 3.10:

$$\tau(x, y, c_x, c_y) = \int\int\int\int \varepsilon(x, y, c_x, c_y) dx dy dc_x dc_y \tag{3.10}$$

where distance between the shower core on the ground and the telescopes is represented by the coordinates (x,y), while (c_x, c_y) represent the incoming direction coordinates on the camera plane. The size of the Cherenkov light pool is dependent on the energy of the cosmic-ray shower, making ε also energy dependent. Moreover, the zenith angle of the shower determines the travel distance, causing the density of the photons to decrease as the zenith angle distance increases. Thus, ε is also dependent on the zenith angle. To calculate $\tau(x, y, c_x, c_y)$, it is necessary to determine it in different energy ranges and then weight it according to the zenith distribution.

Diffuse MC electrons and positrons are simulated uniformly within the MaxImpact and largest viewing angle to estimate $\tau(x, y, c_x, c_y, E)$. The maximum impact I_{max} and viewing angle θ_{max} must be determined carefully so that the residual tail of $\varepsilon(x, y, c_x, c_y)$ beyond it is negligible. Here, $\varepsilon(x, y, c_x, c_y)$ refers to the ratio of the number of events that survived to the total number of simulated electrons and positrons, and the acceptance can be obtained from the Equation 3.11.

$$\tau(x, y, c_x, c_y) = \frac{N_{sur}}{N_{tot}} \cdot \pi \cdot I_{max}^2 \cdot \pi \cdot \theta_{max}^2 \tag{3.11}$$

The acceptance of the two methods is compared in Figure 3.23. The affective area is very flat across the entire energy range which is ideal, this makes determining any breaks or spectral features a lot easier. However, the two methods differ in their absolute values. This difference is crucial for future systematic studies, as the two methods are distinct and can lead to different results.

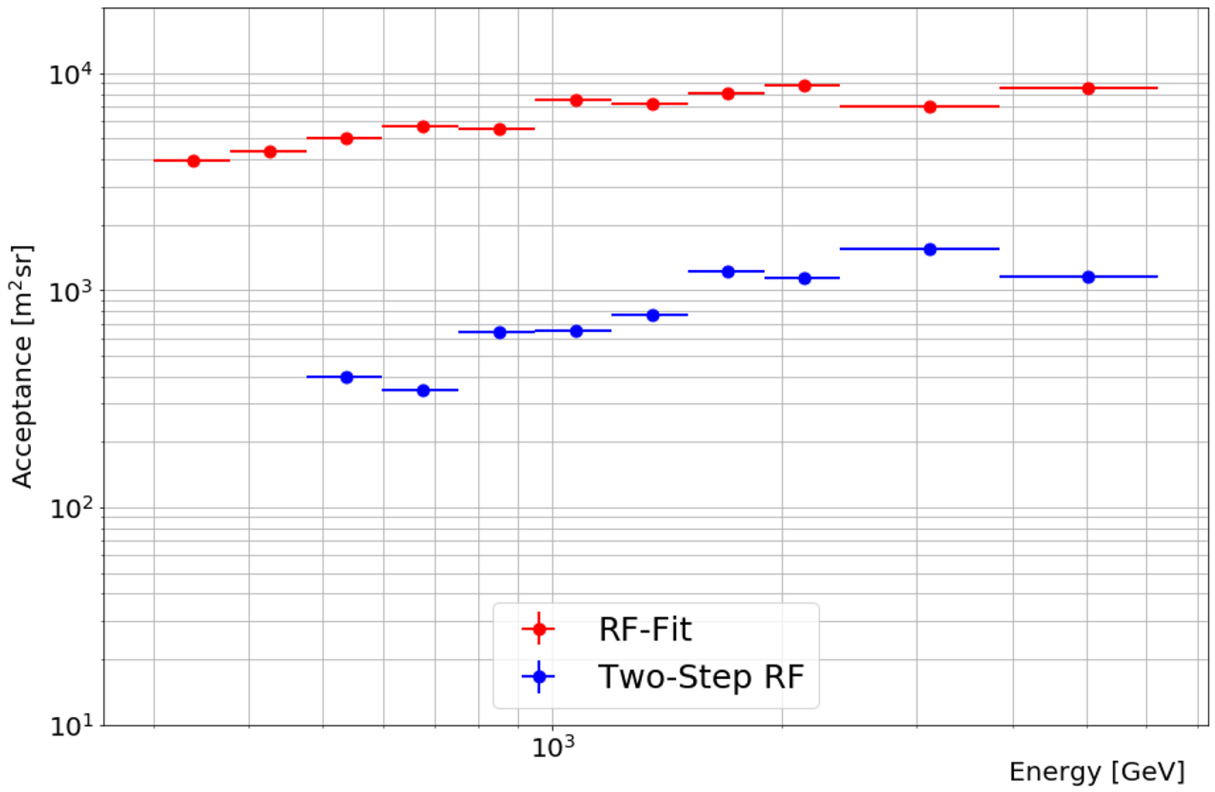

Figure 3.23: Acceptance comparison between the two methods.

3.5.2 Effective Time

Effective time refers to the effective observation time of a source, which is not the same as the elapsed time through the observation. This is because the time loss, known as dead time, between the trigger and data readout, needs to be taken into account. The formula used to calculate t_{eff} is $t_{eff} = t_{elapsed}/(1+\lambda \cdot t_d)$. Here, λ represents the trigger rate, which can be obtained by fitting an exponential distribution to the arriving time differences of the events, and t_d is the dead time per event, which is approximately 26 μs for DRS4 waveform digitizer chip. The dead time causes a time loss of approximately 0.6% to 0.9% for the standard stereo trigger rate, which is 1-2 Hz out of around 250 Hz to 350 Hz.

3.5.3 Number of Excess Events

The number of cosmic-ray electrons and positrons extracted using both the **RF-Fit** and **Two-Step RF** methods are displayed in Table 3.3. For the **RF-Fit** method, after applying the optimized hadronness cut, the number of excess events is obtained by subtracting the product of the number of MC hadrons and the normalization factor, as shown in Equation 3.12. The hadronness cut values and the reduced χ^2 of the template fits are also listed in the table.

$$N_{excess} = N_{obs} - Norm \cdot N_{MC_{hadron}} \tag{3.12}$$

For the **Two-Step RF** method, the number of survived events is obtained by applying hadronness efficiency cuts. The cut efficiencies, corresponding hadronness values, and the contamination rates from protons are also included in the Table 3.3. It's important to note that the survived events are not necessarily pure electrons and positrons,therefore are not labeled as "excess" in the table. The "excess" should be calculated by the survived number of events subtracted the contribution from protons.

	RF-Fit			Two-Step RF		
Energy [GeV]	Number of excess	Hadronness	Reduced χ^2	Number of excess	Efficiency cut	Contamination Rate
300.0-377.7	8597	0.18	78/18			
377.7-475.5	6140	0.14	30/18			
475.5-598.6	5720	0.12	44/18	699	3.5%	27.68%
598.6-753.6	4018	0.11	24/18	530	5%	27.51%
753.6-948.7	2354	0.07	37/18	512	6%	24.05%
948.7-1194.3	1927	0.15	27/18	205	3.5%	17.93%
1194.3-1503.6	937	0.08	34/18	121	3.5%	21.73%
1503.6-1892.9	555	0.1	23/18	106	5%	22.09%
1892.9-2383.0	324	0.12	17/18	60	4%	23.27%
2383.0-3843.7	248	0.05	28/18	65	4.5%	30.69%
3843.7-6199.8	85	0.08	9/18	19	2.5%	44.89%

Table 3.3: Number of all-electron events extracted from the selected FoVs in each energy bin by **RF-Fit** method and **Two-Step RF** method. The hadronness cut values and reduced χ^2 of the best-fit for the **RF-Fit** method, as well as the hadronness efficiency cut values and expected contamination rates from protons for the **Two-Step RF** method are also provided.

3.5.4 Energy and Direction Reconstruction Performance

The energy and direction reconstruction performance is estimated with MC electrons. The most intuitive plot to see the performance of the energy estimation is energy migration matrices (the correlation between estimated energy and true energy) see Figure 3.24. For both methods, there are no significant outliers in the migration matrices. To quantify the

energy reconstructed performance, energy bias is defined by Equation 3.13. In each true energy bin, the distribution of *bias* is fitted with a Gaussian distribution, where the peak position is the bias in the particular energy bin. The 1 σ interval is the energy resolution. The comparison of bias and resolution between the two methods is shown in Figure 3.25. **Two-Step RF** method has a higher energy threshold due to the very tight cuts. The different performances of the two methods are from different cut conditions since the two methods use the same RF for energy estimation. The angular reconstruction is determined by calculating the 1σ interval of the θ distribution, which represents the range within which 68% of the MC electrons are contained. This is illustrated in Figure 3.26.

$$bias = \frac{E_{est} - E_{true}}{E_{true}} \tag{3.13}$$

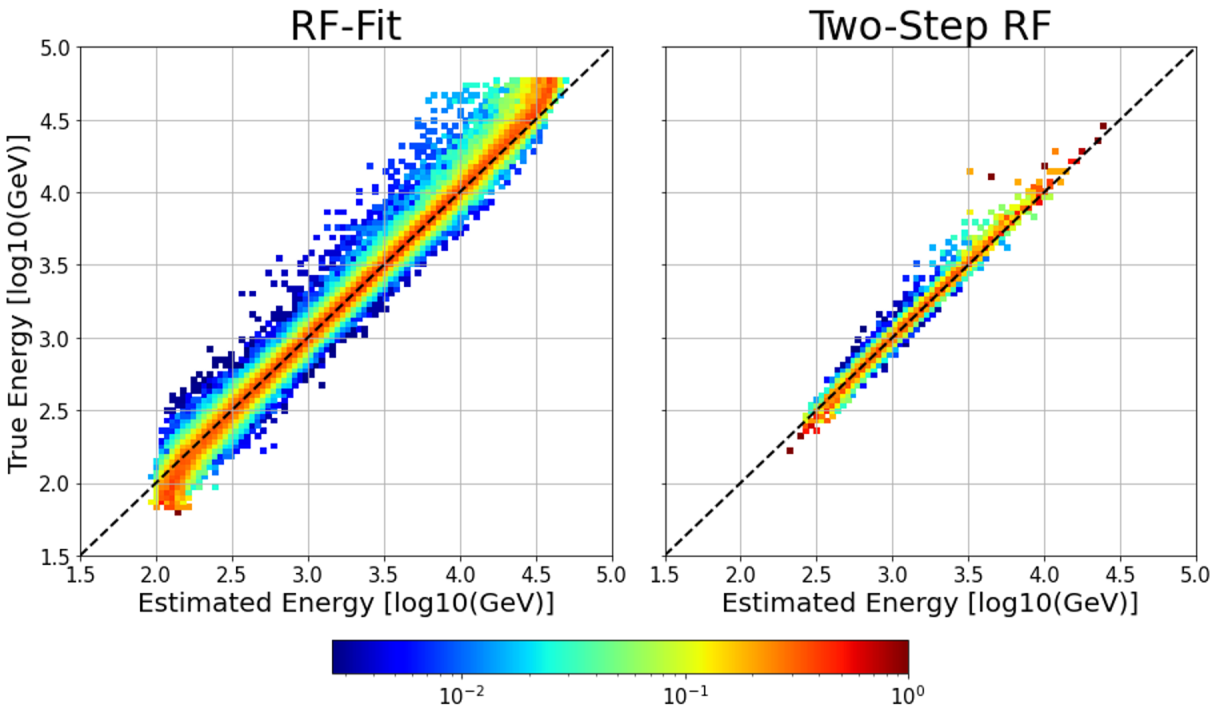

Figure 3.24: Migration Matrices of **RF-Fit** method and **Two-Step RF** method after applying the corresponding cuts.

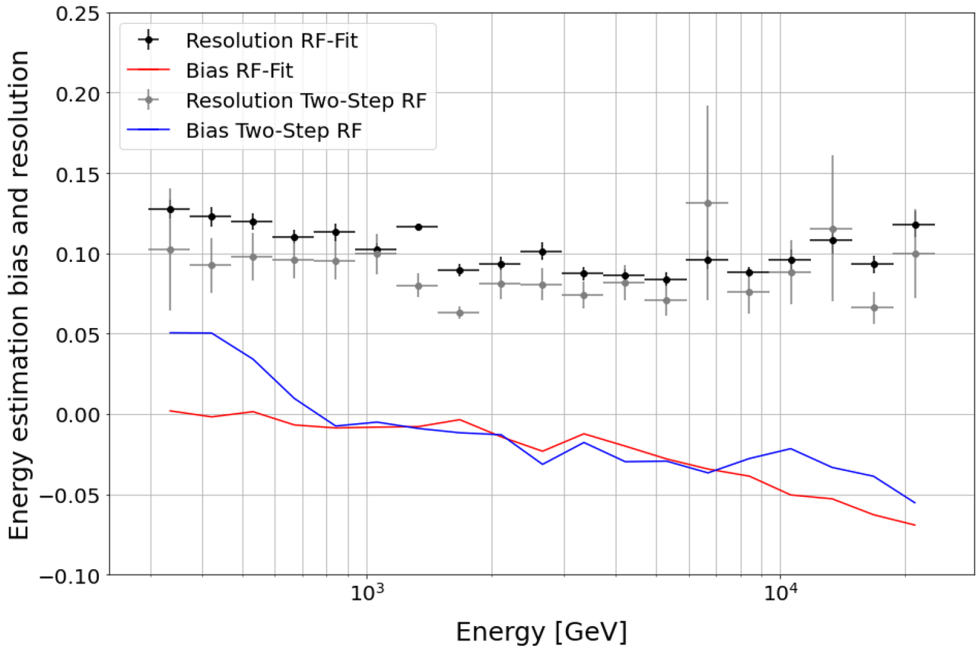

Figure 3.25: Resolution and bias of reconstructed energy for **RF-Fit** method and **Two-Step RF** method shown as a function of true energy.

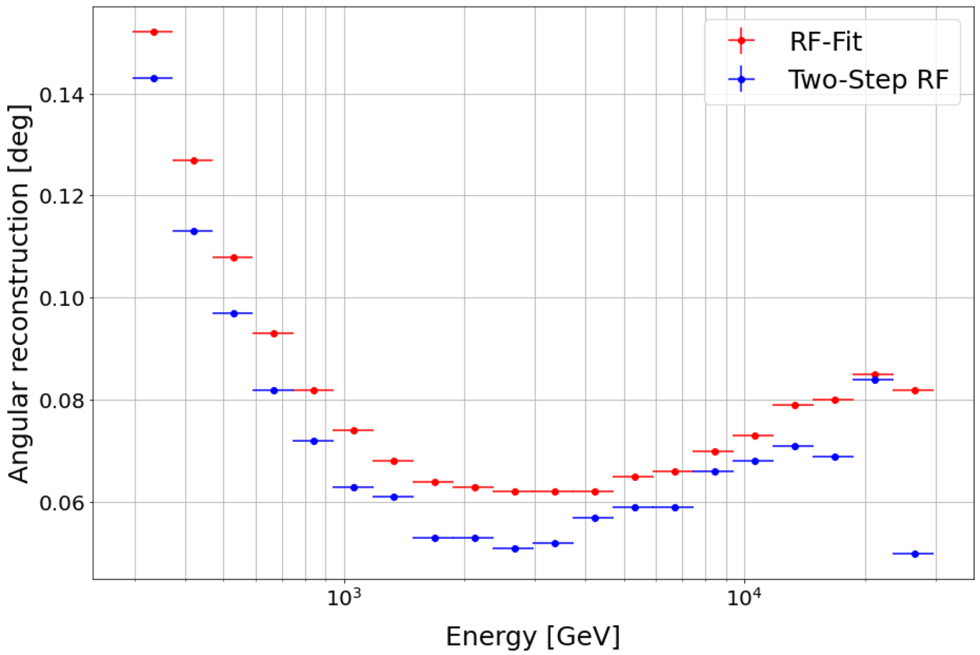

Figure 3.26: Angular resolution from **RF-Fit** and **Two-Step RF** shown as a function of estimated energy.

3.6 Pros and Cons of the Two Methods

Both the **RF-Fit** and **Two-Step RF** methods yield reasonable cosmic-ray all-electron spectra. However, each method has its own advantages and disadvantages.

The validity of the **RF-Fit** method, which is the traditional method of determining the cosmic-ray all-electron spectrum for IACT, has been confirmed by VERITAS (Archer et al., 2018) and H.E.S.S. (Archer et al., 2018). Compared to the **Two-Step RF** method, the **RF-Fit** method has a much larger collection area, as compared in Figure 3.23, resulting in significantly increased statistics. However, the primary challenge of this method is the requirement for a massive amount of proton and helium simulations to obtain a smooth hadronness distribution for an accurate template fit and excess extraction. To achieve a good match between the simulation and observation data, accurate modeling of the hadronic interactions, atmospheric conditions, detectors, and pointing trajectories is necessary. The main source of systematic error in this method is the discrepancy between the simulated background and real data.

The **Two-Step RF** method relies primarily on the separation power of RF to distinguish electrons from signal-like protons. The majority of background events are rejected by applying a tight hadronness cut. Furthermore, the method requires relatively low computational power since only simulated protons are necessary to calculate the contamination rate. The most apparent drawback of this method is the very small collection area resulting from the very tight hadronness efficiency cuts.

These two methods have distinct advantages and disadvantages, and they complement each other, making the final spectrum more reliable.

Chapter 4

Cosmic-Ray All-Electron Spectrum

In this chapter, I present the cosmic-ray all-electron spectra obtained by the two methods and compare the spectra with those measured by other experiments in Section 4.1. In addition, I provide a detailed analysis of the systematics related to the two methods in Section 4.2. The energy spectrum, including the best-fit model, is presented in Section 4.3. Finally, Section 4.2.3 offers an inspection of the flux in each FoV and a brief discussion of the anisotropy study of cosmic-ray electrons and positrons.

4.1 Cosmic-Ray All-Electron Spectrum

The detailed analysis chains of the all-electron spectrum using MAGIC were introduced in Chapter 3, covering everything from data selection to the validation of two flux determination methods. Following these analysis chains, the final cosmic-ray all-electron spectra with two methods compared with other experiments are shown in the Figure 4.5. The **RF-Fit** method can achieve an energy threshold of approximately 300 GeV, while the **Two-Step RF** method can reach a threshold of around 500 GeV. In the overlapping energy ranges, the two spectra of MAGIC are consistent with each other as well as consistent with the spectra from other instruments.

4.2 Systematic Uncertainties

MAGIC, like any other instrumental apparatus, is subject to systematic uncertainties that arise from the IACT technique. These uncertainties can arise from various sources, including factors related to observation conditions such as atmospheric conditions, PMT response, variations in mirror reflectivity, and other sources, as well as factors related to the estimations made during the analysis, such as those involved in MC simulations. Efforts are made to minimize systematic errors from data selection to specific MC simulations for each pointing to reflect reality as accurately as possible. The dominant source of systematic uncertainty in the MAGIC absolute energy scale is attributed to the energy reconstruction process, which results in an uncertainty of approximately 15% (Aleksić and

et al., 2016). To discern the energy structure, the all-electron spectrum is presented as $E^3\times$ flux, where the absolute energy uncertainty $\Delta E = 15\%$ leads to an approximate uncertainty of $\sqrt{3(\Delta E)^2} = 26\%$ in $E^3\times$ flux. Besides the systematic errors inherent in energy reconstruction, the diffuse analysis chain introduces further sources of systematic uncertainty.

4.2.1 RF-Fit Method

As the statistical error in the **RF-Fit** method for electron analysis is very low due to the large number of extracted signal events, determining the systematic error is essential. The following sources of systematic uncertainty and their associated determination methods are listed below:

- The assumed spectral indices for the energy of the simulated protons and helium are varied by $\pm 10\%$ from their nominal values of -2.6 (An et al., 2019) for hadrons. This translates to a spectral index range -2.9 to -2.3 for protons and helium. This contributes to around 5% of the overall systematics.

- Different hadronness fitting ranges are investigated, which included ranges of 0 to 0.3 and 0 to 0.6. This contributes to around 7% of the overall systematics.

Figure 4.1 displays the energy dependence of the systematic uncertainties associated with individual components. Table 4.1 shows the energy range, differential energy flux of cosmic-ray all-electron, with its statistical and individual systematic errors. The ratio of uncertainties as a function of energy is shown in Figure 4.2.

4.2.2 Two-Step RF Method

In addition to the systematic uncertainty arising from energy reconstruction, there are other sources of systematic uncertainty associated with this method.

- To test the robustness of the selected position, the hadronness efficiency bin cut position is shifted from the best-cut position to a position 1% lower than the best-cut position. Additionally, a hadronness cut efficiency of 10% is used to assess the level of contamination control.

- Contamination from helium, which has been investigated and found to be negligible.

The systematic uncertainties associated with individual components are shown as a function of energy in Figure 4.3, while Table 4.2 provides information on the energy range, differential energy flux of cosmic-ray all electrons, as well as their statistical and individual systematic errors. The ratio of uncertainties as a function of energy is shown in Figure 4.4.

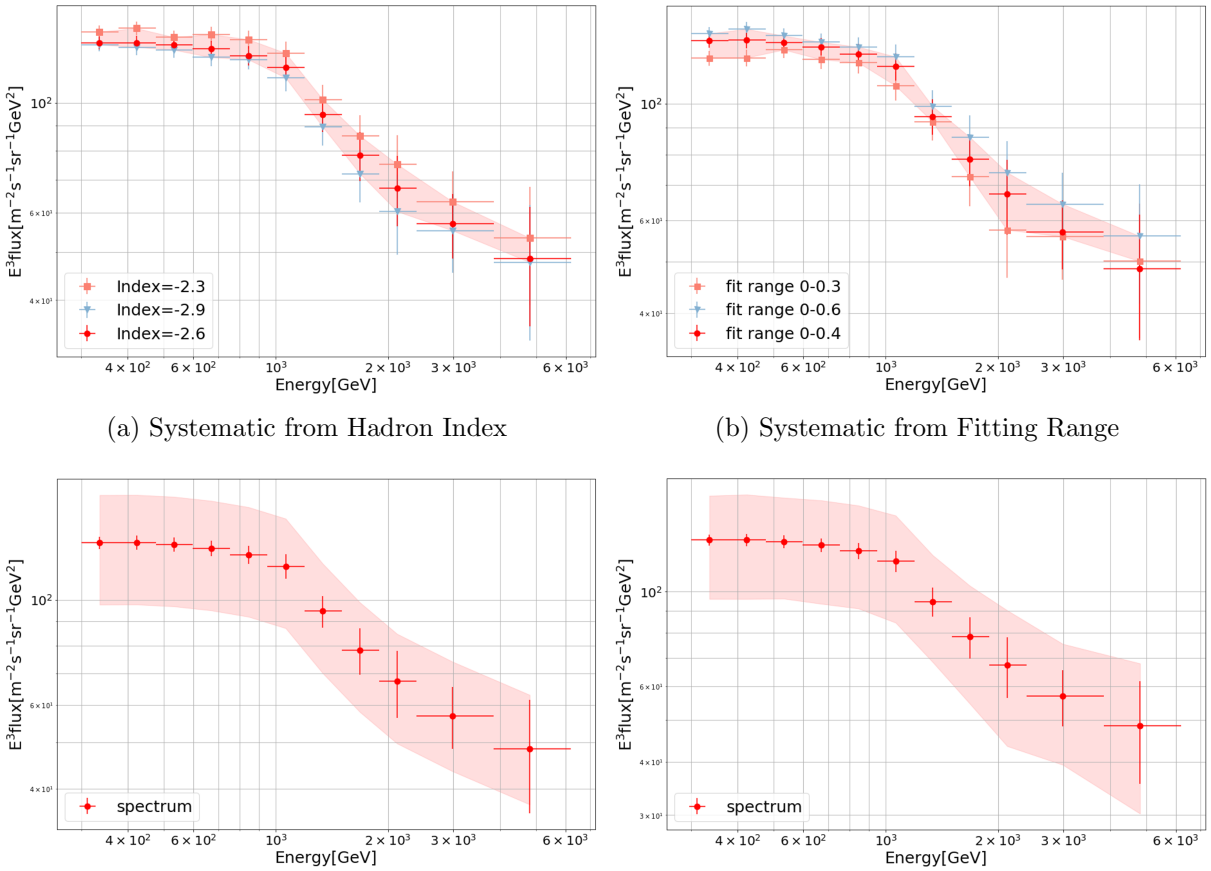

(a) Systematic from Hadron Index

(b) Systematic from Fitting Range

(c) Systematic from Energy Reconstruction

(d) Total Systematic + Statistic

Figure 4.1: Systematics of cosmic-ray all-electron spectrum for the **RF-Fit** method. The systematic error band associated with each component is shown in its respective panel. Upper left (a): The assumed spectral indices for the energy of the simulated hadrons was adjusted by plus or minus 10% from its nominal values of -2.6 for hadrons, as indicated by the red dots. This resulted in a spectral index range of -2.9 to -2.3, shown in light blue triangle and orange square respectively. Upper right (b): The systematic uncertainty arises from the hadronness fitting range, the red dots indicate the spectrum obtained by fitting the hadronness range from 0 to 0.4. The spectra with fitting ranges from hadronness 0 to 0.3 are shown as orange squares, and from hadronness 0 to 0.6 are shown as light blue triangles. Bottom left (c): The red band represents the systematic uncertainty arising from energy reconstruction. The absolute energy uncertainty $\Delta E = 15\%$ propagates to the $E^3 \times flux$ to be approximately $\sqrt{3(\Delta E)^2} = 26\%$. Bottom right (d): The quadrature sum of statistical and all systematic uncertainties.

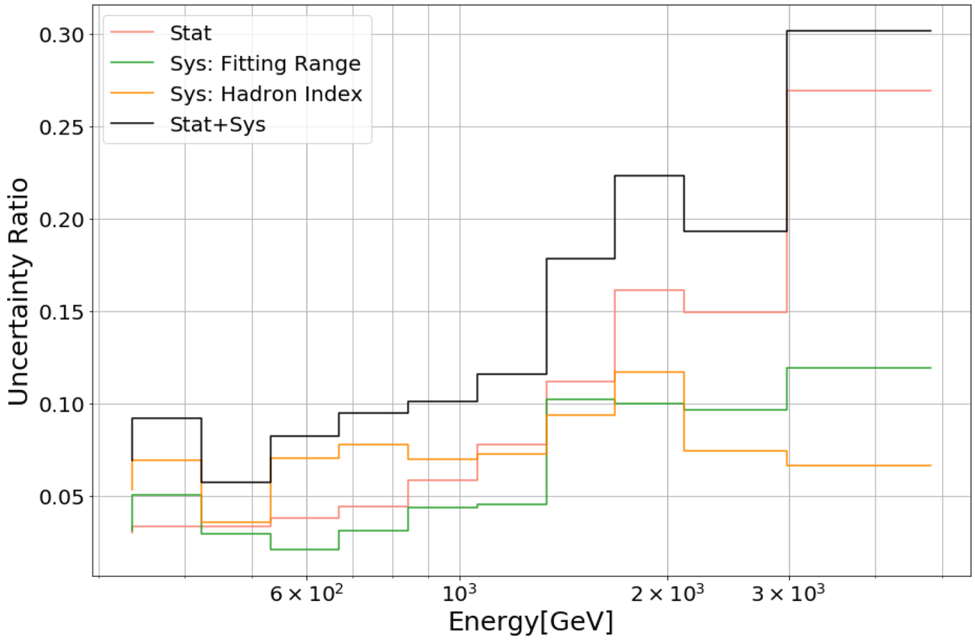

Figure 4.2: The figure displays the ratio of uncertainties as a function of energy. The pink line represents the ratio of statistical uncertainty. The uncertainties associated with each systematic source, including fitting range and hadron index are depicted by the green, and orange lines, respectively. The 15% energy scale uncertainty is not included. The total uncertainty ratio is represented by the black line.

E_{min} (GeV)	E_{max} (GeV)	$\langle E \rangle$ (GeV)	$flux \pm \sigma_{stat} \pm \sigma_{index} \pm \sigma_{fitrange}$ ($\mathrm{GeV^{-1}m^{-2}s^{-1}sr^{-1}}$)
300.0	377.7	335.7	$(3.482 \pm 0.105 \pm^{0.105}_{0.095} \pm^{0.295}_{0.319}) \times 10^{-6}$
377.7	475.5	422.6	$(1.695 \pm 0.059 \pm^{0.082}_{0.035} \pm^{0.127}_{0.174}) \times 10^{-6}$
475.5	598.6	532.1	$(8.673 \pm 0.291 \pm^{0.374}_{0.204} \pm^{0.256}_{0.276}) \times 10^{-7}$
598.6	753.6	669.8	$(4.262 \pm 0.162 \pm^{0.314}_{0.162} \pm^{0.089}_{0.229}) \times 10^{-7}$
753.6	948.7	843.3	$(2.070 \pm 0.091 \pm^{0.184}_{0.038} \pm^{0.064}_{0.078}) \times 10^{-7}$
948.7	1194.3	1061.6	$(9.821 \pm 0.574 \pm^{0.707}_{0.455} \pm^{0.431}_{0.789}) \times 10^{-8}$
1194.3	1503.6	1336.5	$(3.968 \pm 0.308 \pm^{0.290}_{0.220} \pm^{0.180}_{0.094}) \times 10^{-8}$
1503.6	1892.9	1682.6	$(1.648 \pm 0.185 \pm^{0.155}_{0.137} \pm^{0.169}_{0.119}) \times 10^{-8}$
1892.9	2383.0	2118.2	$(7.092 \pm 1.146 \pm^{0.830}_{0.728} \pm^{0.710}_{1.027}) \times 10^{-9}$
2383.0	3843.7	2992.5	$(2.297 \pm 0.351 \pm^{0.155}_{0.127} \pm^{0.166}_{0.121}) \times 10^{-9}$
3843.7	6199.8	4826.7	$(3.981 \pm 1.250 \pm^{0.279}_{0.219} \pm^{0.522}_{0.000}) \times 10^{-10}$

Table 4.1: The flux of cosmic-ray all-electron for **RF-Fit** method in units of $\mathrm{GeV^{-1}m^{-2}s^{-1}sr^{-1}}$, with its statistical and systematic errors. The 15% energy scale uncertainty is not included.

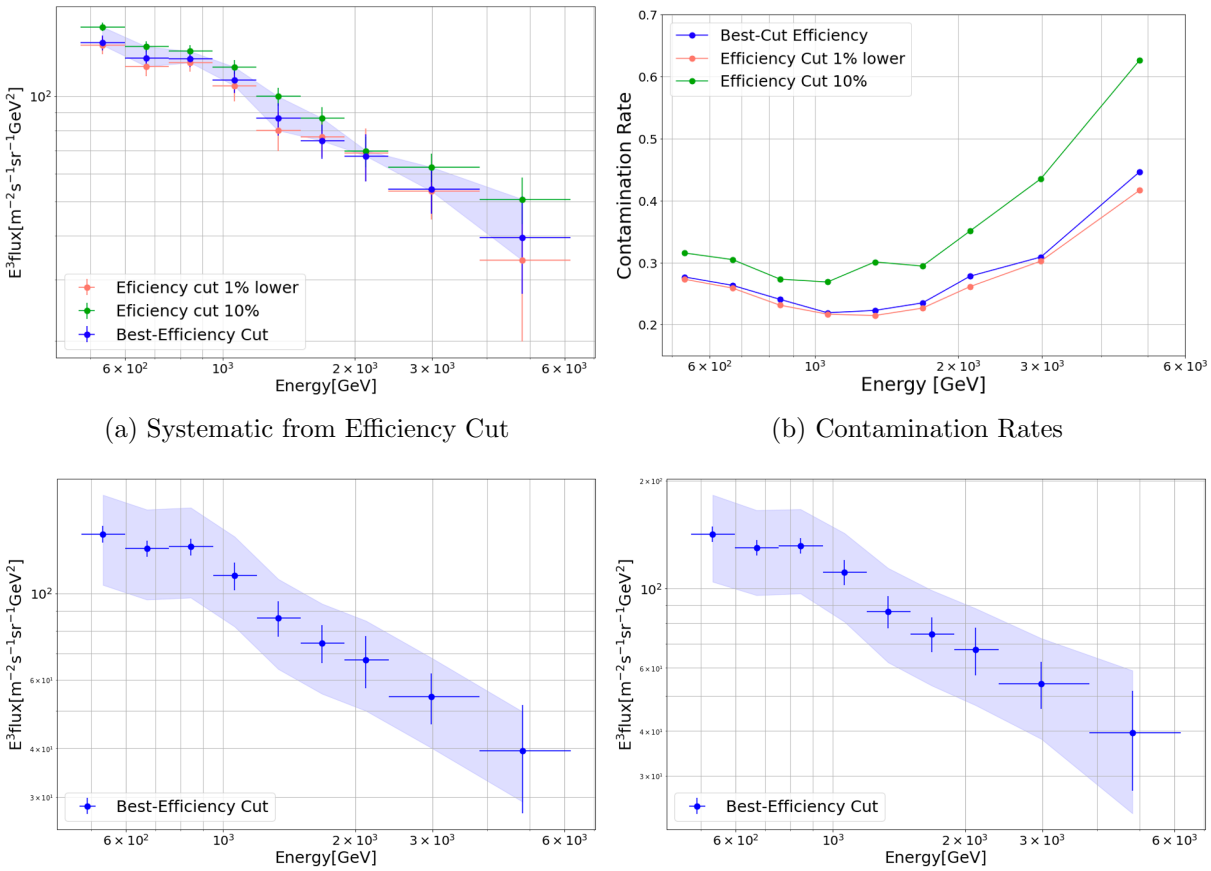

(a) Systematic from Efficiency Cut

(b) Contamination Rates

(c) Systematic from Energy Reconstruction

(d) Total Systematic + Statistic

Figure 4.3: Systematics of cosmic-ray all-electron spectrum for the **Two-Step RF** method. The systematic error band of each component is presented in its respective panel. Upper left (a): the spectra based on different electron hadronness efficiency cut positions are presented. The blue dots represent the spectrum based on the Best-Efficiency cut, while the pink dots and green dots represent the spectrum with an efficiency cut 1% lower than the Best-Efficiency cut position and an efficiency cut of 10%, respectively, labeled as Efficiency cut 10%. Upper right (b): The contamination rates corresponding to the Best-Efficiency cut position, 1% lower than the Best-Efficiency cut position, and Efficiency cut 10% in each energy bin are displayed. Bottom left (c): The blue band represents the systematic uncertainty arising from energy reconstruction. The absolute energy uncertainty $\Delta E = 15\%$ propagates to the $E^3 \times flux$ to be approximately $\sqrt{3(\Delta E)^2} = 26\%$. Bottom right (d): The quadrature sum of statistical and all systematic uncertainties.

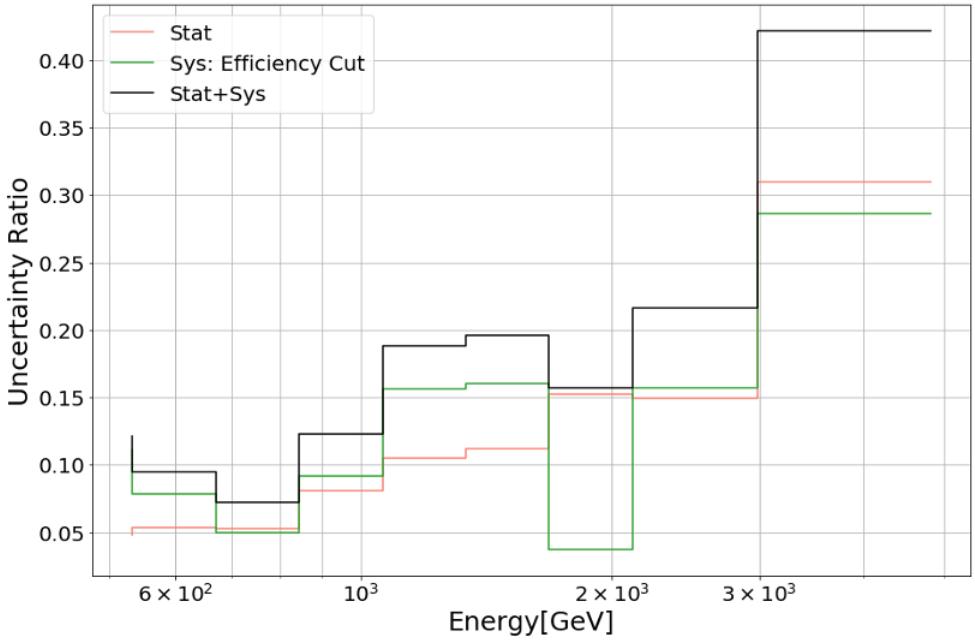

Figure 4.4: The figure displays the ratio of uncertainties as a function of energy the **Two-Step RF**. The pink line represents the ratio of statistical uncertainty. The green line represents the systematic uncertainty associated with efficiency cut position. The 15% energy scale uncertainty is not included. The total uncertainty ratio is represented by the black line.

E_{min} (GeV)	E_{max} (GeV)	$\langle E \rangle$ (GeV)	$flux \pm \sigma_{stat} \pm \sigma_{effcut}$ ($\mathrm{GeV^{-1}m^{-2}s^{-1}sr^{-1}}$)
475.5	598.6	532.1	$(9.412 \pm 0.457 \pm^{1.045}_{0.133}) \times 10^{-7}$
598.6	753.6	669.8	$(4.273 \pm 0.261 \pm^{0.336}_{0.228}) \times 10^{-7}$
753.6	948.7	843.3	$(2.140 \pm 0.121 \pm^{0.106}_{0.054}) \times 10^{-7}$
948.7	1194.3	1061.6	$(9.771 \pm 0.715 \pm^{0.851}_{0.319}) \times 10^{-8}$
1194.3	1503.6	1336.5	$(3.601 \pm 0.339 \pm^{0.566}_{0.273}) \times 10^{-8}$
1503.6	1892.9	1682.6	$(1.588 \pm 0.158 \pm^{0.252}_{0.000}) \times 10^{-8}$
1892.9	2383.0	2118.2	$(7.080 \pm 0.937 \pm^{0.265}_{0.000}) \times 10^{-9}$
2383.0	3843.7	2992.5	$(2.155 \pm 0.250 \pm^{0.320}_{0.024}) \times 10^{-9}$
3843.7	6199.8	4826.7	$(3.282 \pm 0.798 \pm^{1.013}_{0.492}) \times 10^{-10}$

Table 4.2: The flux of cosmic-ray electron and position for **Two-Step RF** method in units of $\mathrm{GeV^{-1}m^{-2}s^{-1}sr^{-1}}$, with its statistical and systematic errors. The 15% energy scale uncertainty is not included.

The cosmic-ray all-electron spectrum obtained using two methods are shown in the Figure 4.5, with spectra multiplied by E^3 and including statistical errors, and the associated

shaded region shows the sum of statistical and systematic errors. The results are compared with the spectra obtained by other experiments.

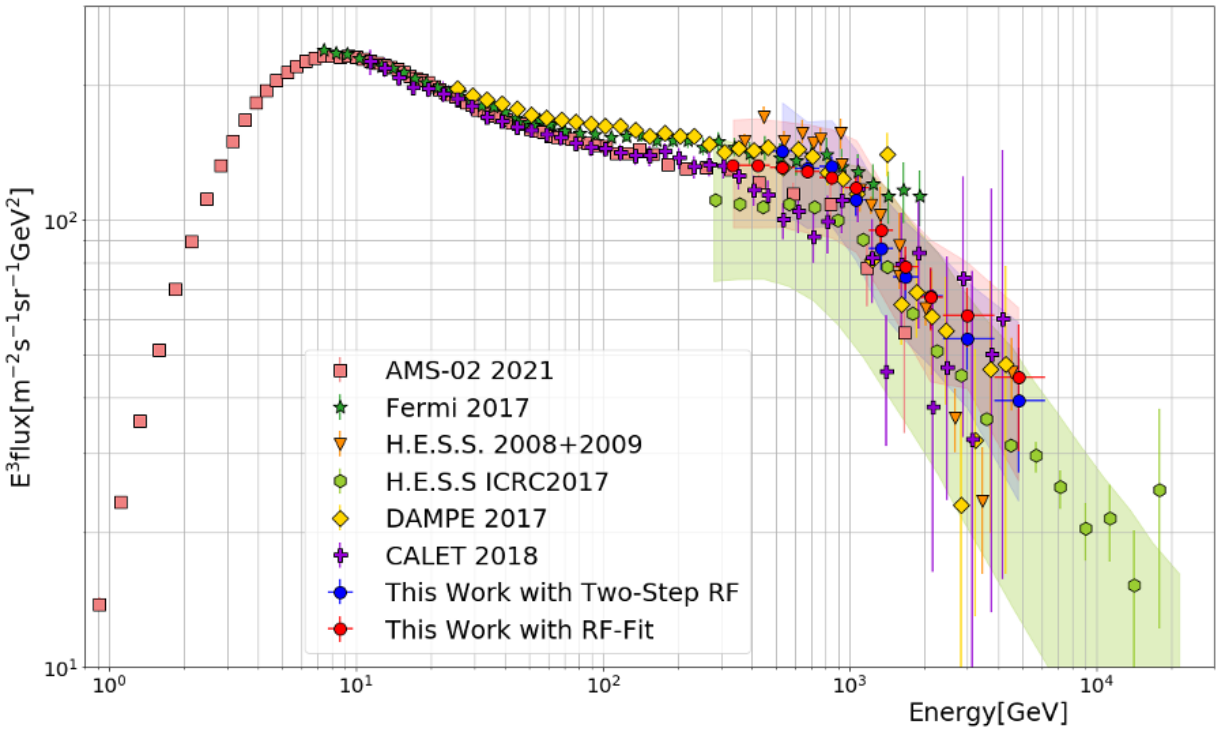

Figure 4.5: The cosmic-ray all-electron spectra obtained by two methods, multiplied by E^3 with their statistical errors, are shown in the plot. The spectrum obtained by the **RF-Fit** method is represented by the red dots, with the red shaded region showing the sum of statistical and systematic errors. The spectrum obtained by the **Two-Step RF** method is represented by the blue dots, with the blue shaded region showing the sum of statistical and systematic errors. The results are compared with those of other experiments, including AMS-02 in 2014 (Aguilar and et al., 2014), and Fermi in 2017 (Abdollahi et al., 2017), H.E.S.S. in 2008, 2009 (Aharonian et al., 2008; Aharonian, F. and et al., 2009) and ICRC2017 (Kerszberg and et al., 2015), DAMPE in 2017 (Ambrosi et al., 2017), CALET in 2018 Adriani and et al. (2018) which are only depicted with quadratic sum of statistical and systematic errors.

4.2.3 Inspection of Flux in Each Direction

The study of anisotropy in cosmic-ray electrons and positrons based on their spectrum is a fascinating subject. However, it poses significant challenges for IACTs due to the considerable systematic uncertainties involved and the limited sky coverage that can be achieved. In this study, only three sources were used, which is insufficient to perform a comprehensive anisotropy study. However, the events of these three sources dominate very distinct zenith and azimuth angles and are located at large distances across the sky, as

summarized in Table 3.1 and illustrated in Figure 3.2. Comparing the fluxes of individual sources is interesting. In this study, only the **RF-Fit** method was used as the statistics is too low to draw the individual spectra for the **Two-Step RF** method.

The cosmic-ray all-electron spectrum for individual FoVs are displayed in Figure 4.6. It is worth noting that most events from Draco, which were observed over a much larger zenith range compared to the other FoV, have a slightly higher energy threshold. Additionally, due to the lack of statistics, the highest energy achieved for Draco is lower than that of the other sources. The spectrum of the Draco FoV is shown in the range of 475 GeV to 2.5 TeV, while for the other FoVs, the range displayed is from 300 GeV to 5 TeV. The spectra computed from different FoVs in the overlapped energy ranges are consistent with each other within a 1 σ statistical uncertainty. The reduced χ^2 are 7.47, 7.22 and 4.60 in case of degree of freedom 8, 8 and 5 for the FoV of M15, ComaBerenice and Draco.

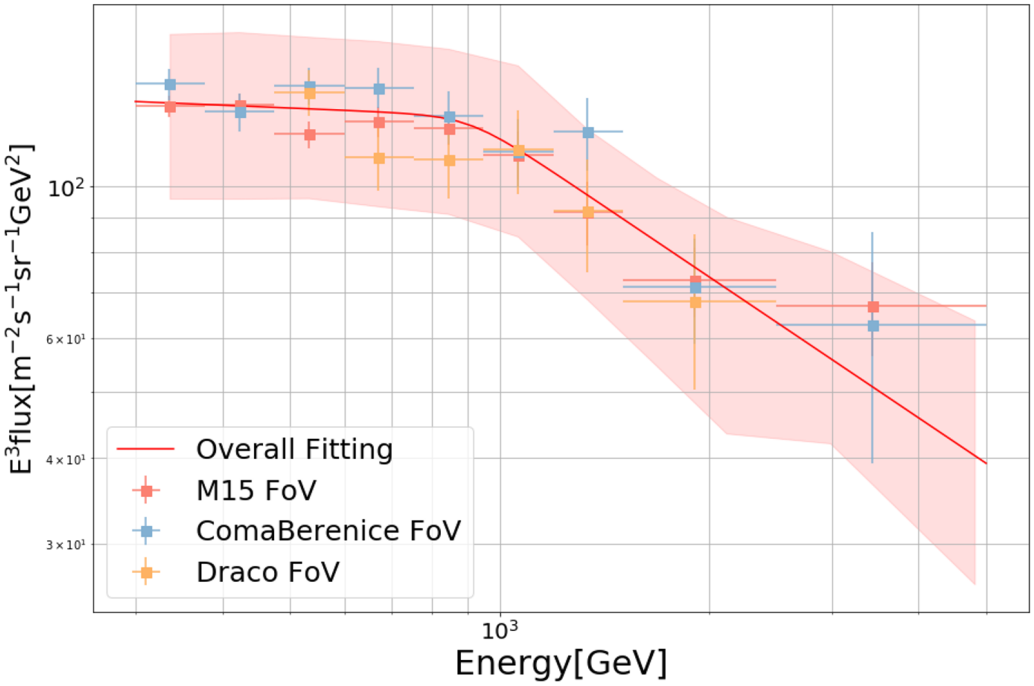

Figure 4.6: Cosmic-ray all-electron spectrum from individual FoV by **RF-Fit** analysis. The spectrum from M15 FoV is represented by the red square, while the light blue and light orange squares denote the spectra from Comaberenice FoVsand Draco FoV, respectively. The red line shows the best-fit broken power law spectrum fitted with all data.

A detailed study of the anisotropy of cosmic-ray all-electron by IACTs are introduced in Kraus (2018). The anisotropy study will be of great importance for the upcoming Cherenkov Telescope Array (CTA), due to the extensive coverage provided by the CTA sites located in both the Northern and Southern hemispheres.

4.3 Spectral Fits

The energy spectra of both the **RF-Fit** and **Two-Step RF** analysis were fitted with a broken power law:

$$dN/dE = N_0(E/E_{break})^{-\Gamma_1}(1 + (E/E_{break})^{1/\alpha})^{-(\Gamma_2-\Gamma_1)\alpha} \quad (4.1)$$

Where N_0 represents the normalization factor, E_{break} represents the transitional energy where the spectral index changes from Γ_1 to Γ_2, and α represents the sharpness of this transition. The energy fitting range is 300 GeV to 6 TeV for the **RF-Fit** method and 475 GeV to 6 TeV for the **Two-Step RF**. Table 4.3 shows the parameters of the best fit models for the two methods. The cosmic-ray all-electron spectra based on the two methods including the best-fit models as well as the sum of statistical and systematic error bands are shown in Figure 4.7.

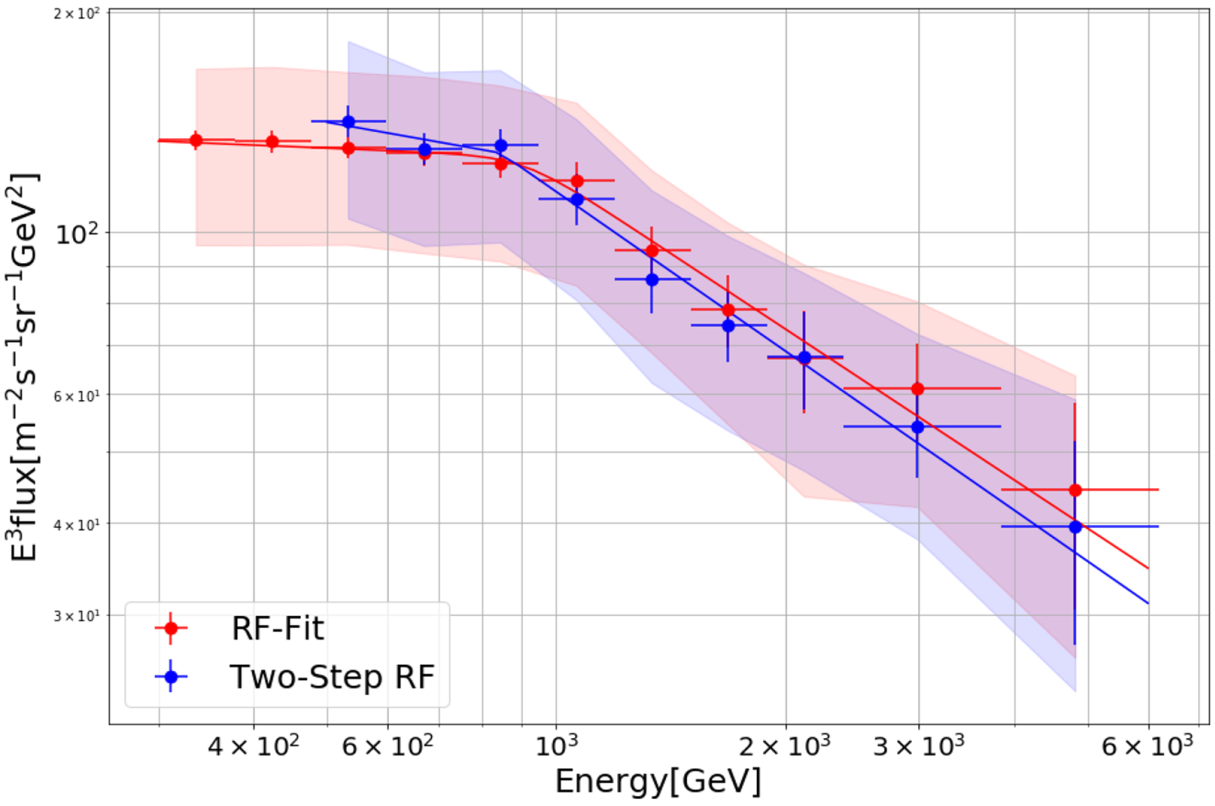

Figure 4.7: The fitted cosmic-ray all-electron spectra based on the two methods. The best-fit model of the data obtained by **RF-Fit** is represented by the red line, accompanied by a red shaded region indicating the combined statistical and systematic errors. Similarly, for the **Two-Step RF** method, the best-fit model is depicted by the blue line, with a blue shaded region representing the sum of statistical and systematic errors.

RF-Fit	**Two-Step RF**
$\Gamma_1 = 3.04 \pm 0.08$	$\Gamma_1 = 3.18 \pm 0.15$
$\Gamma_2 = 3.69 \pm 0.13$	$\Gamma_2 = 3.72 \pm 0.09$
$E_{break} = 905.31 \pm 142.6$	$E_{break} = 845.25 \pm 37.62$
$N_0 = (1.71 \pm 0.90) \times 10^{-7}$	$N_0 = (2.12 \pm 0.34) \times 10^{-7}$
α=0.005	α=0.002
χ^2_R =2.44/6	χ^2_R =1.56/4

Table 4.3: Best-Fit model parameters of the broken power law for **RF-Fit** (left) and **Two-Step RF** (right).

The cosmic-ray all-electron spectra obtained from both analysis methods are well described by broken power laws. The important parameters of the best fit models are in agreement with each other. The spectra exhibit a softening feature after an energy of around 900 GeV. Below this energy, spectral indices of approximately -3 are observed, while above this energy, the spectral indices are around -3.7 for both analysis chains. These findings are consistent with those of previous experiments in the current observation energy range. However, the systematic uncertainty is too large to differentiate between the results obtained by AMS-02 and Fermi.

Chapter 5

Physics Interpretation

High-energy cosmic-ray electrons and positrons undergo significant energy loss during propagation due to synchrotron radiation and inverse Compton scattering. As a result, TeV electrons and positrons should originate from sources less than 1 kpc away, as explained in Section 1.3.3. High-energy cosmic-ray electrons and positrons are fascinating as a distinctive probe for investigating nearby astrophysical particle accelerators. Furthermore, the unexpected increase in the positron fraction spectrum, briefly introduced in Section 1.4, has gained significant interest and presents a new opportunity to uncover the sources of these high-energy cosmic-ray electrons and positrons. According to Delahaye et al. (2010), any model that predicts only the positron fraction or the all-electron spectrum is insufficient, and its consistency cannot be guaranteed. The subsequent chapter will provide a detailed review of the various "advanced models" which can interpret the all-electron spectrum and positron fraction spectrum at the same time. Before introducing these "advanced models" and briefly discussing the dark matter scenario in Section 5.2, a review of the "standard model" will be provided in Section 5.1. Finally, in Section 5.3, I compare these all-electron spectrum models with the MAGIC data obtained in this study. However, the positron fraction models cannot be tested as MAGIC is unable to distinguish between electrons and positrons.

5.1 Standard Model

The "standard model" by Strong et al. (2004) of the cosmic-ray all-electron spectrum assumes the following: (1) For the electron component, most are primary electrons accelerated in the SNR shocks, with only a small portion coming from secondary products in the ISM. Primary electron sources are homogeneously distributed in the Galactic disk and are time-independent; (2) Secondary products resulting from the spallation of hadronic cosmic-ray particles in the ISM are the sole contributors to the positron component; (3) During propagation, the diffusion process steepens the injected spectrum.

Grasso and et al. (2009) attempted to explain the all-electron data from *Fermi*-LAT (Abdo

and et al., 2009) and H.E.S.S. (Aharonian et al., 2008; Aharonian, F. and et al., 2009) as well as the lower energy data using the "standard model" with the numerical CR propagation code GALPROP (Strong and Moskalenko, 2001; Strong et al., 2004). The GALPROP code can fit the pre-*Fermi* data very well with an electron injection index $\gamma_0 = 2.54$ (energy above 4 GeV) and a power-law index of the diffusion coefficient in terms of energy $\delta = 1/3$, as shown by the black solid line in Figure 5.1. To fit the *Fermi*−LAT data, δ and γ_0 were adjusted for better agreement with the data: either $\delta = 1/3$ and $\gamma_0 = 2.42$, presented as the red dashed line, or $\delta = 0.6$ and $\gamma_0 = 2.33$, presented as the blue dashed line in Figure 5.1.

Although these two sets of parameters fit the *Fermi*-LAT data much better, it is worth noting that the AMS-01 (Aguilar and et al., 2002) and HEAT (DuVernois et al., 2001) data are not reproduced well, even after proper solar modulation is applied. Grasso and et al. (2009) pointed that this discrepancy could contribute to the systematic uncertainty of *Fermi*−LAT data. The tension between the model and H.E.S.S. data also exists in the energy range above 1 TeV. To alleviate this tension, Grasso and et al. (2009) considered a model of supernovae within Gould's Belt, superimposed on a uniform distribution of supernovae in the Galactic Plane to enhance the rate of local supernovae. Fluctuations are caused by rapid energy loss at high energies and the stochastic nature of the sources (see Fig. 2 in Grasso and et al. (2009)), and in some cases, *Fermi*−LAT and H.E.S.S. data can be accommodated.

The discrepancy in the cosmic-ray all-electron spectrum may be resolved as mentioned above; however, the issue with the positron fraction spectrum is considerably more problematic. The positron fraction spectrum is fitted using the same parameters of the "standard model" in the right panel of Figure 5.1. The "standard model" cannot account for the increase in energy above 10 GeV observed in the positron fraction spectrum.

To directly observe the positron fraction as a function of energy, an analytical prediction is introduced based on the "standard model" of cosmic-ray propagation (Blasi, 2009). The injected cosmic-ray spectrum by astrophysical sources, accelerated via diffusive shock acceleration (see Section 1.4.1), follows a power-law distribution $\mathrm{Q}_{CR}(E) \propto E^{-\gamma}$. The spectrum observed at Earth is described as $\mathrm{n}_{CR} \propto Q_{CR}(E)\,\tau_{esc}(E)$ due to the diffusion of particles (see Section 1.3.3), where $\tau_{esc}(E)$ is the residence time of a particle in the Leaky Box model. $\tau_{esc}(E)$ is a function of energy, with $\tau_{esc} \propto E^{-\delta}$, where δ is the flux ratio of boron to carbon (see Section 1.3.1) and has a value of approximately 0.3-0.6 (Blasi, 2008).

The injected positron is the secondary component produced by spallation of primary CRs n_{CR} with the ISM n_H and the subsequent decay of the scattering products: $Q_+(E) \propto n_{CR}(E) n_H c\sigma$, where σ is the cross-section of the process. The equilibrium spectrum of positron is $n_+(E) \propto Q_+(E)\,\tau_e(E) \propto E^{-\gamma-\delta}\tau_e(E)$, where $\tau_e(E)$ is determined by the relationship between $\tau_{esc}(E)$ and the energy loss time of positron $\tau_{loss}(E)$, which is $\tau_e(E) \approx \mathrm{Min}[\tau_{esc}(E), \tau_{loss}(E)]$. The injected spectrum of electron is $Q_-(E) = KQ_{CR}(E)$, where

K is a constant. The observed spectrum of electron is $n_-(E) \propto E^{-\gamma}\tau_e(E)$. Therefore, the ratio between positrons and electrons is: $n_+/n_- \propto E^{-\delta}$. This implies that the positron fraction is expected to decrease with increasing energy. Therefore, the surprising increase in the positron fraction above 10 GeV indicates a primary source of positron (Serpico, 2009).

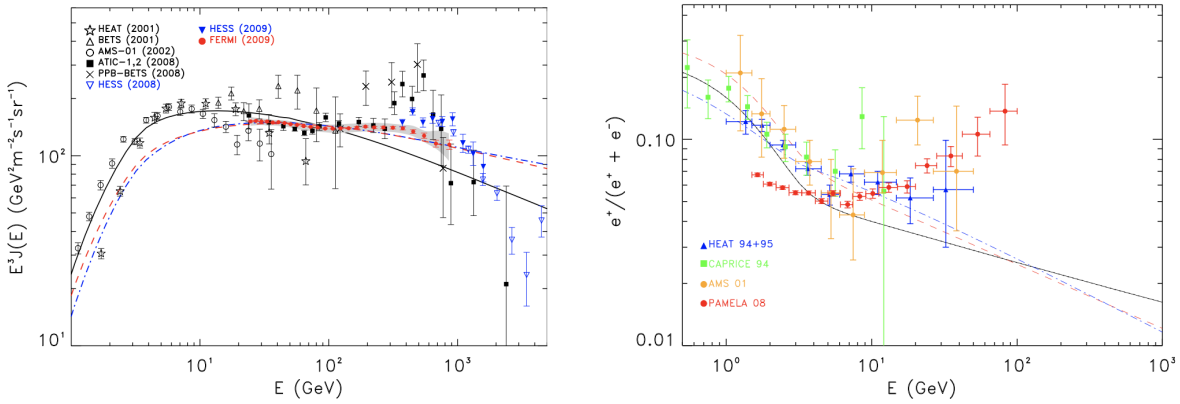

Electrons and Positrons

Positron Fraction

Figure 5.1: Left: The cosmic-ray all-electron data fitted with the "standard model" using the code by Strong et al. (2004). The black solid line represents the model fitted with the pre-Fermi data. The red dashed line and blue dashed line are adjusted to fit *Fermi*−LAT (see details in the text). Right: The positron fraction spectrum fitted using the same model as the left panel (Grasso and et al., 2009).

5.2 Advanced Model

In response to the energy data observed in the high-energy range, several "advanced models" have been proposed to simultaneously explain the new characteristics observed in the cosmic-ray all-electron spectrum and the positron fraction spectrum in the high-energy range. In this section, these "advanced models" are classified as: **SourceA** + **SourceB** interpretation. **SourceA** is responsible for the 1 TeV break; **SourceB** is the main accelerator for the rise of positron fraction. Following this idea, three types of model: **SNRs** + **SNRs**, **SNRs** + **Pulsars**, **Pulsars** + **Pulsars** are introduced.

5.2.1 SNRs+SNRs

Typically, the production of positrons within SNRs is neglected. This is based on the argument that the probability of hadronic interactions inside SNRs is much smaller compared to interactions during propagation in the ISM, as the lifetime of a SNR ($\sim 10^5$ years) is much shorter than the diffusion time in the ISM ($\sim 10^7$ years) (Serpico, 2012). However,

some models explore the possibility of explaining the rising positron fraction by considering positron production by SNRs. In the following, I will provide a brief overview of two models: the first model, proposed by (Blasi, 2009), argues that the positron fraction upturn is attributed to the secondaries produced and accelerated in nearby SNRs. On the other hand, the second model (Kohri et al., 2016) suggests that the upturn is caused by secondary positrons created by SNRs within dense gas clouds. Both models propose that SNRs, being the primary source of electrons, along with secondary electrons and positrons produced within the SNRs, contribute to the 1 TeV break in the all-electron spectrum. Therefore, these models fall under the classification of **SNRs + SNRs** interpretations.

Secondaries Acceleration in SNRs

According to Blasi (2009), the upturn in the positron fraction spectrum is a natural consequence of the standard cosmic-ray model if the secondaries are produced in the same region where the primaries are accelerated, as in this scenario, the secondaries may have a harder spectrum. The production rates of secondary electrons and positrons are as follows:

$$Q_{\pm}(x,E) = \int dE^{'} N_{CR}\left(E^{'},x\right) \frac{d\sigma\left(E^{'},E\right)}{dE^{'}} n_{gas}(x)\, c \tag{5.1}$$

where n_{gas} is the gas density for the proton collision in the shock region, and $\frac{\mathrm{d}\sigma_{\pm}\left(E^{'},E\right)}{\mathrm{d}E^{'}}$ denotes the differential cross section for a proton with energy $E^{'}$ to produce an electron or a positron of energy E (Kamae et al., 2006).

The transport equation, as represented in Equation 5.2, takes into account the influence of diffusion, the presence of the shock, and the advection with the fluid to achieve the equilibrium of the spectrum of electrons and positrons produced in SNRs. Notably, the energy loss term is not included in Equation 5.2 because the energy discussed here is low enough that Synchrotron and inverse Compton effects are negligible. The equilibrium spectrum is defined as:

$$u\frac{\partial f_{\pm}}{\partial x} = D(p)\frac{\partial^2 f_{\pm}}{\partial x^2} + \frac{1}{3}\frac{\mathrm{d}u}{\mathrm{d}x} p \frac{\partial f_{\pm}}{\partial p} + Q_{\pm}(x,p) \tag{5.2}$$

where u is the velocity of the fluid of the medium; $D(p)$ is the diffusion coefficient in terms of the particle momentum p; $f_{\pm}(x,p)$ is the equilibrium spectrum of electron $(-)$ and positron $(+)$. Considering proper boundary conditions (see detail in Blasi (2009)), the solution of Equation 5.2 is:

$$f_{\pm}(x,p) = f_{\pm,0}(p) + \frac{Q_2}{u_2} x. \tag{5.3}$$

In the above equation, Q_2 and u_2 denote the injection rate and fluid velocity downstream, respectively. The spectrum at the shock front is represented by $f_{\pm,0}(p)$, which follows a power-law distribution of $p^{-\gamma+\alpha}$, where $\alpha > 0$ is the index of the diffusion coefficient in the accelerator. Secondary particles produced within a distance less than $D(p)/u$ from both

upstream and downstream can participate in the acceleration process. As D increases with energy, higher-energy particles have a greater chance to return to the shock front and participate in acceleration, resulting in a harder spectrum of secondaries from the accelerator. Similar discussions also apply to the antiproton spectrum, as discussed in Blasi and Serpico (2009); Lu and Zong (2016); Cholis et al. (2019). The positron fraction spectrum and the all-electron spectrum based on this scenario are compared with observational data in Figure 5.2.

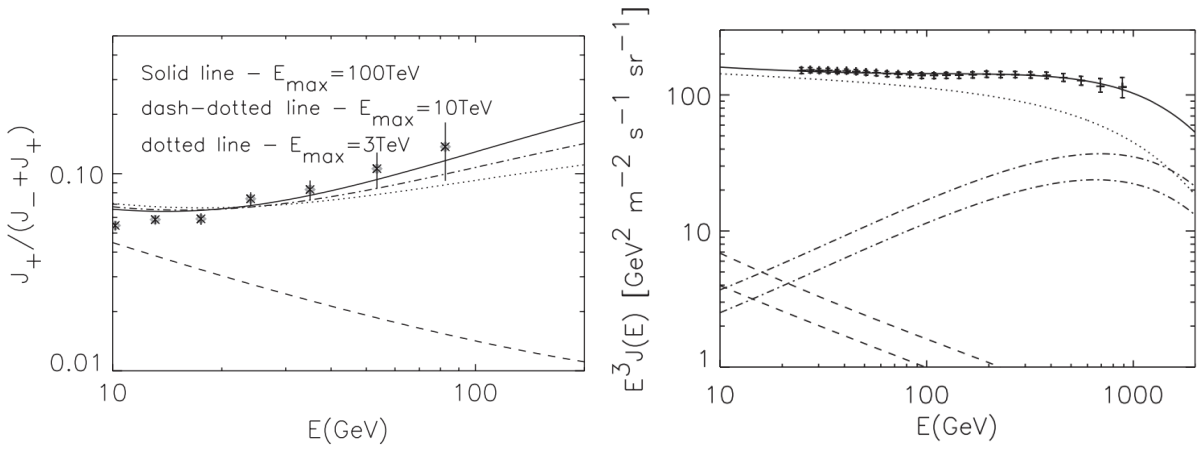

Positron Fraction Electrons and Positrons

Figure 5.2: Left: Positron fraction fitted with PAMELA data for different cutoff energies. Right: All-electron spectrum with a cutoff energy of $E_{max} = 100$ TeV fitted with Fermi-LAT data. The dotted line represents primary electrons; the dashed lines represent contributions from secondary positrons (upper curve) and electrons (lower curve) from interactions with the ISM; the dash-dotted lines represent secondary production of positrons (upper curve) and electrons (lower curve) from interactions in the SNRs (Blasi, 2009).

The positron fraction, which increases with energy as shown in Figure 5.2, can be attributed to secondaries accelerated in the SNRs. These secondaries, along with the primary electrons produced in the SNRs as discussed above, contribute to approximately 50% of the all-electron spectrum. The model predicts a break at around 1 TeV in the cosmic-ray all-electron spectrum, which has been confirmed by later observations from H.E.S.S. (Aharonian et al., 2008; Aharonian, F. and et al., 2009).

However, Cholis and Hooper (2014) argued that if this model is correct, the associated observables, such as the secondary to primary nuclei spectrum, must also increase with energy above ~ 100 GeV. Nonetheless, the observation of the secondary to primary ratio indicates a decreasing trend, as supported by Mertsch and Sarkar (2009); Cholis and Hooper (2014); Mertsch and Sarkar (2014).

SNRs in Dense Gas Cloud

According to Kohri et al. (2016), supernovae located $\sim 100-200$ light years away from the Earth, within a dense gas cloud, could be a source of positrons. In this scenario, protons are accelerated in the shock front of the SNRs and interact with the surrounding Dense Gas Clouds (DCs), resulting in the creation of electrons and positrons. The interaction process is described in Equation 1.40. The spectrum of the proton accelerated in the SNRs is:

$$\frac{dn_p}{dE_p} \propto E_p^{-s} e^{-\frac{E_p}{E_{max,p}}} \tag{5.4}$$

where s is the injection index of the spectrum, and E_{max} is the maximum energy, which can be roughly estimated by Equation 5.5 (Yamazaki et al., 2006):

$$E_{max,p} \sim 2 \times 10^2 v_{s,8}^2 \left(\frac{B_d}{10\mu G}\right) \left(\frac{t_{age}}{10^5 yr}\right) TeV \tag{5.5}$$

where t_{age} represents the age of the SNR, v_s denotes the shock velocity with $v_{s,8} = v_s/10^8 cm\ s^{-1}$, and B_d refers to the magnetic field of downstream. The acceleration of protons is assumed to terminate at the acceleration time t_{acc}, corresponding to a Mach number decrease to 7 (Ryu et al., 2003). For $t_{age} > t_{acc}$, the SNR continues expanding until the cloud is destroyed by the supernova ejecta. The secondaries are presumed to be created during the period t_{pp}, which is defined as the duration from the supernova explosion to the destruction of the dense gas cloud. After the destruction of the supernova, the electrons, positrons, protons, and antiprotons are released into the ISM and begin to diffuse in the local environment.

In this model, a spherical DC with a radius of $R_{DC} = 40$ pc and proton density of $n_0 = 50\ \mathrm{cm}^{-3}$ is assumed. The injection index of the proton spectrum in Equation 5.4 is $s = 2.15$, and the maximum energy is Emax = 100 TeV. The duration of the hadronic process is $t_{pp} = 2 \times 10^5 yr$, and the total energy of accelerated protons is $\mathrm{E_{tot,p}} = 2.6 \times 10^{50}$ erg.

Using the aforementioned parameters for both the positron fraction and all-electron spectra, the model predicts spectra that are consistent with the observation data, as shown in Figure 5.3. In this model, the 1 TeV break and the rising positron fraction are attributed to the protons accelerated in the SNR and their interaction with the surrounding dense gas clouds. This model also predicted an "excess" of antiproton fraction in Fujita et al. (2009), which is in agreement with the latest observation from AMS-02 (Aguilar and et al., 2016a).

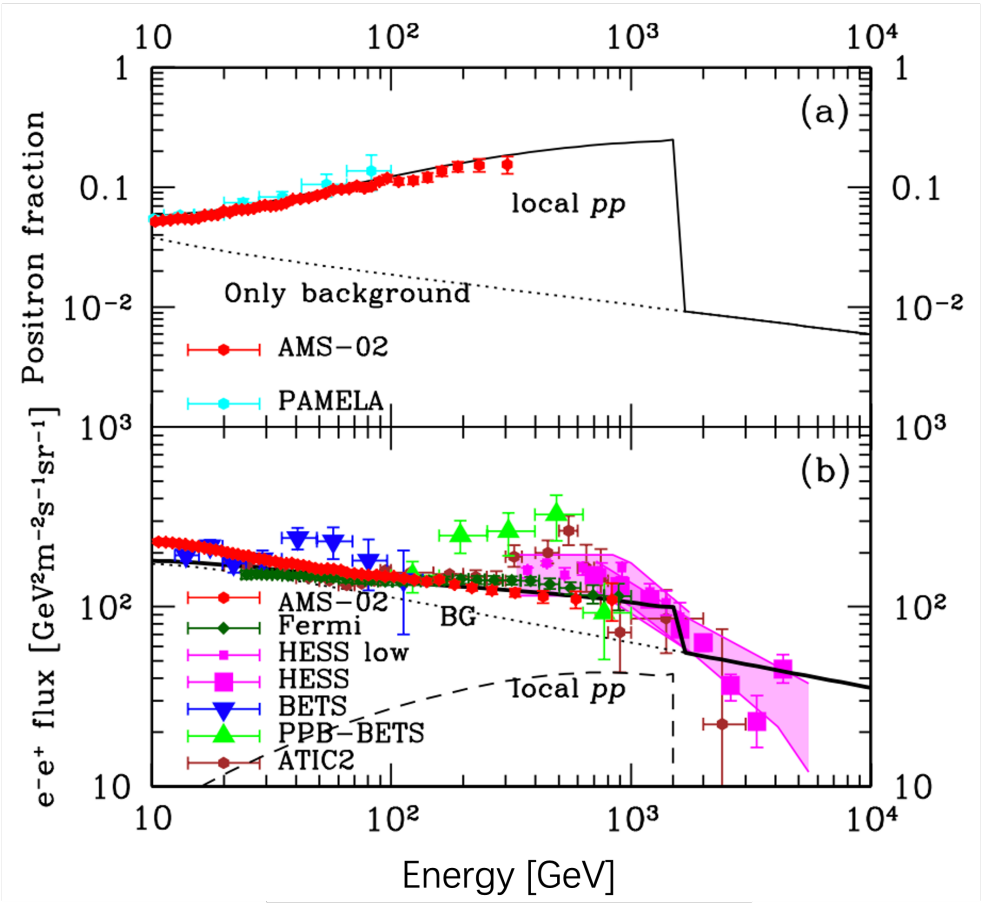

Figure 5.3: (a) Positron fraction spectrum. The solid line represents the contribution from the DC and the background. (b) The all-electron spectrum. The solid line includes electrons and positrons from both the secondaries produced by in DC (dashed line) and the background (dotted line). The data are collected from Fermi, H.E.S.S., BETS, PPB-BETS, and ATIC (Kohri et al., 2016)

Asano et al. (2022) shares the similar opinion that the anomaly observed in the positron fraction can be attributed to proton collisions with the DC. However, the 1 TeV break observed in the cosmic-ray all-electron spectrum may be attributed to an extraordinary event with a very hard injection index of 1.5 and energy released as electrons greater than 10^{49} *erg*. The particles should have been released approximately 400 kyr ago, and the rate of such events should be lower than that of typical supernovae. Based on the low rate, it is suggested that the event may have been a type Ibc supernova or a hypernova.

5.2.2 SNRs+Pulsars

The maximum energy that electrons can attain in the SNR is constrained by the age of the SNR, synchrotron losses, or the size of the acceleration site (Sturner et al., 1997; Reynolds,

1996; Serpico, 2012). Furthermore, the radio and X-ray spectra of observed SNRs suggest that the electron spectrum follows a power law with a cutoff (Reynolds and Keohane, 1999; Hendrick and Reynolds, 2001):

$$Q\left(E\right) = Q_0 \left(\frac{E}{E_0}\right)^{-\gamma} \exp\left(-\frac{E}{E_c}\right) \tag{5.6}$$

where E_c is the cutoff energy, which is expected to be in the TeV range (Atoyan and Aharonian, 1996), Q_0 the normalization factor, γ the power-law index.

In Mauro et al. (2014), the source spectrum of pulsar $Q\left(E\right)$ is assumed to have the same form as SNRs (Equation 5.6) and E_c is fixed to be 2 TeV for both SNRs and PNWs to compute the all-electron flux. The total spin-down energy W_0 of a pulsar as shown in the Equation 5.8 can be used to fix the value of Q_0 (Blasi and Amato, 2010) via Equation 5.7:

$$\int_{E_{min}}^{\infty} EQ\left(E\right) dE = \eta W_0 \tag{5.7}$$

$$W_0 \approx \tau_0 \dot{E} \left(1 + \frac{t_*}{\tau_0}\right)^2 \tag{5.8}$$

Where $\dot{E}$ is the spin-down luminosity, t_* the present age of the pulsar and τ_0 is the typical decay time of the pulsar. Where E_{min} is fixed to be 0.1GeV; $\dot{E}$ and t_* can be found in the pulsar ATNF catalog (Taylor et al., 1993).

The investigation described in Mauro et al. (2014) used four observables, namely $e^+ + e^-$, e^-, e^+, and $e^+/(e^+ + e^-)$, to explore whether a single source model or a combination of sources could account for the AMS-02 data. To fit the observed data across the entire energy range, different components were taken into account. SNRs are the main contributors to the all-electron spectrum $(e^+ + e^-)$, serving as the primary accelerators. This aligns with the "standard model" mentioned earlier. In the paper (Mauro et al., 2014), the SNRs are divided into two components: those within a distance of $d \leq 3$ kpc from Earth are classified as the *local component*, while the rest are regarded as the *far component*. In addition to SNRs, secondary particles and Pulsar Wind Nebulae (PWNe) are also used to fit the spectra. Further details are listed below:

- For the *local component*, the sources were treated as independent and the typical parameters were individually fixed (refer to Mauro et al. (2014) for parameter values).
- For the *far component*, the sources were assumed to be an average source and the typical parameters Q_0 and γ were set as free parameters.
- The secondary positrons and electrons from primary proton and helium collisions, based on the AMS-02 measurement (Haino and AMS-02 Collaboration, 2013), were included and all parameters were fixed.

- The electrons and positrons from PWNe were considered as individual sources. The simplifying hypothesis of setting γ_{PWN} and η to be the same values was adopted, and these parameters were set as free parameters.

In addition to the free parameters Q_0, γ, γ_{PWN}, and η, the modeling approach in Mauro et al. (2014) also involved setting two other parameters as free, namely an overall normalization factor $\tilde{q}_{sec}$ and a factor for the solar modulation potential ϕ (for low energy data).

The analysis presented in Figure. 5.4 demonstrates that in order to simultaneously reconstruct the four observables, the four source components must contribute distinct properties of the spectra. Specifically, at low energies, the all-electron spectrum (for energies less than 100 GeV) is dominated by the SNRs in the *far component*, while the positron spectrum and positron fraction spectrum (for energies less than 20 GeV) are primarily shaped by secondary positrons. At high energies, the 1 TeV break of the all-electron spectrum is determined by the SNRs in the *local component*, and PWNe are the most relevant source for the positron spectrum and the rising of the positron fraction spectrum. The best fit values for the parameters were found to be highly reasonable.

According to Fang et al. (2018), the **SNRs + Pulsars** scenario is further supported by data from DAMPE. The TeV break observed in the all-electron data is attributed to the combined contribution of several nearby SNRs or a single SNR, such as Monogem Ring or Loop I. Additionally, the rising positron fraction is attributed to the presence of a pulsar, such as PSR J0940-5428 or Geminga.

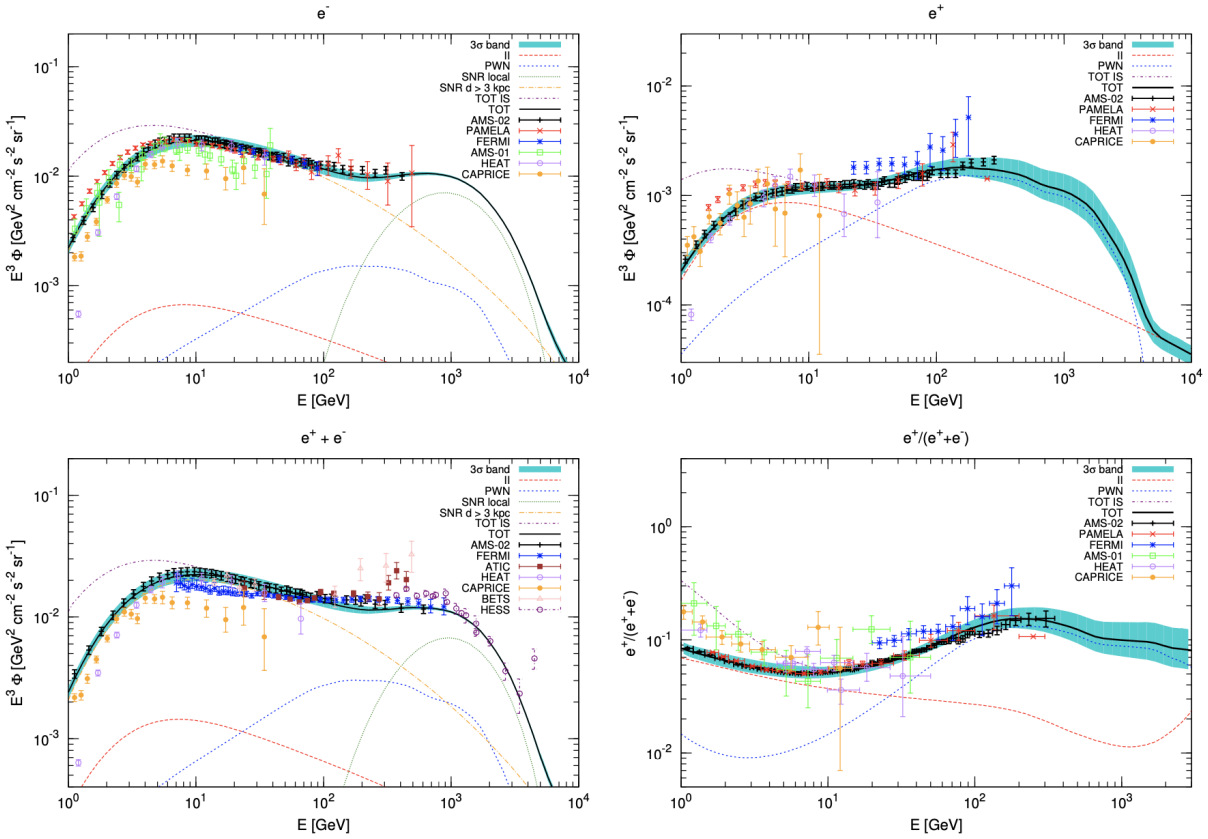

Figure 5.4: The figure shows the electron flux (top left), positron flux (top right), all-electron flux (bottom left), and positron fraction (bottom right) fitted with different components. The *far component* is depicted with a dot-dashed yellow line, the *local component* with a dotted green line, the secondary component of electron and positron with a long dashed red line, and the contribution from PWNe with a short dashed blue line. The data from AMS-02, *Fermi*-LAT, PAMELA, HEAT, CAPRICE, BETS, and H.E.S.S. are used, as shown in the legend. The black solid line represents the best-fit result within its 3σ confidence interval (Mauro et al., 2014).

5.2.3 Pulsars+Pulsars

Some models suggest that pulsars are not only responsible for the increase in the positron fraction with energy, but they also determine the shape of the all-electron spectrum. These models propose that although SNRs account for more than 50% of the all-electron flux as a background (typically calculated using GALPROP code), the break at 1 TeV and the rising positron fraction spectrum are caused by a single nearby pulsar or multiple pulsars that appear above the background and are suppressed at high energy.

Single Pulsar: As pointed out by Linden and Profumo (2013), the positron data from AMS-02 can be fitted by a single nearby pulsar together with the best-fit diffuse cosmic-ray

background model. The contribution from the pulsar is considered as a point-like and burst-like source (Shen, 1970; Panov, 2013). Linden and Profumo (2013) specifically studied the Geminga and Monogem pulsars, both of which are among the most luminous nearby pulsars within the appropriate age and distance range. According to observations, the age and distance of Geminga are set to be 3.42×10^5 years and 0.15 kpc, respectively, while for Monogem, these parameters are set to be 1.11×10^5 years and 0.29 kpc, respectively. Here the time that the electrons and positrons were trapped in the nebula is neglected compared to the age of the pulsars (Profumo, 2012).

To fit the data, the cutoff energy for both pulsars is set to be $E_{cut} = 2$ TeV. The spectral index is set to be $\gamma = 1.9$ for Geminga and $\gamma = 1.95$ for Monogem. The fitting requires a total energy output of $\eta W_0 = 2 \times 10^{49}$ erg for Geminga and $\eta W_0 = 8.6 \times 10^{48}$ erg for Monogem, which are compatible with the expected value for a mature pulsar $5 \times 10^{48} \lesssim W_0/\mathrm{erg} \lesssim 5 \times 10^{50}$ (Malyshev et al., 2009; Delahaye et al., 2010). The pulsar component is combined with the Galactic diffuse background adopted from the GALPROP model, which is assumed to be 20% smaller for additional sources. Figure 5.5 illustrates the model fitted with the positron fraction data from AMS-02 on the left and the all-electron spectrum with data from *Fermi*-LAT and H.E.S.S. on the right.

The positron fraction data can be fitted very well for each of the pulsars. However, in the single pulsar scenario, an anisotropy is expected to be present in the cosmic-ray all-electron spectrum. Based on estimations in the article of Linden and Profumo (2013), detecting the anisotropy produced by Monogem would require a few thousand hours of H.E.S.S. data, while CTA would be needed to detect the anisotropy induced by Geminga. In fact, the cosmic-ray all-electron spectrum as shown in the right panel of Figure 5.5 already suggests a preference for the Monogem pulsar before considering the anisotropy.

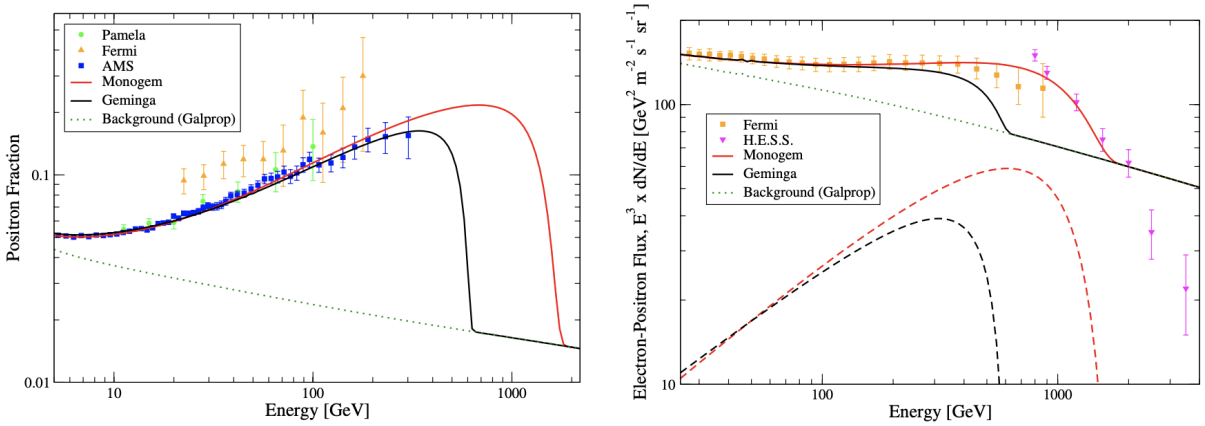

Figure 5.5: Left: The positron fraction spectrum fitted with data from AMS-02, PAMELA, and *Fermi*-LAT is shown, along with the diffused all-electron background from the *Galprop* model in green dotted line. The positron fraction, including the contributions from Geminga (black solid line) and Monogem (red solid line), is also displayed. Right: The all-electron spectrum fitted with data from *Fermi*-LAT and H.E.S.S. is shown, along with the diffused electron and positron background from the same *Galprop* model in green dotted line. The contribution from Monogem is represented by the dashed red line, while the dashed black line represents the contribution from Geminga. The combination of the diffuse background and individual pulsars are shown in red solid line for Monogem and black solid line for Geminga. The diffuse background was not tuned to fit the high-energy data (Linden and Profumo, 2013).

Multiple Pulsars

Another scenario involving pulsars is that the rising positron fraction spectrum, as well as the 1 TeV break in the all-electron spectrum, can be explained by the contribution from multiple pulsars. Using the method proposed in Grasso and et al. (2009), Yin et al. (2013) calculated the combined contribution from 177 pulsars in the ATNF catalogue (Manchester et al., 2005) that satisfied the following conditions: d <3 kpc and $5 \times 10^4 <$ T(yr) $< 10^7$. The energy spectrum of the point-like and burst-like pulsar is parameterized as the Equation 5.9:

$$Q\left(E, r, t\right) = Q_0 E^{-\alpha} \exp\left(-E/E_{cut}\right) \delta\left(r - r_0\right) \delta\left(t - t_0\right) \tag{5.9}$$

Where Q_0 is the normalization parameter, α the spectral index, E_{cut} the cutoff energy.

Each pulsar is assigned random parameters within the following ranges: $700 \leq \mathrm{E}_{cut}$ (GeV) ≤ 3000, $1.5 \leq \alpha \leq 2.3$, and $5\% \leq \eta_{e^\pm} \leq 30\%$, where $\eta_{e^\pm}$ is the fraction of energy converted from rotational energy into electrons and positrons. The overall contribution from the 177 pulsars is fitted to both the positron fraction and all-electron data. As shown in Figure 5.6, the rising feature of the positron fraction spectrum and the 1 TeV break in the all-electron spectrum can be explained by the overall contribution of the 177 pulsars.

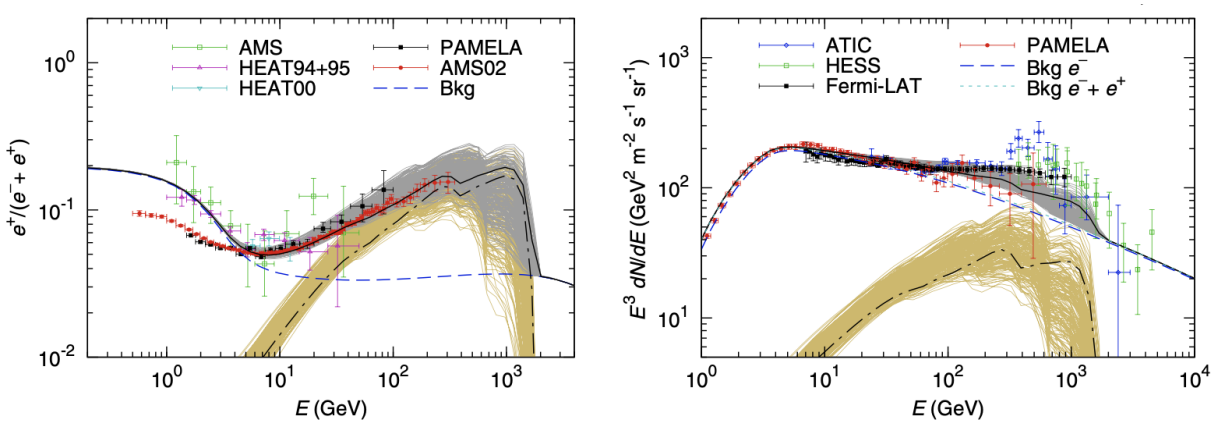

Figure 5.6: The positron fraction (left) and all-electron data (right) are fitted with 117 nearby pulsars in the ATNF catalogue, using the criteria mentioned in the text. The contribution from 177 pulsars is shown in golden lines, where each line represents a combination of randomly assigned parameters, and a representative combination is illustrated in the dot-dashed black line. The background contribution is shown in blue dashed line, and the total contribution is shown in grey lines, with a representative combination illustrated in the solid black line (Yin et al., 2013).

5.2.4 Dark Matter

The anomaly in the positron fraction has sparked numerous discussions regarding the dark matter scenario. The most widely accepted explanation involves WIMP annihilation accounting for the rise in the positron fraction above 10 GeV. Several dark matter annihilation channels have been proposed, including annihilation into quarks, bosons, and leptons as final states. However, these channels face various challenges.

In the hadronic channels, the annihilation cross section $\langle \sigma v \rangle$ is on the order of 10^{-22} to 10^{-21}, which is several orders of magnitude higher than the value of $3\times\ 10^{-26}$ cm^3 s^{-1} suggested by cosmology for the WIMP annihilation cross section, hence requiring a boost factor of the order of 10^4 (Boudaud et al., 2015). Leptons, which have a smaller annihilation cross section are the preferred candidates for dark matter annihilation. However, the annihilation into a single leptonic channel cannot provide a good fit to the positron fraction spectrum (Cholis and Hooper, 2013) and the all-electron spectrum from AMS-02 (Boudaud et al., 2015). The fit can be improved by considering a combination of channels; for example, dark matter can annihilate into a strong dominance of $\tau^+\tau^-$ channel and less than 20% of both e^+e^- and $\mu^+\mu^-$ channels (Cao et al., 2017). However, the large branching ratios into the $\tau^+\tau^-$ channel are inconsistent with the observation of γ rays from the dwarf spheroidal galaxies (Ackermann and et al., 2011; Evans et al., 2004; Geringer-Sameth and Koushiappas, 2011) and the Galactic center (Abramowski and et al., 2011; Abazajian and Harding, 2012; Hooper et al., 2013). Including quarks (Boudaud et al., 2015) or bosons (Cao et al., 2017) can further improve the fit, but the constraints from γ rays remain. Dark

matter annihilating into a pair of light scalars that decay into leptons (or charged pions) can provide a good fit and avoid the restrictions from above, but requires a boost factor on the order of 10^2 (Cholis and Hooper, 2013).

From the discussion above, it appears that the dark matter scenario is disfavored for several reasons, including the large required annihilation cross section and strong constraints from γ-ray observations. However, an "excess" of antiproton fraction (Aguilar and et al., 2016a) observed by AMS-02 support the dark matter scenario or the SNR scenario. This is because the pulsar scenario cannot produce antiprotons. To further distinguish between the dark matter and astrophysical source origin, more accurate transport parameters and larger statistics of high energy positron and electron measurements are needed. As pointed out by Boudaud et al. (2015), propagation uncertainties can introduce larger errors when fitting the parameters. Additionally, the sharpness of the cutoff or the trend of the positron spectrum and anisotropy study of all-electron spectrum may help identify the origin of the high-energy particles.

5.3 Models Compared with MAGIC Data

The models presented above are compared to the MAGIC data, as illustrated in Figure 5.7. Each model's name refers to the primary source responsible for shaping the energy break at approximately 1 TeV in the spectrum. The SNR models, depicted by dashed lines, include "Local pp", which represents the energy break caused by secondaries produced by the SNR in DCs, and "Local SNR", which denotes the energy break caused by a nearby SNR. The Pulsar models, displayed with solid lines, consist of "Multiple Pulsars", which suggests that the break is caused by multiple pulsars; "A Pulsar-like Source", which indicates an unknown pulsar-like source as the cause; and "Monogem Pulsar", which attributes the break to the Monogem pulsar. In addition to these "advanced models", the "Standard Model" is also plotted with dotted line.

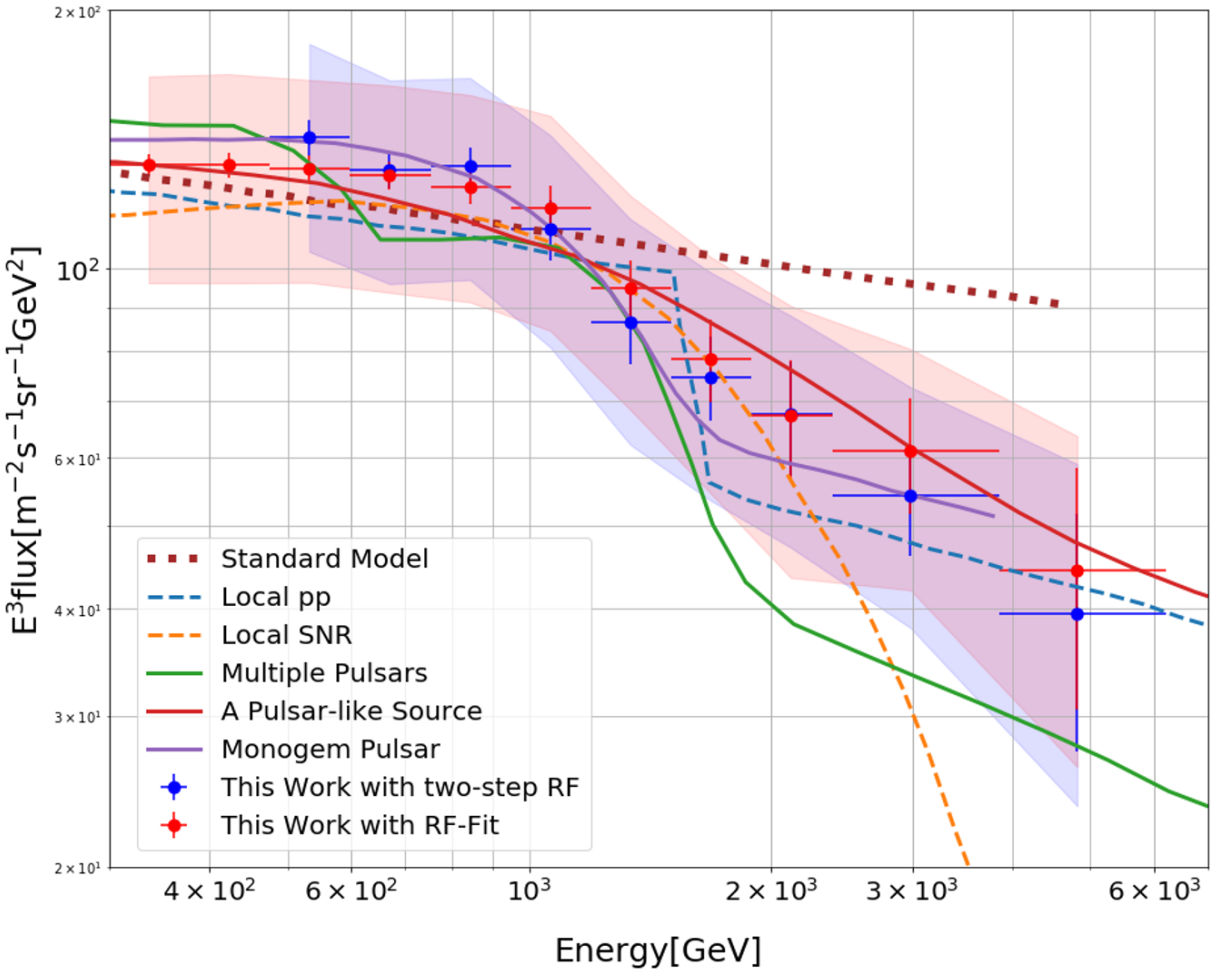

Figure 5.7: Cosmic-ray all-electron spectrum comparison between MAGIC data and the models discussed above. The "Standard Model" Grasso and et al. (2009) is shown by the dotted brown line. The "Local pp" model (Kohri et al., 2016) is represented by the dashed blue line, the "Local SNR" model (Mauro et al., 2014) by the dashed orange line, the "Multiple Pulsars" model (Yin et al., 2013) by the solid green line, the "A Pulsar-like Source" model (Yin et al., 2013) by the solid red line, and the "Monogem Pulsar" model (Linden and Profumo, 2013) by the solid purple line.

The "Standard Model" is ruled out by the MAGIC data as it is inconsistent for energies larger than 1 TeV. All the "advanced models" align with the MAGIC data within the uncertainty band before the 1 TeV break. However, the "Multiple Pulsars" model and the "Local SNR" model do not match the MAGIC data after the break due to their extremely soft spectral indices. It is not possible to differentiate between the "Local pp" model, "A Pulsar-like Source" model, and the "Monogem Pulsar" model, given the large systematic errors. Nevertheless, the "Local pp" model, which predicts a sharper and higher spectral break, does not fit the data very well. Conversely, the single pulsar models - the "A

Pulsar-like Source" model and the "Monogem Pulsar" model, with less sharp breaks, fit the MAGIC data better. The shape of the energy break is in better agreement with the "Monogem Pulsar" model.

Chapter 6

Conclusions

The cosmic-ray all-electron spectrum in the TeV range offers a unique opportunity to examine local sources in our Galaxy. IACTs have the ability to gather significant event statistics for high energy astronomy, owing to their large collection areas. The background events observed during γ-ray observations are considered as unwanted "noise" that must be discarded. However, these events contain a wealth of valuable data for cosmic-ray research. Extracting the valuable information from the background noise poses a challenge for IACTs, since the diffuse nature of CRs prevents an analysis treatment similar to the one adopted for γ rays.

In this study, I focused on exploring the possibility of using data collected by MAGIC, a system of two telescopes designed for the detection of γ-ray sources via the IACT technique, to perform diffuse cosmic-ray analysis. To achieve this goal, I developed and validated two analysis methods: the **RF-Fit** method and the **Two-Step RF** method to produce the cosmic-ray all-electron spectrum. The **RF-Fit** pipeline is based on a template fit method that fits the hadronness distribution of simulated hadrons and signal events to the hadronness distribution of the observation data. However, this method faces challenges due to the strong dependency of the hadronness on the zenith and azimuth distance distributions and the high demand for simulation statistics. To overcome these challenges, I developed a tracking MC simulation method in which the pointing FoVs precisely follow the same tracking as during real observations. The **Two-Step RF** pipeline is based on selecting training data with low hadronness for the second RF to optimize the separation between hadrons and signal events, which have very similar characteristics. The pipeline applies tight efficiency cuts to ensure that the signal events are as pure as possible, and estimates detailed contamination rates. Selecting specific events as training samples to separate events in a certain hadronness range is a novel method employed in MAGIC. This approach leads to an improvement in the hadronness estimation for low hadronness events, which makes it possible to reduce the contamination rate to a reasonable level by applying very tight efficiency cuts. A detailed examination of systematic uncertainties and robustness tests has been conducted for both methods. These two methods are complementary to each other, and produce consistent cosmic-ray all-electron spectra.

The cosmic-ray all-electron spectra produced by the two methods can be described by a broken power-law within the 300 GeV to 6 TeV energy range, confirming an energy break around 900 GeV by MAGIC for the first time. Below 900 GeV, a spectral index of approximately -3 is observed, while above this energy, the spectral index is around -3.7 for both analysis methods. These results are in agreement with those of previous experiments within the observed energy range. However, the systematic uncertainties are too large to differentiate between the data points obtained by AMS-02 and *Fermi*-LAT in the energy range of a few hundred GeV. The fluxes of electrons and positrons appear to be consistent across different pointing directions and energy ranges, as inferred from FoVs used in this study.

In order to find the possible sources for the TeV electrons and positrons, I reviewed several models and compared different SNR and pulsar models with the MAGIC data in Chapter 5. Considering the predicted spectrum before and after the break energy as well as the sharpness of the break, MAGIC favors the model where the broken power-law spectrum originates from a Monogem pulsar that appears above the background and is suppressed at high energy. The Monogem pulsar with the cutoff energy E_{cut} = 2 TeV, the injection spectral index γ = 1.95, the age 1.11×10^5 years and distance 0.29 kpc with the best-fit value of the total energy output $\eta W_0 = 8.6 \times 10^{48}$ erg (Linden and Profumo, 2013) can explain the MAGIC data. This Monogem scenario can also explain the rising of positron fraction spectrum for above 10 GeV.

The 1 TeV break in the all-electron spectrum and the upturn in the positron fraction spectrum disfavor the dark matter scenario. This is because dark matter scenarios are constrained by γ-ray observations, and the benchmark values for the WIMP annihilation cross section and density are too small to explain the observed excess of positrons. Furthermore, astrophysical sources can account for the observed spectral features. However, an "excess" of antiproton fraction (Aguilar and et al., 2016a) and the identical behavior of positron and antiproton spectrum observed by AMS-02 favors the dark matter scenario or the SNR scenario, since the pulsar scenario cannot produce antiproton. To further distinguish between the dark matter and the pulsar scenarios, the sharpness of the cutoff or the trend of the positron spectrum can play an important role. In the case of dark matter origin, we would expect a sharper cutoff. Furthermore, if the spectrum continues to rise at higher energy ranges, the pulsar scenario can be ruled out, as proposed by Boudaud et al. (2015). Additionally, an anisotropy study of the all-electron spectrum can also contribute to this distinction. In a scenario involving a single pulsar, anisotropy would manifest in the all-electron spectrum. Based on the estimation in Linden and Profumo (2013), identifying the anisotropy generated by Monogem several thousand hours of data observed by IACTs would be needed.

To fully understand the source of cosmic-ray all-electron spectrum in the TeV ranges, as

well as the upturn of positron fraction spectrum, data with greater statistics and reduced uncertainties are needed. This is especially true for the higher energy ranges of the positron spectrum and the TeV ranges of the all-electron spectrum from different directions. The forthcoming CTA, which improves over its predecessor experiments in terms of sensitivity, angular resolution, and energy range coverage, is expected to significantly contribute to anisotropy studies and the all-electron spectrum in the TeV ranges in the future. The work presented in this thesis, particularly the two background rejection methods, the calculation of systematic uncertainties, and the dedicated tracking MC simulation method, provides valuable insights into background estimation and reduction for cosmic-ray research with future IACTs.

Appendix A

RF-Input Parameters

A.1 List of RF-Input Parameters

Size_1: 0.025+(0.05∗floor(log10(MHillas_1.fSize)/0.05))
Size_2: 0.025+(0.05∗floor(log10(MHillas_2.fSize)/0.05))
Width_1: MHillas_1.fWidth
Width_2: MHillas_2.fWidth
Length_1: MHillas_1.fLength
Length_2: MHillas_2.fLength
Impact_1: MStereoPar.fM1Impact
Impact_2: MStereoPar.fM2Impact
MaxHeight: MStereoPar.fMaxHeight
TGradient_1: sqrt(MHillasTimeFit_1.fP1Grad∗MHillasTimeFit_1.fP1Grad)
TGraident_2: sqrt(MHillasTimeFit_2.fP1Grad∗MHillasTimeFit_2.fP1Grad)
RMSTime_1: MHillasTime_1.fRMSTime
RNSTime_2: MHillasTime_2.fRMSTime
Incoiming: $(\text{MStereoPar.fDirectionX}*0.00337)^2+(\text{MStereoPar.fDirectionY}*0.00337)^2$
Zenith: (0.5/30)+((1/30)∗floor(cos(MPointingPos_1.fZd∗0.0175/(1/30))))

A.2 Distribution of RF-Input Parameters

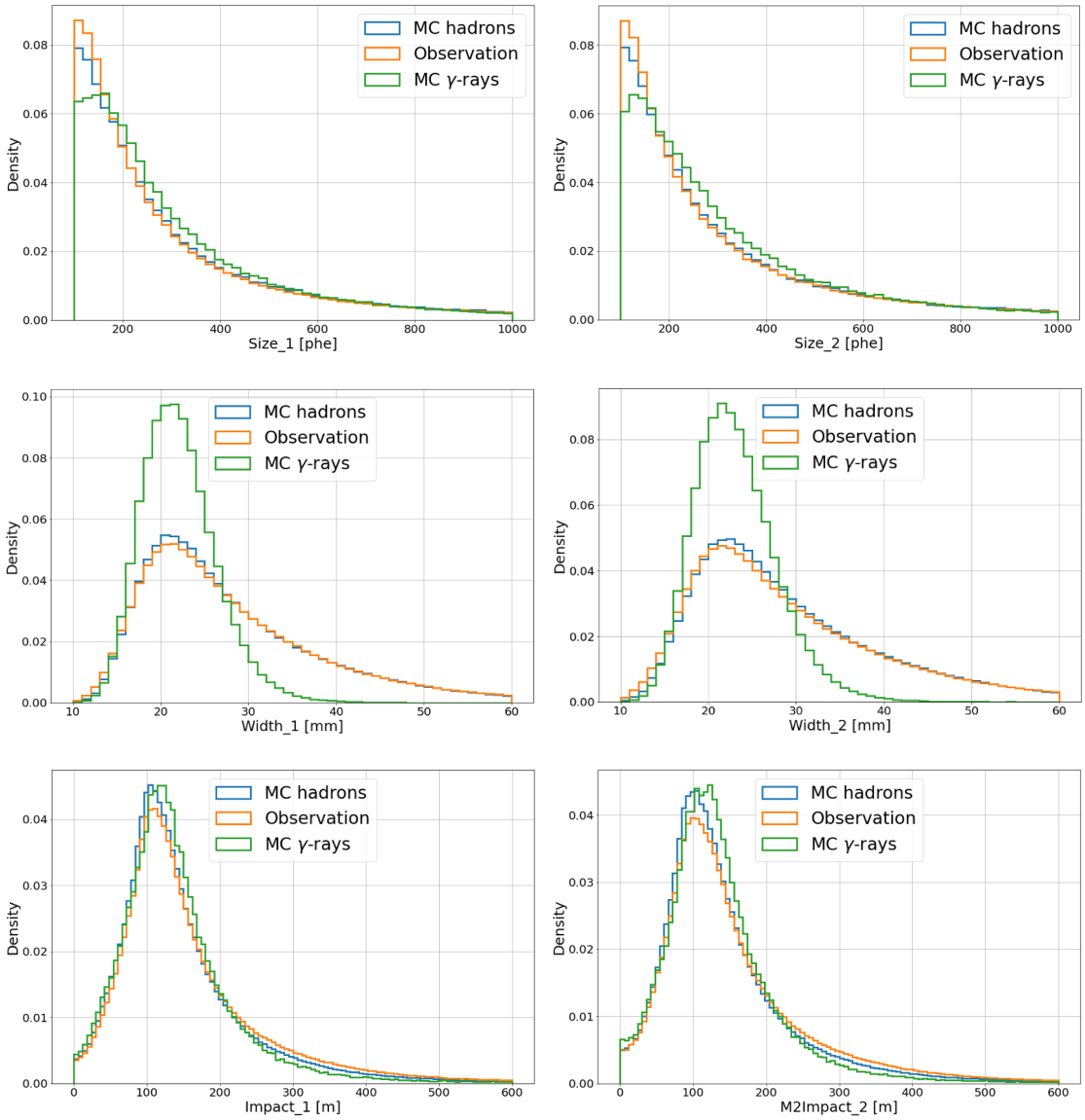

Figure A.1: The parameter distribution of MC hadrons, observation and MC γ-rays.

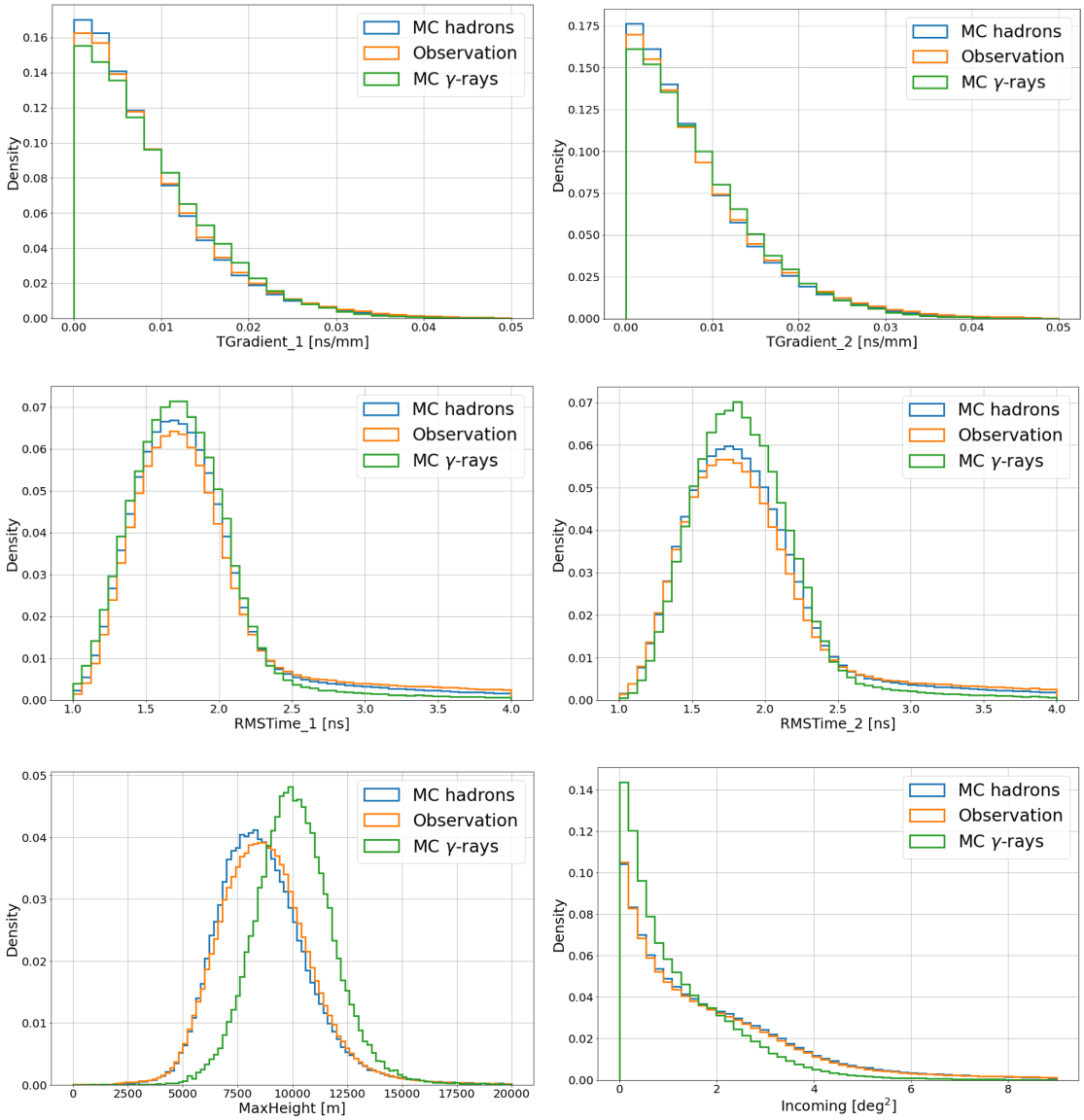

Figure A.1: The parameter distribution of MC hadrons, observation and MC γ-rays.

Appendix B

Hadronness Distribution of Proton and Helium

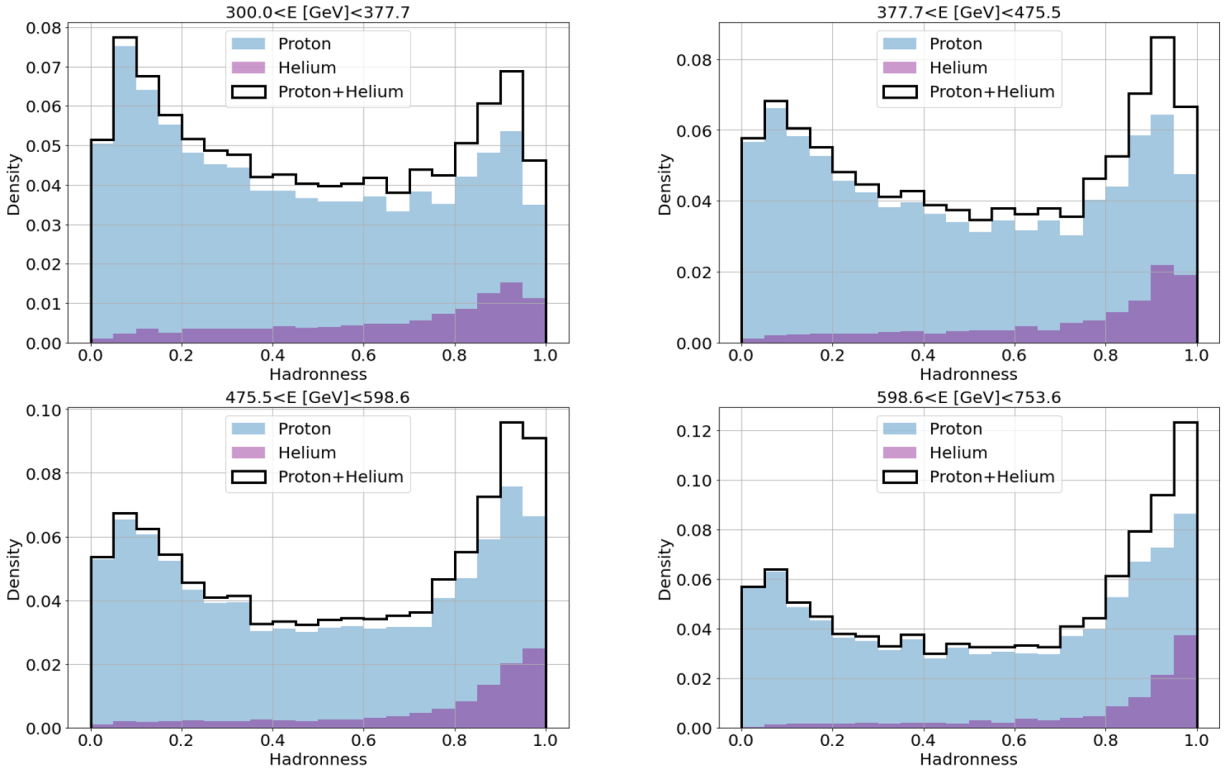

Figure B.1: The hadronness distribution of protons, helium, and their sum, after applying all event cuts and considering the same number of events for both components.

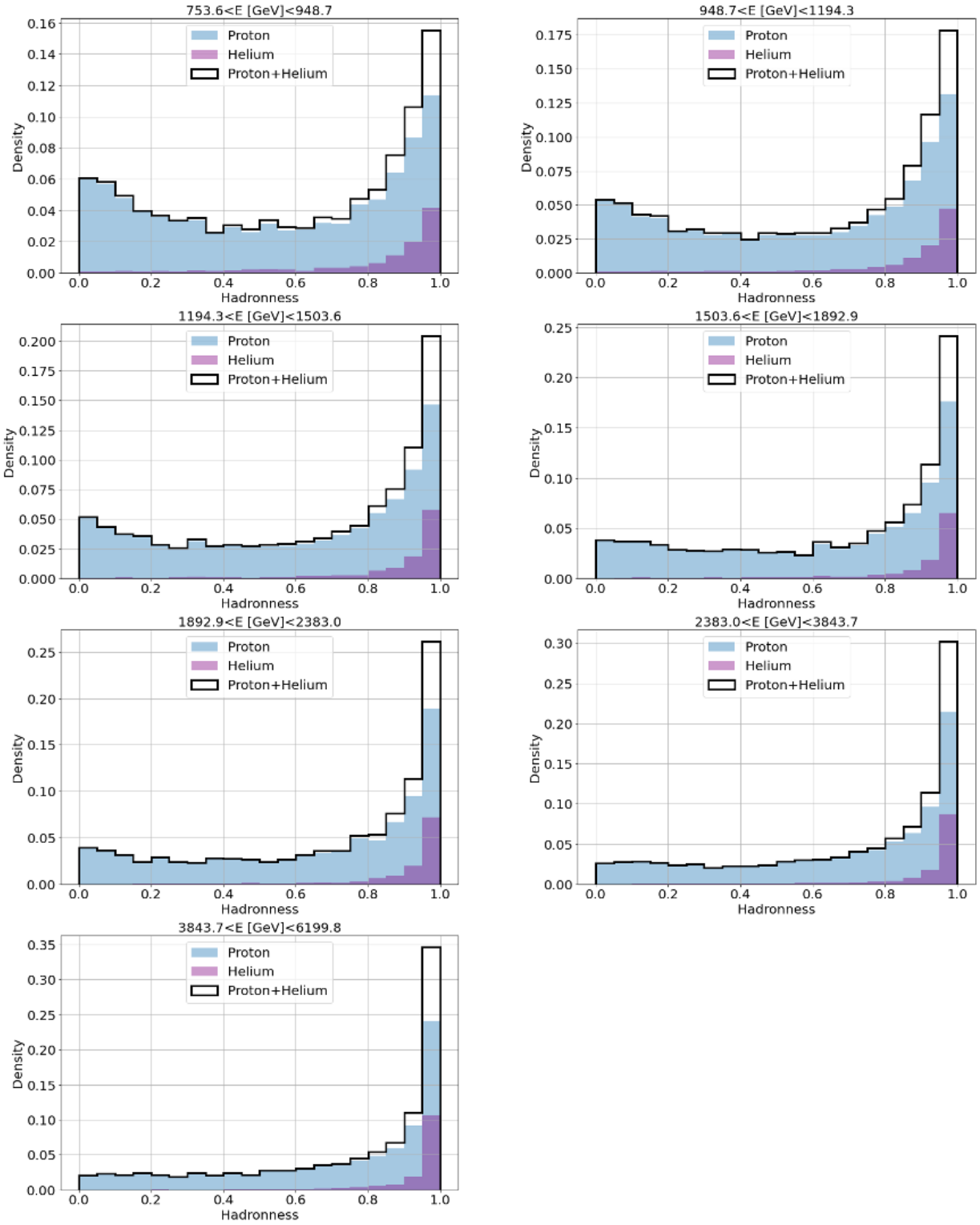

Figure B.1: The hadronness distribution of protons, helium, and their sum, after applying all event cuts and considering the same number of events for both components.

Appendix C

RF-Fit Template Fits

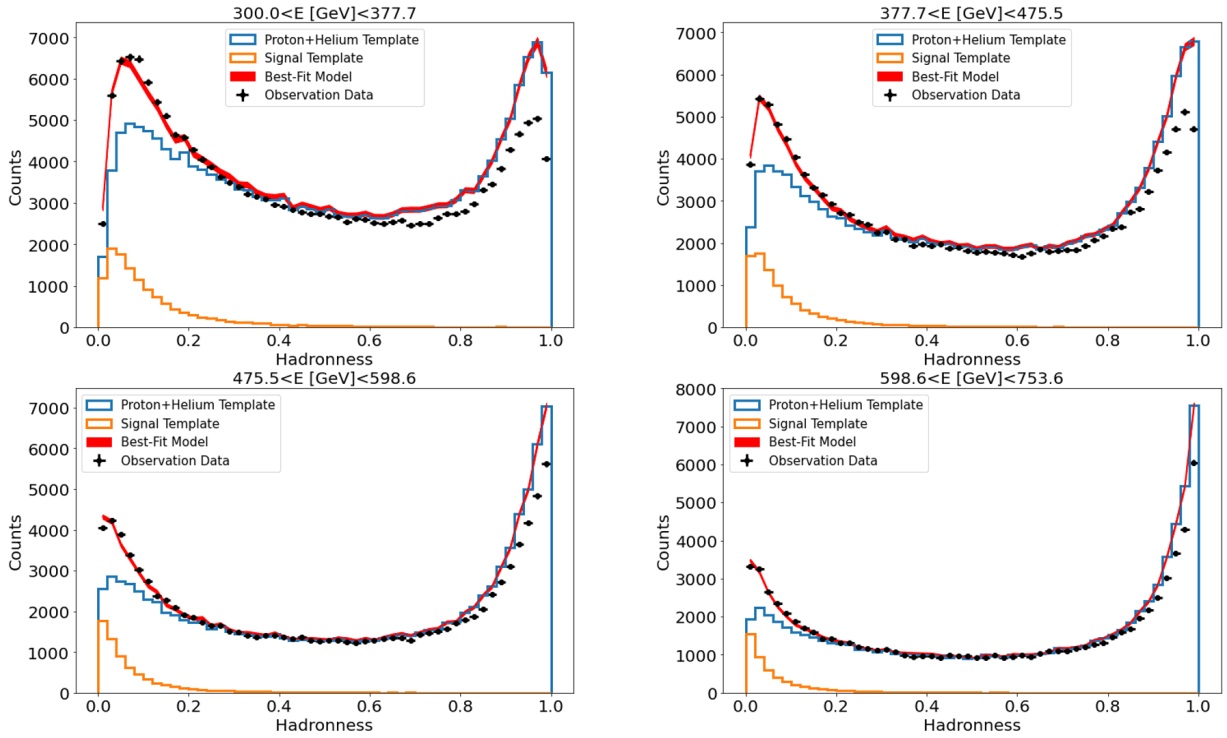

Figure C.1: The hadronness distribution of simulated protons plus gamma fitted with observation data. The shaded band is the best-fit model considering the contribution from electrons and protons at different energy bins.

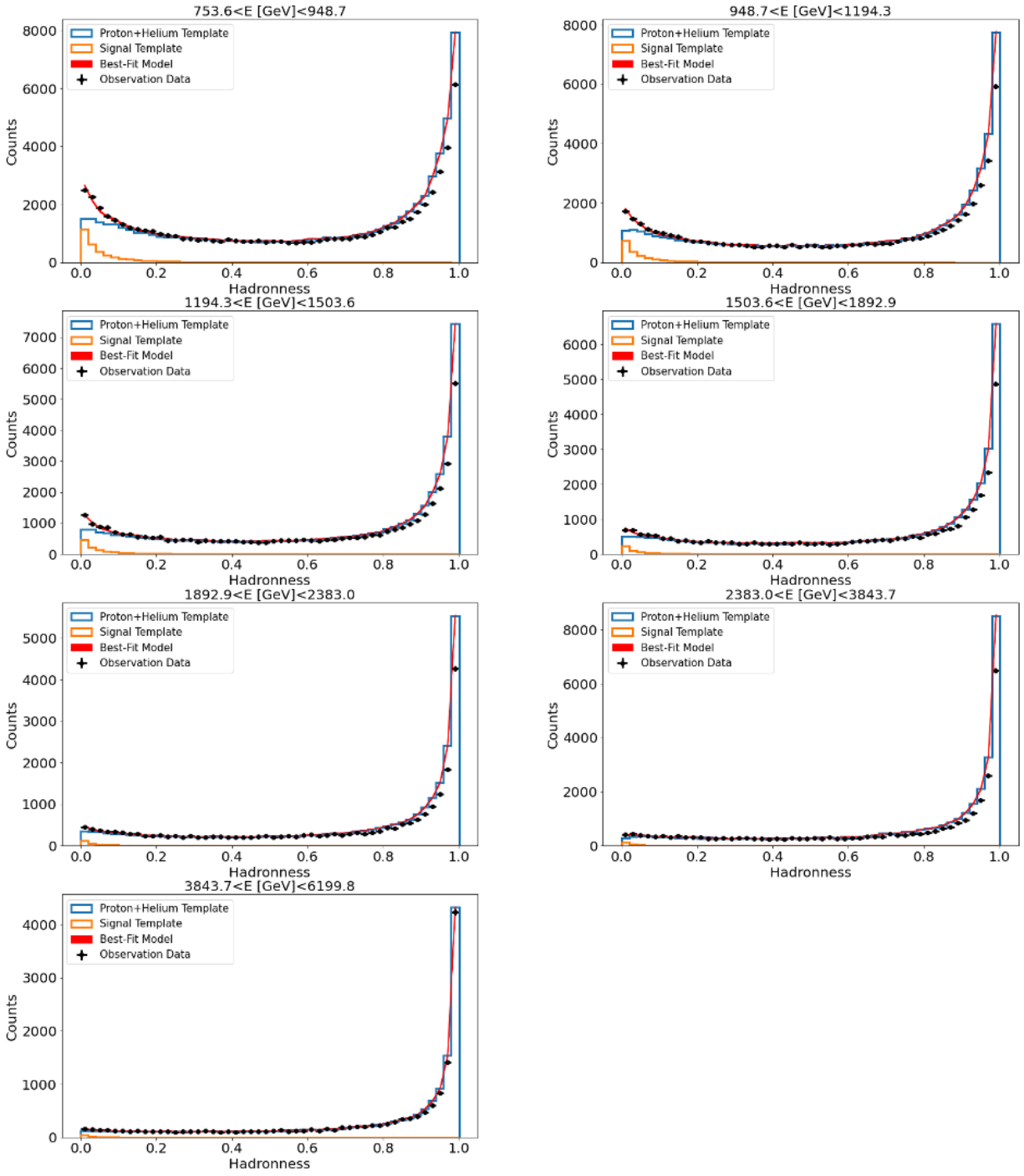

Figure C.1: The hadronness distribution of simulated protons plus gamma fitted with observation data. The shaded band is the best-fit model considering the contribution from electrons and protons at different energy bins.

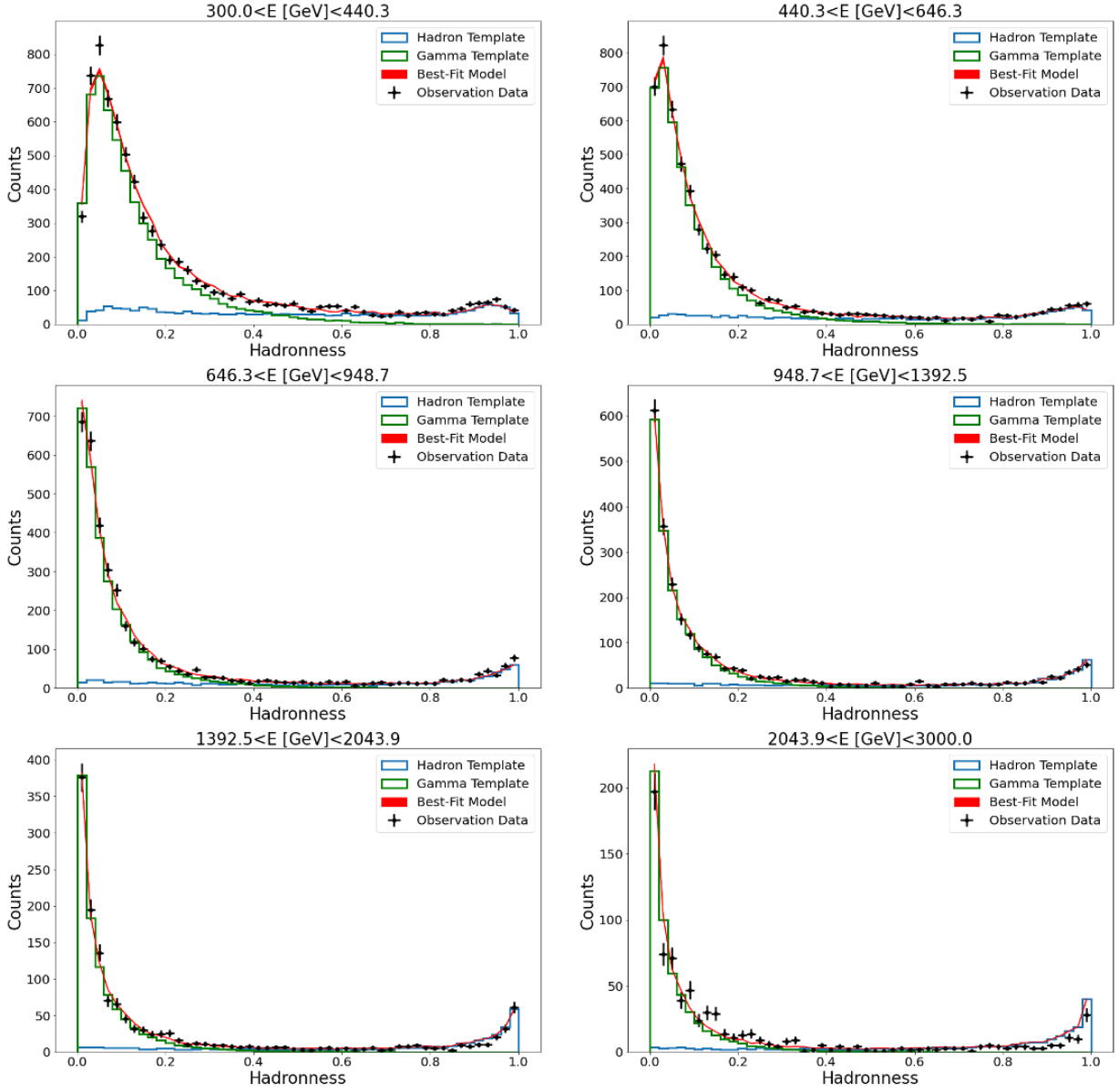

Figure C.2: The hadronness distribution of simulated protons plus gamma fitted with observation data. The shaded band is the best-fit model considering the contribution from electrons and protons at different energy bins.

Appendix D

Hadronness Efficiency Cuts

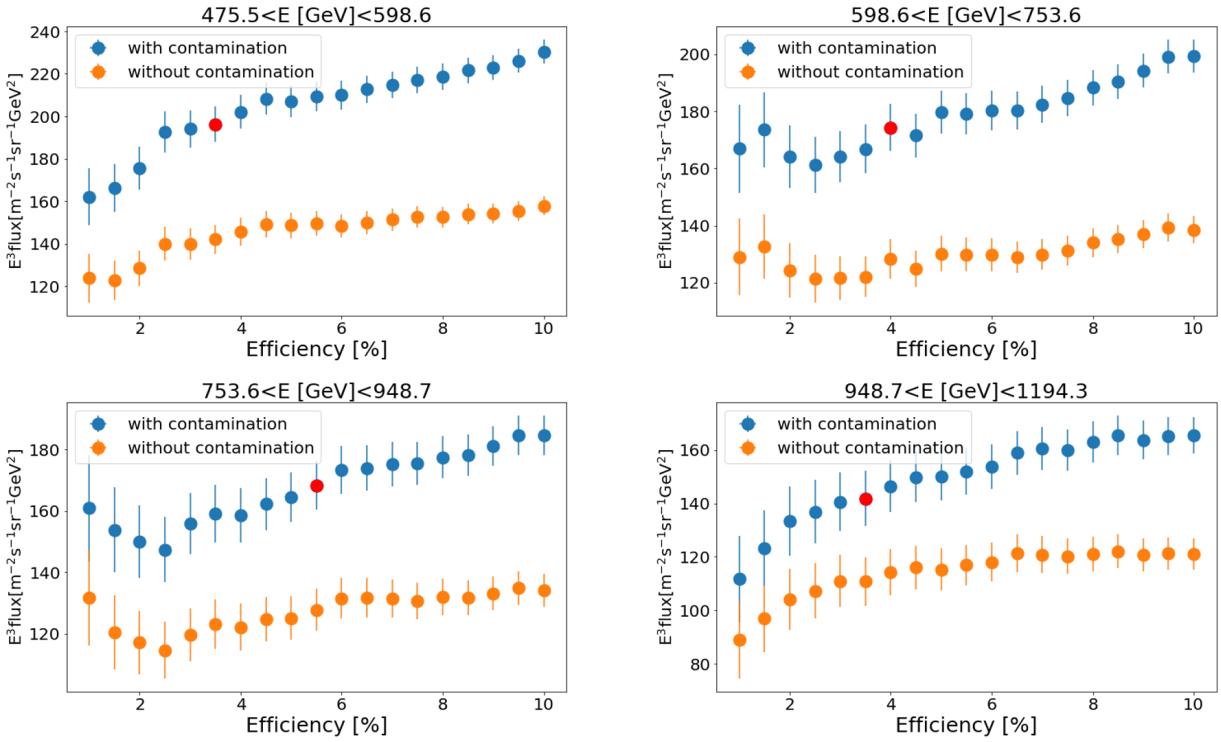

Figure D.1: The SED distribution varies with changes in the hadronness efficiency at different energy ranges. The efficiency cuts for each energy range are indicated in red.

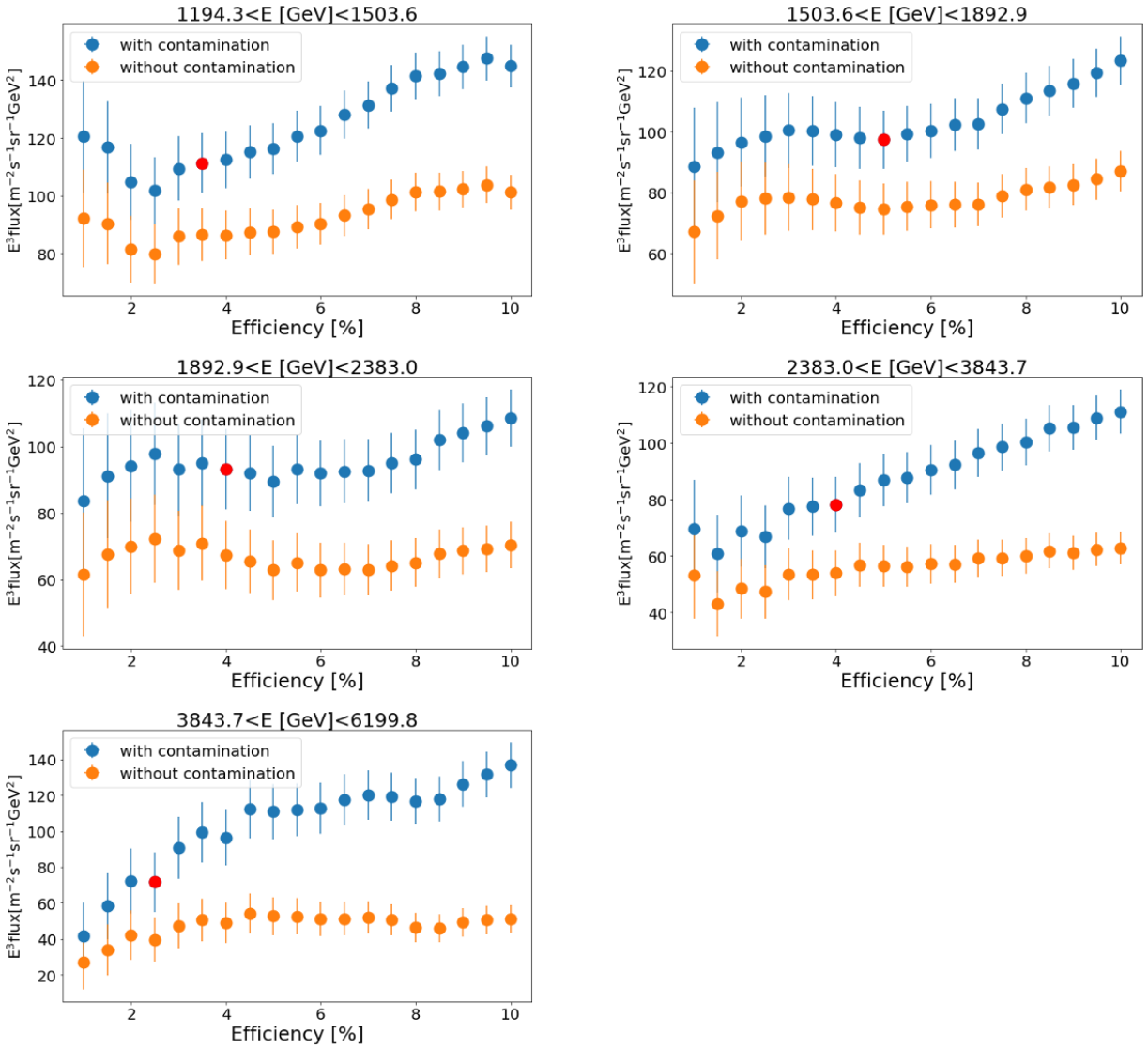

Figure D.1: The SED distribution varies with changes in the hadronness efficiency at different energy ranges. The efficiency cuts for each energy range are indicated in red.

Appendix E

Contamination Rates

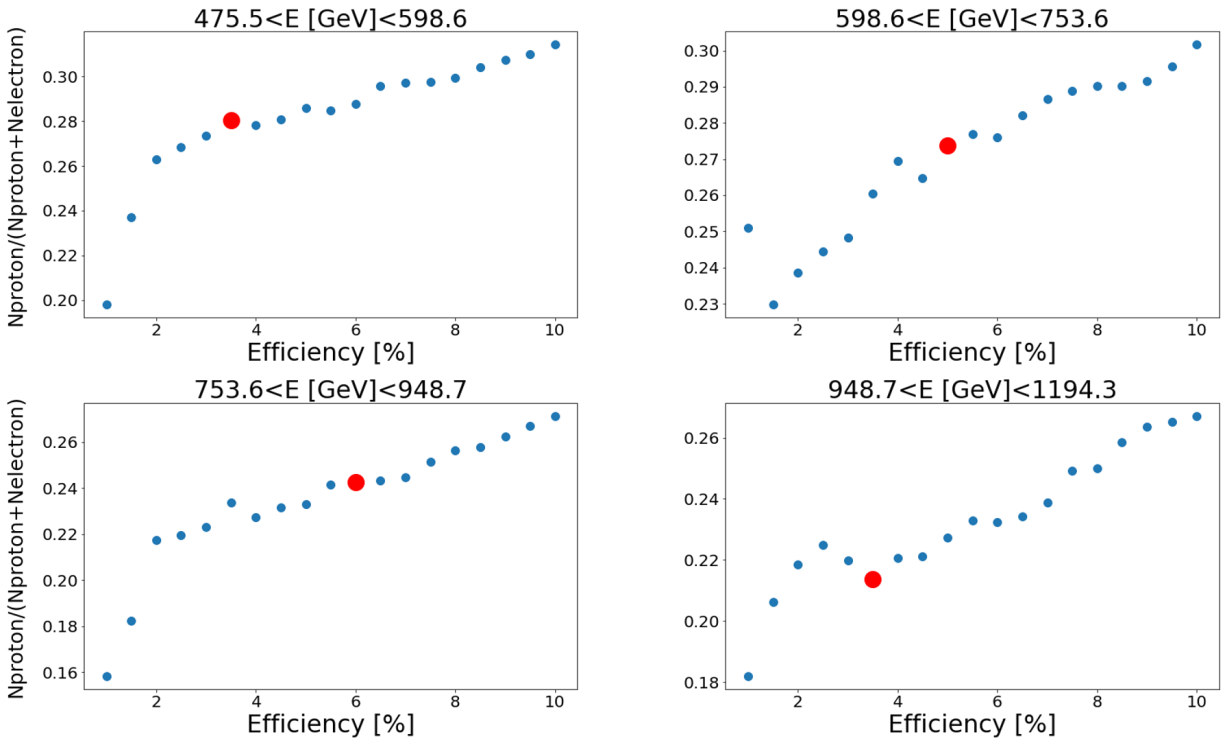

Figure E.1: The SED distribution varies with changes in the hadronness efficiency at different energy ranges. The efficiency cuts for each energy range are indicated in red.

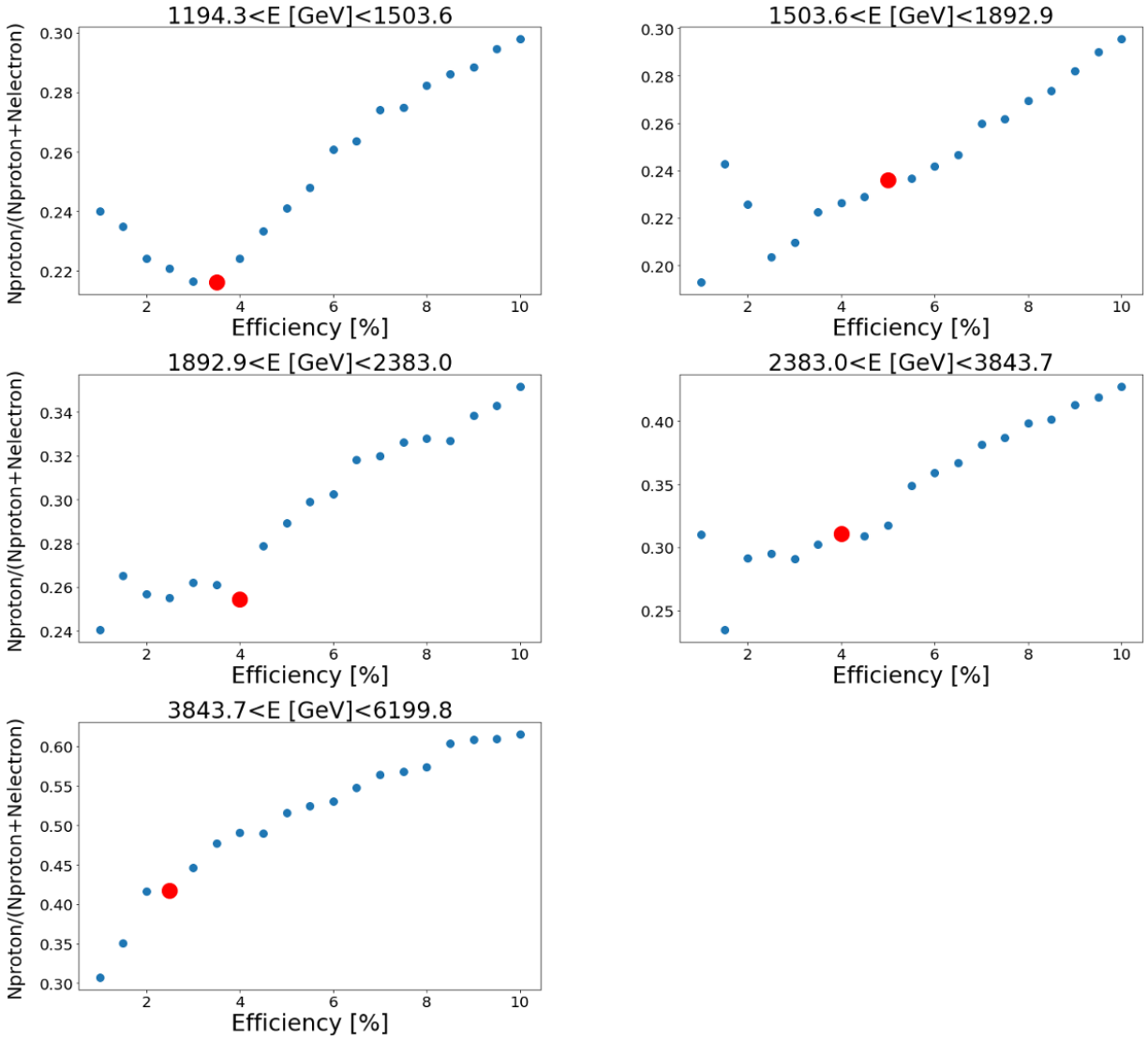

Figure E.1: The contamination rate contributed from protons varies with changes in the hadronness efficiency at different energy ranges. The contamination rates for the best cut positions for each energy range are indicated in red.

List of Abbreviations

ADC analog-to-digital converter

CORSIKA Cosmic Ray Simulations for KASCADE

CR Cosmic Ray

CoG Center of Gravity

CTA Cherenkov Telescope Array

DC Dense Gas Cloud

DGE Diffuse Galactic Emission

DRS4 Domino Ring Sampler 4

DSA Diffusive Shock Acceleration

EAS Extensive Air Shower

FoV Field of View

IACT Imaging Atmospheric Cherenkov Technique

IACTs Imaging Atmospheric Cherenkov Telescopes

IGRB Isotropic Gamma-Ray Background

ISM Interstellar Medium

ISRF Interstellar Radiation Field

LIDAR Light Detection and Ranging

LUT Look-Up Table

MC Monte-Carlo

NSB Night Sky Background

PSF Point Spread Function

PMT Photo Multiplier Tube

PWN Pulsar Wind Nebula

PWNe Pulsar Wind Nebulae

RF Random Forest

SNR Supernova Remnant

TS Test Statistic

WIMP Weakly Interacting Massive Particle

Bibliography

Aab, A. and et al. (2016). Evidence for a mixed mass composition at the 'ankle' in the cosmic-ray spectrum. *Physics Letters B*, 762:288–295. URL: https://doi.org/10.1016%2Fj.physletb.2016.09.039.

Abazajian, K. N. and Harding, J. P. (2012). Constraints on wimp and sommerfeld-enhanced dark matter annihilation from hess observations of the galactic center. *Journal of Cosmology and Astroparticle Physics*, 2012(01):041. URL: https://dx.doi.org/10.1088/1475-7516/2012/01/041.

Abdo, A. A. and et al. (2009). Measurement of the cosmic ray $e^+ + e^-$ spectrum from 20 gev to 1 tev with the fermi large area telescope. *Phys. Rev. Lett.*, 102:181101. URL: https://link.aps.org/doi/10.1103/PhysRevLett.102.181101.

Abdollahi, S., Ackermann, M., Ajello, M., Atwood, W., Baldini, L., Barbiellini, G., Bastieri, D., Bellazzini, R., Bloom, E., Bonino, R., and et al. (2017). Cosmic-ray electron-positron spectrum from 7 gev to 2 tev with the fermi large area telescope. *Physical Review D*, 95(8). URL: http://dx.doi.org/10.1103/PhysRevD.95.082007.

Abramowski, A., Aharonian, F., Ait Benkhali, F., Akhperjanian, A., Angüner, E., Backes, M., Balenderan, S., Balzer, A., Barnacka, A., Becherini, Y., and et al. (2014). Diffuse galactic gamma-ray emission with h.e.s.s. *Physical Review D*, 90(12). URL: http://dx.doi.org/10.1103/PhysRevD.90.122007.

Abramowski, A. and et al. (2011). Search for a dark matter annihilation signal from the galactic center halo with h.e.s.s. *Phys. Rev. Lett.*, 106:161301. URL: https://link.aps.org/doi/10.1103/PhysRevLett.106.161301.

Accardo, L. and et al. (2014). High statistics measurement of the positron fraction in primary cosmic rays of 0.5–500 gev with the alpha magnetic spectrometer on the international space station. *Phys. Rev. Lett.*, 113:121101. URL: https://link.aps.org/doi/10.1103/PhysRevLett.113.121101.

Acciari, V. A. and et al. (2020a). Detection of the geminga pulsar with MAGIC hints at a power-law tail emission beyond 15 GeV. *Astronomy & Astrophysics*, 643:L14. URL: https://doi.org/10.1051%2F0004-6361%2F202039131.

Acciari, V. A. and et al. (2020b). MAGIC very large zenith angle observations of the crab nebula up to 100 TeV. *Astronomy & Astrophysics*, 635:A158. URL: https://doi.org/10.1051%2F0004-6361%2F201936899.

Ackermann, M., Ajello, M., Albert, A., Atwood, W. B., Baldini, L., Ballet, J., Barbiellini, G., Bastieri, D., Bechtol, K., Bellazzini, R., and et al. (2015). The spectrum of isotropic diffuse gamma-ray emission between 100 mev and 820 gev. *The Astrophysical Journal*, 799(1):86. URL: http://dx.doi.org/10.1088/0004-637X/799/1/86.

Ackermann, M. and et al. (2011). Constraining dark matter models from a combined analysis of milky way satellites with the fermi large area telescope. *Phys. Rev. Lett.*, 107:241302. URL: https://link.aps.org/doi/10.1103/PhysRevLett.107.241302.

Adriani, O., B. G. B. G. e. a. (2009). An anomalous positron abundance in cosmic rays with energies 1.5–100 gev. *Nature*, 458(7238):607–609. URL: https://doi.org/10.1038/nature07942.

Adriani, O., Akaike, Y., Asano, K., Asaoka, Y., Bagliesi, M. G., Bigongiari, G., Binns, W. R., Bonechi, S., Bongi, M., Brogi, P., Buckley, J. H., Cannady, N., Castellini, G., Checchia, C., Cherry, M. L., Collazuol, G., Di Felice, V., Ebisawa, K., Fuke, H., and et al. (2017). Energy spectrum of cosmic-ray electron and positron from 10 gev to 3 tev observed with the calorimetric electron telescope on the international space station. *Phys. Rev. Lett.*, 119:181101. URL: https://link.aps.org/doi/10.1103/PhysRevLett.119.181101.

Adriani, O., Barbarino, G. C., Bazilevskaya, G. A., Bellotti, R., Boezio, M., Bogomolov, E. A., Bonechi, L., Bongi, M., Bonvicini, V., Bottai, S., Bruno, A., Cafagna, F., Campana, D., Carlson, P., Casolino, M., and Castellini, G. e. a. (2009). New measurement of the antiproton-to-proton flux ratio up to 100 gev in the cosmic radiation. *Phys. Rev. Lett.*, 102:051101. URL: https://link.aps.org/doi/10.1103/PhysRevLett.102.051101.

Adriani, O. and et al. (2011). Cosmic-ray electron flux measured by the pamela experiment between 1 and 625 gev. *Phys. Rev. Lett.*, 106:201101. URL: https://link.aps.org/doi/10.1103/PhysRevLett.106.201101.

Adriani, O. and et al. (2018). Extended measurement of the cosmic-ray electron and positron spectrum from 11 GeV to 4.8 TeV with the calorimetric electron telescope on the international space station. *Physical Review Letters*, 120(26). URL: https://doi.org/10.1103%2Fphysrevlett.120.261102.

Aguilar, M. and et al. (2002). The alpha magnetic spectrometer (ams) on the international space station: Part i – results from the test flight on the space shuttle. *Physics Reports*, 366(6):331–405. URL: https://www.sciencedirect.com/science/article/pii/S0370157302000133.

Aguilar, M. and et al. (2013). First result from the alpha magnetic spectrometer on the international space station: Precision measurement of the positron fraction in primary cosmic rays of 0.5–350 gev. *Phys. Rev. Lett.*, 110:141102. URL: https://link.aps.org/doi/10.1103/PhysRevLett.110.141102.

Aguilar, M. and et al. (2014). Electron and positron fluxes in primary cosmic rays measured with the alpha magnetic spectrometer on the international space station. *Phys. Rev. Lett.*, 113:121102. URL: https://link.aps.org/doi/10.1103/PhysRevLett.113.121102.

Aguilar, M. and et al. (2016a). Antiproton flux, antiproton-to-proton flux ratio, and properties of elementary particle fluxes in primary cosmic rays measured with the alpha magnetic spectrometer on the international space station. *Phys. Rev. Lett.*, 117:091103. URL: https://link.aps.org/doi/10.1103/PhysRevLett.117.091103.

Aguilar, M. and et al. (2016b). Precision measurement of the boron to carbon flux ratio in cosmic rays from 1.9 gv to 2.6 tv with the alpha magnetic spectrometer on the international space station. *Phys. Rev. Lett.*, 117:231102. URL: https://link.aps.org/doi/10.1103/PhysRevLett.117.231102.

Aguilar, M. and et al. (2019). Towards understanding the origin of cosmic-ray electrons. *Phys. Rev. Lett.*, 122:101101. URL: https://link.aps.org/doi/10.1103/PhysRevLett.122.101101.

Aharonian, F., Akhperjanian, A. G., Barres de Almeida, U., Bazer-Bachi, A. R., Becherini, Y., Behera, B., Benbow, W., Bernlöhr, K., Boisson, C., Bochow, A., and et al. (2008). Energy spectrum of cosmic-ray electrons at tev energies. *Physical Review Letters*, 101(26). URL: http://dx.doi.org/10.1103/PhysRevLett.101.261104.

Aharonian, F. and et al. (2009). *A&A*, 508(2):561–564. URL: https://doi.org/10.1051/0004-6361/200913323.

Ahn, E.-J., Engel, R., Gaisser, T. K., Lipari, P., and Stanev, T. (2009). Cosmic ray interaction event generator sibyll 2.1. *Phys. Rev. D*, 80:094003. URL: https://link.aps.org/doi/10.1103/PhysRevD.80.094003.

Ahnen, M. and et al. (2017). Performance of the MAGIC telescopes under moonlight. *Astroparticle Physics*, 94:29–41. URL: https://doi.org/10.1016%2Fj.astropartphys.2017.08.001.

Albert, J. and et al. (2008). Implementation of the random forest method for the imaging atmospheric cherenkov telescope MAGIC. *Nuclear Instruments and Methods in Physics Research Section A: Accelerators, Spectrometers, Detectors and Associated Equipment*, 588(3):424–432.

Aleksić, J. and et al. (2011). OBSERVATIONS OF THE CRAB PULSAR BETWEEN 25 AND 100 GeV WITH THE MAGIC i TELESCOPE. *The Astrophysical Journal*, 742(1):43. URL: https://doi.org/10.1088%2F0004-637x%2F742%2F1%2F43.

Aleksić, J. and et al. (2012). Performance of the magic stereo system obtained with crab nebula data. *Astroparticle Physics*, 35(7):435–448. URL: https://www.sciencedirect.com/science/article/pii/S0927650511002064.

Aleksić, J. and et al. (2016). The major upgrade of the MAGIC telescopes, part II: A performance study using observations of the crab nebula. *Astroparticle Physics*, 72:76–94. URL: https://doi.org/10.1016%2Fj.astropartphys.2015.02.005.

Aleksić, J. and et al. (2016). The major upgrade of the MAGIC telescopes, Part I: The hardware improvements and the commissioning of the system. *Astroparticle Physics*, 72:61–75. URL: https://ui.adsabs.harvard.edu/abs/2016APh....72...61A.

Alemanno, F. and et al. (2021). Measurement of the cosmic ray helium energy spectrum from 70 GeV to 80 TeV with the DAMPE space mission. *Physical Review Letters*, 126(20). URL: https://doi.org/10.1103%2Fphysrevlett.126.201102.

Aliu, E. and et al. (2008). Observation of pulsed γ-rays above 25 GeV from the crab pulsar with MAGIC. *Science*, 322(5905):1221–1224. URL: https://doi.org/10.1126%2Fscience.1164718.

Aliu, E. and et al. (2009). Improving the performance of the single-dish cherenkov telescope magic through the use of signal timing. *Astroparticle Physics*, 30(6):293–305. URL: https://www.sciencedirect.com/science/article/pii/S0927650508001497.

Ambrosi, G., An, Q., Asfandiyarov, R., Azzarello, P., Bernardini, P., Bertucci, B., Cai, M. S., Chang, J., Chen, D. Y., Chen, H. F., Chen, J. L., Chen, W., Cui, M. Y., Cui, T. S., and et al. (2017). Direct detection of a break in the teraelectronvolt cosmic-ray spectrum of electrons and positrons. *Nature*, 552(7683):63–66. URL: https://doi.org/10.1038/nature24475.

An, Q., Asfandiyarov, R., Azzarello, P., Bernardini, P., Bi, X. J., Cai, M. S., Chang, J., Chen, D. Y., Chen, H. F., and et al. (2019). Measurement of the cosmic ray proton spectrum from 40 gev to 100 tev with the dampe satellite. *Science Advances*, 5(9). URL: http://dx.doi.org/10.1126/sciadv.aax3793.

Archer, A., Benbow, W., Bird, R., Brose, R., Buchovecky, M., Buckley, J., Bugaev, V., Connolly, M., Cui, W., Daniel, M., and et al. (2018). Measurement of cosmic-ray electrons at tev energies by veritas. *Physical Review D*, 98(6). URL: http://dx.doi.org/10.1103/PhysRevD.98.062004.

Asano, K., Asaoka, Y., Akaike, Y., Kawanaka, N., Kohri, K., Motz, H. M., and Terasawa, T. (2022). Monte carlo study of electron and positron cosmic-ray propagation with the

calet spectrum. *The Astrophysical Journal*, 926(1):5. URL: https://dx.doi.org/10.3847/1538-4357/ac41d1.

Atoyan, A. M. and Aharonian, F. A. (1996). On the mechanisms of gamma radiation in the crab nebula. *Monthly Notices of the Royal Astronomical Society*, 278(2):525–541. URL: https://ieeexplore.ieee.org/document/8134827.

Axford, W. I. (1969). *Acceleration of Cosmic Rays by Shock Waves*, pages 155–203. Springer Berlin Heidelberg, Berlin, Heidelberg.

Barlow, R. (1990). Extended maximum likelihood. *Nuclear Instruments and Methods in Physics Research Section A: Accelerators, Spectrometers, Detectors and Associated Equipment*, 297(3):496–506. URL: https://www.sciencedirect.com/science/article/pii/0168900290913348.

Barwick, S. W., Beatty, J. J., Bhattacharyya, A., Bower, C. R., Chaput, C. J., Coutu, S., de Nolfo, G. A., Knapp, J., Lowder, D. M., McKee, S., Müller, D., Musser, J. A., Nutter, S. L., Schneider, E., Swordy, S. P., Tarlé , G., Tomasch, A. D., and Torbet, E. (1997). Measurements of the cosmic-ray positron fraction from 1 to 50 g[CLC]e[/CLC]v. *The Astrophysical Journal*, 482(2):L191–L194. URL: https://doi.org/10.1086%2F310706.

Beatty, J. J., Bhattacharyya, A., Bower, C., Coutu, S., DuVernois, M. A., McKee, S., Minnick, S. A., Müller, D., Musser, J., Nutter, S., Labrador, A. W., Schubnell, M., Swordy, S., Tarlé, G., and Tomasch, A. (2004). New measurement of the cosmic-ray positron fraction from 5 to 15 gev. *Phys. Rev. Lett.*, 93:241102. URL: https://link.aps.org/doi/10.1103/PhysRevLett.93.241102.

Bell, A. R. (1978). The acceleration of cosmic rays in shock fronts – I. *Monthly Notices of the Royal Astronomical Society*, 182(2):147–156. URL: https://doi.org/10.1093/mnras/182.2.147.

Bertone, G., Hooper, D., and Silk, J. (2005). Particle dark matter: evidence, candidates and constraints. *Physics Reports*, 405(5-6):279–390. URL: https://doi.org/10.1016%2Fj.physrep.2004.08.031.

Biland, A., Garczarczyk, M., Anderhub, H., Danielyan, V., Hakobyan, D., Lorenz, E., and Mirzoyan, R. (2007). The active mirror control of the magic telescope. URL: https://arxiv.org/abs/0709.1574.

Bird, D. J., Corbato, S. C., Dai, H. Y., Dawson, B. R., Elbert, J. W., Emerson, B. L., Green, K. D., Huang, M. A., Kieda, D. B., Luo, M., Ko, S., Larsen, C. G., Loh, E. C., Salamon, M. H., Smith, J. D., Sokolsky, P., Sommers, P., Tang, J. K. K., and Thomas, S. B. (1994). The Cosmic-Ray Energy Spectrum Observed by the Fly's Eye. *apj*, 424:491. URL: https://ui.adsabs.harvard.edu/abs/1994ApJ...424..491B.

Bitossi, M., Paoletti, R., and Tescaro, D. (2016). Ultra-Fast Sampling and Data Acquisition Using the DRS4 Waveform Digitizer. *IEEE Transactions on Nuclear Science*, 63(4):2309–2316. URL: https://ui.adsabs.harvard.edu/abs/2016ITNS...63.2309B.

Blandford, R. D. and Ostriker, J. P. (1978). Particle acceleration by astrophysical shocks. *apjl*, 221:L29–L32. URL: https://ui.adsabs.harvard.edu/abs/1978ApJ...221L..29B.

Blasi, P. (2008). Direct measurements, acceleration and propagation of cosmic rays. URL: https://arxiv.org/abs/0801.4534.

Blasi, P. (2009). Origin of the positron excess in cosmic rays. *Phys. Rev. Lett.*, 103:051104. URL: https://link.aps.org/doi/10.1103/PhysRevLett.103.051104.

Blasi, P. (2013). The origin of galactic cosmic rays. *The Astronomy and Astrophysics Review*, 21(1). URL: https://doi.org/10.1007%2Fs00159-013-0070-7.

Blasi, P. and Amato, E. (2010). Positrons from pulsar winds. URL: https://arxiv.org/abs/1007.4745.

Blasi, P. and Serpico, P. D. (2009). High-energy antiprotons from old supernova remnants. *Physical Review Letters*, 103(8). URL: https://doi.org/10.1103%2Fphysrevlett.103.081103.

Boehm, C., Enßlin, T. A., and Silk, J. (2004). Can annihilating dark matter be lighter than a few gevs? *Journal of Physics G: Nuclear and Particle Physics*, 30(3):279. URL: https://dx.doi.org/10.1088/0954-3899/30/3/004.

Boezio, M., Carlson, P., Francke, T., Weber, N., Suffert, M., Hof, M., Menn, W., Simon, M., Stephens, S. A., Bellotti, R., Cafagna, F., Castellano, M., Circella, M., and et al. (2000). The cosmic-ray electron and positron spectra measured at 1 AU during solar minimum activity. *The Astrophysical Journal*, 532(1):653–669. URL: https://doi.org/10.1086/308545.

Bogovalov, S. V. (1999). On the physics of cold mhd winds from oblique rotators. URL: https://arxiv.org/abs/astro-ph/9907051.

Boudaud, M., Aupetit, S., Caroff, S., Putze, A., Belanger, G., Genolini, Y., Goy, C., Poireau, V., Poulin, V., Rosier, S., Salati, P., Tao, L., and Vecchi, M. (2015). A new look at the cosmic ray positron fraction. *A & A*, 575:A67. URL: https://doi.org/10.1051%2F0004-6361%2F201425197.

Brambilla, G., Kalapotharakos, C., Timokhin, A. N., Harding, A. K., and Kazanas, D. (2018). Electron–positron pair flow and current composition in the pulsar magnetosphere. *The Astrophysical Journal*, 858(2):81. URL: https://dx.doi.org/10.3847/1538-4357/aab3e1.

Bransgrove, A., Levin, Y., and Beloborodov, A. (2017). Magnetic field evolution of neutron stars – i. basic formalism, numerical techniques and first results. *Monthly Notices of the Royal Astronomical Society*, 473(2):2771–2790. URL: https://doi.org/10.1093%2Fmnras%2Fstx2508.

Breiman, L. (2001). Random Forests. *Machine Learning*, 45:5–32. URL: https://ui.adsabs.harvard.edu/abs/2001MachL..45....5B.

Bretz, T., Dorner, D., Wagner, R., and Sawallisch, P. (2009). The drive system of the major atmospheric gamma-ray imaging cherenkov telescope. *Astroparticle Physics*, 31(2):92–101. URL: https://doi.org/10.1016%2Fj.astropartphys.2008.12.001.

Brun, R. and Rademakers, F. (1997). Root — an object oriented data analysis framework. *Nuclear Instruments and Methods in Physics Research Section A: Accelerators, Spectrometers, Detectors and Associated Equipment*, 389(1):81–86. URL: https://www.sciencedirect.com/science/article/pii/S016890029700048X.

Cao, Q.-H., Chen, C.-R., and Gong, T. (2017). Leptophilic dark matter confronts ams-02 cosmic-ray positron flux. *Chinese Journal of Physics*, 55(1):10–15. URL: https://www.sciencedirect.com/science/article/pii/S0577907316306426.

Ceribella, G. (2021). *Insights into the 10-100 GeV gamma-ray emission of pulsars from extensive observations of MAGIC*. Dissertation, Technische Universität München, München. URL: https://mediatum.ub.tum.de/doc/1617483/1617483.pdf.

Cerutti, B. and Beloborodov, A. M. (2016). Electrodynamics of pulsar magnetospheres. *Space Science Reviews*, 207(1-4):111–136. UR: https://doi.org/10.1007%2Fs11214-016-0315-7.

Cheng, K. S., Ho, C., and Ruderman, M. (1986). Energetic Radiation from Rapidly Spinning Pulsars. I. Outer Magnetosphere Gaps. *apj*, 300:500. URL: https://ui.adsabs.harvard.edu/abs/1986ApJ...300..500C.

Chi, X., Cheng, K. S., and Young, E. C. M. (1996). Pulsar-wind origin of cosmic-ray positrons. *The Astrophysical Journal*, 459(2):L83. URL: https://dx.doi.org/10.1086/309943.

Cholis, I. and Hooper, D. (2013). Dark matter and pulsar origins of the rising cosmic ray positron fraction in light of new data from the ams. *Phys. Rev. D*, 88:023013. URL: https://link.aps.org/doi/10.1103/PhysRevD.88.023013.

Cholis, I. and Hooper, D. (2014). Constraining the origin of the rising cosmic ray positron fraction with the boron-to-carbon ratio. *Phys. Rev. D*, 89:043013. URL: https://link.aps.org/doi/10.1103/PhysRevD.89.043013.

Cholis, I., Linden, T., and Hooper, D. (2019). A robust excess in the cosmic-ray antiproton spectrum: Implications for annihilating dark matter. *Physical Review D*, 99(10). UR: https://doi.org/10.1103%2Fphysrevd.99.103026.

Cortina, J., Goebel, F., and Schweizer, T. (2009). Technical performance of the magic telescopes. URL: https://arxiv.org/abs/0907.1211.

Cristofari, P., Gabici, S., Casanova, S., Terrier, R., and Parizot, E. (2013). Acceleration of cosmic rays and gamma-ray emission from supernova remnants in the galaxy. *Monthly Notices of the Royal Astronomical Society*, 434(4):2748–2760. URL: https://doi.org/10.1093%2Fmnras%2Fstt1096.

D. Borla Tridon, P. Colin, L. C. M. D. V. S. (2011). Measurement of the cosmic electron plus positron spectrum with the MAGIC telescopes. In *Proceedings of the 32nd International Cosmic Ray Conference (ICRC)*. URL: https://arxiv.org/abs/1110.4008.

Daugherty, J. K. and Harding, A. K. (1982). Electromagnetic cascades in pulsars. *apj*, 252:337–347. URL: https://ui.adsabs.harvard.edu/abs/1982ApJ...252..337D.

Daugherty, J. K. and Harding, A. K. (1996). Gamma-Ray Pulsars: Emission from Extended Polar CAP Cascades. *apj*, 458:278. URL: https://ui.adsabs.harvard.edu/abs/1996ApJ...458..278D.

de Naurois, M. and Mazin, D. (2015). Ground-based detectors in very-high-energy gamma-ray astronomy. *Comptes Rendus Physique*, 16(6):610–627. URL: https://www.sciencedirect.com/science/article/pii/S1631070515001462.

Delahaye, T., Lavalle, J., Lineros, R., Donato, F., and Fornengo, N. (2010). Galactic electrons and positrons at the earth: new estimate of the primary and secondary fluxes. *Astronomy & Astrophysics*, 524:A51. URL: https://doi.org/10.1051%2F0004-6361%2F201014225.

Delahaye, T., Lineros, R., Donato, F., Fornengo, N., Lavalle, J., Salati, P., and Taillet, R. (2009). Galactic secondary positron flux at the earth. *A&A*, 501(3):821–833. URL: https://doi.org/10.1051/0004-6361/200811130.

Donnert, J., Vazza, F., Brüggen, M., and ZuHone, J. (2018). Magnetic field amplification in galaxy clusters and its simulation. *Space Science Reviews*, 214(8). URL: https://doi.org/10.1007%2Fs11214-018-0556-8.

Doro, M., Bastieri, D., Biland, A., Dazzi, F., Font, L., Garczarczyk, M., Ghigo, M., Giro, E., Goebel, F., Kosyra, R., Lorenz, E., Mariotti, M., Mirzoyan, R., Peruzzo, L., Pareschi, G., and Zapatero, J. (2008). The reflective surface of the magic telescope. *Nuclear Instruments and Methods in Physics Research Section A: Accelerators, Spectrometers, Detectors and Associated Equipment*, 595(1):200–203. RICH 2007.

DuVernois, M. A., Barwick, S. W., Beatty, J. J., Bhattacharyya, A., Bower, C. R., Chaput, C. J., Coutu, S., de Nolfo, G. A., Lowder, D. M., McKee, S., Müller, D., Musser, J. A., Nutter, S. L., Schneider, E., Swordy, S. P., Tarlé, G., Tomasch, A. D., and Torbet, E. (2001). Cosmic-ray electrons and positrons from 1 to 100 gev: Measurements with heat and their interpretation. *The Astrophysical Journal*, 559(1):296. URL: https://dx.doi.org/10.1086/322324.

Ellison, D. C., Patnaude, D. J., Slane, P., Blasi, P., and Gabici, S. (2007). Particle acceleration in supernova remnants and the production of thermal and nonthermal radiation. *The Astrophysical Journal*, 661(2):879. URL: https://dx.doi.org/10.1086/517518.

Evans, N. W., Ferrer, F., and Sarkar, S. (2004). A travel guide to the dark matter annihilation signal. *Phys. Rev. D*, 69:123501. URL: https://link.aps.org/doi/10.1103/PhysRevD.69.123501.

Evoli, C. (2018). The cosmic-ray energy spectrum. URL: https://doi.org/10.5281/zenodo.2360277.

F. Schmidt, J. K. (2005). CORSIKA Shower Images. URL: https://www-zeuthen.desy.de/ jknapp/fs/showerimages.html.

Fang, K., Bi, X.-J., Lin, S.-J., and Yuan, Q. (2021). Klein–nishina effect and the cosmic ray electron spectrum. *Chinese Physics Letters*, 38(3):039801. URL: https://doi.org/10.1088%2F0256-307x%2F38%2F3%2F039801.

Fang, K., Bi, X.-J., and Yin, P.-F. (2018). Explanation of the Knee-like Feature in the DAMPE Cosmic {e}{$\hat{}$-}+{e}{$\hat{}$+} Energy Spectrum. *apj*, 854(1):57. URL: https://ui.adsabs.harvard.edu/abs/2018ApJ...854...57F.

Feng, J. L. (2010). Dark matter candidates from particle physics and methods of detection. *Annual Review of Astronomy and Astrophysics*, 48(1):495–545. URL: https://doi.org/10.1146/annurev-astro-082708-101659.

Fermi, E. (1949). On the origin of the cosmic radiation. *Phys. Rev.*, 75:1169–1174. URL: https://link.aps.org/doi/10.1103/PhysRev.75.1169.

Fletcher, R. S., Gaisser, T. K., Lipari, P., and Stanev, T. (1994). sibyll: An event generator for simulation of high energy cosmic ray cascades. *Phys. Rev. D*, 50:5710–5731.

Fomin, V., Stepanian, A., Lamb, R., Lewis, D., Punch, M., and Weekes, T. (1994). New methods of atmospheric cherenkov imaging for gamma-ray astronomy. i. the false source method. *Astroparticle Physics*, 2(2):137–150. URL: https://www.sciencedirect.com/science/article/pii/0927650594900361.

Fruck, C. (2015). *The galactic center resolved with MAGIC and a new technique for atmospheric calibration*. PhD thesis, Munich University of Technology, Germany. URL: https://ui.adsabs.harvard.edu/abs/2015PhDT.....176F.

Fruck, C. and et al. (2022). Characterizing the aerosol atmosphere above the observatorio del roque de los muchachos by analysing seven years of data taken with an GaAsP HPD-readout, absolutely calibrated elastic LIDAR. *Monthly Notices of the Royal Astronomical Society*, 515(3):4520–4550. URL: https://doi.org/10.1093%2Fmnras%2Fstac1563.

Fruck, C., Gaug, M., Zanin, R., Dorner, D., Garrido, D., Mirzoyan, R., and Font, L. (2014). A novel LIDAR-based Atmospheric Calibration Method for Improving the Data Analysis of MAGIC. In *33rd International Cosmic Ray Conference*, page 1054. URL: https://inspirehep.net/literature/1285998.

Fujita, Y., Kohri, K., Yamazaki, R., and Ioka, K. (2009). Is the PAMELA anomaly caused by supernova explosions near the earth? *Physical Review D*, 80(6). URL: https://doi.org/10.1103%2Fphysrevd.80.063003.

Gaensler, B. M. and Slane, P. O. (2006). The evolution and structure of pulsar wind nebulae. *Annual Review of Astronomy and Astrophysics*, 44(1):17–47. URL: https://doi.org/10.1146%2Fannurev.astro.44.051905.092528.

Gaisser, T. K. (1990). *Cosmic rays and particle physics.* URL: https://ui.adsabs.harvard.edu/abs/1990cup..book.....G.

Gaisser, T. K., Engel, R., and Resconi, E. (2016). *Cosmic rays*, page 1–11. Cambridge University Press, 2 edition. URL: https://doi.org/10.1017/CBO9781139192194.

Galbraith, W. and Jelley, J. V. (1953). Light Pulses from the Night Sky associated with Cosmic Rays. *nat*, 171(4347):349–350. URL: https://ui.adsabs.harvard.edu/abs/1953Natur.171..349G.

García, J. R., Dazzi, F., Häfner, D., Herranz, D., López, M., Mariotti, M., Mirzoyan, R., Nakajima, D., Schweizer, T., and Teshima, M. (2014). Status of the new sum-trigger system for the magic telescopes. URL: https://arxiv.org/abs/1404.4219.

Geringer-Sameth, A. and Koushiappas, S. M. (2011). Exclusion of canonical weakly interacting massive particles by joint analysis of milky way dwarf galaxies with data from the fermi gamma-ray space telescope. *Phys. Rev. Lett.*, 107:241303. URL: https://link.aps.org/doi/10.1103/PhysRevLett.107.241303.

Ginzburg, V. L. and Syrovatskii, S. I. (1964). *The Origin of Cosmic Rays.* URL: https://ui.adsabs.harvard.edu/abs/1964ocr..book.....G.

Globus, N., Allard, D., and Parizot, E. (2015). A complete model of the cosmic ray spectrum and composition across the galactic to extragalactic transition. *Physical Review D*, 92(2). URL: https://doi.org/10.1103%2Fphysrevd.92.021302.

Goldreich, P. and Julian, W. H. (1969). Pulsar Electrodynamics. *apj*, 157:869. URL: https://ui.adsabs.harvard.edu/abs/1969ApJ...157..869G.

Grasso, D. and et al. (2009). On possible interpretations of the high energy electron–positron spectrum measured by the fermi large area telescope. *Astroparticle Physics*, 32(2):140–151. URL: https://www.sciencedirect.com/science/article/pii/S0927650509001078.

Green, D. M. (2016). *Measurement of the cosmic-ray proton spectrum from 54 GeV to 9.5 TeV with the Fermi Large Area Telescope*. PhD thesis, University of Maryland, College Park. URL: https://ui.adsabs.harvard.edu/abs/2016PhDT.......131G.

Griest, K. and Kamionkowski, M. (1990). Unitarity limits on the mass and radius of dark-matter particles. *Phys. Rev. Lett.*, 64:615–618. URL: https://link.aps.org/doi/10.1103/PhysRevLett.64.615.

Haino, S. and AMS-02 Collaboration (2013). Precision Measurement of the Proton Flux with AMS. In *International Cosmic Ray Conference*, volume 33 of *International Cosmic Ray Conference*, page 283. URL: https://ui.adsabs.harvard.edu/abs/2013ICRC...33..283H.

Harding, A. K. (2007). Pulsar High-Energy Emission From the Polar Cap and Slot Gap. *arXiv e-prints*, page arXiv:0710.3517. URL: https://ui.adsabs.harvard.edu/abs/2007arXiv0710.3517H.

Heck, D., Knapp, J., Capdevielle, J. N., Schatz, G., and Thouw, T. (1998). *CORSIKA: a Monte Carlo code to simulate extensive air showers.* URL: https://ui.adsabs.harvard.edu/abs/1998cmcc.book.....H.

Hendrick, S. P. and Reynolds, S. P. (2001). Maximum energies of shock-accelerated electrons in large magellanic cloud supernova remnants. *The Astrophysical Journal*, 559(2):903. URL: https://dx.doi.org/10.1086/322341.

Hengstebeck, T. (2007). *Measurement of the energy spectrum of the BL Lac object PG1553+113 with the MAGIC telescope in 2005 and 2006*. PhD thesis, Humboldt-Universität zu Berlin, Mathematisch-Naturwissenschaftliche Fakultät I. URL: https://edoc.hu-berlin.de/handle/18452/16280.

Hess, V. F. (1912). Über Beobachtungen der durchdringenden Strahlung bei sieben Freiballonfahrten. *Phys. Z.*, 13:1084–1091. URL: https://www.mpi-hd.mpg.de/hfm/HESS/public/HessArticle.pdf.

Hillas, A. M. (1984). The origin of ultra-high-energy cosmic rays. *Annual review of astronomy and astrophysics*, 22:425–444. URL: https://articles.adsabs.harvard.edu/pdf/1984ARA%26A..22..425H.

Hillas, A. M. (1985). Cerenkov Light Images of EAS Produced by Primary Gamma Rays and by Nuclei. In *19th International Cosmic Ray Conference (ICRC19), Volume 3*, volume 3 of *International Cosmic Ray Conference*, page 445. URL: https://ui.adsabs.harvard.edu/abs/1985ICRC....3..445H.

Hooper, D., Kelso, C., and Queiroz, F. S. (2013). Stringent constraints on the dark matter annihilation cross section from the region of the galactic center. *Astroparticle Physics*, 46:55–70. URL: https://www.sciencedirect.com/science/article/pii/S0927650513000753.

Hoyle, F. and Fowler, W. A. (1960). Nucleosynthesis in Supernovae. *apj*, 132:565. URL: https://ui.adsabs.harvard.edu/abs/1960ApJ...132..565H.

Ishio, K. (2020). Improvement in the gamma-ray energy reconstruction of magic and impact on the spectral analysis of the first gamma ray burst detected at tev energies. URL: http://nbn-resolving.de/urn:nbn:de:bvb:19-275991.

Jungman, G., Kamionkowski, M., and Griest, K. (1996). Supersymmetric dark matter. *Physics Reports*, 267(5-6):195–373. URL: https://doi.org/10.1016%2F0370-1573%2895%2900058-5.

Kamae, T., Karlsson, N., Mizuno, T., Abe, T., and Koi, T. (2006). Parameterization of $\gamma, e^{\pm}$, and neutrino spectra produced by p-p interaction in astronomical environments. *The Astrophysical Journal*, 647(1):692–708. URL: https://doi.org/10.1086/505189.

Kerszberg, D. and et al. (2015). Talk at the icrc2017. URL: https://pdfs.semanticscholar.org/26b3/e7071f5b0e912759e1660060e28fa7cfa9af.pdf.

Kobayashi, T., Komori, Y., Yoshida, K., and Nishimura, J. (2004). The most likely sources of high-energy cosmic-ray electrons in supernova remnants. *The Astrophysical Journal*, 601(1):340–351. URL: https://doi.org/10.1086/380431.

Kohnle, A. and et al. (1996). Stereoscopic imaging of air showers with the first two hegra cherenkov telescopes. *Astroparticle Physics*, 5(2):119–131. URL: https://www.sciencedirect.com/science/article/pii/0927650596000114.

Kohri, K., Ioka, K., Fujita, Y., and Yamazaki, R. (2016). Can we explain AMS-02 antiproton and positron excesses simultaneously by nearby supernovae without pulsars or dark matter? *Progress of Theoretical and Experimental Physics*, 2016(2):021E01. URL: https://doi.org/10.1093%2Fptep%2Fptv193.

Kotera, K. and Olinto, A. V. (2011). The astrophysics of ultrahigh-energy cosmic rays. *Annual Review of Astronomy and Astrophysics*, 49(1):119–153. URL: https://doi.org/10.1146/annurev-astro-081710-102620.

Kraus, M. (2018). *The Cosmic-Ray Electron Anisotropy Measured with H.E.S.S. and Characterization of a Readout System for the SST Cameras of CTA*. PhD dissertation, Friedrich-Alexander-Universität Erlangen-Nürnberg. URL: https://ecap.nat.fau.de/wp-content/uploads/2018/07/2018_Kraus_Dissertation.pdf.

Krymskii, G. F. (1977). A regular mechanism for the acceleration of charged particles on the front of a shock wave. *Akademiia Nauk SSSR Doklady*, 234:1306–1308. URL: https://ui.adsabs.harvard.edu/abs/1977DoSSR.234.1306K.

Lagage, P. O. and Cesarsky, C. J. (1983). The maximum energy of cosmic rays accelerated by supernova shocks. *aap*, 125:249–257. URL: https://ui.adsabs.harvard.edu/abs/1983A&A...125..249L.

Lessard, R., Buckley, J., Connaughton, V., and Bohec, S. L. (2001). A new analysis method for reconstructing the arrival direction of TeV gamma rays using a single imaging atmospheric cherenkov telescope. *Astroparticle Physics*, 15(1):1–18. URL: https://doi.org/10.1016%2Fs0927-6505%2800%2900133-x.

Li, T.-P. and Ma, Y. (1983). Analysis methods for results in gamma-ray astronomy. *The Astrophysical Journal*, 272:317–324. URL: https://ui.adsabs.harvard.edu/abs/1983ApJ...272..317L/abstract.

Linden, T. and Profumo, S. (2013). PROBING THE PULSAR ORIGIN OF THE ANOMALOUS POSITRON FRACTION WITH AMS-02 AND ATMOSPHERIC CHERENKOV TELESCOPES. *The Astrophysical Journal*, 772(1):18. URL: https://doi.org/10.1088%2F0004-637x%2F772%2F1%2F18.

Longair, M. S. (2011). *High Energy Astrophysics (3rd ed.)*. Cambridge university press. URL: https://www.cambridge.org/core/books/high-energy-astrophysics/CF25E2E5FC0EDFC51FCD7846A262C0AE.

López Coto, R. (2017). *The Imaging Atmospheric Cherenkov Technique and the IACTs MAGIC and CTA*, pages 15–64. Springer International Publishing, Cham. URL: https://doi.org/10.1007/978-3-319-44751-3_2.

Lorenz, E. (2004). Status of the 17 m diameter magic telescope. *New Astronomy Reviews*, 48(5):339–344. 2nd VERITAS Symposium on the Astrophysics of Extragalactic Sources.

Lu, B.-Q. and Zong, H.-S. (2016). Limits on dark matter from AMS-02 antiproton and positron fraction data. *Physical Review D*, 93(10). URL: https://doi.org/10.1103%2Fphysrevd.93.103517.

Majumdar, P., Moralejo, A., Bigongiari, C., Blanch, O., and Sobczynska, D. (2005). Monte Carlo simulation for the MAGIC telescope. In *29th International Cosmic Ray Conference*. URL: https://inspirehep.net/literature/695612.

Mallot, A. K. (2017). The energy spectrum of cosmic electrons measured with the magic telescopes. URL: https://www.semanticscholar.org/paper/The-energy-spectrum-of-cosmic-electrons-measured-Mallot/461128b9935afc7d1a629477e1d84906b8b3c959.

Malyshev, D., Cholis, I., and Gelfand, J. (2009). Pulsars versus dark matter interpretation of ATIC/PAMELA. *prd*, 80(6):063005. URL: https://ui.adsabs.harvard.edu/abs/2009PhRvD..80f3005M.

Manchester, R. N., Hobbs, G. B., Teoh, A., and Hobbs, M. (2005). The australia telescope national facility pulsar catalogue. *The Astronomical Journal*, 129(4):1993. URL: https://dx.doi.org/10.1086/428488.

Mathis, J. S., Mezger, P. G., and Panagia, N. (1983). Interstellar radiation field and dust temperatures in the diffuse interstellar medium and in giant molecular clouds. *aap*, 128:212–229. URL: https://ui.adsabs.harvard.edu/abs/1983A&A...128..212M.

Matthews, J. (2001). Energy flow in extensive air showers. In *Proceedings of ICRC*, volume 2001. URL: http://dpnc.unige.ch/ams/ams_beta/ICRC/ICRC-01/ICRC2001/papers/ici6261_p.pdf.

Matthews, J. (2005). A heitler model of extensive air showers. *Astroparticle Physics*, 22(5):387–397. URL: https://www.sciencedirect.com/science/article/pii/S0927650504001598.

Mauro, M. D., Donato, F., Fornengo, N., Lineros, R., and Vittino, A. (2014). Interpretation of AMS-02 electrons and positrons data. *Journal of Cosmology and Astroparticle Physics*, 2014(04):006–006. URL: https://doi.org/10.1088%2F1475-7516%2F2014%2F04%2F006.

Mertsch, P. and Sarkar, S. (2009). Testing astrophysical models for the PAMELA positron excess with cosmic ray nuclei. *Physical Review Letters*, 103(8). URL: https://doi.org/10.1103%2Fphysrevlett.103.081104.

Mertsch, P. and Sarkar, S. (2014). AMS-02 data confront acceleration of cosmic ray secondaries in nearby sources. *Physical Review D*, 90(6). URL: https://doi.org/10.1103%2Fphysrevd.90.061301.

Moraal, H. (2013). Cosmic-ray modulation equations. *Space Science Reviews*, 176(1):299–319. URL: https://doi.org/10.1007/s11214-011-9819-3.

Moralejo, A. (2003). The Reflector Simulation Program v.0.6. *Internal MAGIC-TDAS*, pages note 02–11. URL: https://magic.mpp.mpg.de/backend/tdas-notes.

Moralejo, A., Gaug, M., Carmona, E., Colin, P., Delgado, C., Lombardi, S., Mazin, D., Scalzotto, V., Sitarek, J., and Tescaro, D. (2009). Mars, the magic analysis and reconstruction software. URL: https://arxiv.org/abs/0907.0943.

Moskalenko, I. V. and Strong, A. W. (1998). Production and Propagation of Cosmic-Ray Positrons and Electrons. *apj*, 493(2):694–707. URL: https://ui.adsabs.harvard.edu/abs/1998ApJ...493..694M.

Nakajima, D., Fink, D., Hose, J., Mirzoyan, R., Paneque, D., Saito, K., Schweizer, T., Teshima, M., Toyama, T., and Wetteskind, H. (2013). New Imaging Camera for the MAGIC-I Telescope. In *International Cosmic Ray Conference*, volume 33 of *International Cosmic Ray Conference*, page 3044. URL: https://ui.adsabs.harvard.edu/abs/2013ICRC...33.3044N.

Neronov, A. and Semikoz, D. (2020). Galactic diffuse gamma-ray emission at tev energy. *Astronomy & Astrophysics*, 633:A94. URL: http://dx.doi.org/10.1051/0004-6361/201936368.

Olaf Behnke, Kevin Kröninger, G. S. (2013). *Data Analysis in High Energy Physics*. WileyVCH GmbH. URL: https://onlinelibrary.wiley.com/doi/book/10.1002/9783527653416.

Orusa, L., Manconi, S., Donato, F., and Mauro, M. D. (2021). Constraining positron emission from pulsar populations with AMS-02 data. *Journal of Cosmology and Astroparticle Physics*, 2021(12):014. URL: https://doi.org/10.1088%2F1475-7516%2F2021%2F12%2F014.

Ostapchenko, S. (2011). Monte carlo treatment of hadronic interactions in enhanced pomeron scheme: Qgsjet-ii model. *Phys. Rev. D*, 83:014018. URL: https://link.aps.org/doi/10.1103/PhysRevD.83.014018.

Ostriker, J. P. and Gunn, J. E. (1969). On the Nature of Pulsars. I. Theory. *apj*, 157:1395. URL: https://ui.adsabs.harvard.edu/abs/1969ApJ...157.1395O.

Panov, A. D. (2013). Electrons and positrons in cosmic rays. *Journal of Physics: Conference Series*, 409(1):012004. URL: https://dx.doi.org/10.1088/1742-6596/409/1/012004.

Pétri, J., Heyvaerts, J., and Bonazzola, S. (2002). Global static electrospheres of charged pulsars. *aap*, 384:414–432. URL: https://ui.adsabs.harvard.edu/abs/2002A&A...384..414P.

Pierog, T., Karpenko, I., Katzy, J. M., Yatsenko, E., and Werner, K. (2015). Epos lhc: Test of collective hadronization with data measured at the cern large hadron collider. *Phys. Rev. C*, 92:034906. URL: https://link.aps.org/doi/10.1103/PhysRevC.92.034906.

Planck Collaboration, Ade, P. A. R., and et al. (2014). Planck 2013 results. XVI. Cosmological parameters. *aap*, 571:A16. URL: https://ui.adsabs.harvard.edu/abs/2014A&A...571A..16P.

Profumo, S. (2012). Dissecting cosmic-ray electron-positron data with Occam's razor: the role of known pulsars. *Central European Journal of Physics*, 10(1):1–31. URL: https://ui.adsabs.harvard.edu/abs/2012CEJPh..10....1P.

Ptuskin, V. (2012). Propagation of galactic cosmic rays. *Astroparticle Physics*, 39-40:44–51. URL: https://www.sciencedirect.com/science/article/pii/S0927650511002039.

Rees, M. J. and Gunn, J. E. (1974). The origin of the magnetic field and relativistic particles in the crab nebula. *Monthly Notices of the Royal Astronomical Society*, 167(1):1–12. URL: https://doi.org/10.1093/mnras/167.1.1.

Reynolds, S. P. (1996). Synchrotron models for x-rays from the supernova remnant sn 1006. *The Astrophysical Journal*, 459(1):L13. URL: https://dx.doi.org/10.1086/309936.

Reynolds, S. P. and Keohane, J. W. (1999). Maximum energies of shock-accelerated electrons in young shell supernova remnants. *The Astrophysical Journal*, 525(1):368. URL: https://dx.doi.org/10.1086/307880.

Rossi, B. and Greisen, K. (1941). Cosmic-ray theory. *Rev. Mod. Phys.*, 13:240–309. URL: https://link.aps.org/doi/10.1103/RevModPhys.13.240.

Rubin, V. C. and Ford, W. Kent, J. (1970). Rotation of the Andromeda Nebula from a Spectroscopic Survey of Emission Regions. *apj*, 159:379. URL: https://ui.adsabs.harvard.edu/abs/1970ApJ...159..379R.

Ruderman, M. A. and Sutherland, P. G. (1975). Theory of pulsars: polar gaps, sparks, and coherent microwave radiation. *apj*, 196:51–72. URL: https://ui.adsabs.harvard.edu/abs/1975ApJ...196...51R.

Ryu, D., Kang, H., Hallman, E., and Jones, T. W. (2003). Cosmological shock waves and their role in the large-scale structure of the universe. *The Astrophysical Journal*, 593(2):599. URL: https://dx.doi.org/10.1086/376723.

Serpico, P. D. (2009). Possible causes of a rise with energy of the cosmic ray positron fraction. *Phys. Rev. D*, 79:021302. URL: https://link.aps.org/doi/10.1103/PhysRevD.79.021302.

Serpico, P. D. (2012). Astrophysical models for the origin of the positron "excess". *Astroparticle Physics*, 39-40:2–11. URL: https://www.sciencedirect.com/science/article/pii/S0927650511001654.

Shalchi, A. (2009). *Nonlinear Cosmic Ray Diffusion Theories*. Springer Berlin, Heidelberg. URL: https://link.springer.com/book/10.1007/978-3-642-00309-7#bibliographic-information.

Shen, C. S. (1970). Pulsars and Very High-Energy Cosmic-Ray Electrons. *apjl*, 162:L181. URL: https://ui.adsabs.harvard.edu/abs/1970ApJ...162L.181S.

Silk, J. et al. (2010). *Particle Dark Matter: Observations, Models and Searches*. Cambridge Univ. Press, Cambridge. URL: https://inspirehep.net/literature/895273.

Sitarek, J., Gaug, M., Mazin, D., Paoletti, R., and Tescaro, D. (2013). Analysis techniques and performance of the domino ring sampler version 4 based readout for the MAGIC telescopes. *Nuclear Instruments and Methods in Physics Research Section A: Accelerators, Spectrometers, Detectors and Associated Equipment*, 723:109–120. URL: https://doi.org/10.1016%2Fj.nima.2013.05.014.

Sob'yanin, D. N. (2016). Breakdown of the goldreich–julian relation in a neutron star. *Astronomy Letters*, 42(11):745–751. URL: https://doi.org/10.1134%2Fs1063773716110049.

Staszak, D. (2015). A cosmic-ray electron spectrum with veritas. URL: https://doi.org/10.48550/arxiv.1508.06597.

Stone, R. C. (1996). An accurate method for computing atmospheric refraction. *Publications of the Astronomical Society of the Pacific*, 108(729):1051. URL: https://dx.doi.org/10.1086/133831.

Strong, A. and Moskalenko, I. (2001). Models for galactic cosmic-ray propagation. *Advances in Space Research*, 27(4):717–726. URL: https://www.sciencedirect.com/science/article/pii/S0273117701001120.

Strong, A. W., Moskalenko, I. V., and Reimer, O. (2004). Diffuse galactic continuum gamma rays: A model compatible with egret data and cosmic-ray measurements. *The Astrophysical Journal*, 613(2):962. URL: https://dx.doi.org/10.1086/423193.

Sturner, S. J., Skibo, J. G., Dermer, C. D., and Mattox, J. R. (1997). Temporal evolution of nonthermal spectra from supernova remnants. *The Astrophysical Journal*, 490(2):619. URL: https://dx.doi.org/10.1086/304894.

Sturrock, P. A. (1971). A Model of Pulsars. *apj*, 164:529. URL: https://ui.adsabs.harvard.edu/abs/1971ApJ...164..529S.

Tatischeff, V. (2009). Radio emission and nonlinear diffusive shock acceleration of cosmic rays in the supernova SN 1993j. *Astronomy & Astrophysics*, 499(1):191–213. URL: https://doi.org/10.1051%2F0004-6361%2F200811511.

Taylor, J. H., Manchester, R. N., and Lyne, A. G. (1993). Catalog of 558 Pulsars. *apjs*, 88:529. URL: https://ui.adsabs.harvard.edu/abs/1993ApJS...88..529T.

Tescaro, D. (2012). The upgraded readout system of the magic telescopes. In *2012 IEEE Nuclear Science Symposium and Medical Imaging Conference Record (NSS/MIC)*, pages 1901–1904. URL: https://ieeexplore.ieee.org/document/6551440.

Tong, H. (2015). Pulsar braking: magnetodipole vs. wind. *Science China Physics, Mechanics & Astronomy*, 59(1). URL: https://doi.org/10.1007%2Fs11433-015-5752-x.

Truelove, J. K. and McKee, C. F. (1999). Evolution of nonradiative supernova remnants. *The Astrophysical Journal Supplement Series*, 120(2):299. URL: https://dx.doi.org/10.1086/313176.

Unger, M., Farrar, G. R., and Anchordoqui, L. A. (2015). Origin of the ankle in the ultrahigh energy cosmic ray spectrum, and of the extragalactic protons below it. *Physical Review D*, 92(12). https://doi.org/10.1103%2Fphysrevd.92.123001.

Velazquez, P. F., Gomez, D. O., Dubner, G. M., de Castro, G. G., and Costa, A. (1998). Study of the Rayleigh-Taylor instability in Tycho's supernova remnant. *aap*, 334:1060–1067. URL: https://ui.adsabs.harvard.edu/abs/1998A&A...334.1060V.

Venter, C. (2017). New advances in pulsar magnetosphere modelling. URL: https://arxiv.org/abs/1702.00732.

Weekes, T. C., Cawley, M. F., Fegan, D. J., Gibbs, K. G., Hillas, A. M., Kowk, P. W., Lamb, R. C., Lewis, D. A., Macomb, D., Porter, N. A., Reynolds, P. T., and Vacanti, G. (1989). Observation of TeV Gamma Rays from the Crab Nebula Using the Atmospheric Cerenkov Imaging Technique. *apj*, 342:379. URL: https://ui.adsabs.harvard.edu/abs/1989ApJ...342..379W.

Will, M. (2017). Atmospheric Monitoring at the Site of the MAGIC Telescopes. In *European Physical Journal Web of Conferences*, volume 144 of *European Physical Journal Web of Conferences*, page 01002. URL: https://ui.adsabs.harvard.edu/abs/2017EPJWC.14401002W.

Woltjer, L. (1972). Supernova Remnants. *araa*, 10:129. URL: https://ui.adsabs.harvard.edu/abs/1972ARA&A..10..129W.

Workman, R. L. and Others (2022). Review of Particle Physics. *PTEP*, 2022:083C01. URL: https://pdg.lbl.gov/2022/reviews/rpp2022-rev-cosmic-rays.pdf.

Yamazaki, R., Kohri, K., Bamba, A., Yoshida, T., Tsuribe, T., and Takahara, F. (2006). TeV γ-rays from old supernova remnants. *Monthly Notices of the Royal Astronomical Society*, 371(4):1975–1982. URL: https://doi.org/10.1111%2Fj.1365-2966.2006.10832.x.

Yin, P.-F., Yu, Z.-H., Yuan, Q., and Bi, X.-J. (2013). Pulsar interpretation for the ams-02 result. *Phys. Rev. D*, 88:023001. URL: https://link.aps.org/doi/10.1103/PhysRevD.88.023001.

Zanin, R. (2013). MARS, the MAGIC analysis and reconstruction software. In *33rd International Cosmic Ray Conference*, page 0773. URL: https://inspirehep.net/literature/1412925.

Zhang, L. and Cheng, K. S. (2001). Cosmic-ray positrons from mature gamma-ray pulsars. *aap*, 368:1063–1070. URL: https://ui.adsabs.harvard.edu/abs/2001A&A...368.1063Z.

Zhao, F., Tang, Z.-C., Li, Z.-H., Zhang, C., Sun, Z.-T., Zhang, F.-Z., Hu, J.-Y., Chen, G.-M., and Chen, H.-S. (2021). Improvement of cosmic-ray proton measurement with the electromagnetic calorimeter of the alpha magnetic spectrometer. *Radiation Detection Technology and Methods*, 5:90–94. URL: https://link.springer.com/article/10.1007/s41605-020-00222-9.

Zwicky, F. (1937). On the Masses of Nebulae and of Clusters of Nebulae. *apj*, 86:217. URL: https://ui.adsabs.harvard.edu/abs/1937ApJ....86..217Z.

Acknowledgements

First, I would like to express my heartfelt gratitude to my supervisors Prof. Masahiro Teshima. Thank you for providing the opportunity to a shy and nervous girl like me to study and work at the Max-Planck-Institut für Physik. I am truly thankful for your support and trust, even when there was little progress during the initial three years. I also wish to extend my sincere appreciation to my official supervisor, Prof. Christian Kiesling. Thank you for accepting me as your student at the Ludwig-Maximilian-Universität München. Your genuine interest, and invaluable and timely feedback have been crucial to my academic journey.

I want to thank my additional supervisors. Dr. David Green, thank you for proposing this topic to me and for your continuous support and invaluable guidance throughout, and Dr. David Paneque, thank you for your expert advice and patient mentorship on this topic. I must also acknowledge Dr. Razmik Mirzoyan, whose expertise ignited my passion for this field.

I also want to thank my electron team members, Dr. Kazuma Ishio, Dr. Daniel Kerszberg and Dr. Salvatore Mangano. Your active involvement, valuable advice and discussion have been a constant source of inspiration for me to continue this project, even during the countless moments of hopelessness.

I extend my heartfelt gratitude to all the current and former researchers within our group who welcomed me into MPP. Dr. Yusuke Suda's insightful suggestions greatly contributed to the project. Dr. Martine Will's comprehensive knowledge of telescopes proved invaluable in enhancing my understanding. Dr. Giovanni Ceribella is so knowledgeable and supportive when it comes to helping with my research and so considerate as a friend in my life. Dr. Alessio Berti has offered valuable advice for my thesis and has been a strong supporter of this project in the collaboration. Alexander Hahn, no matter what time I need his help, he is always there to give me a hand. Juliane van Scherpenberg's continuous encouragement to engage in group activities has helped integrate me into both the team and the country. Dr. Lea Heckmann is capable of taking care of everything when working with her. Of course all the wonderful girls – Dr. Lea Heckmann, Juliane van Scherpenberg, Marine Pihet, Angela Bautisa, and Elli Jobst – who organized and shared many unforgettable girls' nights with me.

I would also like to acknowledge the fresh perspectives brought by those who joined the group after me: Dr. Axel Arbet-Engels, Jarred Green, Dr. Seiya Nozaki, Giorgio Pirola and Felix Schmuckermeier.

Furthermore, I want to extend my appreciation to Diana Werner, our group's secretary. Whenever I seek her help, she can always find a way to solve all the problems.

Lastly, I would like to thank my family. Their unwavering trust and support have served as constant pillars throughout this challenging yet profoundly meaningful journey.